

Technical Report Documentation Page

1. Report No. FHWA/TX-13/0-6491-1		2. Government Accession No.		3. Recipient's Catalog No.	
4. Title and Subtitle Non-Destructive Evaluation of In-Service Concrete Structures Affected by Alkali-Silica Reaction (ASR) or Delayed Ettringite Formation (DEF)—Final Report, Part I				5. Report Date October 2012; Published April 2013	
				6. Performing Organization Code	
7. Author(s) E. Giannini, K. Folliard, J. Zhu, O. Bayrak, K. Kreitman, Z. Webb, and B. Hanson				8. Performing Organization Report No. 0-6491-1	
9. Performing Organization Name and Address Center for Transportation Research The University of Texas at Austin 1616 Guadalupe St., Suite 4.202 Austin, TX 78701 Texas A&M Transportation Institute The Texas A&M University System College Station, Texas 77843-3135				10. Work Unit No. (TRAIS)	
				11. Contract or Grant No. 0-6491	
12. Sponsoring Agency Name and Address Texas Department of Transportation Research and Technology Implementation Office P.O. Box 5080 Austin, TX 78763-5080				13. Type of Report and Period Covered Technical Report; 9/1/2009–8/31/2012	
				14. Sponsoring Agency Code	
15. Supplementary Notes Project performed in cooperation with the Texas Department of Transportation and the Federal Highway Administration.					
16. Abstract Alkali-silica reaction (ASR) and delayed ettringite formation (DEF) are expansive reactions that can lead to the premature deterioration of concrete structures. Both have been implicated in the deterioration of numerous structures around the world, including many transportation structures in Texas. Research on various aspects of ASR has been conducted since the late 1930s and has led to the identification of the mechanism of the reaction and subsequent expansion, as well as measures to prevent its occurrence in new construction. It consists of a reaction between alkali hydroxides in the pore solution and certain forms of silica in aggregate particles; with sufficient moisture, the product of the reaction swells and leads to expansion and cracking of the concrete. Eliminating any one of these components will prevent deleterious effects.					
17. Key Words ASR, DEF, non-destructive, alkali-silica reaction, delayed ettringite formation, concrete structures			18. Distribution Statement No restrictions. This document is available to the public through the National Technical Information Service, Springfield, Virginia 22161; www.ntis.gov.		
19. Security Classif. (of report) Unclassified	20. Security Classif. (of this page) Unclassified	21. No. of pages 228		22. Price	



Non-Destructive Evaluation of In-Service Concrete Structures Affected by Alkali-Silica Reaction (ASR) or Delayed Ettringite Formation (DEF)—Final Report, Part I

Eric R Giannini
Kevin J. Folliard
Jinying Zhu
Oguzhan Bayrak
Kerry Kreitman
Z. Webb
Brian Hanson

CTR Technical Report:	0-6491-1
Report Date:	October 2012
Project:	0-6491
Project Title:	Non-Destructive Evaluation of In-Service Concrete Structures Affected by Alkali-Silica Reaction (ASR) or Delayed Ettringite Formation (DEF)
Sponsoring Agency:	Texas Department of Transportation
Performing Agency:	Center for Transportation Research at The University of Texas at Austin Texas A&M Transportation Institute

Project performed in cooperation with the Texas Department of Transportation and the Federal Highway Administration.

Center for Transportation Research
The University of Texas at Austin
1616 Guadalupe St., Suite 4.202
Austin, TX 78701
www.utexas.edu/research/ctr

Copyright (c) 2012
Center for Transportation Research
The University of Texas at Austin

All rights reserved
Printed in the United States of America

Disclaimers

Author's Disclaimer: The contents of this report reflect the views of the authors, who are responsible for the facts and the accuracy of the data presented herein. The contents do not necessarily reflect the official view or policies of the Federal Highway Administration or the Texas Department of Transportation (TxDOT). This report does not constitute a standard, specification, or regulation.

Patent Disclaimer: There was no invention or discovery conceived or first actually reduced to practice in the course of or under this contract, including any art, method, process, machine manufacture, design or composition of matter, or any new useful improvement thereof, or any variety of plant, which is or may be patentable under the patent laws of the United States of America or any foreign country.

Notice: The United States Government and the State of Texas do not endorse products or manufacturers. If trade or manufacturers' names appear herein, it is solely because they are considered essential to the object of this report.

Engineering Disclaimer

NOT INTENDED FOR CONSTRUCTION, BIDDING, OR PERMIT PURPOSES.

Project Engineer: Dr. David W. Fowler
Professional Engineer License State and Number: Texas No. 27859
P. E. Designation: Researcher

Acknowledgments

The authors express appreciation to the TxDOT Project Director (Mr. Kevin Pruski), members of the Project Monitoring Committee, and the staff at the Concrete Durability Center.

Table of Contents

Chapter 1. Introduction.....	1
1.1 Background.....	1
1.2 Project Overview	2
1.3 Report Summary.....	4
Chapter 2. Literature Review	5
2.1 Overview.....	5
2.2 Deterioration Mechanisms.....	5
2.2.1 Alkali-Silica Reaction (ASR).....	6
2.2.2 Delayed Ettringite Formation (DEF)	7
2.3 Effects of ASR and DEF.....	8
2.3.1 Cracking.....	9
2.3.2 Mechanical Properties of Concrete.....	10
2.3.3 Structural Behavior: Strength	10
2.3.4 Structural Behavior: Serviceability.....	11
2.4 Potentially Applicable Nondestructive Test Methods	11
2.4.1 Visual Inspection	12
2.4.2 Expansion Monitoring	13
2.4.3 Stress Wave Methods.....	13
2.4.4 Electromagnetic Methods	22
2.5 Core-Based Evaluation Methods	23
2.5.1 Mechanical Testing.....	24
2.5.2 Chemical Testing	27
2.5.3 Residual Expansion Testing.....	32
2.5.4 Petrographic Analysis	34
2.6 Current State of Practice: FHWA Protocol.....	37
Chapter 3. Exposure Site Specimens.....	41
3.1 Specimen Design and Construction	41
3.1.1 Materials and Mixture Proportions	41
3.1.2 Specimen Types and Fabrication	42
3.2 Experimental Program	47
3.2.1 Overview of Testing Program.....	47
3.2.2 Expansion Monitoring	49
3.2.3 In-Situ NDT	52
3.3 Results and Discussion: In-Situ Monitoring.....	64
3.3.1 Expansions	64
3.3.2 In-Situ NDT	68
3.3.3 Impact-Echo.....	72
3.4 Results and Discussion: Tests on Cores	76

3.4.1 NDT	78
3.4.2 Resonant Frequency	79
3.4.3 Mechanical Testing	80
3.4.4 Stiffness Damage Test	80
3.4.5 Elastic Modulus and Compressive Strength	83
3.4.6 Chemical Testing	85
3.4.7 Pore Solution Analysis	88
3.4.8 Residual Expansions	89
3.4.9 Petrographic Testing	92
3.5 Summary	93
Chapter 4. Small-Scale Mechanical Testing	95
4.1 Overview	95
4.2 Experimental Program	95
4.2.1 Materials and Mixture Proportions	95
4.2.2 Specimen Fabrication and Conditioning	97
4.2.3 Expansion Monitoring	98
4.2.4 Mechanical Testing	99
4.2.5 Resonant Frequency Testing	100
4.3 Results and Discussion	100
4.3.1 Expansions	100
4.3.2 Stiffness Damage Test	102
4.3.3 Elastic Modulus and Compressive Strength	108
4.3.4 Resonant Frequency Testing	112
4.4 Summary	113
Chapter 5. Full-Scale Beams: Fabrication and Monitoring	115
5.1 Overview	115
5.2 Specimen Design, Fabrication, and Conditioning	115
5.2.1 Design	116
5.2.2 Specimen Geometry and Reinforcement	116
5.2.3 Materials and Mixture Proportions	119
5.2.4 Instrumentation	120
5.2.5 Fabrication	121
5.2.6 Concrete Mixing and Placement	123
5.2.7 High-Temperature Curing	124
5.2.8 Conditioning Regime	125
5.3 Experimental Procedures	128
5.3.1 Match-Cured Prisms	128
5.3.2 Expansion Monitoring	129
5.3.3 In-Situ NDT	130
5.3.4 UPV and Impact-Echo	130
5.3.5 SASW and SWT	131
5.3.6 Nonlinear Acoustics	132
5.3.7 Full-Scale Dynamic Test	132

5.4 Results and Discussion	133
5.4.1 Match-Cured Specimens	134
5.4.2 Visual Observations	135
5.4.3 Expansions	136
5.4.4 In-Situ NDT	139
5.4.5 Impact-Echo	141
5.4.6 SASW and SWT	144
5.4.7 Nonlinear Acoustics	148
5.4.8 Full-Scale Dynamic Test	148
5.5 Summary	150
Chapter 6. Full-Scale Beams: Core Sample Testing.....	151
6.1 Core Sampling Protocol and Test Matrix	151
6.2 Experimental Procedures: Cores	153
6.2.1 Residual Expansion Tests	153
6.2.2 NDT	154
6.2.3 Mechanical Testing	154
6.2.4 Chemical Testing	154
6.2.5 Petrographic Analysis	154
6.3 Results and Discussion	155
6.3.1 Residual Expansion Testing	156
6.3.2 NDT	158
6.3.3 Mechanical Testing	158
6.3.4 Chemical Testing	163
6.3.5 Petrographic Analysis	164
6.4 Summary	169
Chapter 7. Full-Scale Beams: Flexural Behavior.....	171
7.1 Overview	171
7.2 Experimental Procedures	171
7.2.1 Preparation for Testing	171
7.2.2 Test Setup	172
7.2.3 Flexural Test Procedure	175
7.3 Flexural Capacity and Serviceability Predictions	176
7.3.1 Analysis Based on 28-Day Properties	177
7.3.2 Analysis Based on Core Properties	177
7.3.3 Alternate Approaches	178
7.4 Test Results	180
7.4.1 Loads and Deflections	180
7.4.2 Expansion Measurements	182
7.4.3 Visual Observations	182
7.5 Discussion of Results	184
7.5.1 Comparison to Core Properties and Expansions	185
7.5.2 Comparison to In-Situ NDT	186

7.5.3 Implications for Evaluating Structures	187
7.6 Summary.....	189
Chapter 8. Conclusions.....	191
8.1 Overview.....	191
8.2 Conclusions.....	191
8.3 Recommendations for Evaluation of Structures	193
8.4 Synthesis	194
8.5 Recommendations for Future Work	196
References.....	199

List of Figures

Figure 1.1: TxDOT 0-6491 overview.	3
Figure 2.1: Mechanism of alkali-silica reaction, from Kreitman 2011.....	6
Figure 2.2: Mechanism of delayed ettringite formation, adapted from Kreitman 2011.	8
Figure 2.3: Crushing failure of pavement from ASR, from Swamy 1992.....	9
Figure 2.4: Crack patterns of (a) plain concrete and (b) reinforced concrete, from Kreitman 2011.	10
Figure 2.5: Fractured stirrups in ASR-affected bridge piers in Japan, from Miyagawa, et al. 2006; Torii, et al. 2008.....	11
Figure 2.6: Compression and shear wave propagation, from Kreitman 2011.	13
Figure 2.7: Surface wave and Lamb wave propagation, from Kreitman 2011.....	14
Figure 2.8: Typical UPV test setup, from Kreitman 2011.....	15
Figure 2.9: Conventional impact-echo theory, showing (a) undamaged concrete and (b) concrete with an internal defect, adapted from Sansalone and Streett 1997.	17
Figure 2.10: Noisy frequency spectrum from ASR-affected bridge deck, from Henriksen 1995.....	18
Figure 2.11: Impact and accelerometer locations for (a) longitudinal and (b) transverse modes of vibration, adapted from ASTM C215-08 2008.	18
Figure 2.12: Resonant frequency test results: (a) time domain signal and (b) frequency spectrum, from Kreitman 2011.....	19
Figure 2.13: Resonant frequency shift test results, from Chen, et al. 2010.....	20
Figure 2.14: Phase shift and amplitude variation in time shift nonlinear acoustic testing, from Kodjo, et al. 2009.....	21
Figure 2.15: Surface wave test setup, from Kreitman 2011.	22
Figure 2.16: Electromagnetic stress measurements of a steel pipeline, from Lasseigne 2012.....	23
Figure 2.17: Typical stiffness damage test data.....	25
Figure 2.18: Gel pat test specimen at 56 days, from Fournier 2009.....	35
Figure 2.19: FHWA flowchart for evaluation and management of ASR-affected structures, from Fournier, et al. 2010.....	38
Figure 3.1: Reinforcement sketch of Jobe (F1) blocks 2 and 4.	44
Figure 3.2: On-grade slab before (left) and after (right) concrete placement.....	45
Figure 3.3: Column reinforcement schematic.....	45
Figure 3.4: Bridge deck reinforcement and supports.....	46

Figure 3.5: Bridge deck forms (left) and completed specimen on rail ties (right).....	47
Figure 3.6: Sequence of core testing.....	49
Figure 3.7: Mayes Instruments DEMEC strain gauge.....	50
Figure 3.8: Expansion measurement locations for exposure block specimen.....	50
Figure 3.9: Expansion measurement locations for on-grade slab specimen.....	51
Figure 3.10: Column expansion measurements—vertical (left) and circumference with PI tape (right), from Bentivegna 2009.....	51
Figure 3.11: UPV measurement locations for exposure site specimens.....	52
Figure 3.12: Impact echo test equipment.....	53
Figure 3.13: Impact-echo locations for bridge deck and column.....	54
Figure 3.14: Surface wave test equipment.....	54
Figure 3.15: Surface wave sensor (circles) and impact (X's) locations for bridge deck and column.....	55
Figure 3.16: Coring rig mounted on exposure block.....	56
Figure 3.17: Resonant frequency test equipment.....	57
Figure 3.18: Core sample instrumented for transverse (left) and longitudinal (right) resonant frequency measurements.....	57
Figure 3.19: Stiffness damage test setup.....	58
Figure 3.20: Pulverized concrete sample before (L) and after (R) boiling.....	59
Figure 3.21: Collection vial and base piece.....	61
Figure 3.22: Assembled pore solution expression apparatus.....	62
Figure 3.23: Average expansions of the Jobe (F1) exposure blocks.....	65
Figure 3.24: Average expansions of the Wright (F7) exposure blocks.....	65
Figure 3.25: Average expansions of the El Indio (C2) exposure blocks.....	66
Figure 3.26: Transverse to longitudinal expansion ratio of Jobe (F1) blocks.....	66
Figure 3.27: Expansion data for selected slab and deck specimens.....	67
Figure 3.28: Expansion data for selected columns.....	68
Figure 3.29: Average initial velocity for exposure blocks (1 m/s = 3.28 ft/s).....	69
Figure 3.30: Change in UPV vs. average expansion for Jobe (F1) exposure blocks.....	70
Figure 3.31: Change in transverse and longitudinal UPV vs. average (left) and directional (right) expansion, Blocks 2 and 4.....	70
Figure 3.32: Change in UPV vs. average expansion for Wright (F7) exposure blocks.....	71
Figure 3.33: Change in UPV vs. average expansions for El Indio (C2) exposure blocks.....	71
Figure 3.34: Change in UPV vs. average expansion of columns.....	72

Figure 3.35: P-wave velocities vs. expansion for Slab 3 and Deck 3 (1 m/s = 3.28 ft/s).	74
Figure 3.36: Change in 16 kHz phase velocity vs. expansion for Jobe (F1) exposure blocks.	75
Figure 3.37: Normalized transmission coefficients vs. expansion for Jobe (F1) exposure blocks.	76
Figure 3.38: UPV vs. expansion for core samples. (1 m/s = 3.28 ft/s).	79
Figure 3.39: Dynamic modulus of elasticity (from resonant frequency tests) vs. expansion for core samples (145 ksi = 1 GPa).	80
Figure 3.40: Sample SDT data and analysis parameters.	81
Figure 3.41: Averaged 1 st Cycle Area vs. expansion for core samples.	82
Figure 3.42: Averaged total plastic strain for core samples.	82
Figure 3.43: Averaged elastic moduli vs. expansion of core samples.	84
Figure 3.44: Averaged compressive strength vs. expansion of core samples.	84
Figure 3.45: Water-soluble alkalis vs. average block expansion.	87
Figure 3.46: Residual expansions and mass gain of Wright (F7) exposure block cores.	91
Figure 3.47: Residual expansions and mass gain of El Indio (C2) exposure block cores.	92
Figure 4.1: Curing temperature profile to promote DEF.	97
Figure 4.2: Cylinders in ramping oven used for high-temperature curing cycle.	98
Figure 4.3: Averaged expansions of Jobe (F1) reference cylinders.	101
Figure 4.4: Averaged expansions of Placitas (C10) reference cylinders.	101
Figure 4.5: DEF cylinder with open crack at surface.	102
Figure 4.6: Typical SDT stress-strain data for Jobe (F1) ASR cylinders (1 MPa = 145 psi).	103
Figure 4.7: Averaged 1 st Cycle Area vs. expansion for Jobe (F1) cylinders.	104
Figure 4.8: Averaged 1 st Cycle Area vs. expansion for Placitas (C10) cylinders.	105
Figure 4.9: Averaged total plastic strain vs. expansion for Jobe (F1) cylinders.	106
Figure 4.10: Averaged total plastic strain vs. expansion for Placitas (C10) cylinders.	106
Figure 4.11: Averaged elastic moduli vs. expansion of Jobe (F1) cylinders.	109
Figure 4.12: Averaged elastic moduli vs. expansion of Placitas (C10) cylinders.	109
Figure 4.13: Averaged compressive strength vs. expansion of Jobe (F1) cylinders.	110
Figure 4.14: Averaged compressive strength vs. expansion of Placitas (C10) cylinders.	110
Figure 4.15: Linear resonant frequency results (E_d vs. expansion).	112
Figure 4.16: Nonlinear resonant frequency results for Placitas (C10) cylinders.	113
Figure 5.1: Timeline of beam fabrication and conditioning, from Kreitman 2011.	116

Figure 5.2: Cross-sectional view of beam specimen, from Kreitman 2011.....	117
Figure 5.3: Elevation view of beam specimen, from Kreitman 2011.....	118
Figure 5.4: Instrumentation layout for beam specimens, from Kreitman 2011.....	120
Figure 5.5: Targets for mechanical expansion measurements, from Kreitman 2011.....	121
Figure 5.6: Full-scale beam fabrication process, from Kreitman 2011.....	122
Figure 5.7: Sure Cure cylinder molds, from Kreitman 2011.....	123
Figure 5.8: Temperature evolution with time for beam specimens (1 °C = 1.8 °F), from Kreitman 2011.....	124
Figure 5.9: Distribution of maximum temperatures through specimen cross section (1 °C = 1.8 °F), from Kreitman 2011.....	125
Figure 5.10: Beam specimens in outdoor exposure and under load, from Kreitman 2011.....	126
Figure 5.11: Loads and reactions (top) and shear and moment diagrams (bottom), from Kreitman 2011.....	127
Figure 5.12: Load conditioning setup, from Kreitman 2011.....	127
Figure 5.13: Match-cured prisms in storage bucket (a), and being measured for length change (b), from Kreitman 2011.....	128
Figure 5.14: Expansion measurement system, from Kreitman 2011.....	129
Figure 5.15: Expansion measurements and target locations, from Kreitman 2011.....	130
Figure 5.16: Locations of UPV and impact-echo measurements, from Kreitman 2011.....	131
Figure 5.17: Schematic of surface wave test grid, from Kreitman 2011.....	131
Figure 5.18: Nonlinear acoustic test setup for beam specimens, from Kreitman 2011.....	132
Figure 5.19: Impacts for dynamic testing of beam specimen.....	133
Figure 5.20: Expansions of match-cured prism specimens in ASTM C1293 conditions, from Kreitman 2011.....	134
Figure 5.21: Average dynamic moduli of match-cured prisms vs. expansion, from Kreitman 2011.....	135
Figure 5.22: Cracking of second reactive specimen at one year of age, from Kreitman 2011.....	136
Figure 5.23: Expansions for beam specimens.....	138
Figure 5.24: UPV vs. vertical expansion of beam specimens.....	140
Figure 5.25: Typical impact-echo frequency spectra for beam specimens, from Kreitman 2011.....	142
Figure 5.26: Compression wave velocities vs. vertical expansion of beam specimens, (1 m/s = 3.28 ft/s), from Kreitman 2011.....	143
Figure 5.27: Compression wave velocities from UPV and IE testing of second reactive specimen (1 m/s = 3.28 ft/s).....	144

Figure 5.28: Surface wave velocity vs. vertical expansion of beam specimens, (1 m/s = 3.28 ft/s), from Kreitman 2011.	145
Figure 5.29: Surface wave velocity vs. time for nonreactive specimen (1 m/s = 3.28 ft/s), from Kreitman 2011.	146
Figure 5.30: Surface wave transmission coefficients vs. vertical expansion of beam specimens, from Kreitman 2011.	147
Figure 5.31: Surface wave transmission vs. time for nonreactive specimen, from Kreitman 2011.	148
Figure 5.32: Representative frequency spectra for longitudinal mode dynamic tests.	149
Figure 6.1: Extraction of 2 in. (51 mm) diameter cores from second reactive specimen and repaired core holes.	152
Figure 6.2: 4 in. (100 mm) diameter core locations for first reactive beam.	153
Figure 6.3: Residual expansion tests of beam cores.	157
Figure 6.4: SDT—1 st Cycle Area of beam cores compared to cylinder tests.	160
Figure 6.5: SDT—Total Plastic Strain of beam cores compared to cylinder tests.	160
Figure 6.6: Elastic moduli of beam cores compared to cylinder tests.	162
Figure 6.7: Compressive strength of beam cores compared to cylinder tests.	163
Figure 6.8: Photomicrograph of polished section showing (a) microcracks in fine aggregate particles and (b) ASR gel in a void, from Rothstein 2012b.	166
Figure 6.9: Normalized DRI scores, including all features related to ASR and DEF, adapted from Rothstein 2012b.	167
Figure 6.10: Normalized DRI scores, counting only DEF-related features, adapted from Rothstein 2012b.	168
Figure 6.11: Reflected light (a and b) and backscatter SEM (c and d) images of ettringite deposits (indicated by arrows) in the ITZ around aggregate particles, from Rothstein 2012b.	169
Figure 7.1: Expansions of specimens after removal of conditioning load.	172
Figure 7.2: Schematic of test setup for four point flexural loading, from Hanson 2012.	173
Figure 7.3: First reactive specimen in test setup (top), free body, shear and moment diagrams (bottom), adapted from Kreitman 2011.	174
Figure 7.4: Roller-bearing assembly at applied load.	175
Figure 7.5: Electromagnetic sensors, second reactive specimen.	176
Figure 7.6: Overall approach for predicting nominal moment capacity, from Hanson 2012.	176
Figure 7.7: Confinement in reinforced concrete affected by ASR and DEF, from Webb 2011.	179

Figure 7.8: Load vs. deflection for all specimens.....	181
Figure 7.9: Crack propagation in middle region of test specimens.	183
Figure 7.10: Crushing failure, first reactive specimen.....	184
Figure 7.11: Comparison of specimen flexural stiffness, core elastic modulus and core compressive strength.....	186

List of Tables

Table 2.1: Interpretation of residual expansion results: testing at >95% RH and 100°F (38°C), from Fournier, et al. 2010.	33
Table 2.2: Classification of expansion potential, from Bérubé, et al. 2000.	33
Table 2.3: Expansion tests for the diagnosis of potential for ASR, DEF or combination of mechanisms, from Folliard, Thomas, and Fournier 2007.	34
Table 2.4: Typical DRI weighting factors for ASR, adapted from Grattan-Bellew and Mitchell 2006.	36
Table 2.5: Investigation tools for evaluating ASR-affected structures, from Fournier, et al. 2010.	39
Table 3.1: Aggregates used in exposure site specimens.	41
Table 3.2: Mixture proportions for exposure site specimens.	42
Table 3.3: Exposure site specimens.	43
Table 3.4: NDT program for exposure site specimens.	48
Table 3.5: Core sample testing program for exposure site specimens.	48
Table 3.6: P-wave velocities from UPV and Impact-echo tests. (1 m/s = 3.28 ft/s).....	73
Table 3.7: List of cores extracted from Wright (F7) exposure blocks.	77
Table 3.8: List of cores extracted from El Indio (C2) exposure blocks.	78
Table 3.9: SDT results for exposure block cores.	83
Table 3.10: Elastic modulus and compressive strength results for exposure block cores.	85
Table 3.11: Water-soluble alkali results, Wright (F7) cores.	86
Table 3.12: Water-soluble alkali results, El Indio (C2) cores.	86
Table 3.13: Comparison of hot vs. cold water extracted water-soluble alkalis.	87
Table 3.14: Water-soluble alkalis in Wright (F7) and Jobe (F1) sands.	88
Table 3.15: Pore solution analysis.	89
Table 3.16: Residual expansion summary.	90
Table 4.1: Summary of small-scale mechanical test program.	95
Table 4.2: Aggregates used in small-scale test specimens.	96
Table 4.3: Mixture proportions for small-scale test specimens.	96
Table 4.4: SDT results for ASR cylinders.	107
Table 4.5: SDT results for ASR+DEF cylinders.	108
Table 4.6: SDT results for DEF cylinders.	108
Table 4.7: Elastic modulus and compressive strength results for ASR cylinders.	111

Table 4.8: Elastic modulus and compressive strength results for ASR+DEF cylinders.....	111
Table 4.9: Elastic modulus and compressive strength results for DEF cylinders.....	112
Table 5.1: As-batched mixture proportions and 28-day strengths.....	120
Table 5.2: Full-scale dynamic test results after unloading of beams.....	149
Table 6.1: Core sample testing program.....	151
Table 6.2: DRI weighting factors, from Rothstein 2012b.....	155
Table 6.3: UPV and Resonant Frequency results for beam cores.....	158
Table 6.4: SDT Data for beam cores.....	159
Table 6.5: Elastic modulus and compressive strength data for beam cores.....	161
Table 6.6: Water-soluble alkali results for beam cores.....	163
Table 6.7: Normalized DRI analysis, from Rothstein 2012b.....	167
Table 7.1: Predicted moment capacities and deflections based on 28 day strength.....	177
Table 7.2: Predicted moment capacities and deflections based on core properties.....	178
Table 7.3: Predicted and measured moment capacities.....	181
Table 7.4: Predicted and measured deflections at mid-span.....	181
Table 7.5: Reinforcement strains in middle test region before and after loading.....	182
Table 7.6: Comparison of deflections to expansions and mechanical properties of core samples.....	185
Table 7.7: Comparison of full-scale dynamic test results and flexural stiffness.....	187
Table 8.1: Summary of tests performed.....	195

Chapter 1. Introduction

1.1 Background

Alkali-silica reaction (ASR) and delayed ettringite formation (DEF) are expansive reactions that can lead to the premature deterioration of concrete structures. Both have been implicated in the deterioration of numerous structures around the world, including many transportation structures in Texas. The value of affected transportation structures under the jurisdiction of the Houston District of the Texas Department of Transportation (TxDOT) was estimated at \$1 billion in 2008 (Deschenes 2009).

Research on various aspects of ASR has been conducted since the late 1930s and has led to the identification of the mechanism of the reaction and subsequent expansion, as well as measures to prevent its occurrence in new construction. It consists of a reaction between alkali hydroxides in the pore solution and certain forms of silica in aggregate particles; with sufficient moisture, the product of the reaction swells and leads to expansion and cracking of the concrete. Eliminating any one of these components will prevent deleterious effects.

DEF is a form of internal sulfate attack, and is primarily the consequence of curing temperatures in excess of 158 °F (70 °C). Heat-curing of concrete has been commonly used to increase the rate of strength gain in precast structural elements, and similar curing temperatures can occur in mass concrete elements. DEF should be avoidable in new construction through limitations on the maximum curing temperature and/or through the use of DEF-resistant binders (e.g., containing 30 percent or more Class F fly ash).

What remains is the problem of evaluating and managing the existing stock of structures damaged by these mechanisms. Considerable research has been conducted in both of these areas. Unfortunately, once these forms of distress are identified, there appears to be little in the way of effective mitigation options. It is also not economically feasible to simply demolish and reconstruct every affected structure. Therefore, management decisions will rely on the effective evaluation of the extent of distress.

The most recent protocol for the evaluation of ASR-affected structures has been published by the United States Federal Highway Administration (FHWA) (Fournier, et al. 2010), and a similar document is expected to be published by RILEM in late 2012 or early 2013. Guidance for structures affected by ASR and DEF was published by TxDOT in 2007 (Folliard, Thomas and Fournier 2007). Earlier guidance that has served as the foundation for the above documents has been published by CSA International (2000), the European Community Innovation Programme CONTECVET (2000) and the British Institute of Structural Engineers (ISE 1992).

Published guidance relies primarily on the use of core samples for the diagnosis of ASR and DEF, determination of the effects of the mechanical properties of the concrete, and the potential for future distress. Quantification of surface cracking is also recommended to obtain a rough estimate the expansion of the concrete to date and track the progression of damage with time. Most of the documents listed provide only limited guidance on assessing the structural effects of ASR (in some cases, less than one page). They do note that in reinforced structures, the load carrying capacity and serviceability are typically much better than mechanical tests of cores of the visual appearance of the structure would suggest. The exceptions are the ISE and CONTECVET guidance documents; the latter includes several appendices regarding structural

effects and strength assessment, and recommends linear elastic analyses for ASR-affected structures.

While the published guidance is very effective at diagnosing the presence of ASR and DEF, there remain significant weaknesses with respect to the evaluation of structural safety and serviceability. First, structural analyses procedures remain based on the mechanical properties of concrete either derived from core samples, or estimated based on a visual assessment of surface cracking. This is despite the fact that these mechanical properties have little apparent influence on the performance of the overall structure, when ASR or DEF are present. Second, the published guidance documents do not recommend significant use of nondestructive testing (NDT) aside from visual inspection and ultrasonic pulse velocity (UPV). Core samples can provide a great deal of information about the condition of the concrete at selected locations at a single point in time, while NDT can be used to assess the condition of large areas of a structure. Repeated NDT measurements can be made over long periods of time to monitor changes in the condition of the structure.

Most research to date involving applications of NDT methods for assessing concrete affected by ASR and DEF have focused on small, unreinforced laboratory specimens. These behave very differently than large scale reinforced concrete structural elements, in which the scale of the structure and the confining effects of reinforcement play very important roles in the behavior of the structure. Such tests are necessary and certainly more convenient than testing field structures, for which there are too many uncertain variables that can affect measurements when developing a test method. However, field structures are the end concern. Therefore, it is essential that NDT methods be evaluated on larger scale structural elements in field exposure conditions with realistic reinforcement details.

ASR is comparatively more common than DEF. However, most observed cases of DEF in field structures have been accompanied by ASR, which is thought to play a contributing role in the development of DEF. Note that the expansions caused by the combination of ASR and DEF are frequently much greater than those caused by ASR alone. For this reason, it is important to assess the effects of both ASR and the combination of ASR and DEF, and to investigate the applicability of NDT methods to both cases.

1.2 Project Overview

The research presented in this report was funded as part of TxDOT project 0-6491, “Nondestructive Evaluation of In-Service Concrete Structures Affected by ASR and/or DEF.” This project took place from 2009 to 2012 and was conducted jointly by researchers at The University of Texas at Austin (UT-Austin) and Texas A&M University (TAMU). An overview of the project organization and scope is provided in Figure 1.1.

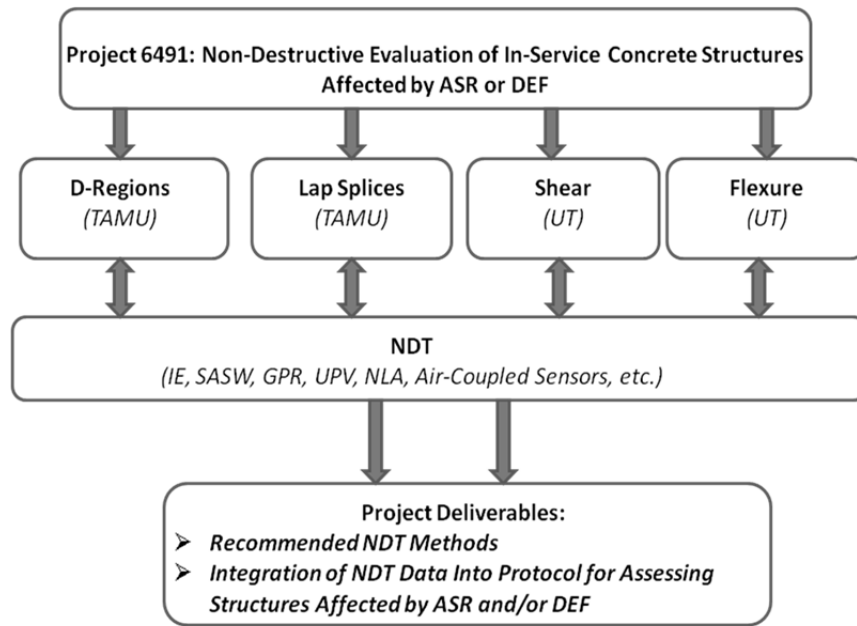


Figure 1.1: TxDOT 0-6491 overview.

Despite the title of the project, nondestructive testing and evaluation were not the sole focus of the project. However, a major goal of the project was to identify applicable NDT methods that could be integrated into the existing TxDOT evaluation protocol for structures affected by ASR or DEF (Folliard, Thomas, and Fournier 2007). In order to do so, the NDT methods were investigated for their ability to detect deterioration of concrete and to correlate to structural performance. To achieve this goal, both plain and reinforced concrete specimens were tested and structural testing of several failure modes was conducted.

The work at TAMU utilized specimens designed to test the effects of ASR and DEF on D-regions and the development length of lap splices. Impact-echo was also investigated as a potential tool for detecting debonding of reinforcement in affected structures. Preliminary results have been published (Pagnotta, Trejo, and Gardoni 2012), and the overall findings of the TAMU research is contained under separate cover as Part II of this final project report.

Researchers at UT-Austin conducted a wide range of tests on plain and reinforced concrete at multiple scales. This included small cylinders and prisms, larger plain and reinforced concrete specimens in outdoor exposure, full-scale reinforced concrete beams, and core samples from the outdoor exposure specimens and full-scale reinforced concrete beams. Many laboratory tests currently recommended by the FHWA and TxDOT guidance documents were conducted on the core samples, including mechanical tests, petrographic examination, chemical analyses, and residual expansion tests. Nondestructive test methods were applied at all scales, and the full-scale beams were also tested in four-point flexure to determine the effects of ASR and DEF on flexural strength and serviceability. Shear tests conducted on similar full-scale beam specimens fabricated for a previous project (Deschenes 2009) will be also be addressed in the final project report, but are not in the scope of this dissertation. This comprehensive test program allowed not only for an assessment of the ability of NDT methods to characterize concrete deterioration and correlate to structural performance, but also to compare their effectiveness to that of tests currently recommended in the FHWA and TxDOT guidance documents.

The author worked in partnership with three Masters students, each of whom has produced a thesis or report detailing part of the work conducted at UT-Austin. Kerry Kreitman (2011) presented the results of the in-situ monitoring of the full-scale beams through the summer of 2011. This dissertation includes updated data and analysis, as well as tests that have not previously been discussed. Zachary Webb presented a satellite study of the potential for rebar fracture in ASR- and DEF-affected concrete (2011); this study is not discussed further in this dissertation. Finally, Brian Hanson presented results and preliminary analysis of the flexural load tests conducted on the full-scale beams (2012). An expanded analysis is presented in this dissertation. Although these students' written work is primarily focused on structural aspects or nondestructive tests on the full-scale structural specimens, they also provided significant contributions with respect to the fabrication and testing of the smaller-scale specimen.

1.3 Report Summary

Chapter 2 provides a review of literature relevant to this study: the mechanism and effects of ASR and DEF, various test methods that may be used to evaluate affected structures, and FHWA protocol for evaluating ASR-affected structures. Particular emphasis will be given to topics not covered in theses of Kreitman (2011) and Webb (2011), which contain extensive reviews of nondestructive test methods and the structural effects of ASR and DEF. Chapter 3 details a simulated field investigation using plain and reinforced concrete elements in outdoor exposure. Chapter 4 presents an expanded investigation into the stiffness damage test (SDT) and the effects of ASR and DEF on the elastic modulus and compressive strength of laboratory specimens. Chapters 5 through 7 discuss the testing of full-scale reinforced concrete beams. Fabrication and in-situ monitoring are covered in Chapter 5, tests on core samples in Chapter 6, and the flexural load tests in Chapter 7. Much of the information in Chapters 5 through 7 has been previously presented in Kreitman's thesis and a report by Hanson (2012); however, this report is the first work that considers the aggregate of all the tests performed on the full-scale beams. Conclusions drawn from this research, as well as suggestions for future work and changes to the existing evaluation methodology are presented in Chapter 8.

Chapter 2. Literature Review

2.1 Overview

In recent decades, there has been a significant increase in the number of transportation structures affected by alkali-silica reaction (ASR) and delayed ettringite formation (DEF) in Texas. Deschenes (2009) provided a comprehensive review of the problem, although a few key points will be summarized herein. Infrastructure construction methods made frequent use of high-early strength cements, mixture proportions with high cement contents, and in some cases, steam curing of precast elements. This resulted in a large number of concrete structures with aggregates that were not previously known to be susceptible to ASR and elevated alkali loadings and that also experienced very high curing temperatures. In most cases, supplementary cementing materials (SCMs) were not used. The increased alkali contents compared to older structures were sufficient to induce ASR, while the high curing temperatures were sufficient to promote the development of DEF. Similar issues have plagued transportation structures elsewhere in the United States and around the world, particularly with respect to ASR.

Considerable research has been conducted on ASR, and a series of fourteen international conferences devoted to the subject (ICAARs) have been organized, beginning in 1974. The proceedings of these conferences contain a wealth of information on both laboratory research and case studies from around the world.

In response to what Deschenes termed an “outbreak” of ASR and DEF cases, the TxDOT has funded numerous research projects over the past two decades. This research has paralleled efforts by the FHWA to prevent ASR in new concrete (Ahlstrom, Mullarky and Faridazar 2008), and to improve the management of existing structures affected by ASR. The former goal has been largely successful—new test methods and improved construction practices should sharply reduce the number of cases of ASR and DEF from new construction. However, a large number of existing structures have shown signs of deterioration and may still develop deterioration in the future. The latter goal remains a work in progress, both with respect to evaluating structures and deciding a course of action based on the condition of the structure.

This chapter will review the state of practice with respect to the evaluation of existing structures affected by ASR and DEF. This will include a review of the two deterioration mechanisms (Section 2.2), their effects on concrete structures (Section 2.3), potentially applicable nondestructive test methods for in-situ evaluation (Section 2.4), core sample test methods (Section 2.5), and finally, a summary of the FHWA evaluation protocol (Section 2.6). Theses by Deschenes (2009), Kreitman (2011), and Webb (2011) have included an exhaustive review of the structural impacts of ASR and DEF, and nondestructive test methods. These will be covered to a more limited extent, to allow for an expanded discussion of core sample testing and the FHWA protocol.

2.2 Deterioration Mechanisms

ASR and DEF are expansive reactions that produce similar visual indications of distress (primarily surface cracking). However, the mechanism of each is significantly different. A short discussion of the two mechanisms is provided below.

2.2.1 Alkali-Silica Reaction (ASR)

Alkali silica reaction (ASR) in concrete is a deleterious chemical reaction between alkali hydroxides in the pore solution and reactive silica found in some aggregates. The reaction results in the formation of a hydrophilic gel (ASR gel) that swells in the presence of moisture. This causes expansion and cracking of concrete structures; the surface cracking can leave the concrete exposed to other deterioration mechanisms such as corrosion and frost action. As with many chemical reactions, higher temperatures will increase the rate of reaction, leading to more rapid development of distress in warmer climates. Figure 2.1 illustrates the mechanism of ASR.

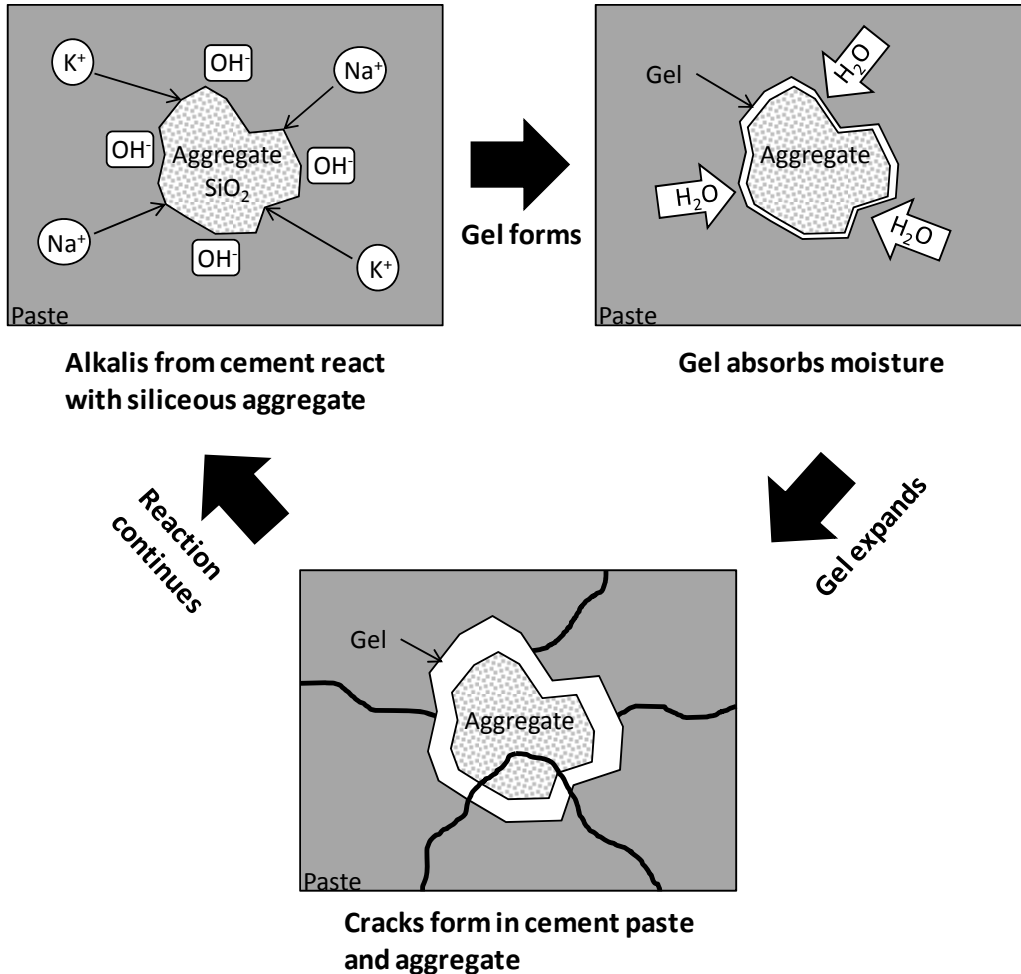


Figure 2.1: Mechanism of alkali-silica reaction, from Kreitman 2011.

The expansion can result in the misalignment of structural elements, closing of expansion joints and/or surface “popouts.” ASR was first identified by Stanton over 70 years ago as a cause of concrete deterioration (Stanton 1940). Since that time, ASR has been identified as a cause of deterioration of numerous concrete structures. Although research has yielded considerable success in understanding the mechanism of the reaction and how to minimize the risk of expansive ASR in new construction, knowledge of the structural effects of ASR and how to best assess the extent of damage to existing structures continues to lag, and remains a major topic of ongoing research.

2.2.2 Delayed Ettringite Formation (DEF)

Delayed Ettringite Formation (DEF) in concrete is a form of internal sulfate attack, driven by high curing temperatures and unfavorable cement chemistry (Kelham 1996, Folliard, et al. 2006). Many laboratory studies have confirmed that 70°C is the critical curing temperature for expansion due to DEF, but merely exceeding this temperature will not guarantee expansion, even for cements susceptible to DEF (Kelham 1996).

The hydration of cement and formation of C-S-H is greatly accelerated as curing temperature increases (Folliard, et al. 2006); this is consistent with the increased rate of early strength development. The rapidly growing “outer” C-S-H is somewhat different than that which forms at lower temperatures and traps dissolved sulfates before they can react to form ettringite, another normal product of cement hydration (Folliard, et al. 2006, Scrivener and Lewis 1999). With sustained temperatures above 70°C, ettringite becomes thermodynamically unstable and either does not form or returns to solution (Ramlochan, 2003). Based on thermodynamics and X-ray diffraction observations, other hydration products, stable at high temperatures, such as calcium monosulfoaluminate (monosulfate) and hydrogarnet form instead from the decomposing ettringite and remaining aluminates, ferrites, and sulfates in solution (Ghorab 1999, Ramlochan 2003).

Once temperatures return to “normal” levels experienced by concrete in service, thermodynamics favor the formation of ettringite. Trapped sulfates may be released from the C-S-H and react with water and monosulfate to form ettringite; this can lead to deleterious expansion and cracking of the concrete (Folliard et al, 2006). A simplified illustration of the mechanism of DEF is shown in Figure 2.2.

Curing at temperature > 158 °F (70 °C)

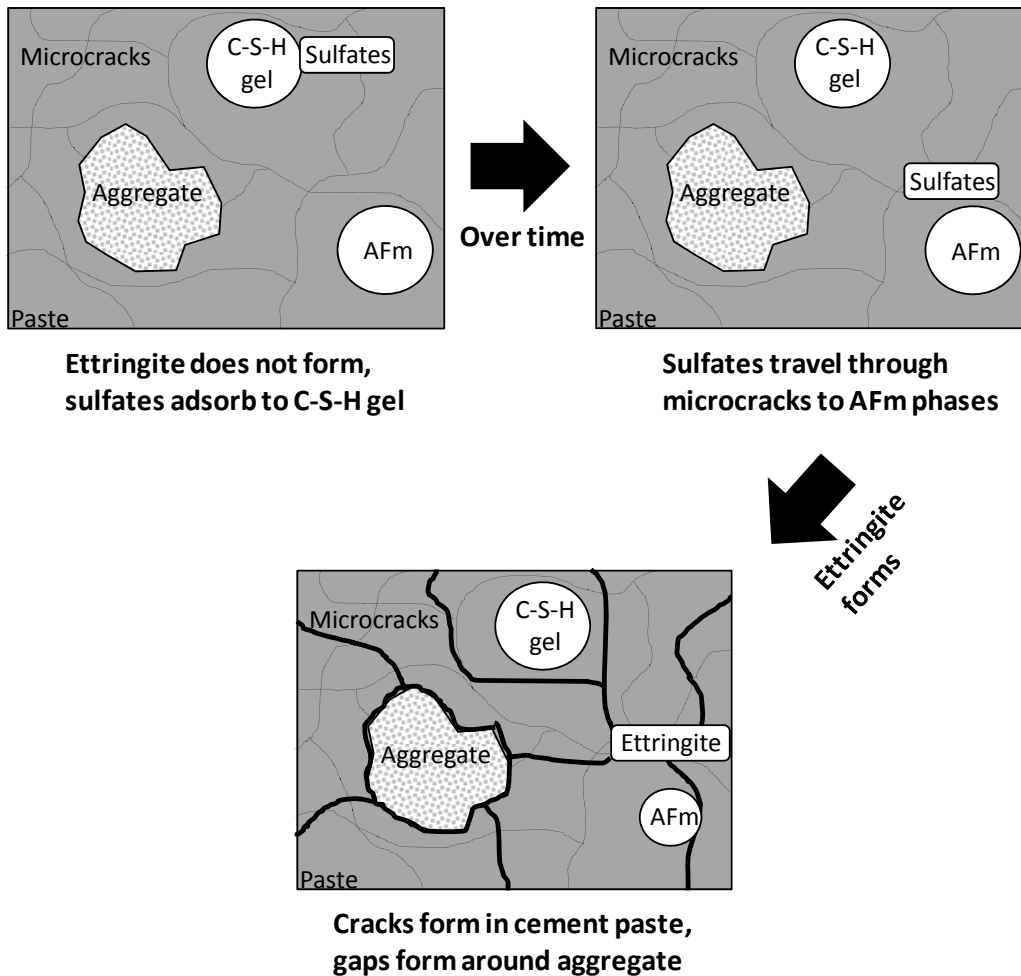


Figure 2.2: Mechanism of delayed ettringite formation, adapted from Kreitman 2011.

As with ASR, knowledge of the conditions needed to cause DEF should cause it to be rare or nonexistent in new construction. But there remain structures in service that have developed or may still develop distress from DEF. In most cases, DEF has been accompanied by ASR, and may have been triggered in part by ASR (Folliard et al. 2006); cases of DEF as the sole cause of distress are very rare (Thomas, et al. 2008).

2.3 Effects of ASR and DEF

The expansion and cracking caused by ASR and DEF affect both the concrete and, in reinforced structures, the reinforcing steel. Cracking is the most obvious sign of distress, however similar crack patterns can also be produced by other distress mechanisms, including drying shrinkage and other forms of sulfate attack. Popouts, or conical spalls above reacting aggregate particles, staining and discoloration from exuded ASR gel, and closing of expansion joints also can be observed in affected structures.

Although ASR and DEF can result in severe degradation of the mechanical properties of concrete, catastrophic failures of affected structures are rare. Figure 2.3 shows an unreinforced

airfield pavement in New Zealand that experienced crushing failure at the expansion joints due to excessive expansions from ASR (Swamy 1992). The expansion of the concrete also stresses the reinforcing bars in reinforced structures; in some cases, this can be sufficient to yield the steel. Steel in tension will correspondingly compress the concrete, setting up a situation similar to post-tensioned concrete, with important implications for structural behavior.

The remainder of this section will discuss the typical crack patterns that result from ASR and DEF, the effects on the mechanical properties of concrete, and the implications for structural behavior for reinforced transportation structures.



Figure 2.3: Crushing failure of pavement from ASR, from Swamy 1992.

2.3.1 Cracking

Internal microcracking from ASR and DEF is manifested as macrocracking at exposed surfaces, where dryer conditions result in less expansion of the concrete; the surface layer is, in effect, torn open by the underlying expanding concrete. The surface crack patterns are very different for plain and reinforced concrete structures, as shown in Figure 2.4. This figure shows that plain concrete structures typically exhibit random, or “map” cracking patterns due to the lack of restraint, while reinforced structures exhibit cracking that is parallel to the orientation of the primary reinforcement due to the confinement provided in that direction. In pavements where expansion joints have closed, anisotropic restraint also develops, forcing the development of aligned, parallel cracking.

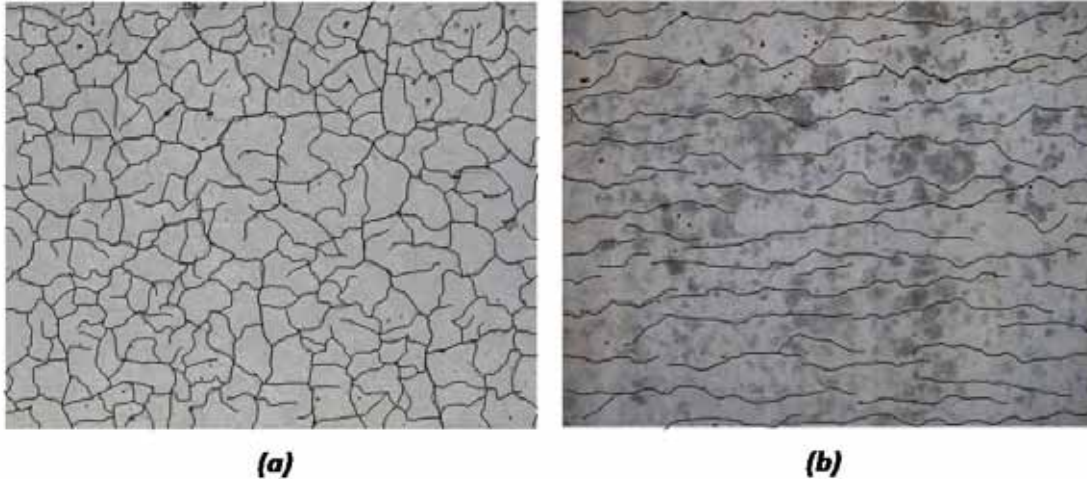


Figure 2.4: Crack patterns of (a) plain concrete and (b) reinforced concrete, from Kreitman 2011.

2.3.2 Mechanical Properties of Concrete

ASR and DEF can cause significant degradation in the mechanical properties of concrete. This includes the stiffness (elastic modulus), as well as the strength of the concrete. Not all properties are affected to the same extent, and effects vary depending on the reactive aggregate in ASR-affected concrete. The high curing temperatures required for DEF also results in an immediate and deleterious impact on the strength and stiffness of concrete, even before any expansion or cracking has occurred (Giannini and Zhu 2012). More detail regarding the effects of ASR and DEF on the elastic modulus, compressive strength, and tensile strength of concrete is provided in Section 2.5.1, along with details of test methods used to evaluate these properties.

2.3.3 Structural Behavior: Strength

Most studies of ASR-affected reinforced concrete structures have indicated that despite large expansions, extensive cracking, and the degradation of the strength and stiffness of the concrete, the load-bearing capacity of affected structures is not compromised (Chana and Korobokis 1992, Bach, Thorson and Nielsen 1992, Monette 1997). A notable exception would be a study by Swamy and Al-Asali (1989), who reported losses in the flexural strength of singly reinforced beams of up to 25% in four-point loading. It should be noted that these specimens contained no shear reinforcement in the central constant moment region. Only a few published studies involve full-scale load tests of in-service structures (Blight, et al. 1983, Imai, et al. 1983, Blight, et al. 1989); however these all indicated that the strength and stiffness of the bridge structures tested were either unaffected or adequate for service loads. Laboratory studies involving shear and flexural load tests of full-scale specimens damaged by ASR and DEF have typically come to the same conclusions, with the load capacity either less than expected (Boenig 2000), or lower than less-damaged and undamaged specimens, but still in excess of predicted capacity (Deschenes 2009, Larson 2010). A more extensive review of previous load tests can be found in Deschenes (2009) and Kreitman (2011).

Reinforcing steel fracture in ASR-affected structures in Japan has attracted significant attention. At least 30 cases of fractured bars have been discovered in structures also damaged by ASR (Mikata, et al. 2012). As shown in Figure 2.5, brittle fractures have been found at the

corners of stirrups, often with many adjacent stirrups all fractured. Because fracture of the bars can lead to a loss of confinement, which is thought to be the saving grace in the performance of ASR-affected structures, this is a major concern. Japan is an active seismic zone, so the concern there is elevated to an even greater degree. Mikata et al. (2012) found that when stirrup fracture is combined with corrosion of the reinforcement, the risk of decreased structural performance is increased. Webb (2011) provides a more extensive review of the rebar fracture problem in Japan and conducted an investigation into the possibility of fracture with steel grades and reinforcement detailing used in the United States. To date, no cases have been reported outside Japan. However, it is critical to develop an understanding of the cause of the fractures and how to detect existing or incipient fractures.

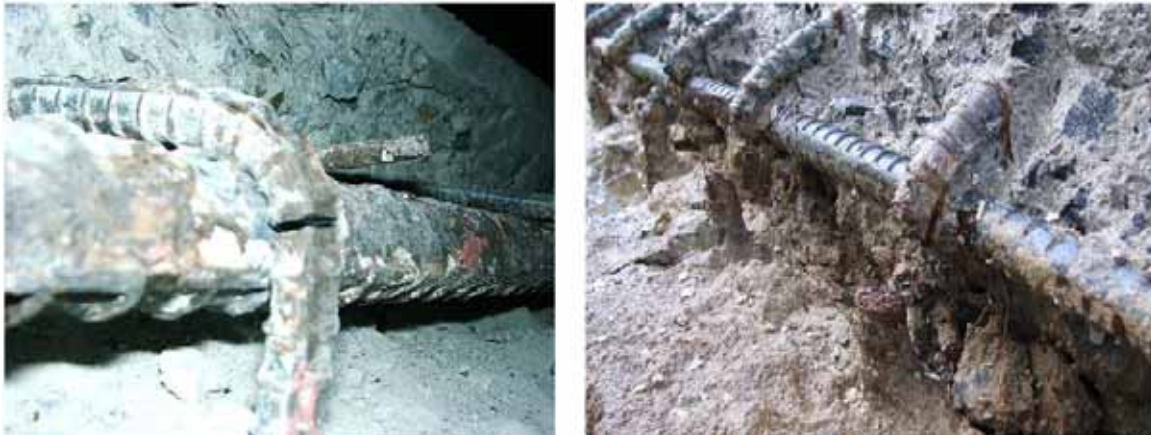


Figure 2.5: Fractured stirrups in ASR-affected bridge piers in Japan, from Miyagawa, et al. 2006; Torii, et al. 2008.

2.3.4 Structural Behavior: Serviceability

The serviceability of concrete structures includes the resistance to excessive deflections, as well as a host of other durability concerns that can shorten the service life of a structure, including frost action and corrosion. Large surface crack widths, and deep penetration of open surface cracks promote the ingress moisture and any dissolved aggressive agents, such as chlorides. Additionally, the loss of concrete stiffness and potential for reinforcement yield is a concern for deflections. While the load tests discussed in the previous section gave no indication of excessive deflections, most were live load tests, and did not measure any creep deflections that may develop over a long period of service. Swamy and Al-Asali (1989) noted that excessive hogging (camber) of singly reinforced beams developed as a result of expansion gradients in the specimens, which were able to expand more freely on the unreinforced compression face. Several researchers also noted that during the load tests, new cracks did not form until failure was imminent (Deschenes 2009, Larson 2010). Therefore, less warning is given by the structure; in field structures it could be expected that typical shear and flexural cracks that would indicate that the structure was overloaded may not be present in structures affected by ASR and DEF.

2.4 Potentially Applicable Nondestructive Test Methods

Nondestructive test methods can be broadly grouped into four categories:

- Visual inspection

- Expansion monitoring
- Stress wave methods
- Electromagnetic methods

Each of these categories will be discussed below, with attention given to specific test methods and methods of analysis that may be applicable to structures affected by ASR and DEF. A more complete review of the stress wave methods can be found Kreitman's thesis (2011).

2.4.1 Visual Inspection

Visual inspection is the simplest form of nondestructive testing, and is inevitably the first step in any investigation of a distressed structure. Every case study in the literature of ASR and DEF includes a description of the symptoms of distress observed through a visual inspection of the structure. These symptoms often include cracking, gel staining and exudation, popouts, closed expansion joints, etc. Cracking is often described both with respect to the size (width) of the crack openings and the patterns of cracking observed.

Several techniques of crack mapping have been proposed, with the goal of obtaining an estimate of expansion to date. One method involves the summation of crack widths along five parallel lines drawn on the concrete surface, and dividing the total openings by the length of the lines to determine the expansion along the axis of the lines (ISE 1992). Some researchers have used different line lengths and numbers of lines, depending on the dimensions of the structure. Another method developed by the LCPC in France involves summing crack widths along two perpendicular lines and two intersecting diagonals at 45° angles between the perpendicular lines (Godart, Fasseau and Michel 1992). The total crack openings are divided by the length of the lines to determine a cracking index (CI), which is interpreted to give an order-of-magnitude of the severity of the distress.

Conflicting judgments about the usefulness of these methods have been made. Jones and Clark (1994) found a poor correlation between estimated expansion from crack widths and the actual measured expansion of eighty laboratory specimens. Smaoui et al. (2004a, 2004b) found that estimated expansions from crack summation were lower than the actual expansion of laboratory specimens, while estimated expansions for specimens in outdoor exposure varied relative to the actual expansion depending on the exposure of a particular face of the specimen. The same group of researchers later came to the conclusion that crack summation applied to field structures was "rather reliable" so long as the most severely exposed sections of the structure were examined (Bérubé, et al. 2005). Of course, in field structures, the expansion is unknown, so it is difficult to judge if this was a valid conclusion. Deschenes (2009) compared estimates based on crack width summation to measured expansions of four full-scale laboratory specimens and found that crack widths consistently underestimated the measured expansion, in some cases by as much as 40%.

Despite this uncertainty, crack width summation techniques remain one of the better methods for estimating expansion of field structures. They are certainly preferable to more invasive methods such as the elastic rebound test, which involves exposing, gauging and severing a reinforcing bar to determine the expansive strain in the direction of the reinforcement (Danay 1994). They can also be used as part of long-term monitoring programs to track continuing expansion of the structure and the growth and propagation of cracks (Giannini 2009).

2.4.2 Expansion Monitoring

Expansion monitoring is an important component of long-term monitoring programs for structures affected by ASR and DEF. This typically involves the installation of DEMEC-type gauge points for use with mechanical strain gauges, or affixing strain gauges to the concrete surface. While expansion monitoring cannot aid in assessing expansions which have already occurred, measurements over several years are useful for determining the current *rate* of expansion, which is a critical piece of information for determining how to manage the structure (Fournier, et al. 2010). Different courses of action may be recommended if expansions are accelerating, continuing at a steady rate, slowing or even have ceased completely. Expansion measurements have also been used to gauge the effectiveness of mitigation methods (Giannini 2009, Bentivegna 2009).

2.4.3 Stress Wave Methods

Stress waves, or acoustic waves, have a variety of uses for the detection of flaws and condition assessment of concrete. Four types of waves will be examined in this review: compression, or P-waves, shear, or S-waves, surface, or R-waves, and Lamb waves.

Compression waves oscillate parallel to the direction of propagation, alternately compressing and dilating the material. Shear waves induce vibrations perpendicular to the direction of motion and move slower than compression waves. Figure 2.6 illustrates the propagation of compression and shear waves.

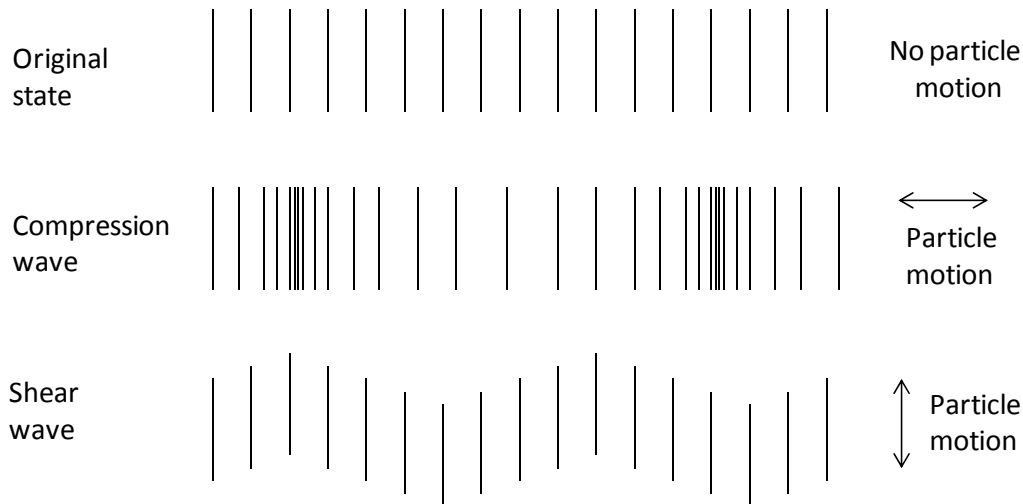


Figure 2.6: Compression and shear wave propagation, from Kreitman 2011.

Surface waves, as their name implies, propagate along the surface of a medium, inducing elliptical particle motion. Because of this, they are influenced to some extent by conditions below the surface, but energy of surface waves rapidly decreases with depth; at a depth of 1.5 wavelengths is just 10% of the surface amplitude (Carino 2004). As a result, the primary influence on surface waves in concrete is the surface conditions. Lamb waves, which have implications for impact-echo testing, can occur in thin plate elements, and are formed through the interactions of compression and shear waves, inducing particle motion similar to surface waves (Gibson 2004). Surface wave and Lamb wave propagation are illustrated in Figure 2.7.

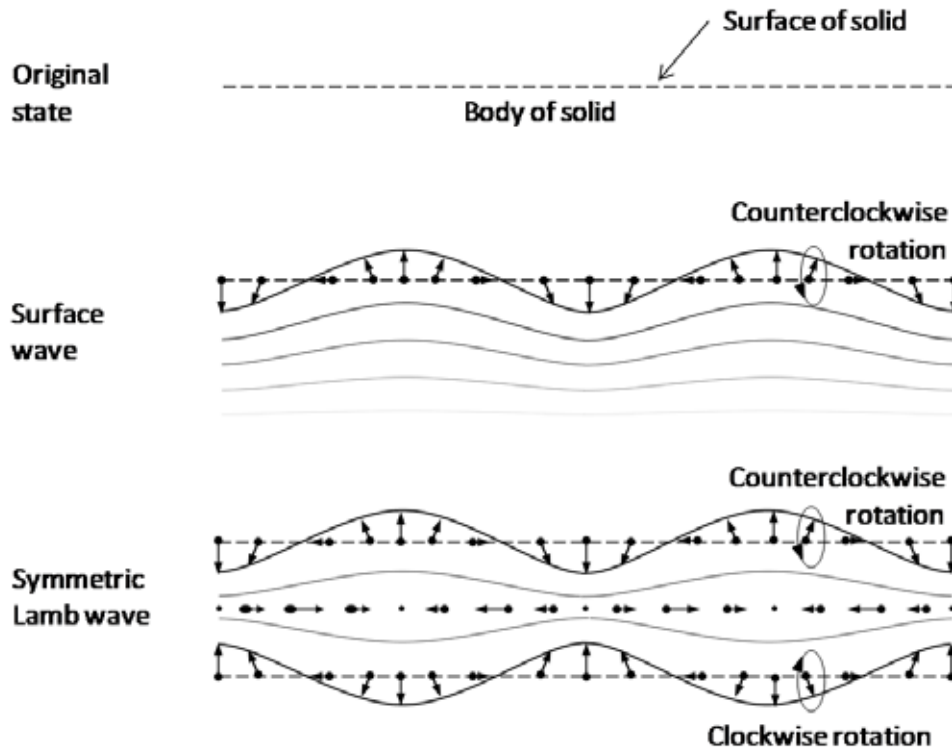


Figure 2.7: Surface wave and Lamb wave propagation, from Kreitman 2011.

Ultrasonic Pulse Velocity (UPV)

Through-transmission UPV of concrete is a simple method for testing the uniformity of concrete quality within a structure and has seen field use since the 1960s (Naik, Malhotra, and Popvics 2004). ASTM C597 (2002) describes the standard test method for measuring UPV of a specimen or structure. The travel time of an ultrasonic pulse between two transducers is measured, and the velocity of the compression wave calculated by simply dividing the distance traveled by the travel time. Figure 2.8 illustrates a typical UPV test setup. From this test, significant variations in the overall quality of concrete may be readily apparent; however, the correlation of velocity to quantitative values of compressive strength and elastic modulus are a more complicated matter.

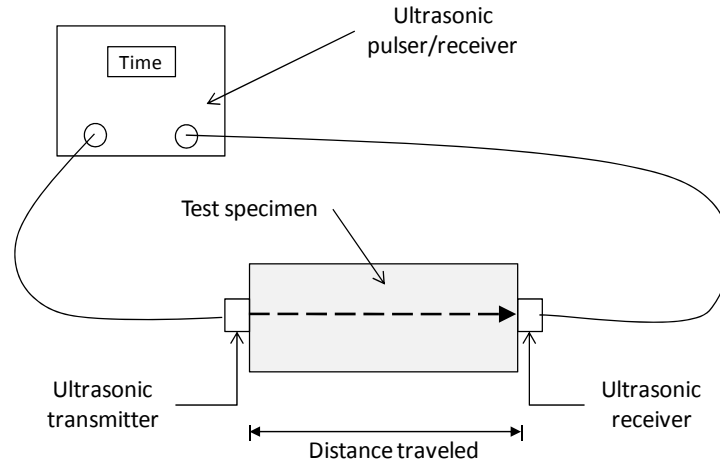


Figure 2.8: Typical UPV test setup, from Kreitman 2011.

Concrete is a porous, heterogeneous material, and the many interfaces between the cement paste, aggregates and voids create a complex acoustical environment with significant scattering of pulse energy (Naik, Malhotra and Popovics 2004). To minimize attenuation and scattering, relatively low frequencies must be used, such that the wavelength is greater than the maximum aggregate size (Naik, Malhotra, and Popovics 2004). Microcracking associated with mechanical damage, ASR or DEF leads to further attenuation and also reduces the apparent velocity as pulses must then take a longer path around the cracks (ACI Committee 228 2003).

This reduction in velocity can be quite significant; published research has shown that a decrease of 20 to 25% is possible with increasing expansion due to ASR (Ahmed, et al. 2003, Nakagawa, et al. 2008). The degree of moisture saturation can also affect the observed UPV of concrete by up to 5% (Naik, Malhotra and Popovics 2004). A more in-depth review of previous research involving UPV and ASR-affected concrete can be found in (Kreitman 2011). This includes a discussion of quantifying ASR damage by ultrasonic attenuation, or energy loss, rather than travel time. That method is less practical for use in the field, because attenuation is strongly influenced by the coupling of the transducers to the concrete. Results of UPV testing of DEF-damaged concrete could not be located in the literature.

Various relationships have been proposed for correlating UPV to the strength and elastic modulus of concrete, and there is considerable debate on the subject. Since UPV is proportional to the square root of the elastic modulus (ACI Committee 228 2003), and elastic modulus is commonly cited to be proportional to the square root of the compressive strength of concrete, it would seem to follow that compressive strength is proportional to velocity raised to the fourth power. However, experimental data do not support this relationship, which is based on unreasonable assumptions on homogeneity and linear elasticity (Popovics 1998).

The second-order relationship between modulus and UPV is less disputed, but it should be noted that this relationship is greatly influenced by Poisson's ratio (Naik, Malhotra and Popovics 2004). More specifically, UPV is related to the dynamic modulus—this is effectively the initial tangent modulus due to the extremely low stresses imparted by the test—and is not the same as the static secant modulus which is of greater importance to structural behavior (Neville 1963).

An additional complication in relating UPV and compressive strength stems from the fact that velocity is calculated from the shortest travel time at a particular test location, while

compressive strength of a concrete member is a function of the weakest pathway through it (Teodoru 1994). Despite the difficulties in creating a generalized quantitative relationship between velocity and strength, it is possible to construct an empirical relationship for a given mixture (Naik, Malhotra and Popovics 2004).

Impact-Echo

Impact-echo testing was originally developed by Sansalone (1997) to detect flaws in plate-like concrete elements such as pavement slabs and bridge decks. Typically, the flaws which impact-echo was developed to detect are larger voids or delaminated regions. However, the technique may have some applicability to the distributed damage characteristic of ASR and DEF. As noted in Chapter 1, researchers at Texas A&M University are also investigating its use for detecting debonding of reinforcement caused by ASR and DEF (Pagnotta, Trejo, and Gardoni 2012).

The test involves exciting a concrete element with an impact from a small steel ball or hammer; a transducers near the impact then measures the vibrations at the surface (Figure 2.9). The stress waves reflect, or echo off the boundaries of the element, as well as any internal defects and interfaces. Plate-like elements are preferred, so that the reflections are primarily between the impacted surface and back surface of the element. If defects are present, the echoes will arrive at the transducer more frequently. The time domain signal is converted to a frequency spectrum using FFT, where the dominant echo frequencies can be identified. Figure 2.9 illustrates this principle, showing the theoretical response of an undamaged element vs. one with a large defect at mid-depth. In the defective specimen, the peak frequency is much higher.

If the compression wave velocity is known, then the depth to the defect can be calculated; alternately, if no major defects are present, but the thickness of the specimen is known, then the compression wave velocity can be calculated. The relationship between frequency (f), compression wave velocity (V_p), and element thickness or depth to a defect (D) is:

$$f = \frac{\beta V_p}{2D} \quad \text{Equation 2.1}$$

where β is a shape factor dependent on the geometry of the element (Sansalone 1997). For plate-like elements, β has been found to be 0.96, but various for other cross-sectional geometries. According to Gibson and Popovics (2005), the vibrations in a plate will be non-propagating, first-order symmetric Lamb waves, and explain the need for a shape factor of 0.96.

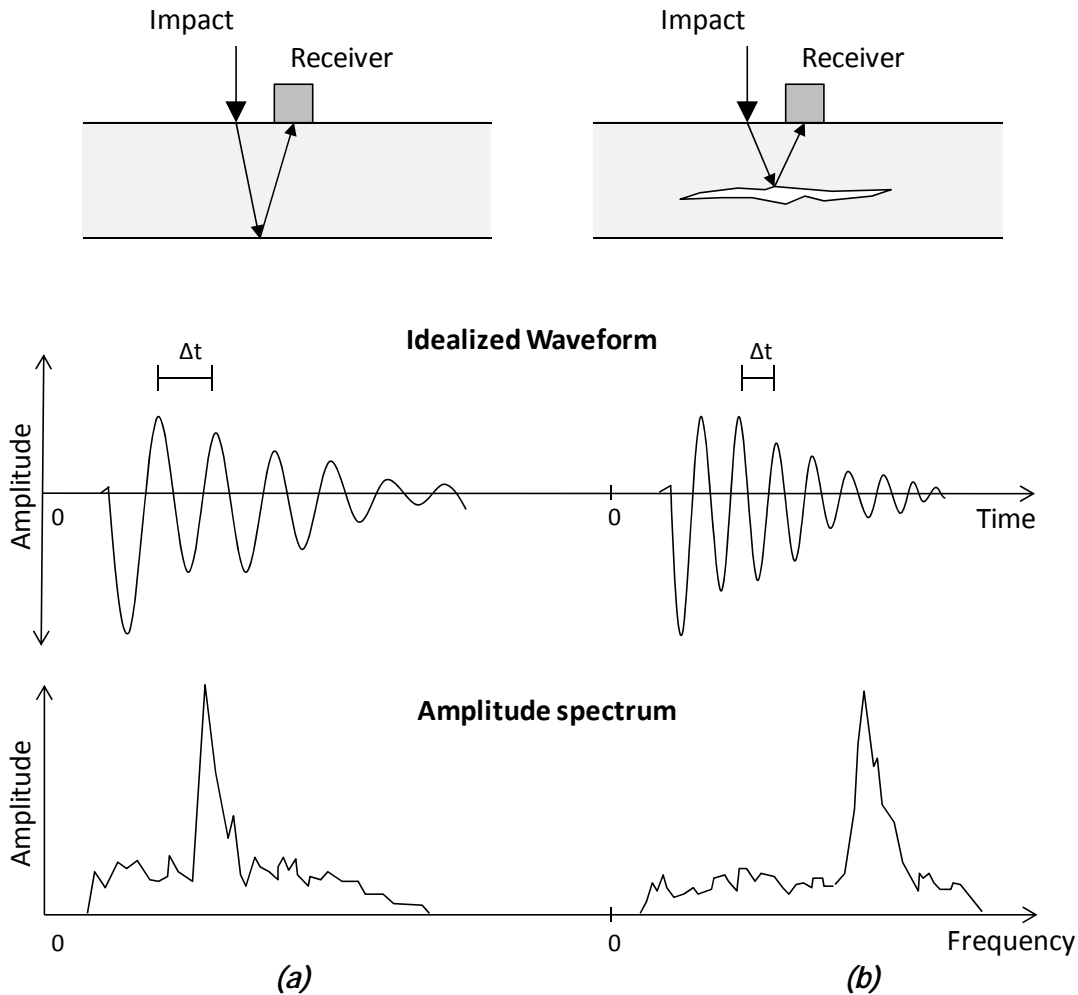


Figure 2.9: Conventional impact-echo theory, showing (a) undamaged concrete and (b) concrete with an internal defect, adapted from Sansalone and Streett 1997.

The method described above is one form of frequency domain analysis that could be applied to detecting distributed damage from ASR and DEF. As the compression wave velocity decreases, the peak frequency will shift downward. In cases where UPV cannot be applied due to lack of access to two sides of a structure, impact-echo could be an acceptable substitute, so long as the distance to the back surface is known (Carino 2004).

The frequency domain of concrete with distributed damage is also likely to be noisier than one that is undamaged or containing a clearly defined defect, that is, the peak frequency will be less defined, and several smaller peaks may be evident (Henriksen 1995). This is caused by additional scattering of waves off the internal microcracks. Figure 2.10 shows an example of a noisy frequency spectrum obtained from a bridge deck affected by ASR.

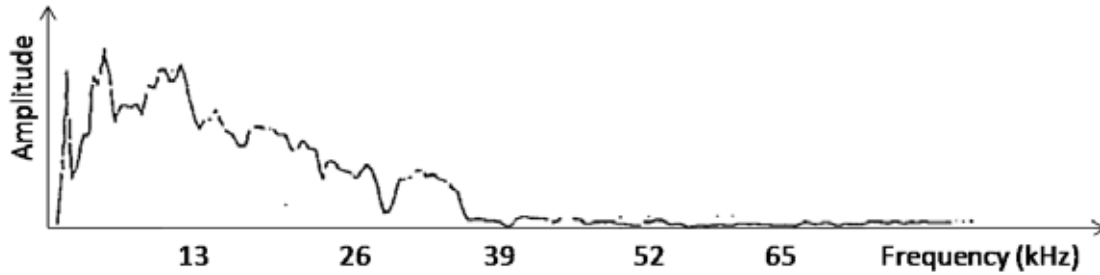


Figure 2.10: Noisy frequency spectrum from ASR-affected bridge deck, from Henriksen 1995.

For additional information regarding impact-echo theory, results of previous research, and a discussion of a time-domain method of analysis, refer to (Kreitman 2011). The latter attempts to quantify the decay of the time domain signal, which may have some correlation to ASR damage (Tinkey, Fowler and Klingner 2002, Kesner, Sansalone and Poston 2004).

Resonant Frequency Test

All solids have natural periods of vibration, also known as resonant frequencies, which will tend to vibrate at when excited. This is a function of the dimensions, stiffness, density, and boundary conditions (external restraint) of the solid. If two objects of different stiffness, but otherwise identical, are compared, the stiffer object will have a higher resonant frequency (shorter natural period). ASR and DEF reduce the stiffness of concrete, which can be detected by measuring the resonant frequency.

The resonant frequency test (ASTM C215-08 2008) provides instructions for determining the dynamic modulus of elasticity of simple rectangular or cylindrical prismatic concrete specimens in the laboratory. The ASTM standard provides procedures for measuring the longitudinal, transverse, and torsional modes of vibration. A small steel ball impacts the specimen, and an accelerometer measures vibrations; changing the location of the impact and accelerometer allows testing for different modes of vibration. Figure 2.11 shows the locations to be used for the longitudinal (2.10a) and transverse (2.10b) modes of vibration.

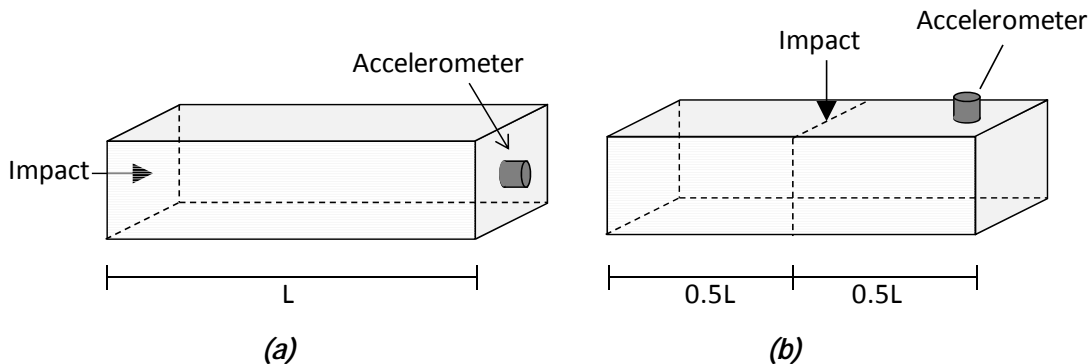


Figure 2.11: Impact and accelerometer locations for (a) longitudinal and (b) transverse modes of vibration, adapted from ASTM C215-08 2008.

The vibrations measured by the accelerometer are converted from a time-domain signal to a frequency spectrum with FFT. From this, the resonant frequencies can be identified; the lowest frequency is normally the fundamental resonant frequency, which higher modes of vibration may also be evident. Figure 2.12 shows an idealized time domain signal and corresponding frequency spectrum.

A more common application of this test method has been to quantify the damage in laboratory freezing and thawing tests (ASTM C666-03 2008), but it has also been applied to ASR. Swami and Al-Asali (1988) observed reductions of up to 82% in the dynamic modulus of mortar prisms that had axial expansions of 1.5%. Rivard and Saint-Pierre (Rivard and Saint-Pierre 2009) tested concrete prisms and noted that reactive prisms with axial expansions of 0.2% had dynamic moduli 13% lower than corresponding nonreactive prisms.

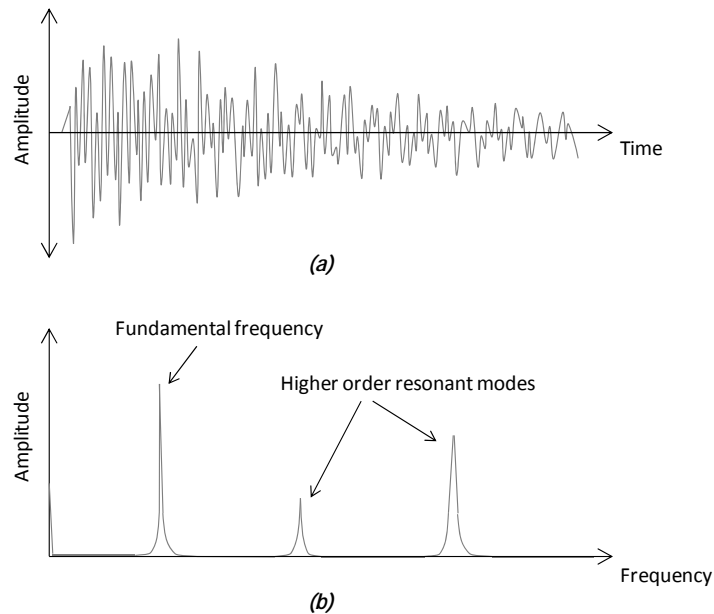


Figure 2.12: Resonant frequency test results: (a) time domain signal and (b) frequency spectrum, from Kreitman 2011.

Large Scale Dynamic Testing

The concept of resonant frequency testing has also been considered for application to field structures. This method is global in nature, that is, the entire structure is tested. Therefore, if the stiffness structure of the structure has been reduced by ASR, or increased due to a self-post-tensioning effect from the reinforcement, it may be detectable by measuring the dynamic response of the structure.

However, at this scale, some complications exist. A larger impact or other excitation force is required. Geometries are often irregular (not simple prismatic shapes) and external restraints will prevent free vibration, leading to different modes of vibration than predicted by ASTM C215. Thus, structural modeling is necessary to predict the modes of vibration, and models are typically refined by comparing to experimental data (Huang, Gardoni and Hurlebaus 2009, Baber, Lydzinski and Turnage 2009). External restraints can include connections to other structural elements, or be seemingly insignificant as a guardrail attached to a bridge. Even the

latter can have a significant influence on the dynamic response (Baber, Lydzinski and Turnage 2009).

Ono (1992) measured the dynamic response of T-shaped bridge piers affected by ASR, finding that those which exhibited more distress also had lower resonant frequencies. The dynamic moduli of the piers were higher than those of cores drawn from the piers, most likely a combined result of the structure being under load and confinement against expansion provided by the reinforcement. However, Ono also noted that the dynamic response of the pier was dominated by the column portion, limited the test's effectiveness in assessing the bent (top of the "T").

Non-Linear Acoustics

Most stress wave methods are linear tests, that is, they are based on the assumption that the material being tested is linear-elastic. The reality is that concrete is not a linear-elastic material, although in certain ranges of the stress-strain relationship, this is an acceptable approximation for most purposes. Linear test methods have proven reasonably effective for locating larger defects, but test methods based on nonlinear behavior may be many times more sensitive to microcracks and distributed damage characteristic of ASR and DEF. Kreitman (2011) provides an in-depth review of nonlinear theory and multiple test methods. Two methods which were applied in this research will be described briefly below.

The first is the resonant frequency shift method, which is essentially the same as ASTM C215 (2008), except that repeated impacts of increasing force are used. The resonant frequency experiences a downward shift as the force of the impacts increases, and this shift is increasingly prominent in specimens with microcracking (Muller, et al. 2005). Sample data from undamaged and ASR-damaged mortar bars tested by Chen et al. (2010) is shown in Figure 2.13.

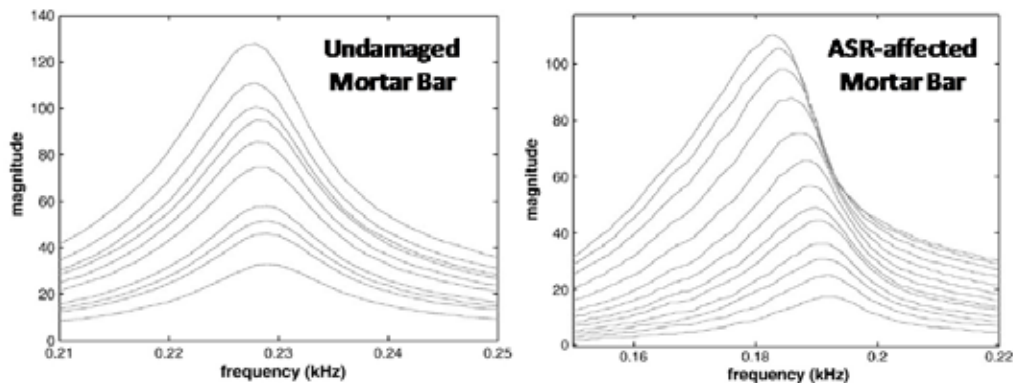


Figure 2.13: Resonant frequency shift test results, from Chen, et al. 2010.

The results of the mortar bar tests by Chen et al. (2010) indicated that the resonant frequency shift method could detect the onset of damage more quickly than expansion measurements in ASTM C1260 (2007) accelerated mortar bar testing. However, the strength of the resonant frequency shift peaked quickly, and then decreased as expansion of the mortar bars increased, suggesting that this method may have difficulty detecting more severe damage from ASR and DEF.

The second method will be referred to as the "time shift nonlinear acoustic method," and was developed by Kodjo et al. (2009). This method uses a large impact to disturb ultrasonic pulses being passed through a concrete element under investigation. This impact opens and

closes microcracks, causing both an increase in travel time and a decrease in amplitude of the received pulses. The increase in travel time causes a phase shift in the received signal. Over time, the effects of the impact disappear, and the phase and amplitude of the received signals return to the pre-impact condition. The phase shift is then plotted against the amplitude, and the slope of this plot is taken to be the hysteretic nonlinear parameter, α . The slope (and nonlinear parameter) increases with the development of microcracking in the concrete. Figure 2.14 shows an example of data from tests on an unreinforced concrete block affected by ASR (Kodjo, et al. 2009).

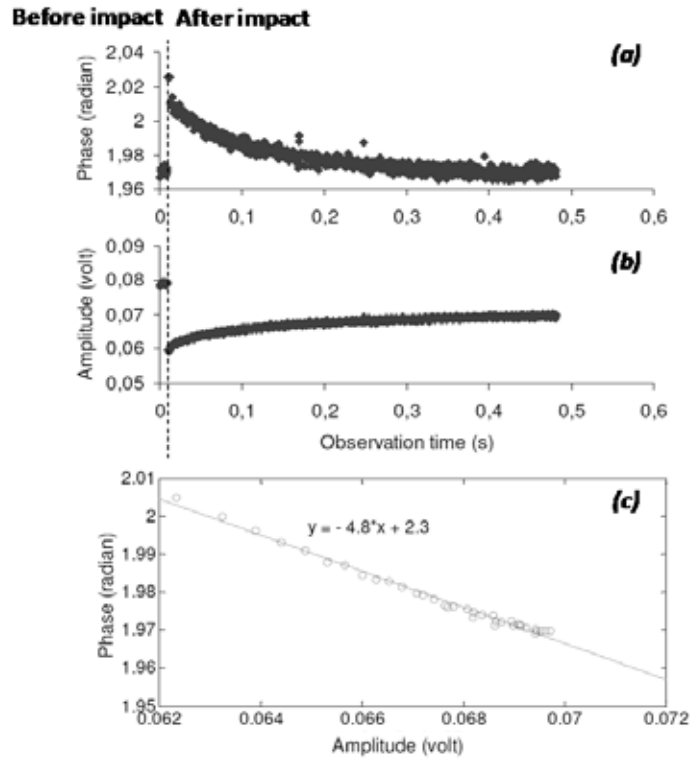


Figure 2.14: Phase shift and amplitude variation in time shift nonlinear acoustic testing, from Kodjo, et al. 2009.

Surface Wave Methods

Surface wave methods have received comparatively little attention for the evaluation of concrete affected by ASR and DEF. However, since surface waves are strongly influenced by near-surface layers of the concrete, it is not unreasonable to attempt to detect and quantify damage as the open cracking which is the first sign of distress is found on and near the surface. Two methods will be described briefly, but a more complete discussion can be found in (Kreitman 2011).

The spectral analysis of surface waves (SASW) was originally developed to analyze soil and pavement layers (Carino 2004). In concrete with ASR, a layered system may also be present, with internal microcracking and surface macrocracking. Different frequencies of surface waves are influenced by the stiffness at different depths; thus the technique may shed light on how the stiffness of concrete affected by ASR and DEF changes with depth. The test involves impacting the concrete on either side of a set of two receivers, and often repeated with multiple impacts and sensor locations (Figure 2.15). Complex signal processing is then used to calculate a dispersion

curve, which plots surface wave velocity against frequency. For a layered system, the velocity will vary depending on the frequency, and the term “phase velocity” is used to describe the velocity of a particular surface wave frequency. In a material of constant stiffness, the dispersion curve is flat. A significant advance in surface wave testing is the use of air-coupled sensors—sensitive microphones that do not need to be affixed to the test surface. Their use greatly speeds up the testing process (Zhu 2005).

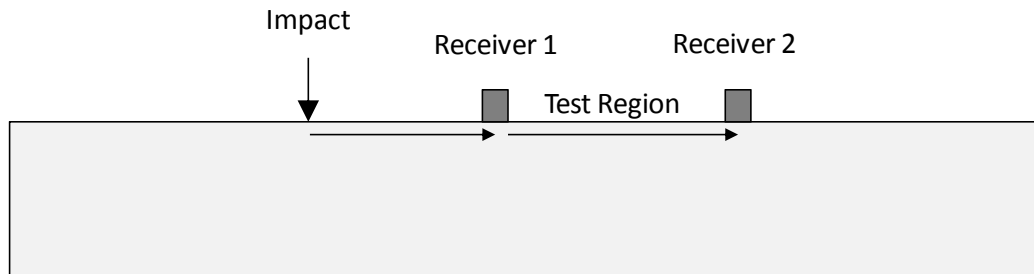


Figure 2.15: Surface wave test setup, from Kreitman 2011.

A second method, surface wave transmission (SWT), uses the same test setup, but a different analytical method. This method, developed by Kee and Zhu (2010) measures the energy transmission of a range of surface wave frequencies between the two sensors. It was initially developed for determining the depth of a single surface-breaking crack, and the sensors were positioned on either side of the crack. The presence of cracks between the sensors reduces the energy received by the second sensor, and can be correlated to the crack depth.

Initial tests attempting to correlate energy transmission to expansion from ASR and DEF at the University of Texas at Austin were met with some success (Kee 2010), and deemed worthy of more work. A potential issue with this method is the “near-field effect,” in which scattering of waves from cracks near the impact or the receivers can result in difficult-to-interpret data. ASR and DEF result in many surface cracks, and it may not be possible to locate the impacts and sensors far enough from the cracks to avoid the near-field effect.

Acoustic Emissions Monitoring

Acoustic emissions monitoring has been frequently applied to corrosion monitoring. This test method is a long-term monitoring method, in which acoustic emissions from the concrete resulting from the progression of reinforcement corrosion are counted; the number and frequency of these “hits” is correlated to the development of distress and the rate of corrosion. Tinkey et al. (2002) applied this technique to monitoring concrete beams affected by ASR and DEF, and noted that it might be a viable in-place monitoring method, if issues related to external environmental noise could be overcome.

2.4.4 Electromagnetic Methods

Electromagnetic methods have seen very little application to date in evaluating or monitoring structures affected by ASR and DEF. They are frequently used in concrete to locate reinforcement and also have been shown to detect defects in reinforcement, including broken prestressing strands (Lauer 2004). The latter capability could be extremely valuable for detecting fractured stirrups, although the fact that the stirrup fractures have only been observed at 90°

bends will require development of a different type of sensor than that used to investigate straight prestressing strands.

The pipeline industry has also sought out electromagnetic sensors that are capable of measuring the strain in steel. When steel is under strain, both the electromagnetic conductivity and permeability of the material are affected, and advanced non-contact sensors can be used to measure strain (and calculate the stress) of the steel, even if a coating is present (Westwood, et al. 2008). Some of these sensors are capable of measuring stress and strain variation in three dimensions, as seen in sample data shown in Figure 2.16 (Lasseigne 2012). This figure shows the stress in a section of damaged pipeline steel in both a plan view and through the thickness of the pipeline wall.

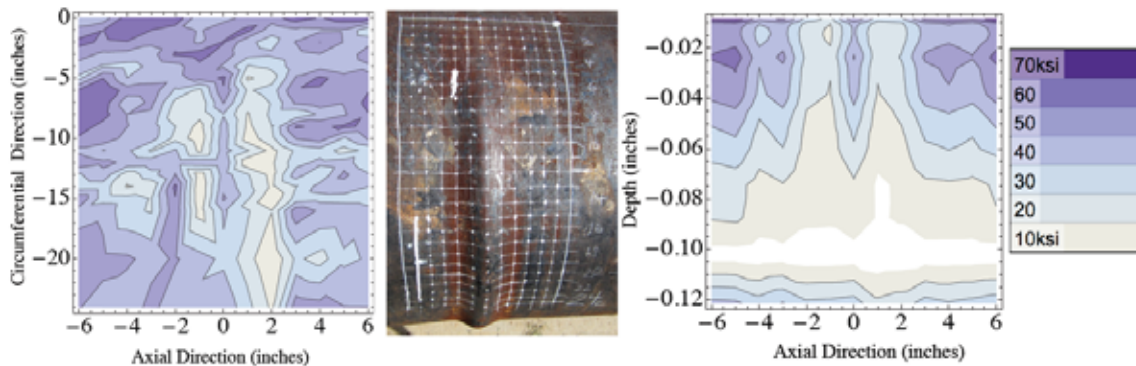


Figure 2.16: Electromagnetic stress measurements of a steel pipeline, from Lasseigne 2012.

If similar sensors can penetrate the concrete cover to measure the strain of the reinforcement, the implications for civil engineering are enormous. The applicability of this technology to structures affected by ASR and DEF is that it could be used to potentially detect incipient failure of reinforcement, and also be used to estimate the expansion of the concrete, assuming the reinforcement strain is equal to the expansion of the concrete.

Ground penetrating radar (GPR) methods have also been proposed for assessing ASR-affected concrete. GPR signals are primarily influenced by the dielectric of the material they are probing, and can be useful in locating reinforcement, delaminations, and interfaces between various layers in a pavement (Lauer 2004). Water has a very high dielectric, and is also an important ingredient in ASR. Tinkey et al. (2002) applied GPR in the same study that acoustic emission monitoring was used, but found little use for the technique. As with UPV testing, greater penetration with GPR is achieved with lower frequencies, but this necessarily limits the resolution of the signals to detecting very large defects.

2.5 Core-Based Evaluation Methods

Extraction and testing of core samples from concrete structures is extremely useful in the diagnosis and evaluation of structures affected by ASR and DEF, and a core component of all evaluation protocols. Core sampling is akin to taking a biopsy in medicine—an invasive procedure that generally does little harm to the structure. It would be difficult to classify it as non-destructive in the sense of the tests described in the previous section, but the extraction of cores does not destroy the structure. Through careful selection of the core location to avoid

reinforcing steel and highly stressed regions of the structure, the effects of core sampling on the performance of the structure can be minimized.

Most tests conducted on core samples are destructive to the sample, with the exception of several nondestructive techniques described in the previous section. The stiffness damage test (SDT) and static elastic modulus test described below also result in minimal distress to the specimen, and do not preclude additional tests from being conducted afterwards. In fact, it will be shown that a series of tests can be assembled to obtain a considerable range of information from a single core sample; this can minimize the number of cores that must be extracted from the structure.

Tests conducted on cores can be grouped into five classes; non-destructive acoustic tests (described in Section 2.3), petrographic analysis, tests of mechanical properties, chemical analysis, and residual expansion tests. The last four will be discussed below for their significance in evaluating structures affected by ASR and DEF, and some consideration will be given to the combinations of tests that can be conducted on a single core sample.

2.5.1 Mechanical Testing

Mechanical tests of core samples can provide important information on the condition of concrete affected by ASR and DEF. Compressive strength is commonly used to assess the quality of concrete, and an important component of any structural analysis. However, other mechanical properties, such as stiffness (elastic modulus) or tensile strength, are generally more sensitive to ASR and DEF and should also be tested whenever possible (ISE 1992, Bremner, et al. 1996, CSA 2000, Folliard, Thomas and Fournier 2007, Fournier, et al. 2010). Additionally, not all concretes will experience the same effects on their mechanical properties for a given amount of expansion. The response appears to be aggregate-specific (Swamy and Al-Asali 1988, Ahmed, et al. 2003, Smaoui, et al. 2004a). A review of applicable test methods is provided below.

Stiffness Damage Test

The stiffness damage test (SDT) was developed to quantify damage to concrete from ASR and other mechanisms by analyzing the load-deformation data obtained when cyclic loads are applied to core samples. Several versions of the test and associated data analysis have been proposed, but the basic principle remains the same; damaged concrete will have a reduced stiffness and will accumulate more plastic strain during the test compared to sound concrete. The test is intended to be conducted with low enough loads that it can be considered non-destructive to the cores sample; this allows standard elastic modulus and compressive or splitting tensile strength tests to be conducted without affecting the results. Strength tests can be followed with chemical tests on the broken concrete, such as water-soluble alkalis or analysis of expressed pore solution. Alternately, the stiffness damage test could be followed by residual expansion testing or petrographic examination.

As originally developed by Crouch and Wood (1988), the test involved applying five cycles of 800 psi (5.5 MPa) compressive load to a core specimen and measuring the stress-strain response. They recommended a length/diameter (L/D) ratio of 2.5 for core samples to be tested. In ASR-damaged concrete, the elastic modulus decreases, while the stress-strain hysteresis loops increase in size and increasing amounts of plastic strain accumulate during the course of the test (Crouch and Wood 1988, Chrisp, Waldron and Wood 1993). Chrisp et al. (1993) placed emphasis on the elastic modulus, plastic strain and size of the hysteresis loops of the second

through fifth cycles and largely discarded the data from the first load cycle. They also proposed calculating a non-linearity index (NLI), which is the ratio of the elastic moduli of the first and second halves of the loading curve. Unfortunately, these researchers were reluctant to publish test data as much of their work was conducted for private clients, so it is difficult to evaluate the effectiveness of this version of the test. The data they have published is not correlated to any specific amount of ASR expansion.

Further development of the test method by Smaoui et al. (2004a) at Université Laval resulted in a recommended loading level of 1450 psi (10 MPa) and identified the area of the first hysteresis loop and the accumulated plastic strain over all five cycles as the most important parameters. They proposed that a linear relationship between these parameters and expansion could be established using laboratory specimens or core samples extracted from larger specimens of known expansion levels (Smaoui, et al. 2004a, Smaoui, et al. 2004b). They also noted that concrete made with different reactive aggregates will exhibit varying responses in the stiffness damage test; that is, linear relationships must be established for multiple reactive aggregate types in order to estimate the expansion of a variety of field structures. Finally, they proposed shortening the L/D ratio of the test specimens from 2.5 to 2.0. An L/D of 2.0 is a more reasonable value for drilled core specimens and consistent with standard test cylinder sizes. Figure 2.17 shows typical stress-strain data obtained using this version of the test.

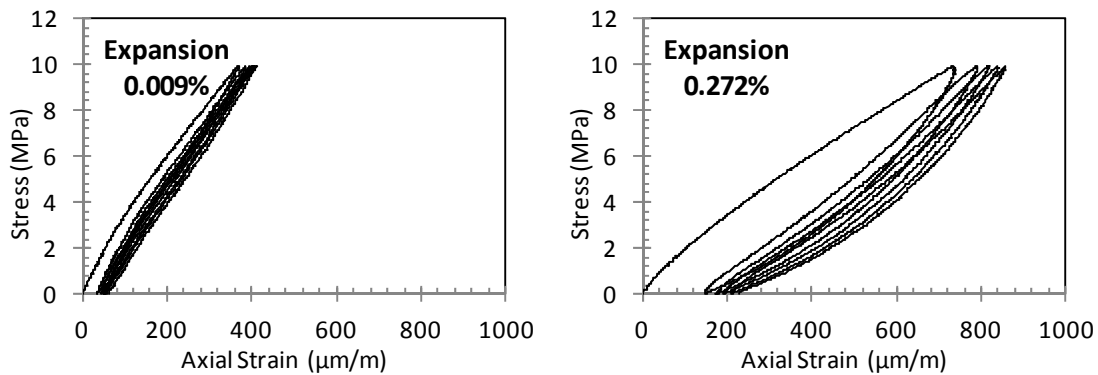


Figure 2.17: Typical stiffness damage test data.

The 1450 psi (10 MPa) version of the test has been adopted by the FHWA (Fournier, et al. 2010) and TxDOT (Folliard, Thomas and Fournier 2007) in their current evaluation protocols. Several papers describe the application of this version of the SDT to field structures damaged by ASR, primarily by researchers at Université Laval and UT-Austin (Bérubé, et al. 2005, Sanchez, et al. 2012b, Thomas, et al. 2012, Tremblay, et al. 2012). In these studies, the test is generally able to provide a qualitative assessment of the degree of damage from ASR; however, estimating the expansion to-date remains a challenge. As of this writing, no studies have been published regarding the use of SDT to characterize damage from DEF or a combination of ASR and DEF.

More recent work at Université Laval by Sanchez et al. (2012a) suggests that the maximum applied stress in the test should not be a fixed value because useful data can only be obtained if it is at least 30% of the compressive strength. If the load is less than 30% of the compressive strength, which would be greater than 1450 psi (10 MPa) for concrete stronger than 4830 psi (33.3 MPa), and greater than 800 psi (5.5 MPa) for all but the weakest concretes, then it is very difficult to quantify ASR damage with SDT. The authors recommended conducting the

test at 40% of the design compressive strength. However, it may be more prudent to base the test on the current strength, rather than design strength, which would be the same load specified for the determination of the static modulus of elasticity by ASTM C469 (2010).

Elastic Modulus

The static modulus of elasticity is greatly affected by ASR and DEF. Reductions of 60 to 70% have been reported for concrete with very large ASR-induced expansions (ISE 1992, Fournier, et al. 2010). ASTM C469 (2010) covers the measurement of the secant modulus, which involves loading a cylindrical specimen to 40% of the compressive strength and measuring the deformation of the central portion of the specimen. This test is well suited to core samples, however the compressive strength often must be estimated; alternately, deformations can be recorded at multiple loads, and the modulus calculated using the load nearest 40% of the compressive strength. Popovics (1998) stated that the secant modulus should be relatively constant if the maximum load is between 30 and 45% of the compressive strength. However, since the stress-strain curve for concrete damaged by ASR and DEF becomes increasingly nonlinear in the stiffness damage test, it is best to measure the elastic modulus using a load as near as possible to 40% of the compressive strength.

If the maximum load in the SDT is 40% or less of the compressive strength, then it should not impact the results of a test to determine the elastic modulus. Alternately, the elastic modulus can be calculated using SDT load-deformation data; this would not comply with ASTM C469, but it would negate the need for two separate tests.

Compressive Strength

Concrete affected by ASR and DEF typically exhibits a loss of compressive strength, although the effect is more modest compared to the effects on the elastic modulus. Reductions of 40 to 60% have been reported for severe expansions (ISE 1992, Swamy and Al-Asali 1988), although not all cases of ASR will be as damaging. Compressive strength can be measured by breaking core samples according to ASTM C42 (2011), which is based on ASTM C39 (2010), or in-situ with the Penetration Resistance Test (PRT), also known as the Windsor Probe Test.

It should be noted that since concrete normally continues to gain strength with time and design strengths are commonly exceeded, compressive strengths in some ASR-and DEF-affected structures may exceed design strengths, but still have experienced a reduction in strength. Martin et al. (2012) reported a compressive strength gain of 70% for laboratory cylinders that expanded 0.20% from ASR, which they attributed to a “self-healing” effect from continued hydration of cement in the moist storage conditions. Corresponding cylinders affected by DEF experienced a similar decrease in compressive strength at much higher expansions (approximately 1.5%); they suggested that the rate of DEF expansion exceeded the rate at which the concrete could heal itself. Silva et al. (2008) reported on tests of core samples from a hydroelectric power plant in Brazil affected by ASR, comparing compressive strengths to both the 28-day cylinder strength and the projected undamaged concrete strength using a formula derived by Helene (1987). Despite a 30% reduction in elastic modulus, the compressive strengths of the cores were all well in excess of the 28-day cylinder strengths and were only slightly reduced from the projected undamaged strength for the age of the concrete in the structure.

Tests of ASR-affected concrete at the Seabrook Nuclear Power Plant, a prominent case at the time of this writing, indicated a 21.7% reduction in compressive strength over a 31-year period as measured by core sample and cylinder tests, and a 20.8% reduction in strengths measured using the PRT (U. S. Nuclear Regulatory Commission 2011). PRT strengths should

not be directly compared to compressive strengths measured with core samples or cylinders as these tests may not necessarily provide similar values. For example, the PRT tests at the Seabrook plant were approximately 10% greater than tests of core samples extracted from the same concrete (U. S. Nuclear Regulatory Commission 2011). Part of this variation may be due to the fact that concrete in core samples is removed from the in-situ stress state (CSA 2000).

Although compressive strength has not been strongly correlated to the performance of structures affected by ASR and DEF, it is a, or perhaps more accurately, *the* benchmark mechanical property of hardened concrete. As a result this may be the only mechanical property available for comparison in construction records for a structure under investigation. It may also be useful in assessing the severity of distress to compare compressive strengths of core samples to the tensile strength or elastic modulus (Fournier, et al. 2010). Compressive strength tests can also be performed on a core that has been previously tested for elastic modulus, and concrete from the broken specimen can be reserved for later chemical testing.

Tensile Strength

Micro-cracking that accompanies expansion due to ASR and DEF leads to a greater loss of tensile strength compared to compressive strength. Reductions of up to 60 to 80% of the splitting and direct tensile strengths have been reported with large expansions (ISE 1992, Fournier, et al. 2010).

However, it is difficult to directly measure the tensile strength of concrete and instead is often assumed based on the compressive strength. A direct tension test using dumbbell-shaped briquette specimens (BS 6319 1985) has been used in laboratory testing (Ahmed, et al. 2003), but it is not adaptable to core samples. Given that the effects on tensile strength are more severe, it is not acceptable to calculate tensile strength based on an assumed relationship to compressive strength in concrete affected by ASR and DEF (Bremner, et al. 1996). A decrease in the ratio of tensile to compressive strength may be useful in assessing the severity of damage caused by ASR (Nixon and Bollinghaus 1985).

The two standardized methods recognized by ASTM are the splitting tensile strength test (ASTM C496-11 2011) and the flexural strength test (ASTM C78-10 2010). The latter is conducted on rectangular prism specimens, which rarely extracted from field structures. Splitting tensile strength tests are conducted on cylindrical specimens, which can include core samples. An indirect tensile test proposed by the Building Research Establishment was applied to ASR-affected laboratory cylinders by Bremner et al. (1996). This test uses a sealed chamber and pressured nitrogen gas to apply a uniform load to the specimen, with the gas pressure at failure of the specimen taken as the tensile strength of the concrete. Bremner et al. suggested that this test is better suited to deteriorated concrete than the splitting tensile test, in which the maximum force develops in a single plane.

2.5.2 Chemical Testing

Chemical testing of concrete suspected to be suffering from ASR has commonly focused on determining the alkalinity of the concrete (or, current alkali loading), which can explain whether there are sufficient alkalis for ASR to have occurred or continue to occur. These “available alkalis” are considered to reside in the pore solution; however, the possibility exists that alkalis from internal sources (aggregates) may be released in the future, thus becoming available for reaction. The contribution from aggregates can range from negligible to extraordinary (Bérubé, et al. 2002a, De Ceukelaire 1992).

It is possible to extract the precipitated alkalis from dry, finely ground concrete samples in water, acid, or other solutions. Extraction in water is covered in greater detail later in this section. The acid-soluble alkali test is standardized in ASTM C114 (2011) for the analysis of cement, and involves extracting the alkalis in a boiling HCl solution. Acid solutions have the potential to dissolve substantial amounts of alkalis from aggregate particles, as well as those which have been bound in the various hydration products and the alkali-silica reaction products (CSA 2000). Therefore, it is difficult to estimate either the available alkalis for ASR or the initial alkali loading of the concrete using this test. Goguel (1995) describes selective dissolution of the paste in various alkaline solutions designed to leave the aggregates intact. Sagüés et al. (1997) describe the use of water small drilled cavities as an analogue to the pore solution, allowing the water to equilibrate with the surrounding concrete. However, this technique is unlikely to be feasible in assessing concrete in the field, where the near-surface region is typically unsaturated and would likely absorb the small volume of water. A portion of the pore solution can also be expressed under high pressure from pastes or mortars and analyzed for its chemical composition. A detailed review of this technique is also provided later in this section.

Water-Soluble Alkali Content Analysis

The water-soluble alkali test has been standardized for the analysis of cement in ASTM C114 (2011), and involves extraction of the alkalis in room-temperature water. A variation on this, known as the hot-water extraction method, has been described by Rogers and Hooton (1989) and Bérubé et al. (2002b) for the purpose of analyzing the alkali content of a powdered concrete sample, using extraction in boiling water, although the latter authors questioned the necessity boiling the solution. The resulting solution is filtered and analyzed using either flame photometry or inductively coupled plasma (ICP) techniques. This particular procedure been followed at the University of Texas at Austin, and is well-documented in Williams' thesis (2005) for the investigation of the San Antonio Y, the first published case of DEF without ASR (Thomas, et al. 2008).

The goal of the test is to extract primarily the alkalis that were present in the pore solution, and thus available for reaction, but not alkalis that were bound in cement hydration products or ASR reaction products. Bérubé et al. (2002b) suggest that this is the case, although work by others suggests that alkalis could be released from amorphous (but not microcrystalline) ASR reaction products (Davies and Oberholster 1988), and that not all pore solution alkalis may be recovered if the concrete has dried before the test (Diamond 1996). Some aggregates do, however, release significant alkalis, and unless this can be accounted for, can lead to an overestimation of the current available alkalis. Bérubé et al. (2002b) showed that about 40% of the original alkalis are bound in cement hydration products in concrete where portland cement is the only binder; if the aggregate contribution in the test can be accounted for, then it is possible to not only estimate the current, but also the original alkali loading of the concrete.

The propensity of feldspar minerals to release alkalis in water has been known for some time (Parmelee and Monack 1930) and aggregates containing feldspars tend to release large amounts of alkalis compared to other aggregates (Bérubé, et al. 2002a). Constantiner and Diamond (2003) confirmed that alkalis can be released by feldspars into concrete pore solution. Bérubé et al. (2002a) tested the potential alkali contribution of 17 Canadian aggregates. This included a variety of soak solutions (pure water, lime solution with an excess of solid lime, and alkaline solutions containing 0.7N NaOH or KOH), extraction temperatures, agitation methods, and soak times (up to 578 days). They concluded that the alkaline solutions would most closely represent the conditions inside concrete and therefore the potential alkali release during the life

of the concrete. After 578 days, the alkalis released by the aggregates ranged from 0.2 to 21.4 lb/yd³ (0.1 to 12.7 kg/m³), with an average of 3.7 lb/yd³ (2.2 kg/m³), assuming they were used in concrete in normal proportions. These values were typically several times higher than those obtained from soaking in lime solution or pure water. This is not the same as what could be released in the hot-water extraction test, which involves pure water, and a soak time of just 24 h. However, this study is useful in explaining cases where water-soluble alkali levels have been found to be in excess of what should be possible given the alkali loading from the cement alone. In the same paper, the authors examined water-soluble alkali tests on cores from 23 dams, finding that 80% exceeded the estimated contribution from the cement, and an average excess of 2.2 lb/yd³ (1.0 kg/m³) that they attributed to contributions by the aggregates. Similar results were reported by Grattan-Bellew (1994, 1995) in his investigation of the Saunders Generating Station in Ontario, Canada. He noted that the aggregate was only marginally alkali-silica reactive, and that the damage from ASR was likely triggered by the additional alkalis contributed by the aggregates.

The primary utility of this method in evaluating structures exhibiting damage characteristic of ASR is to determine whether sufficient alkalis are available to either have caused or sustain ASR in the future. The threshold value varies depending on the reactive aggregate, although Hobbs (1981) suggested that there may be a critical ratio of water-soluble alkalis to reactive silica (in this case, opal). It may be possible to monitor the progress of the reaction with time by taking cores as the structure ages; tests on laboratory specimens with very highly reactive aggregates have shown a 25 to 44% reduction in the water-soluble alkali content (Bérubé, et al. 2002b). These tests, however, used very high initial alkali contents in addition to high-temperature, high-humidity storage conditions to accelerate the reaction. Some leaching is possible in these conditions, and the reaction progresses much faster than in the field. Therefore, the utility of long-term alkali monitoring may be limited at best, and would require great patience in the investigation. However, it has been suggested that monitoring the depletion of portlandite may be more useful (Bérubé, et al. 2002b); during alkali recycling, portlandite continues to be depleted as a source of hydroxyls. Since portlandite is crystalline, X-ray diffraction would be useful in monitoring its depletion.

The use of water-soluble alkali testing is also complicated by the variability in alkali contents within a structure, particularly large structures which may be constructed using various material sources. A study by Shayan et al. (2000) presented the water-soluble alkali contents of 13 samples taken from a 223 ft- (68 m) long core (the full depth of a dam). Alkali contents ranged from 1.75 to 5.46 lb/yd³ (1.04 to 3.24 kg/m³). Bérubé et al. (2002a) recommended that field specimens be taken from at least 1.6 ft (0.5 m) depth, if possible, to avoid near-surface variations. This is possible in very massive structures, but not in all cases.

Expression and Analysis of Pore Solution

The expression of concrete pore solution under high pressure was first described by Longuet et al. (1973) and further refined by Barneyback and Diamond (1981) at Purdue University. The usefulness of this technique is that it allows for direct study of concrete pore solution, and in the case of ASR and DEF, changes in the pore solution that accompany these reactions. This technique also possesses certain advantages over the extraction of alkalis in water or acid, in that the hydroxyl concentration (and therefore, pH) and sulfate concentration of the pore solution can be determined, and it should avoid the leaching of alkalis from ground aggregate particles that can skew the results of water-soluble alkali tests. The significance of the pore solution has been challenged (Chatterji 1991), and the composition of the significantly

larger fraction of the pore solution that resists expression under high pressure is far from certain. Nevertheless, this technique has seen considerable use and no comparable method exists to study the composition of the pore solution.

The technique involves the use of a high-strength steel die and piston to essentially squeeze out a fraction of the pore solution contained in a sample of hydrated cement paste, or from a sample of hardened concrete or mortar fragments. The sample is pressed inside the die by the piston, against a high-strength steel platen located below the die. The platen contains a machined trench that directs the expressed pore solution to a drain, through which it is collected in a plastic vial located below the platen or in a syringe through plastic tubing inserted in the drain. The recovered solution, generally on the order of just a few mL in specimens more than a day old (usually containing 10-20% of the evaporable water), can then be analyzed to determine the ionic species present. Barneyback's dissertation (1981) contains a more complete discussion of the construction of the apparatus used at Purdue, as well as the techniques used to analyze the expressed pore solution.

The analytical methodology described by Barneyback (1981) is summarized here and remains generally representative of those described by subsequent researchers in the literature. Hydroxyl concentration, $[\text{OH}^-]$, and therefore pH, are typically determined through titration against HCl; the use of glass electrode pH meters is not recommended because of the aggressive nature of the solution. Alkali metals (Na^+ , K^+ , Li^+) can be measured using flame photometry, while atomic absorption spectrometry is useful in measuring other cations of interest, including Si^{4+} , Al^{3+} , Mg^{2+} and Ca^{2+} . Sulfate concentrations can be determined indirectly through barium sulfate precipitation in a solution of BaCl_2 . While Barneyback mentions titration to a methyl red end point for $[\text{OH}^-]$ determination, the use of a phenolphthalein end point has also been reported in the literature (Bérubé and Tremblay 2004, Durand, et al. 1990, Kagimoto, Sato and Kawamura 2000). Other strong acids may also be used in place of HCl. Hydroxyl concentrations are also sometimes simply assumed to be in balance with the sum of the sodium and potassium concentrations; in the case of mature concretes where other ionic species have decreased to comparatively insignificant levels, this can be considered an appropriate, although not exact, assumption (Bérubé and Tremblay 2004, Duschene and Bérubé 1994, Kagimoto, Sato and Kawamura 2000). Finally, ICP methods can also be used for determining various ionic concentrations in place of flame photometry or atomic absorption (Bérubé and Tremblay 2004).

Over the years, the pressures used to express pore solution have progressively increased, as use of higher pressures is generally equated with a greater volume of expressed solution, although the relationship may not necessarily be linear. Longuet et al. (1973) used pressures of up to 50,700 psi (350 MPa), while apparatus at Purdue was designed for pressures of 80,000 psi (550 MPa). More recently, Cyr et al. (2008) describe an apparatus that is designed for up to 145,000 psi (1000 MPa) that may be able to recover up to 40% of the pore solution. Researchers at Université Laval have also reported the expression of pore solution using similar pressures, and note that a maximum pressure of 203,000 psi (1400 MPa) may be attainable (Bérubé and Tremblay 2004). Great care must be exercised, for such high pressures carry the risk of damaging or even catastrophically failing the die.

Some researchers who have separately analyzed pore solution expressed at increasing pressure increments have noted that the alkalinity of the expressed solution increases slightly with increased pressures, with the larger fraction of the increase being attributed to a rise in sodium concentration (Constantiner and Diamond 1997, Bérubé and Tremblay 2004, Duschene and Bérubé 1994). Therefore, sodium may be somewhat more difficult to express than

potassium. This is supported by data presented by Bérubé and Tremblay (2004) comparing pore solution expression to the hot-water extraction technique. The expressed pore solution had similar potassium concentrations, but lower sodium concentrations. Of course, it is difficult to prove which test provides the most accurate results.

In concrete or mortar containing non-reactive aggregates, the pore solution increases in alkalinity at early ages, at first rapidly due to the depletion of sulfates as ettringite is formed, then more slowly due to a loss of pore water from continuing hydration. The alkali hydroxide concentration then stabilizes somewhere between 0.35N (low-alkali cement, low cement content) and 1.0N (high-alkali cement, rich mixture with low w/cm) (Diamond 1983). However, when reactive aggregates are used, the alkalinity of the pore solution eventually begins to decrease as alkalis are incorporated into the reaction product (ASR gel). If the reaction progresses far enough, a steady-state alkalinity is eventually reached. This was first shown by Barneyback (1981) using mortars containing near-pessimum quantities of Beltane opal sand—alkali hydroxide concentrations decreased from a peak of 0.80N, finally stabilizing around 0.35N. Diamond (1983) notes that this steady-state alkalinity is likely to vary depending on the particular system under study (aggregate, cement, w/cm, etc.), although he notes that there likely exist threshold concentrations of alkali hydroxides, below which ASR cannot continue. Because of the possibility of alkali recycling, the steady-state concentration may be higher than the threshold value. Of course, leaching of alkalis, particular in small or thin elements, can work to bring the concentration of alkalis below the threshold. Rivard et al. (2007) noted significant decreases in the pore solution alkalinity of both reactive and non-reactive concrete prisms stored in accelerated laboratory conditions. A significant portion of the decreases were attributed leaching, determined by sampling water used to maintain humidity in the storage container, although the non-reactive specimens did maintain higher alkali concentrations than the reactive specimens.

The usefulness of this technique should extend beyond the laboratory; alkali hydroxide concentrations in the pore solution of core specimens from field structures may be able to help diagnose the presence of ASR and the progress of the reaction. This is similar to the goal of the alkali extraction tests described earlier: to determine if there are sufficient alkalis present for ASR to occur (and continue to occur). Studies published by Kagimoto et al. (2000) and Langley et al. (2000) have included analysis of pore solution expressed from crushed core samples in the evaluation of ASR-affected structures. The former study showed extremely low alkali hydroxide concentrations in a severely damaged retaining wall, ranging from 0.03M to 0.21M.

With regards to DEF, the pore solution composition is slightly more complex. In the pore solution of concrete susceptible to DEF as a result of high curing temperatures, sulfates are not depleted in the first day for the formation of ettringite. Instead, sulfates remain in the pore solution, with higher alkali contents and higher curing temperatures generally linked to higher sulfate concentrations (Ramlochan 2003). As mentioned earlier, a decrease in the pH of the pore solution is critical for DEF to occur. Ramlochan (2003) also studied the changes in pore solution of specimens cured at 95°C and then soaked in saturated limewater at 23°C. He found that while both the alkali hydroxides and sulfates decreased dramatically in concentration (OH^- concentrations were approximately 0.05M), only the alkalis were found to have leached into the soak solution. His hypothesis was that the sulfates, rather than leaching out, must have left the pore solution to form ettringite. In terms of evaluating field structures, the presence of significant sulfate concentrations in the pore solution of mature concrete suffering from ASR may be a warning of a future risk of DEF.

2.5.3 Residual Expansion Testing

Long-term in-situ monitoring of a field structure can be used to determine the annual rate of expansion, but this requires several years of data collection—a time period that is unacceptable for many owners. Residual expansion tests attempt to determine the future potential for expansion (current rate and ultimate expansion) by placing core samples in conditioning regimes to accelerate ASR and/or DEF. These conditioning regimes are often similar to those used in standard accelerated expansion tests such as ASTM C1293 and ASTM C1260.

The conditioning regime has a great effect on the expansive behavior of cores in residual expansion tests. If the cores are stored in air over water, the storage temperature needs to be higher than the structure experiences in the field in order to obtain results more quickly than in-situ monitoring; however this often results in a lower ultimate expansion than tests conducted at lower temperatures (ISE 1992). The ISE suggests that a test at 100°F (38°C) be used for rapid diagnosis of the likelihood of continued expansion due to ASR, although this will ultimately underestimate the total potential unconfined expansion. They cite an average summer temperature in the UK of 68°F (20°C) and an annual average of 55°F (13°C) in support of using a lower testing temperature for a more accurate prediction of ultimate expansion. However, for well-reinforced structures, this procedure may actually overestimate expansion due to the removal of the core sample from confinement (CONTECVET 2000).

Testing at 100°F (38°C) over water (>95% RH) is also recommended by the CSA (2000), TxDOT (Folliard, Thomas and Fournier 2007), and the FHWA (Fournier, et al. 2010). Bérubé et al. (2000) used the results of this test as a component of a model to predict the expansion rate and ultimate expansion, based on many other factors. In this and other residual expansion test methods, it is also important to account for the water uptake by the core, as in-service concrete is rarely completely saturated. Therefore, the mass change of the cores should also be measured; when examined in combination with the expansion of the cores, it is possible to isolate the expansion resulting from continued ASR from that resulting from re-wetting and the loss of confining pressure. Table 2.1 shows the FHWA-recommended interpretation of test results. Expansions of 0.003% per year are considered to be indicative of some expansion potential, with higher expansion rates linked to more rapid expansion in the field (Bérubé, et al. 2000, Fournier, et al. 2010). Table 2.2 shows the classification of expansion potential proposed by Bérubé et al. (2000) for their prognostic model.

Table 2.1: Interpretation of residual expansion results: testing at >95% RH and 100°F (38°C), from Fournier, et al. 2010.

1-yr exp. ¹ (percent)	Case	Conclusion about the concrete	Preexisting ASR gel (before test)	Secondary ASR gel (after test)	Result for companion cores tested at 38°C (100°F) in 1N NaOH	Further expansion expected in the field
<0.003	1	Non-expansive since construction	No/small amounts	No/small amounts	Non-expansive (non-reactive aggregates) or expansive (low alkali concrete content)	Non-expansive (non-reactive aggregates or low-alkali content)
	2	Non-expansive anymore	Yes	No/small amounts	Non-expansive (aggregates non-reactive anymore) or expansive (alkali content not sufficiently high anymore)	Non-expansive (aggregates non-reactive anymore or alkali content not sufficiently high anymore)
	3	Reactive but non-expansive (cracked/porous concrete)	Yes or no depending on age and humidity	Yes	Non-expansive (porous/ cracked concrete) or expansive (concrete not as cracked)	Expansive or non-expansive depending on porosity/ cracking, humidity, and confinement
>0.003	4	Expansive	Yes or no depending on age and humidity	Yes	Expansive	Expansive or non-expansive depending on humidity and confinement

¹ Excluding the preconditioning period. The expansion results obtained could be underestimated if the concrete tested is significantly more porous/cracked (open spaces for free expansion of the ASR gel) than the overall concrete of the field member under study.

Table 2.2: Classification of expansion potential, from Bérubé, et al. 2000.

Coefficient RCE - Residual concrete expansivity in the laboratory (core testing in air at >95 percent RH and 38°C (100°F))					
percent exp./yr ¹	Residual exp. ¹	RCE ¹	percent exp./yr ¹	Residual exp. ¹	RCE ¹
< 0.003	negligible	0	0.015 to 0.02	moderate	6
0.003 to 0.005	very low	1	0.02 to 0.025	high	9
0.005 to 0.01	low	2	0.025 to 0.03	high	12
0.01 to 0.015	moderate	4	> 0.03	very high	16

Several other methods of residual expansion testing have been proposed or recommended. Swamy (1992, 1997) noted that concrete from structures more likely to be exposed to salts (marine environment or from deicing activities) should be immersed in a 4% NaCl solution at 100°F (38°C). Immersion in a 1N solution of NaOH at 100°F (38°C) or 176°F (80°C) is recommended to provide an estimate of remaining aggregate reactivity, although the expansions will be unrealistically high, especially at 176°F (80°C) (Bérubé, et al. 2000, Fournier, et al. 2010).

A combination of three residual expansion tests can also be used to aid in the diagnosis of the deterioration mechanism when DEF is suspected. These parallel tests, and their diagnostic purposes, are shown in Table 2.3. This was initially detailed in (Folliard, et al. 2006) and later adopted by TxDOT (Folliard, Thomas and Fournier 2007). Test A indicates susceptibility to additional expansion due to ASR, as the alkaline storage solution prevents DEF. Test B indicates susceptibility to DEF, as limewater immersion leaches alkalis and prevents expansion from ASR. Test C will allow both mechanisms to occur, and can provide a more realistic estimate future

expansion. Cores which expand in both tests A and B indicate that both ASR and DEF may occur, while those which expand in only one test allow for the isolation of a single mechanism.

Table 2.3: Expansion tests for the diagnosis of potential for ASR, DEF or combination of mechanisms, from Folliard, Thomas, and Fournier 2007.

<i>EXPANSION TEST DESIGNATION</i>	<i>SPECIMEN DETAILS</i>	<i>NUMBER OF SPECIMENS</i>	<i>STORAGE CONDITIONS</i>	<i>MEASUREMENT DETAILS</i>	<i>NOTES</i>
A	2 in. diameter cores, 10 in. length. Gauge studs epoxied into end of cores.	3	Fully immersed in 1 N NaOH solution at 176 °F	Measure expansion weekly for six months	Main objective is determining maximum potential for future ASR-induced expansion or remaining amount of reactive silica in aggregates. This testing regime will suppress DEF due to the high pH and temperature of the soak solution. Storage conditions similar to ASTM C 1260.
B	2 in. diameter cores, 10 in. length. Gauge studs epoxied into end of cores.	3	Fully immersed in lime water at 73 °F	Measure expansion weekly for one year (or longer if no expansion has yet occurred)	Main objective is determining maximum potential for future DEF-induced expansion. This testing regime promotes DEF only if concrete was exposed to excessive curing temperatures (i.e., above 158 °F). This testing regime will suppress ASR as the alkalis present in the concrete will leach into the lime water.
C	4 in. diameter cores, 10 in. length. Gauge studs epoxied into end of cores.	3	Stored above water at 100 °F	Measure expansion weekly for up to two years	Main objective is to trigger ASR, DEF, or both in a more realistic storage condition. This test promotes ASR by submitting the cores to high temperatures and high humidities and by also avoiding direct immersion and excessive leaching. This test promotes DEF by triggering some leaching, and also, if ASR does occur internally, it can then trigger DEF.

2.5.4 Petrographic Analysis

Petrography techniques are extremely valuable tools in the diagnosis of ASR and DEF in concrete. Core samples, or more typically, polished and thin sections of core samples, are examined for characteristic damage features of each distress mechanism. ASTM C856 (2011) covers standard concrete petrography techniques, while non-standardized techniques in use include the Gel Pat Test (GPT) and Damage Rating Index (DRI). Most petrographic techniques are qualitative in nature, although the DRI is an attempt to quantify the deterioration caused by ASR and DEF.

Qualitative Petrography

Qualitative petrography ranges from macroscopic examination of freshly-extracted core samples to scanning electron microscopy of very small samples. Macroscopic examination is typically conducted at less than 10X magnification, polished sections are examined at magnifications up to 100X, and higher magnifications are employed in thin-section and scanning electron microscopy (CSA 2000). Both the CSA and FHWA (Fournier, et al. 2010) have published excellent guides with numerous photographs that detail the various characteristic features of ASR to be noted by petrographers. These include, but are not limited to, macro- and micro-cracking, gel staining around cracks and aggregates, alteration rims around aggregate particles, and the presence of ASR gel in voids and on broken surfaces. Many of these features can be observed at multiple scales, and staining techniques can be used to highlight ASR gel present in the sample.

Thin section examination and the GPT are also useful for the identification of the alkali-silica reactive components in a sample. The use of polarized light and a rotating sample stage in thin-section petrography allow for the identification of strained or disordered silica that are most susceptible to ASR (CSA 2000). In its earliest incarnation, the GPT can be traced to Stanton (1943), but has evolved over the years as the initial test could typically only identify opaline phases. A more recent version involves submerging a polished specimen in a 1N NaOH solution stored at 100°F (38°C) and examining the specimen periodically for the formation of ASR gel (Fournier and Bérubé 1993). Figure 2.18 shows an example of a GPT specimen with significant gel formation after 56 d of exposure.



Figure 2.18: Gel pat test specimen at 56 days, from Fournier 2009.

Many cases of DEF will appear similar to ASR, in many cases because ASR is also contributing to the distress. However, certain petrographic features are more indicative of DEF; these include ettringite-filled gaps around aggregate particles and two-toned reaction rims around cement grains than indicate a high-temperature early-age curing (Ramlochan 2003, Folliard, Thomas and Fournier 2007). These are features which are best observed using a scanning electron microscope, as petrographic diagnosis of DEF requires magnifications of 1000X or more (Rothstein 2012a).

Quantitative Petrography: DRI

DRI was developed to characterize the damage caused by ASR in concrete where the coarse aggregate is the reactive phase, and has been most frequently used in Canada and the United States. In order to determine the DRI for a core, it is cut in half lengthwise and one

surface is polished. It is then coated in uranyl acetate, which is absorbed the ASR gel and fluoresces under UV light. A grid composed of 0.4-in. (10-mm) sided squares is drawn on the polished surface. Each square of the grid is examined at 16X magnification and the number of a set of defects associated primarily with ASR is noted. Some of these defects are also associated with other forms of concrete deterioration or natural defects in the coarse aggregate particles. Therefore, the importance of each type of defect is reflected in a weighting factor that is applied to the raw count of defects. Defects that contain gel receive the highest weighting factors, so great care must be taken in the preparation of the sample because ASR gel can be easily damaged or dissolved. (Grattan-Bellew 1995)

The results are then normalized for an area of 15.5 in² (10,000 mm²). The DRI weighting factors have evolved over the years since this method was first developed. Table 2.4 provides a typical set of weighting factors for determining DRI. In general, a DRI above 40 or 50 is indicative of significant damage due to ASR. Efforts have been made to calibrate DRI to specific levels of expansion; however, this is specific to each aggregate source (Smaoui, et al. 2004a, Smaoui, et al. 2004b, Rivard and Ballivy 2005). Shrimmer (2000) cautions that accelerated laboratory specimens do not develop damage in the same manner as concrete in the field; thus, any calibration of DRI data is best achieved with cores from concrete in field exposure conditions.

Table 2.4: Typical DRI weighting factors for ASR, adapted from Grattan-Bellew and Mitchell 2006.

Feature Measured	Factor
Cracks in coarse aggregate	X 0.75
Cracks in coarse aggregate + gel	X 2.0
Open cracks in coarse aggregate	X 4.0
Coarse aggregate debonded	X 3.0
Reaction rims	X 0.5
Paste with cracks	X 2.0
Paste with cracks + gel	X 4.0
Gel in air voids	X 0.5

Calibration of DRI values to expansion requires tremendous effort, and the test is likely more valuable for characterizing the relative degree of damage, rather for estimating expansion to date. Because of the greater weight given to features characteristic to ASR, this technique should be able to differentiate between damage caused by ASR and other mechanisms. DRI has been used in numerous field investigations, reported most recently in (Tremblay, et al. 2012, Sanchez, et al. 2012b, Thomas, et al. 2012). Another advantage of this test is that DRI measures the internal distress of the structural core, which can be quite different than what surface crack measurements can detect (Shrimmer 2000).

DRI has also been applied to concrete affected by DEF and can assist in the diagnosis, although an investigator must be cognizant of the fact that the test was not designed to evaluate damage from DEF (Folliard, Thomas and Fournier 2007). High DRI scores are likely for DEF-damaged concrete, but different characteristic features will dominate, as compared to concrete affected by ASR. Debonding or ettringite-filled gaps around the aggregate, as well as an absence of ASR gel, should be expected if DEF is the sole damage mechanism, while the presence of gel

would indicate that ASR is also occurring (Grattan-Bellew and Mitchell 2006, Rothstein 2012a). Much work remains before the application of DRI to concrete affected by DEF, either alone or in combination with ASR, can approach the level of acceptance that it has for evaluating ASR-affected concrete.

A major challenge of DRI is that it is extremely operator dependent, and multiple weighting scales have been and are currently used. Grattan-Bellew and Mitchell (2006) studied the variability of the test, and reported a single-operator CV for six tests on a single specimen of 6%. Multi-operator, single laboratory variability was 22%, which they stated was “acceptable;” however, they noted that it may be as high as 50% for operators in multiple laboratories. Since this study, a workshop held in 2008 involving 20 petrographers resulted in a refined DRI procedure, and greater agreement on the rating system, which should reduce variability in the test among different petrographers (Villeneuve, Fournier and Duchesne 2012).

2.6 Current State of Practice: FHWA Protocol

The most recent guidance regarding the evaluation of ASR-affected structures is provided by the FHWA (Fournier et al. 2010). It is specific to ASR and does not address issues specific to DEF. This document outlines three levels of increasingly detailed investigations for structures in which ASR is suspected as a cause of distress. These investigations are summarized in a global flowchart, shown in Figure 2.19.

The initial investigation (Level 1) is a visual condition survey; if this indicates at least a moderate possibility of ASR based on visible symptoms, then a preliminary investigation (Level 2) is initiated. The preliminary investigation relies primarily on petrography of core samples to diagnose whether ASR is a cause of distress. Crack mapping by the LCPC method (Godart, Fasseau and Michel 1992) to determine the cracking index is also recommended to gain an initial estimate of the severity of the expansion to date. If ASR is diagnosed as a cause of distress and the cracking index exceeds a certain level of severity, a detailed investigation (Level 3) is initiated.

The detailed investigation involves an extensive core sample testing program and in-situ testing program. These tests (summarized in Table 2.5) comprise many of the techniques described above in Sections 2.4 and 2.5, and seek to further quantify the degree of distress in the structure and the potential for future expansion. In-situ tests include expansion monitoring, more detailed visual inspections, repeated cracking index measurements, elastic rebound testing, installation of temperature and humidity sensors, UPV and impact-echo testing, and evaluation by a structural engineer. In severe cases, a full-scale load test is recommended. Recommended core sample tests include quantitative petrography (DRI), compressive and tensile strength, static elastic modulus, SDT, residual expansion, and water-soluble alkalis.

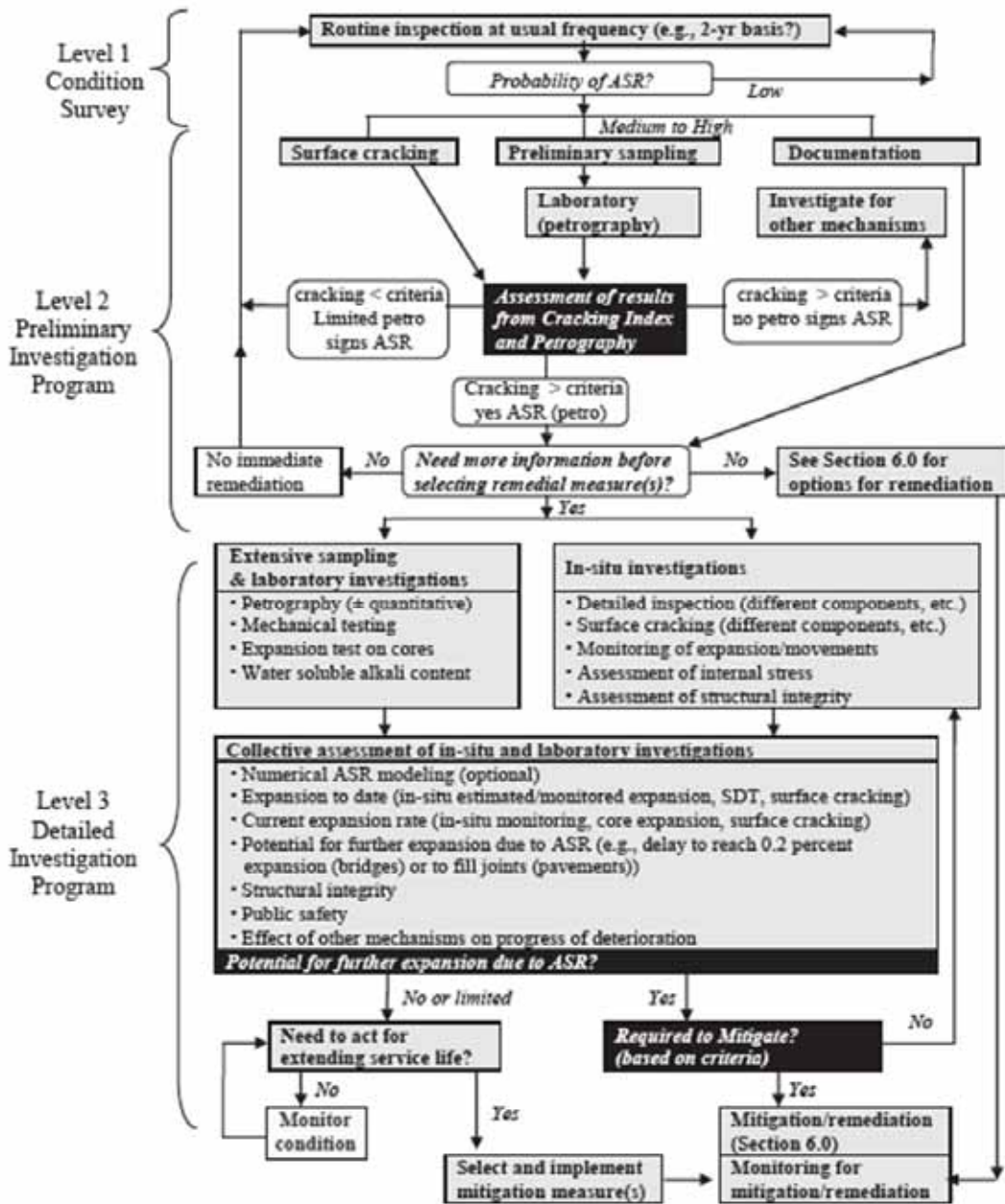


Figure 2.19: FHWA flowchart for evaluation and management of ASR-affected structures, from Fournier, et al. 2010.

Table 2.5: Investigation tools for evaluating ASR-affected structures, from Fournier, et al. 2010.

Test / investigation	Main Objective	Diagnosis	Prognosis
Site investigation (condition survey)	<ul style="list-style-type: none"> Assess the nature and extent of distresses and deterioration, and the risks relative to structural integrity and public safety Assess the exposure conditions Select sites for sampling and cracking measurements 	XXX	X
Documentary evidence on concrete structures investigated	Collect and review available documents relating to the design, construction, survey and maintenance of the structure(s)	XXX	X
Initial and periodic measurement of cracks (Cracking Index)	<ul style="list-style-type: none"> Assess deterioration and expansion level reached to date Assess current rate of expansion rate Assess potential for future expansion 	XXX	XX
Petrographic examination			
<ul style="list-style-type: none"> Macroscopic description 	<ul style="list-style-type: none"> Describe general condition of concrete cores Identify macroscopic features of ASR 	XXX	X
<ul style="list-style-type: none"> Microscopic examination using polished slabs, thin sections (impregnated or not), broken pieces of concrete (possible uranyl acetate treatment) 	<ul style="list-style-type: none"> Identify reactive rock types and distribution Identify presence and distribution of reaction products Identify sites of expansive reaction Identify pattern of internal cracking 	XXX	X
<ul style="list-style-type: none"> Quantitative petrographic analysis on polished slabs 	Quantify extent of ASR damage due to ASR (e.g. cracking, gel) and possibly progression with time	XX	X
Mechanical testing			
<ul style="list-style-type: none"> Compression and splitting tensile testing 	<ul style="list-style-type: none"> Assess general condition of concrete Assess structural properties of members 	XX	
<ul style="list-style-type: none"> Direct tensile strength, flexural strength, and Young modulus 	<ul style="list-style-type: none"> Assess possible ASR Assess structural properties of members 	XX	
<ul style="list-style-type: none"> Stiffness Damage Test 	<ul style="list-style-type: none"> Assess internal damage due to ASR Assess the expansion level reached to date 	XXX	
Expansion test on concrete cores			
<ul style="list-style-type: none"> Cores at 38°C, R.H. > 95 percent 	<ul style="list-style-type: none"> Confirmation of deleterious expansion Assess current rate of expansion Assess potential for future expansion 	XX	XXX
<ul style="list-style-type: none"> Cores in 1N NaOH at 38°C 	<ul style="list-style-type: none"> Identification of reactive aggregates Assess residual reactivity of aggregates Assess potential for future expansion 	X	XX
Determination of the water soluble alkali content of concrete	<ul style="list-style-type: none"> Assess potential sources of alkalis Assess potential for future expansion 	XX	XX
Monitoring of expansion and movements	<ul style="list-style-type: none"> Confirmation of deleterious expansion Assess current rate of expansion Assess potential for future expansion 	XX	XXX
In-situ assessment of internal stresses and structural integrity	<ul style="list-style-type: none"> Stresses in concrete and reinforcements Assessment of structural damage and integrity 	XX	
Numerical AAR modeling	<ul style="list-style-type: none"> Confirmation of deleterious expansion Assessment of structural damage and integrity Forecasting future expansion and stability Predict structural responses to remedial actions 	XX	XX

X: Results could be useful if test can be done; XX: Do when possible; XXX: Important test

These investigations are designed to provide the engineer and owner of the structure the information needed to make a decision as to whether mitigating measures should be applied to extend the service life of the structure, or, in the most severe cases, whether the structure is fit to

remain in service. The test procedures are extremely comprehensive with regards to the materials aspect of ASR, but are lacking in several areas.

Coverage of structural safety assessment is extremely limited in comparison to some earlier guidance documents, including (ISE 1992, CONTECVET 2000). It is difficult to endorse the use of the elastic rebound test for estimating expansion, as this is a very destructive test, and may do little to improve strength and serviceability assessments. The SDT, as described in Appendix E of the protocol, may be in need of refinement, based on the recent work of Sanchez et al. (2012a). The LCPC method of crack summation neglects the fact that in reinforced structures expansion will be anisotropic. Finally, guidance in interpreting NDT data is nonexistent. An important goal of this research project is to suggest improvements to the FHWA protocol for adoption by TxDOT, and these will be discussed in Chapter 8.

Chapter 3. Exposure Site Specimens

3.1 Specimen Design and Construction

The exposure site specimens were designed to represent a variety of concrete materials and structural elements that may be encountered in field investigations of ASR and DEF. By placing the specimens outdoors, they are exposed to realistic climatic conditions that can be expected in central Texas, rather than standardized laboratory conditions of constant high temperatures and near 100% relative humidity. The scale of the specimens also reduces the alkali leaching issues that can occur in smaller laboratory specimens. Boosted alkali contents are still required to obtain significant expansions within project time constraints; however, the specimens are otherwise able to undergo expansion and cracking that mimics, as much as possible, deterioration in the field. The use of multiple reactive aggregates and both plain and reinforced concrete was designed to allow investigation of the effects of these parameters on NDT measurements and tests conducted on core samples.

3.1.1 Materials and Mixture Proportions

Table 3.1 lists the aggregates used for the exposure site specimens. This table includes both the designations used in previous TxDOT research projects (starting with project 0-4085) to provide anonymity to the aggregate provider, as well as the common name used by researchers and geographical origin. This provides some continuity to readers familiar with previous TxDOT research and testing involving these aggregates, although this results in a discontinuous numbering scheme for this project.

Table 3.1: Aggregates used in exposure site specimens.

Aggregate		Source	Mineralogy and Aggregate Type	Reactivity
ID	Common Name			
F1	Jobe (Newman)	El Paso, TX	Natural sand: quartz, feldspars, siliceous volcanics, chert	Very highly reactive
F6	Evans Road	San Antonio, TX	Manufactured sand: limestone	Non-reactive
F7	Wright	Robstown, TX	Natural sand: quartz and chert	Highly reactive
C2	El Indio	Eagle Pass, TX	River gravel: dolomite, carbonate, siliceous volcanics	Highly reactive
C6	Martin Marietta	San Antonio, TX	Crushed limestone	Non-reactive

Portland cements with high alkali contents were “boosted” with 50% w/w NaOH solution to ensure that all specimens would undergo significant expansions within the time constraints of the project. Type III cement with a Na_2O_e of 0.80% was used in the Jobe (F1) exposure blocks. Type I cement with a Na_2O_e of 0.83% was used in all other specimens. With the addition of

NaOH, the total equivalent alkali loading was 1.25% by mass of cement, or 8.85 lb/yd³ (5.25 kg/m³).

Common mixture proportions were used for all specimens containing each reactive aggregate under study, generally adhering to the requirements of ASTM C1293 (2008). However, the mixture proportions for the Jobe (F1) exposure blocks represent a departure from the standard in order to match the proportions used for the full-scale beams. Table 3.2 shows the mixture proportions used for the exposure site specimens. The mixtures are classified based on the reactive aggregate; the corresponding non-reactive aggregate is also listed in the table.

Table 3.2: Mixture proportions for exposure site specimens.

Component	Jobe (F1)	Wright (F7)	El Indio (C2)
Coarse Aggregate (SSD) lb/yd ³ (kg/m ³)	Martin Marietta (C6)		2028 (1203)
	1546 (917)	1866 (1107)	
Fine Aggregate (SSD) lb/yd ³ (kg/m ³)	1136 (674)	1046 (621)	Evans Road (F6)
			885 (525)
Cement lb/yd ³ (kg/m ³)	Type III	Type I	
	708 (420)		
NaOH added	4.10 (2.43)	3.84 (2.28)	
Total Na ₂ O _e , lb/yd ³ (kg/m ³)	8.85 (5.25)		
w/cm	0.55	0.42	
Water	389 (231)	297 (176)	

3.1.2 Specimen Types and Fabrication

Four primary types of exposure site specimens were fabricated for this study, detailed in Table 3.3. It should be noted that with the exception of two Jobe (F1) blocks, the specimens were designed to expand from ASR only. The exposure block dimensions are identical to those commonly used for specimens located at the Concrete Durability Center's adjacent long term exposure site. The column dimensions and reinforcement are identical to those used in a FHWA-funded project (Bentivegna 2009), and which are located adjacent to the specimens in this study. That project also involved reinforced bridge decks and unreinforced on-grade slabs; however, the specimen sizes were increased for this study to allow for full development of the reinforcement in the bridge decks. General procedures used in the fabrication of the various specimens will be discussed first, followed by details specific to each specimen type.

Table 3.3: Exposure site specimens.

Specimen Type	Dimensions in. (mm)	Reactive Component		
		Jobe (F1)	Wright (F7)	El Indio (C2)
Block	15 x 15 x 28 (380 x 380 x 710)	4	4	4
Unreinforced Slab-on grade	48 x 48 x 11.25 (1220 x 1220 x 286)		2	2
Reinforced Column	24 (dia) x 48 (h) 610 x 1220		2	2
Reinforced Bridge Deck	48 x 48 x 8.5 (1220 x 1220 x 216)		2	2

General Procedures

All concrete for the exposure site specimens was mixed in a 9 CF (255 L) rotary drum mixer using the proportions in Table 3.2, and in accordance with ASTM C192 (2007). Because freezing and thawing is not an issue in Austin, Texas, air entrainment was not required. Thus, NaOH, added to the mixing water in the form of a 50% w/w aqueous solution, was the only additive used. Due to the enormous volume of material involved, aggregates were used in as-received condition, although the material was homogenized in the mixer during the batching process. This ensured that the moisture content samples would be representative of the aggregate used in each batch. Specimens were also moist-cured for seven days after placement using wet burlap and plastic. Three 4 x 8 in. (100 x 200 mm) cylinders were cast from each batch for quality control and tested in compression at 28 days of age.

Exposure Blocks

The Jobe (F1) blocks were each unique, and functioned as a smaller study of the effects of reinforcement on expansions due to ASR and DEF, and the impact of anisotropic expansions on UPV measurements. These blocks were numbered 1 through 4, with additional designations based on the damage mechanism expected (ASR = A, ASR+DEF = AD) and the presence of reinforcement (U = unreinforced, R = reinforced). These will be referred to later in the chapter; thus, for clarity, a summary is provided here:

- Block 1 = A/U
- Block 2 = A/R
- Block 3 = AD/U
- Block 4 = AD/R

Blocks 2 (ASR) and 4 (ASR+DEF) were reinforced using a design described by Wehrle (2010), a sketch of which is shown in Figure 3.1. The reinforcement consisted of four 24 in. (610 mm) #6 bars (Grade 60) in the longitudinal direction, and four #3 stirrups (Grade 60) bent to form 11 x 11 in. (280 x 280 mm) loops and spaced 6 in. on center. The longitudinal bars had 1 x 1.5 x 0.25 in. (25.4 x 38.1 x 6.4 mm) header plates welded to each end to allow full development of the reinforcement. The resulting ratio of longitudinal to transverse reinforcement was 3.73.

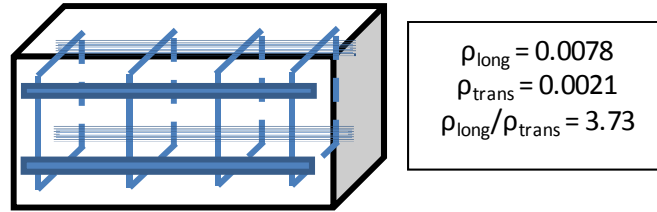


Figure 3.1: Reinforcement sketch of Jobe (F1) blocks 2 and 4.

The Wright (F7) and El Indio (C2) sets of exposure blocks were all unreinforced and all mixing and placement for each set took place in a single day. The Wright (F7) blocks were numbered 5 through 8, and the El Indio (C2) blocks were numbered 9 through 12. In addition to the four blocks in each set, four 3 x 3 x 11.25 in. (75 x 75 x 286 mm) prisms were fabricated with concrete sampled from the batch for the first block in the set. The prisms were moist-cured for 24 h, demolded, stored, and monitored for expansion for one year per ASTM C1293 specifications (2008). The Wright (F7) prisms expanded 0.195%, while the El Indio (C2) prisms expanded 0.117%; these results are within 0.01% of those reported in an earlier study using the exact grading and proportions specified in ASTM C1293 (Folliard, et al. 2006). This suggests that the use of aggregates in the as-received condition did not significantly alter the reactivity of the specimens.

The blocks were placed and consolidated in two layers in wood forms. A plastic bracket holding four 0.375 in. (9.5 mm) diameter stainless steel bolts used for expansion measurements was installed prior to initial set of the concrete. Moist-curing took place in a temperature and humidity controlled room maintained at 73 °F (23 °C) and >50% relative humidity. After seven days, they were moved outside and installed on a bed of crushed limestone (the outdoor exposure site).

Additional procedures were involved in the fabrication of Jobe (F1) blocks 3 and 4 to encourage the development of DEF. These procedures are identical to those described in the thesis of Drimalas (2004). The cement and aggregates were heated in sealed buckets to 140 °F (60 °C) before mixing, while the mixing water was heated to 100 °F (38 °C). The fresh concrete was quickly transported to a 140 °F (60 °C) chamber, placed, and consolidated in foam-insulated wood forms. The forms were then covered in heavy blankets to minimize heat loss. After twelve hours, the heater for the chamber was turned off. The chamber was opened and the specimen allowed to slowly cool to ambient temperatures. Thermocouples recorded the temperature in the top, middle, and base of the specimen. A peak curing temperature of 187 °F (86.1 °C) was recorded in Block 3, while Block 4 reached 179 °F (81.7 °C); both were well above the threshold necessary for the development of DEF.

Unreinforced On-Grade Slabs

The unreinforced on-grade slabs were cast in place on the outdoor exposure site. Wood formwork was assembled and leveled on the gravel bed, and a layer of sand was compacted to provide a level base. Threaded inserts in each side of the formwork anchored the DEMEC target bolts. Three batches of concrete were mixed, placed, and consolidated in rapid succession (under 1 h) for each specimen. A wood bracket containing the DEMEC targets for the top of the specimen was then installed atop the formwork. Figure 3.2 shows the forms before and after concrete placement. Forms were removed after two days and specimens were moist cured for a total of seven days.



Figure 3.2: On-grade slab before (left) and after (right) concrete placement.

Reinforced Columns

Formwork for the reinforced columns consisted of rigid concrete tubes with a 24 in. (610 mm) inner diameter. Reinforcement details were in accordance with the TxDOT Bridge Design Manual (Texas Department of Transportation 2009). Longitudinal reinforcement consisted of eight #7 (Grade 60) vertical bars with 1.75 x 1.75 x 0.25 in. (44.5 x 44.5 x 6.4 mm) header plates welded to each end. Confinement was provided by #3 spiral reinforcement (Grade 60) at a pitch of 6 in. (152 mm). Figure 3.3 shows a plan and elevation view of the column reinforcement.

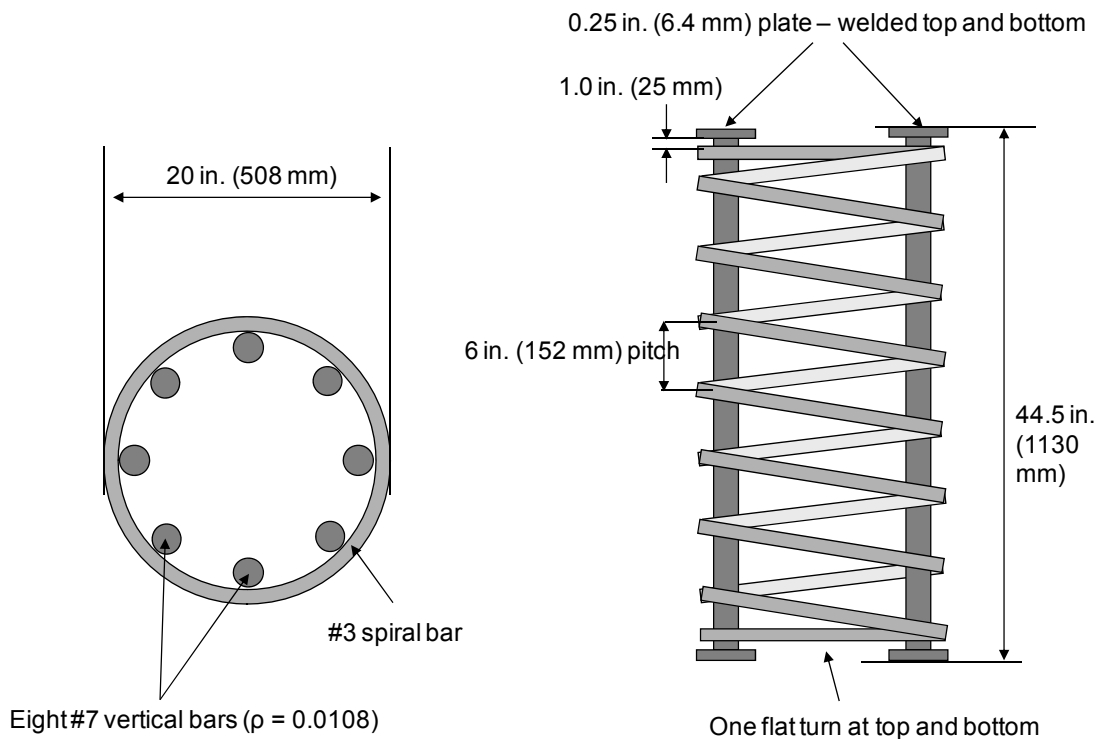


Figure 3.3: Column reinforcement schematic.

The columns were cast in place on the outdoor exposure site. Reinforcement chairs were used to ensure even cover and hold the cage in place inside the forms. Metal stakes anchored the forms to prevent floatation during concrete placement. Three batches of concrete were mixed, placed, and consolidated in rapid succession (under 1 h) for each specimen. Forms were removed after two days and specimens were moist cured for a total of seven days.

Reinforced Bridge Decks

The reinforced bridge decks were fabricated indoors. Wood side forms similar to the on-grade slabs were assembled and attached to a three piece base with wood screws. The base design allowed for the completed specimen to be picked up with a forklift for transport to the exposure site. Two layers of Grade 60 longitudinal and transverse reinforcement were used, per the TxDOT Bridge Design Manual (Texas Department of Transportation 2009). Transverse reinforcement consisted of #5 bars on 6.0 in. (152 mm) centers, with 180 degree hooks at each end to ensure full development of the bars. Longitudinal reinforcement consisted of a top layer of #4 bars on 8.7 in. (221 mm) centers and a bottom layer of #5 bars on 9.0 in. (229 mm) centers. Figure 3.4 shows the reinforcement details and the specimen supports. Deck 3 also contained several Bender elements intended to take internal ultrasonic pulse velocity measurements; however the measurements were ultimately unsuccessful.

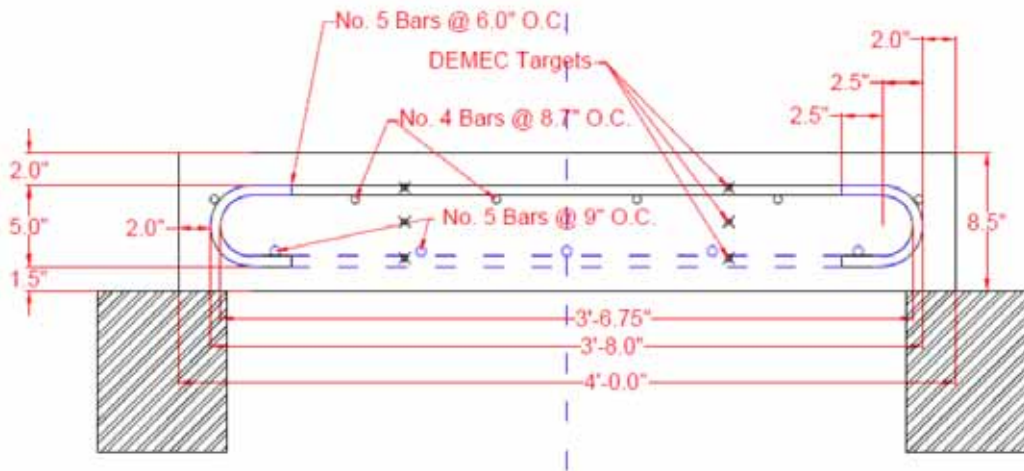


Figure 3.4: Bridge deck reinforcement and supports.

Placement and curing of the concrete took place in a non-climate controlled loading bay located adjacent to the mixing room. As with the on-grade slabs and reinforced columns, three batches of concrete were mixed, placed, and consolidated in rapid succession (under 1 h) for each specimen. A wood bracket containing the DEMEC targets for the top of the specimen was then installed atop the formwork. After seven days of moist curing, they were moved to the outdoor exposure site and placed on wood rail ties. Figure 3.5 shows the assembled formwork and a completed specimen on the exposure site.



Figure 3.5: Bridge deck forms (left) and completed specimen on rail ties (right).

3.2 Experimental Program

An extensive testing program was devised for the exposure site specimens. Ultimately, the exposure blocks and cores obtained from the exposure blocks became the primary focus of this portion of the project. This was due to a reduced emphasis on in-situ NDT of the larger specimens and difficulties with obtaining core samples in the reinforced specimens. A more detailed overview of the test program is provided below, followed by a discussion of specific experimental procedures.

3.2.1 Overview of Testing Program

The testing program for the exposure site specimens can be classified into three main areas:

1. Expansion measurements
2. In-situ NDT
3. Core sample testing

Expansion measurements were conducted on all specimens, while in-situ NDT and core sample testing was used more selectively. Specific test procedures are discussed more thoroughly in section 3.2. The Wright (F7) and El Indio (C2) exposure blocks were the primary source of core samples; near the end of the project, a smaller set of core samples was extracted and tested from the El Indio (C2) unreinforced slabs. Table 3.4 shows an overview of the in-situ NDT test program, while Table 3.5 shows the core sample testing program.

Non-destructive techniques applied on the exposure site were ultrasonic pulse-velocity (UPV), impact-echo (IE), spectral analysis of surface waves (SASW) and surface wave transmission (SWT). The latter two techniques are two different data analysis methods for a single test. UPV was the primary technique, due to its simplicity and the reliability of the equipment.

Table 3.4: NDT program for exposure site specimens.

Specimen Type	Reactive Aggregate	UPV	Impact Echo	SASW + SWT
Block	Jobe (F1)	X	X	X
	Wright (F7)	X	\	\
	El Indio (C2)	X	\	X
Slab	Wright (F7)	\	\	\
	El Indio (C2)	\	\	\
Column	Wright (F7)	X	\	\
	El Indio (C2)	X	\	\
Bridge Deck	Wright (F7)	\	\	\
	El Indio (C2)	\	\	\

X - Extensively applied

\ - Limited use of technique

Based on the testing plan, seven core samples were required from each exposure block. Three were to be used for a series of progressively more destructive tests, beginning with NDT (UPV and resonant frequency), followed by stiffness damage testing (SDT), determination of the static elastic modulus and compressive strength, and culminating with water-soluble alkali testing. Because of time limitations, two of the three were randomly selected for water-soluble alkali testing following compressive strength testing. This series of tests is illustrated in Figure 3.6. In practice, because some cores broke off significantly shorter than intended, more than seven cores were obtained from most blocks. These extra specimens were typically broken in compression to provide an initial estimate of compressive strength for the elastic modulus test. One core was selected for pore solution expression and analysis (PSEA in Table 3.5). Two cores were used for residual expansion testing and one core (sometimes two shorter cores) was sent to Université Laval for petrographic analysis. An inventory of all cores obtained and the tests performed on them is presented in Section 3.3.

Table 3.5: Core sample testing program for exposure site specimens.

Specimen Type	Reactive Aggregate	NDT	Mechanical Testing	Chemical Testing		Residual Expansion	Petrography
				WSA	PSEA		
Block	Wright (F7)	3		2	1	2	1
	El Indio (C2)						
Slab	El Indio (C2)	4		0	0	0	0

**Numbers are cores tested from each block or slab*

NDT = UPV and Resonant Frequency

Mechanical Testing = SDT, elastic modulus (E) and compressive strength (f'_c)

WSA = Water-soluble alkalis

PSEA = Pore solution analysis

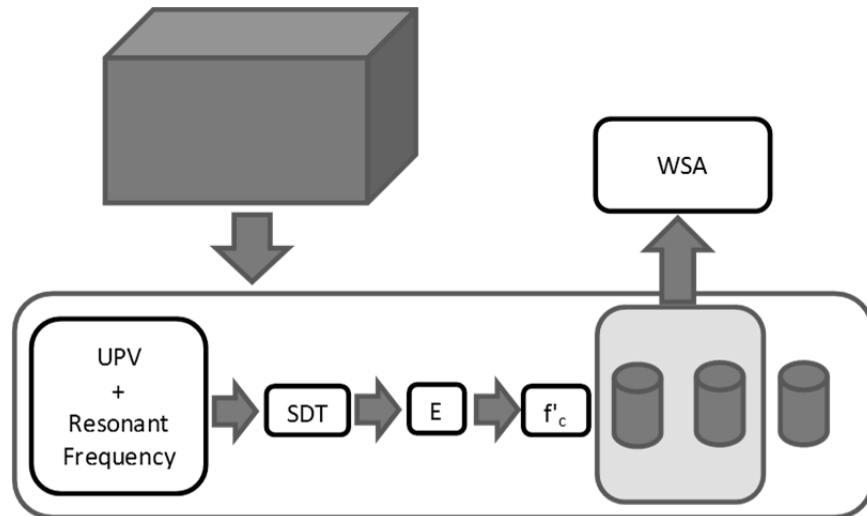


Figure 3.6: Sequence of core testing.

3.2.2 Expansion Monitoring

Expansions of the various specimens were monitored with varied frequency. Since the exposure blocks were either targeted for core extraction at increasing levels of expansion, or contained the highly reactive Jobe (F1) aggregate, they were monitored most frequently. The larger specimens were initially targeted primarily for nondestructive tests, and therefore only required expansion measurements to take place near the time the tests were conducted. However, as nondestructive tests were eventually abandoned on the larger specimens, expansion monitoring became much less frequent. To minimize environmental effects, care was taken to perform expansion measurements in similar conditions. The ideal conditions were 73 ± 3 °F (23 ± 1.7 °C), under mostly cloudy or cloudy skies, with no precipitation in the preceding two days. Some extended warm or cold periods necessitated measurements taken slightly outside the temperature range, to ensure that critical data were not missed. For all exposure site elements, initial expansion measurements were taken at an age of 7 days, following removal of forms and cessation of wet-curing blankets.

DEMEC mechanical strain gauges, with gauge lengths of 19.7 in. (500 mm) and 5.9 in. (150 mm), were used to measure expansions of the exposure site specimens, with the exception of the transverse expansions of the reinforced columns. The DEMEC gauges, manufactured by Mayes Instruments (Figure 3.7), have digital indicators with a precision of 0.00005 in. (0.001 mm) and approximately 0.28 in. (7 mm) travel on the movable tip. The specimens were instrumented with 0.375 in. (9.5 mm) diameter stainless steel bolts with machined divots that matched the conical tips of the DEMEC gauges. For the exposure blocks, on-grade slabs, and reinforced bridge decks, the bolts were embedded in the specimen at the time of concrete placement; the machined tips were inserted into protective threaded housings that were unscrewed just prior to removal forms.



Figure 3.7: Mayes Instruments DEMEC strain gauge.

For the exposure blocks, four 19.7 in. (500 mm) and four 5.9 in. (150 mm) gauge lengths were used. Expansions were measured in the longitudinal and transverse directions on the tops of the blocks, the longitudinal direction on the front and back faces, and the vertical direction on the left and right faces. The 19.7 in. (500 mm) gauge lengths were used to measure longitudinal expansions, while the 5.9 in. (150 mm) gauge lengths measured transverse and vertical (or simply referred to as transverse) expansions. Figure 3.8 shows the locations of the expansion measurements for the exposure blocks. For the on-grade slabs and reinforced bridge decks, a set of three 19.7 in. (500 mm) gauge lengths was located on each of the four sides of the specimen to measure expansions at three depths from the top surface (referred to as high, middle and low). The high and low measurements were located 2.0 in. (50 mm) from the top and bottom of the specimen, with the middle measurement at mid-depth. A fourth 5.9 in. (150 mm) gauge length centered on each side measured the vertical expansion of the specimen. Four 19.7 in. (500 mm) gauge lengths were also arranged in a square on the top of the specimen. Figure 3.9 shows the locations of the expansion measurements for the on-grade slabs; an identical arrangement is used for the reinforced bridge decks.

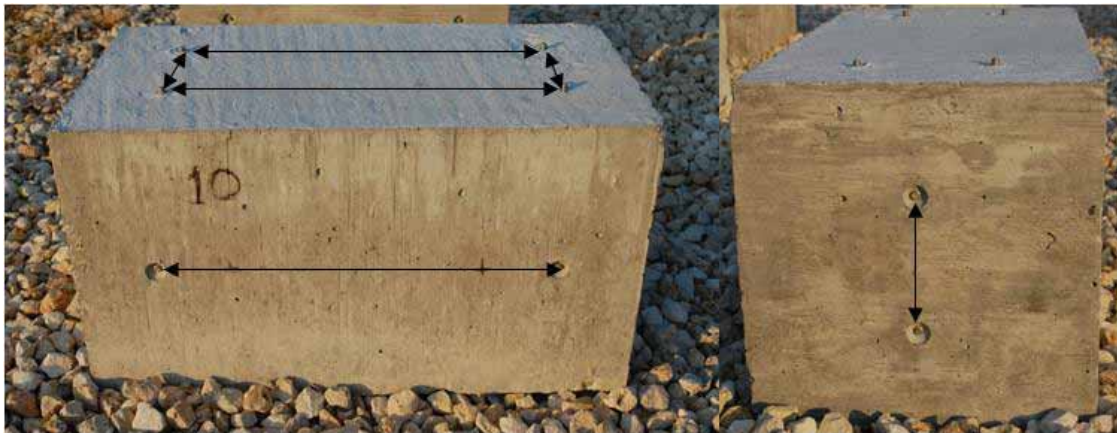


Figure 3.8: Expansion measurement locations for exposure block specimen.

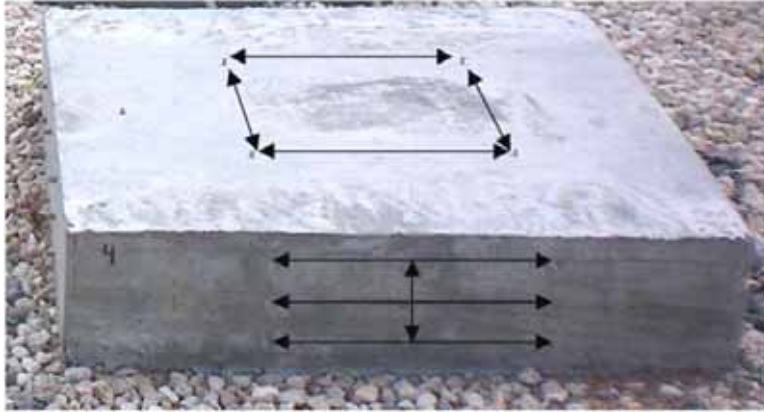


Figure 3.9: Expansion measurement locations for on-grade slab specimen.

The cardboard tube forms for the reinforced columns prevented use of this technique, and required that the bolts be installed following form removal. For these specimens, the hexagonal heads of the bolts were cut off prior to installation. A hammer drill and a metal spacer jig were used to drill pairs of holes at 19.7 in. (500 mm) spacing for vertical expansion measurements on the north, east, south and west faces of the columns. The bolts were then dipped in a rapid-set epoxy and inserted into the holes. This is similar to the method described by Bentivegna (2009), except that four vertical gauge lengths are used instead of two.

Expansion of the columns in the lateral direction (increasing diameter) was measured using a PI tape. The PI tape is a stainless steel measuring tape marked with an English-unit Vernier scale, enabling measurement of the column diameter to a precision of 0.001 in. (0.025 mm). Four reference points were marked on the sides of each column at a distance of 20 in. (508 mm) from the top to ensure that the PI tape was held in the same location every time. Figure 3.10 shows the expansion measurement locations on the columns.



Figure 3.10: Column expansion measurements—vertical (left) and circumference with PI tape (right), from Bentivegna 2009.

3.2.3 In-Situ NDT

A variety of NDT techniques were applied to the exposure site specimens in an attempt to determine which parameters measured by these techniques could be correlated to increasing degrees of damage from ASR and DEF. Expansions were either measured on the same day as performing NDT measurements or interpolated based on expansions measured before and after the NDT measurements.

UPV

UPV was measured using a PUNDIT7 pulse velocity meter and two 54 kHz transducers located on opposite sides of a specimen and coupled to the concrete surface with a water-based ultrasound gel. For each specimen, measurements were taken in two directions (typically east-west and north-south) at several points at mid-height of the specimen (slightly higher for the columns). Figure 3.11 shows the UPV measurement locations for the blocks, columns, and reinforced bridge deck specimens (the on-grade slabs were tested in a similar fashion). The travel time was allowed to stabilize and the lowest stable value was recorded to the nearest 0.1 μ s. Velocities were calculated using nominal travel distances, as precise measurements of the distance between the transducers was not possible. These distances were 28 in. (710 mm) for the long axis of the blocks, 15 in. (380 mm) for the short axis of the blocks, 24 in. (610 mm) for the columns and 48 in. (1220 mm) for the on-grade slabs and reinforced bridge decks.

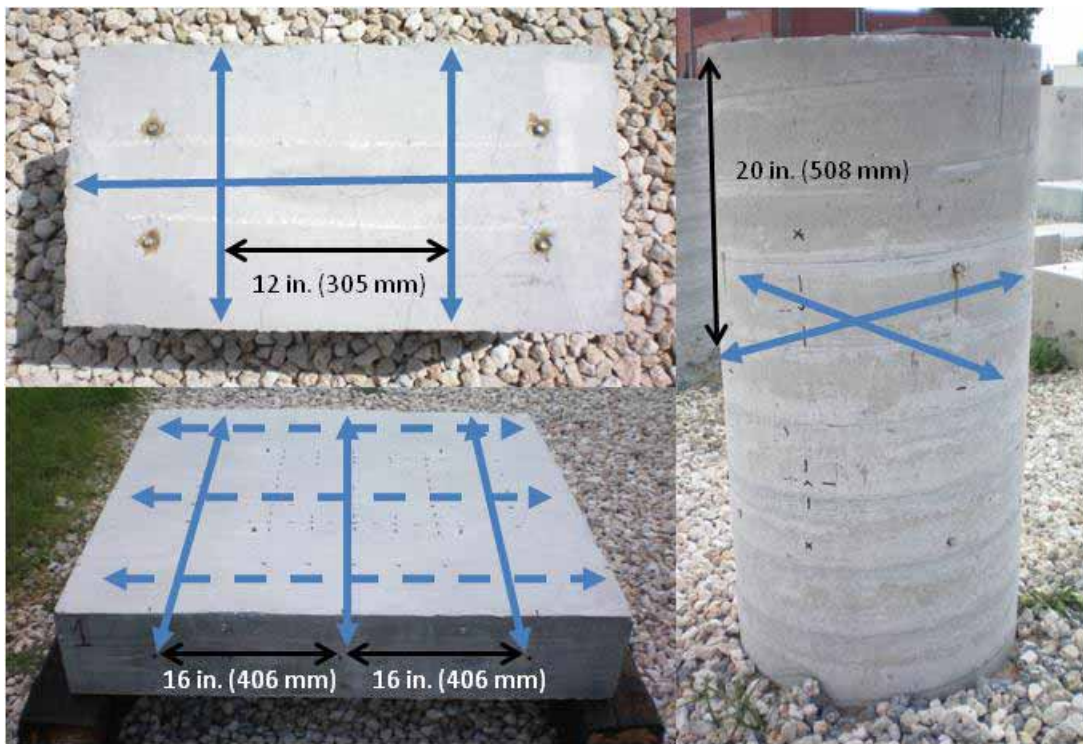


Figure 3.11: UPV measurement locations for exposure site specimens.

Measurements commenced in March 2010, before any measurable expansion could occur in the specimens. For the exposure blocks, this corresponded to an age of 13 to 83 days. For the

larger specimens, initial UPV measurements were taken at an age of three to five weeks, again, before any measureable expansion had occurred.

Impact-Echo

Impact-echo testing on the exposure site specimens was complicated by the geometry of the specimens and therefore was limited in scope. This test method is best suited to thin, plate-like elements; the on-grade slabs and reinforced bridge decks were, therefore, the best candidates. It was primarily investigated as an alternative to UPV for determining p-wave velocity from the peak frequency when access to only a single side of a structure is possible. More extensive tests were conducted on the full-scale beams and are detailed in Chapter 5. In addition to the work performed at UT-Austin, researchers at Texas A&M University have investigated the applicability of the impact-echo method for detecting debonding of the reinforcement that may result from ASR and DEF (Pagnotta, Trejo, and Gardoni 2012).

A small steel ball or ball-peen hammer was used to generate the impacts, while a Germann Instruments DOCTer receiver was used to detect the vibrations. Data was collected for 10 ms through an 8-bit digitizer and LabVIEW software at a sampling rate of 100 kHz, providing a frequency resolution of 100 Hz. A MATLAB program was used to analyze the data. Figure 3.12 shows the test equipment.



Figure 3.12: Impact echo test equipment.

Impact-echo test for the exposure blocks was conducted at a single location at the center of the top face of the block. A 3 x 3 point grid was used for the on-grade slabs and reinforced bridge decks, with the points spaced 8.0 in. (203 mm) apart. On the columns, impacts were measured both on top (center) of the specimens and at four points, each located at mid-height and offset 45 degrees along the circumference of the column from the expansion measurement axes. Figure 3.13 shows the impact echo locations on a reinforced bridge deck and a column specimen.



Figure 3.13: Impact-echo locations for bridge deck and column.

SASW and SWT

Surface wave (SASW and SWT) measurements were conducted using non-contact sensors (two microphones sensitive to frequencies between 4 and 80 kHz) that detected changes in air pressure generated by surface waves in the concrete. The microphones were isolated from ambient noise using acoustic insulation. A 0.5 in. (12.7 mm) diameter steel ball provided the impact source; 5 impacts were generated at a constant distance on either side of the pair of microphones. Vibration data from the microphones were collected through a 3-channel signal conditioner and 8-bit digitizer. Data was then viewed and saved using a LabVIEW program and analyzed in MATLAB. Figure 3.14 shows the test equipment.



Figure 3.14: Surface wave test equipment.

Surface wave testing on the exposure blocks consisted of only one pair of microphone positions, aligned at 6.5 in. (165 mm) spacing in the longitudinal direction, with impacts generated at a distance of 6.5 in. (165 mm) from the microphones. Although a grid pattern is typically desired for surface wave measurements (particularly for SWT analysis), so that many data sets can be averaged, the relatively small size of the specimens precluded this.

A similar problem exists for the columns, this time due to the rounded surface. Measurements were taken along four vertical axes, centered on the impact-echo locations, with the microphones spaced 12.0 in. (305 mm) apart and the impacts located 5.0 in. (127 mm) from the microphones. Figure 3.15 shows the measurement and impact locations for the columns.

For the slabs and bridge decks, a grid pattern was established based on the impact-echo grid. It consisted of five north-south and five east-west axes, spaced 4.0 in. (102 mm) apart. The microphones were placed 16.0 in. (406 mm) apart and impacts were located 8.0 in. (203 mm) from the microphones. Figure 3.15 also shows the measurement and impact locations on a bridge deck.

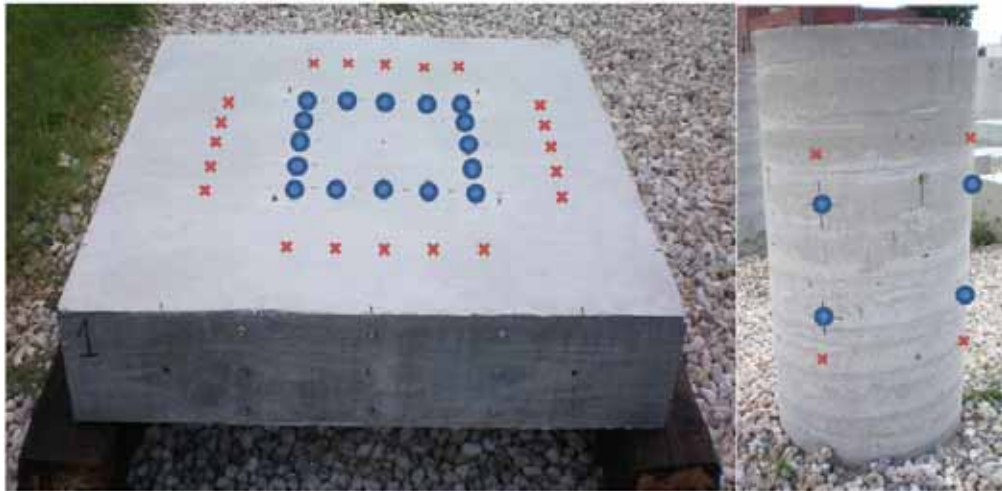


Figure 3.15: Surface wave sensor (circles) and impact (X's) locations for bridge deck and column.

Core Sampling and Preparation

Core samples were extracted using a 4.00 in. (100 mm) (nominal) inside diameter diamond core barrel and drill rig. The only exception was the first El Indio (C2) block, which used a 3.77 in. (96 mm) (nominal) inside diameter barrel. Figure 3.16 shows the coring rig mounted on a block in preparation for extracting a core. Core samples were extracted within several days of the final expansion and UPV measurements for the block or slab. Following extraction, the cores were washed with tap water, patted dry and their approximate usable length was measured (that is, the length of intact concrete through the entire cross-section of the core). They were photographed and significant cracks were noted. Their original location on the block or slab was plotted, and the parent specimens photographed after all samples were extracted. Details of preparation specific to each test are discussed in the appropriate section below.



Figure 3.16: Coring rig mounted on exposure block.

NDT of Cores

Nondestructive testing of the core samples consisted of UPV and resonant frequency measurements. Core samples were prepared first by cutting them to length with a lapidary saw; because a 2:1 length to diameter ratio is preferred for compressive strength testing, the cores were cut to a nominal length of 8.0 in. (200 mm). They were then placed in a loosely covered bucket in a moist curing room for 48 to 72 h prior to testing to ensure that all specimens would be at uniform moisture content (saturated). The specimens were weighed every 24 h; specimens were deemed sufficiently saturated if they gained less than 0.1% mass in the previous 24 h. Finally, the length and diameter of the cores were measured using calipers with 0.001 in. (0.0025 mm) precision.

UPV

UPV was measured using a PUNDIT7 pulse velocity meter and 54 kHz transducers coupled to each end of the core. As with the in-situ UPV measurements, the travel time was allowed to stabilize and the lowest stable value was recorded to the nearest 0.1 μ s. The ultrasonic pulse velocity and the dynamic modulus of elasticity were calculated according to ASTM C597 (2009).

Resonant Frequency

The resonant frequency was measured in both the longitudinal and transverse modes, and used to calculate the dynamic modulus of elasticity, as described in ASTM C215 (2008). An accelerometer was affixed to the specimen with putty, and the specimen placed on a foam pad to allow free vibration. The specimen was struck with a 0.43 in. (11 mm) diameter steel ball. A signal conditioner and 8-bit digitizer collected the vibration data, which was analyzed using a

LabVIEW program that identified the fundamental resonant frequency. A sampling frequency of 50 kHz was used and 100 ms of data were collected, providing a frequency resolution of 10 Hz. Figure 3.17 shows the equipment used for the test, while Figure 3.18 shows a specimen instrumented for measurements. The test was repeated three times for each mode, and the results averaged.

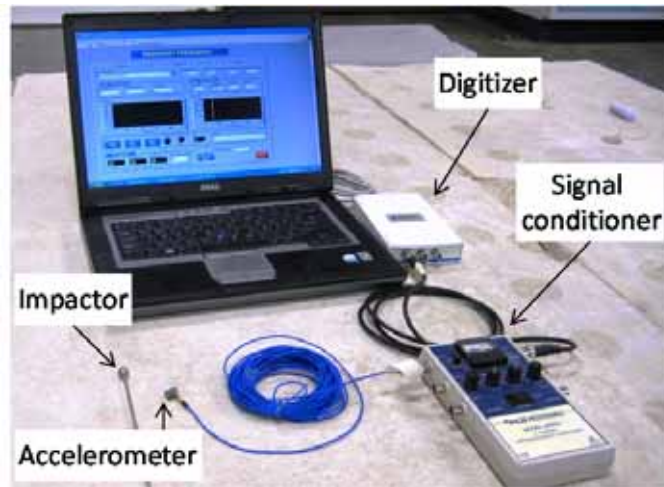


Figure 3.17: Resonant frequency test equipment.



Figure 3.18: Core sample instrumented for transverse (left) and longitudinal (right) resonant frequency measurements.

Mechanical Testing of Cores

Mechanical testing of the cores consisted of stiffness damage testing, static elastic modulus and compressive strength testing, in that order. These tests were typically completed within 24 h of the nondestructive tests. Prior to the mechanical tests, the ends of the specimens were made plane and parallel with a diamond grinder. After grinding and in between each test in the series, the specimens were stored in water to ensure they remained saturated with moisture.

Stiffness Damage Test

The stiffness damage test, as performed in this study, followed the procedure outlined by Smaoui et al. (2004a). The core or cylinder was placed in a compressometer described by ASTM C469 (2010) and subjected to five load cycles with a 22 kip (98 kN) capacity MTS closed-loop hydraulic testing machine. Since the platens installed on the load frame were fixed, a spherically-seated platen was inserted on top of the specimen. A loading and unloading rate of 14.5 psi/s (0.1 MPa/s) was applied, with a peak compressive stress of 1450 psi (10 MPa). An LVDT mounted in the compressometer provided specimen deformation data, while the MTS controller recorded the

applied load. Data was sampled four times per second. The load-deformation data was used to calculate and plot the stress-strain curve for each specimen. The area of the first load cycle hysteresis loop was calculated by subtracting the area under the unloading curve from the area under the loading curve. Figure 3.19 shows the stiffness damage test setup.

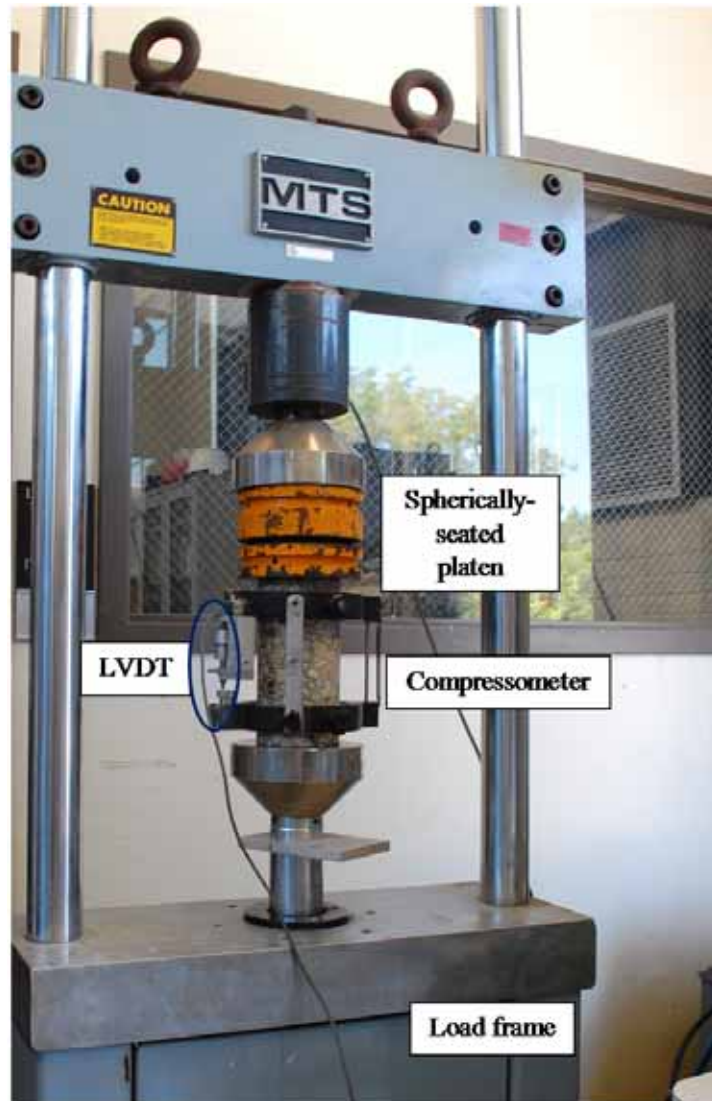


Figure 3.19: Stiffness damage test setup.

Elastic Modulus and Compressive Strength

Following the stiffness damage test, the static secant modulus of elasticity and compressive strength of the cores were determined in accordance with ASTM standards (ASTM C42-11 2011, ASTM C469-10 2010). An estimated compressive strength (f'_c) was used to determine the applied load for the first elastic modulus test, and subsequent tests were based on the compressive strength of the previously tested cores. The goal was to apply a load of $0.40f'_c$, however, the actual applied load varied from 0.33 to $0.43f'_c$ for the core specimens. Secant moduli should be nearly identical for peak loads of 0.30 to $0.45 f'_c$; the loads used in this study are well within that range (Popovics 1998).

Chemical Testing of Cores

Chemical testing was conducted on three cores samples from each exposure block. Of the three cores used for NDT and mechanical testing, two were randomly selected for water-soluble alkali testing. One additional core from each block was selected specifically for pore solution expression and analysis.

Water-Soluble Alkalis

The principal test method used to determine the water-soluble alkali content of the cores was the hot-water extraction method described by Bérubé et al. (2002b), which is summarized below. The core samples were wrapped in plastic and frozen after compressive strength testing to halt the progress of the reaction, and thawed prior to preparation for testing. This allowed all sixteen cores to be processed and tested in a reasonably short timeframe.

From each core, a 4.4 lb (2.0 kg) sample—approximately half of the core—was first crushed in a jaw crusher, and then ground in a pulverizer until the entire sample passed a no. 100 sieve (150 μm). The sample was then reduced by quartering per ASTM C702 (ASTM C702-11 2011) to produce three 0.02 lb (10 g) sub-samples. Each sub-sample was then mixed with 100 mL of deionized water and boiled for 10 minutes. Figure 3.20 shows a sample before and after boiling. The resulting pulp was allowed to cool and rest for 24 h and then filtered to remove solids. Deionized water is added to the filtered solution to adjust the volume back to 100 mL. Sodium and potassium concentrations are then determined through flame photometry. In some cases, the solution required additional dilution for analysis, as the reference solutions contained a concentration of 20 ppm (mg/L) each of sodium and potassium.

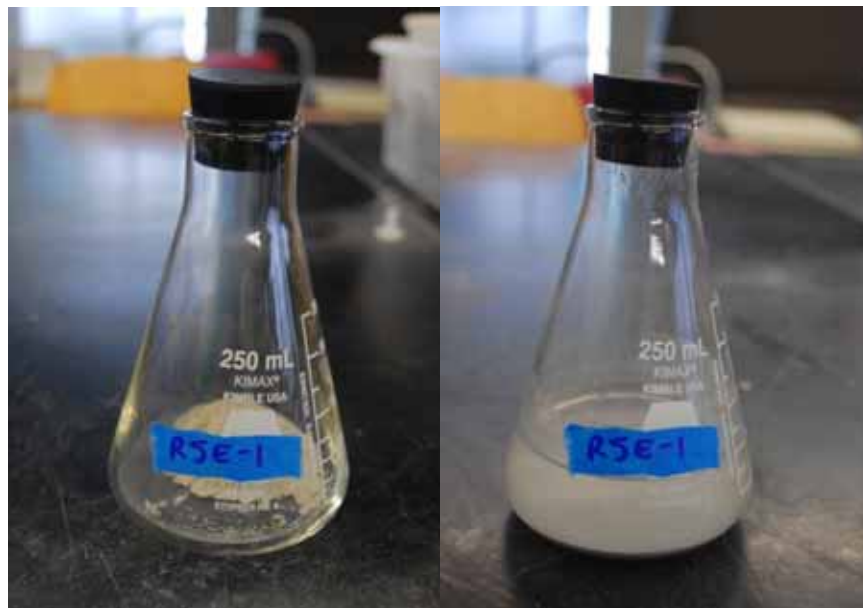


Figure 3.20: Pulverized concrete sample before (L) and after (R) boiling.

The measured concentrations are then used to calculate the available, or current, alkali loading, reported as equivalent soda (Na_2O_e). The mass ratio of alkalis/concrete is first calculated using the solution proportions. Equation 3.1 shows this for sodium.

$$\frac{\text{mass of } Na^+}{\text{mass of concrete}} = [Na^+] \cdot \frac{100 \text{ mL } H_2O}{10 \text{ g concrete}} \cdot \frac{L}{1000 \text{ mL}} \cdot \frac{g}{1000 \text{ mg}}$$

$$= [Na^+] \cdot \frac{L \text{ } H_2O}{100,000 \text{ mg concrete}}$$
Equation 3.1

This is then converted to a mass ratio of sodium oxide or potassium oxide, by dividing the molecular weight of the alkali oxide by that of the alkali ions, seen below in Equation 3.2 for sodium. For potassium, the corresponding molecular weights are 39.098 g/mol for K⁺ and 94.196 g/mol for K₂O.

$$\frac{\text{mass of } Na_2O}{\text{mass of concrete}} = \frac{\text{mass of } Na^+}{\text{mass of concrete}} \cdot \frac{61.979 \text{ g/mol}}{2 \cdot 22.990 \text{ g/mol}}$$
Equation 3.2

These mass ratios are multiplied by 100 to give the mass percentage of each alkali oxide in the sample. The equivalent soda is then calculated using Equation 3.3, and this is then multiplied by the known or assumed density of the concrete to give the current alkali loading in lb/yd³ or kg/m³.

$$\% Na_2O_e = \% Na_2O + 0.658 \cdot \% K_2O$$
Equation 3.3

Several extra samples were prepared and tested using extraction in room-temperature deionized water. The same procedure as the hot-water extraction method was used, except that in lieu of boiling, the solution was shaken for approximately 30 seconds and then allowed to rest for 24 h.

Expression and Analysis of Pore Solution

One core sample from each of the eight exposure blocks was selected for pore solution expression and analysis. The samples were sealed in plastic and frozen after extraction to halt the progress of the reaction; according to literature, this should not impact the results (Bérubé and Tremblay 2004). This allowed expression of pore solution from all eight samples to be conducted in the same week, so that same standard solutions could be used for their analysis. The samples were later thawed for 24 h prior to preparation for testing. A hammer was used to break up the core into fragments of 0.375 in. (9.5 mm) or smaller. Where possible, coarse aggregate fragments were broken out and discarded. Since pore solution exists only in the paste fraction, it is critical that the as much paste (or more practically, mortar) is used for the test. This process was continued until at least 0.55 lb (250 g) of material was prepared.

The apparatus in use at the University of Texas at Austin is similar to that described in Barneyback (1981), with the significant difference that pore solution is collected into a plastic vial located in the base piece (Figure 3.21), rather than through a syringe and plastic tubing system. The apparatus can withstand pressures of at least 125,000 psi (860 MPa). Figure 3.22 shows the assembled apparatus, with each part labeled.



Figure 3.21: Collection vial and base piece.

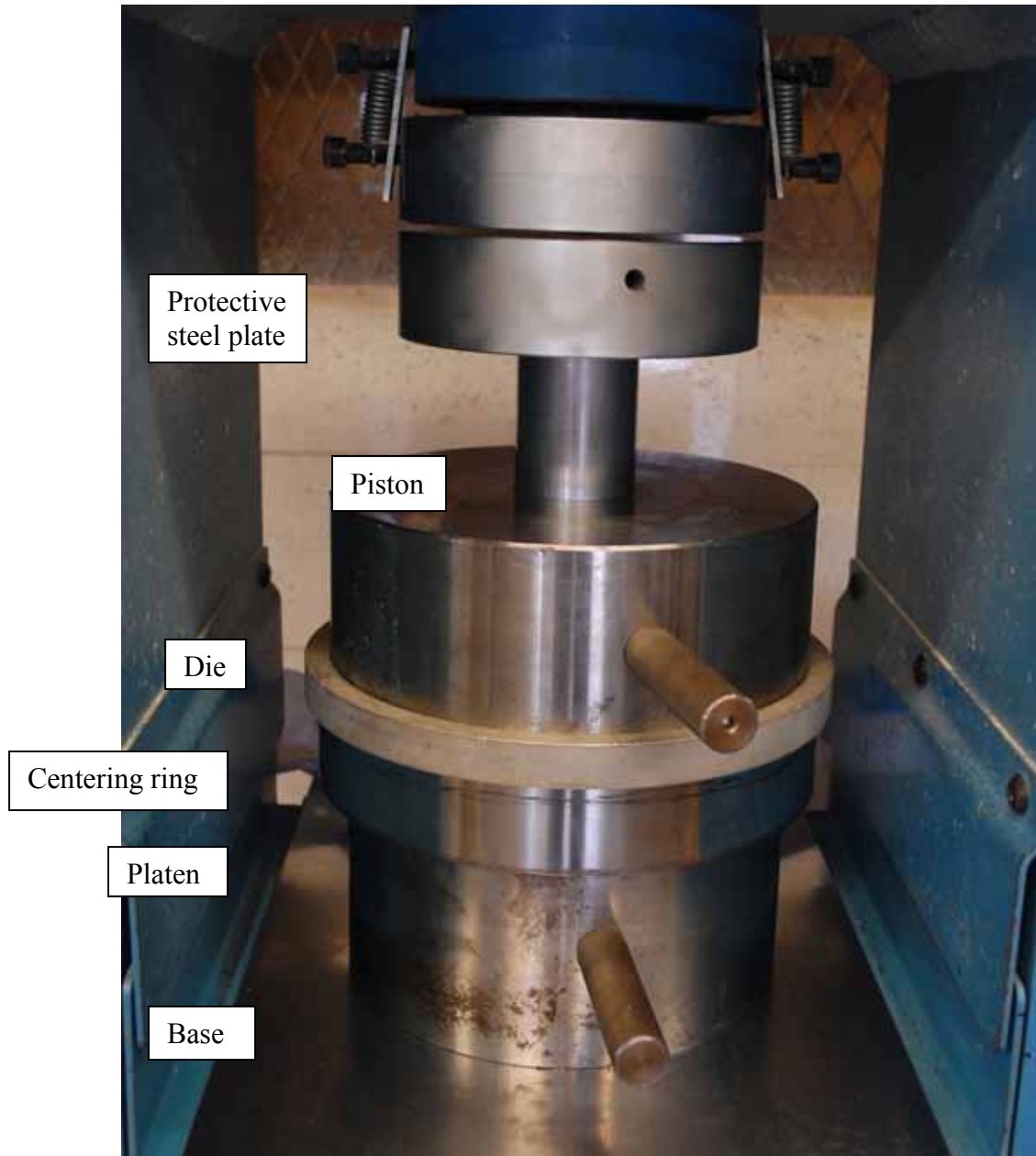


Figure 3.22: Assembled pore solution expression apparatus.

Approximately 0.50 lb (230 g) of material was then weighed in a 250 mL beaker, along with a 2.25 in. (57 mm) diameter, 3/16 in. (5 mm) thick Teflon disc, which serves as a seal between the sample material and the piston. Once the apparatus was assembled in the compression testing machine, the sample material was then introduced and compacted in three layers into the die cavity, and the Teflon disc placed on top. Next, the piston was inserted and 5,000 lbf (22 kN) of load applied, then released, to square off the upper bearing plate of the compression test machine, and ensure that the piston has been properly inserted. Load was then applied at a rate of 30,000 to 40,000 lbf/min (133 to 178 kN/min) until a maximum load of approximately 400,000 lbf (1780 kN) was reached. This corresponds to a pressure of approximately 100,000 psi (690 MPa). The maximum load was held for three to five minutes,

then slowly released (instantaneous release can damage the apparatus and/or compression testing machine). The apparatus was then disassembled and the vial of expressed solution immediately sealed to prevent carbonation or other contamination. The vial was weighed to determine the amount of recovered pore solution. The remaining sample material was ejected from the die, and the weighed before and after 24 h of drying in a 226 °F (107 °C) oven, to determine the remaining evaporable water content. This allowed calculation of the percentage of pore solution recovered.

The extremely small volume of expressed pore solution combined with its very high concentrations of Na^+ , K^+ and OH^- required very high dilution ratios for analysis. OH^- concentrations were determined within a few hours of expression, to prevent carbonation of the solution. Two 25 mL samples were prepared from pore solution diluted 50:1 with high purity (18 M Ω resistivity) deionized water, were titrated against 0.05M standard HCl to the phenolphthalein end point. If they did not agree within 0.1 mL of HCl, a third sample was prepared and titrated. The advantage to this dilution ratio and HCl concentration is that the molarity of the pore solution is simply 1/10 the volume of HCl used in the titration, in mL. Na^+ and K^+ were measured using flame photometry. Standard reference solutions consisted of 20 ppm each Na^+ and K^+ , this required dilution ratios 400:1 or 500:1 for analysis.

Residual Expansion of Cores

Residual expansion tests were conducted on two cores each from two Wright (F7) and three El Indio (C2) exposure blocks. The first Wright (F7) block to be cored did not yield enough cores of sufficient length for residual expansion testing. Also, the final blocks from each set were cored near the end of the project, so there was insufficient time to conduct the test. If necessary, the cores were wrapped in plastic and placed in a refrigerator to temporarily stop any expansion before testing could commence. Cores were trimmed to a length 8 ± 0.125 in. (203 ± 3 mm). In each end, a 0.25 in. (6.4 mm) diameter hole was drilled and a stainless steel gauge stud bonded in place with epoxy. The cores were placed in a moist curing room for 24 h to ensure they were saturated with moisture prior to starting the test. Finally, an initial length measurement was taken relative to a 6.81 in. (173 mm) gauge length and the cores were placed in a sealed bucket. They were stored at 100 °F (38 °C) and $\geq 95\%$ relative humidity, although they were cooled to 73 °F (23 °C) for 16 ± 4 h prior to periodic axial expansion measurements. The cores were monitored for five to twelve months.

This technique was determined to be more reliable than affixing DEMEC gauge points to the sides of the cores with epoxy. Past experience with that technique at UT-Austin has shown that the gauge points are prone to shifting while the epoxy sets; this can require several attempts before the gauge points are properly positioned so that measurements can be taken. Additionally, at least three sets of gauge points should be installed if placed on the sides for reliable measurements, while end installation requires (and allows for) only a single pair of gauge studs.

Petrographic Testing of Cores

One core sample from each exposure block was sent to Dr. Benoît Fournier's laboratory at Université Laval for petrographic analysis. Quantitative assessment of the effects of ASR was determined using the Damage Rating Index (DRI). Prior to shipment, the cores were sealed in plastic and stored in a refrigerator to slow the progress of the reaction. The cores were also refrigerated upon arrival at Dr. Fournier's laboratory until they could be prepared for analysis.

Preparation and examination of the cores for DRI is described in greater detail by Grattan-Bellew (1995), however a short summary is provided here. The core is sawn in half

lengthwise and the sawn surface of one half is polished. The polished face is coated with uranyl acetate, which fluoresces under UV light. A grid composed of 0.4 in. (10 mm) sided squares is drawn, and each square is examined under 16X magnification and defects characteristic of ASR are noted. Defects involving ASR reaction product (gel) are weighted most heavily; careful preparation of the sample is critical to avoid damaging or dissolving the reaction product. The results are then normalized for an area of 15.5 in² (10,000 mm²) to provide a DRI score.

3.3 Results and Discussion: In-Situ Monitoring

This section presents the results of the in-situ monitoring program, including expansion measurements and non-destructive testing (NDT). Expansion is the most common measurement for the progress of ASR and DEF in concrete. As such, it is important to determine if the results of the NDT methods can be correlated to expansion of the specimens.

3.3.1 Expansions

Expansion monitoring results for the twelve exposure blocks are presented below. Figures 3.23, 3.24 and 3.25 show the average expansions with time for the Jobe (F1), Wright (F7) and El Indio (C2) exposure blocks, respectively. In Figure 3.23, the effects of high temperature curing are quite apparent, as blocks 3 and 4 experienced approximately twice the expansion of blocks 1 and 2. Blocks 3 and 4 also begin to expand sooner after fabrication; however, they were fabricated in February 2010, two months later than blocks 1 and 2, which meant that they did not have to wait as long before being exposed to warmer spring and summer temperatures. This figure also shows that the use of reinforcement had only a minimal impact on the average expansion. Figures 3.24 and 3.25 show that the four blocks in each series experienced similar expansion histories.

The effects of reinforcement on the Jobe (F1) exposure blocks is further explored in Figure 3.26, which shows the evolution of the ratio of average transverse to average longitudinal expansion. Data for expansions less than 0.01% are omitted. Although the average expansions of the reinforced blocks (2 and 4) are only slightly less than the unreinforced blocks (1 and 3), the reinforcement clearly had an impact. The ratio of the unreinforced blocks is always close to 1. In the reinforced blocks, expansions in the transverse direction (lightly reinforced with stirrups) quickly rise to approximately twice that of the longitudinal (principal reinforcement) direction. The expansion ratio for block 2 eventually stabilizes around 2.5; in block 4 the ratio approaches 2.9, before falling to 2.6 by the end of the study.

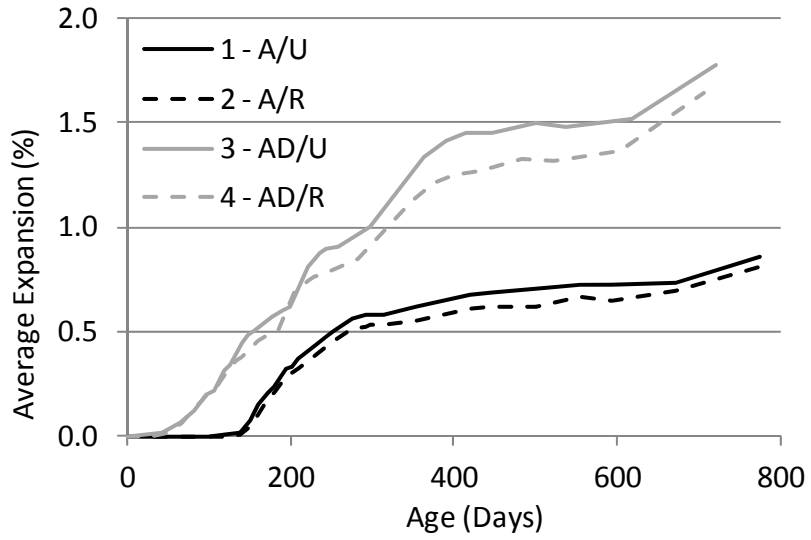


Figure 3.23: Average expansions of the Jobe (F1) exposure blocks.

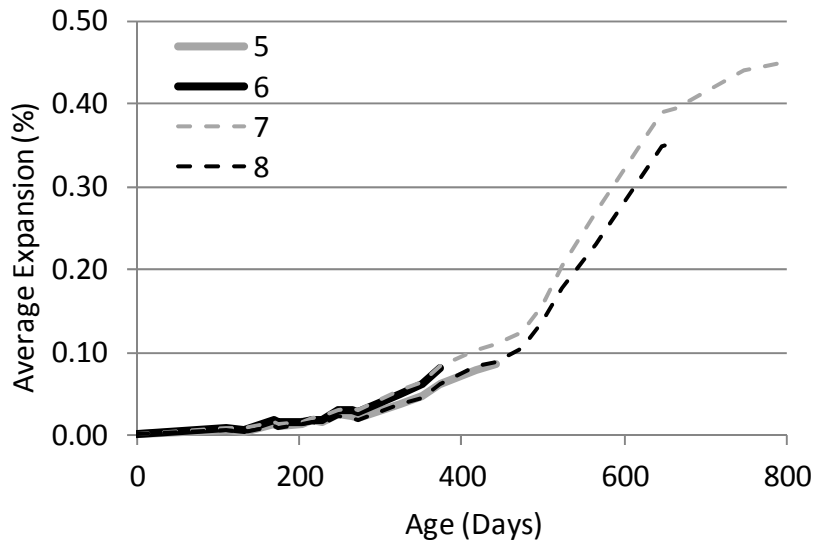


Figure 3.24: Average expansions of the Wright (F7) exposure blocks.

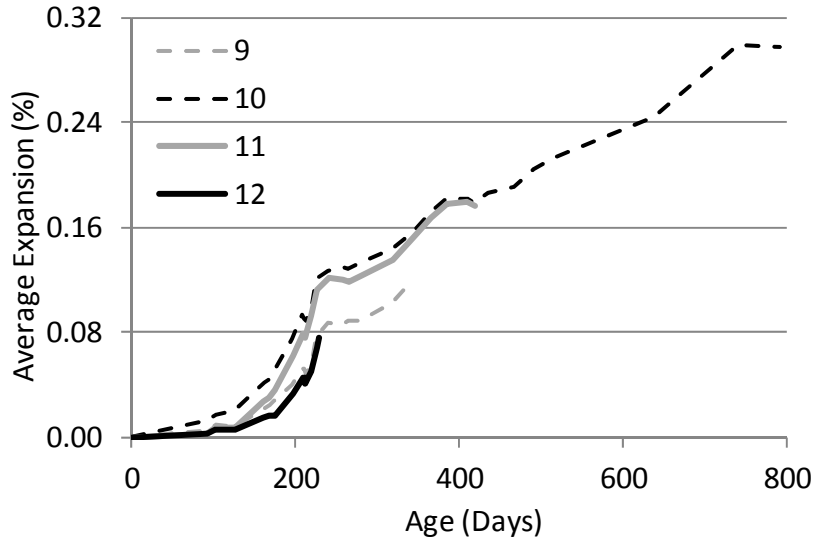


Figure 3.25: Average expansions of the El Indio (C2) exposure blocks.

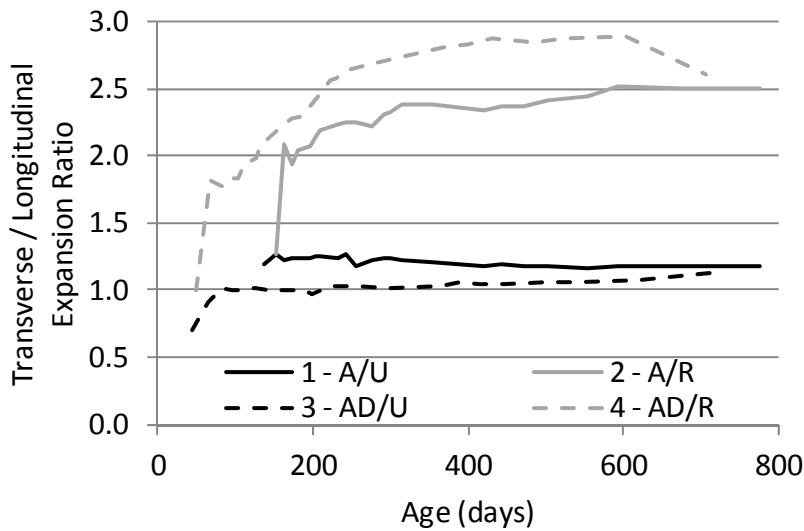


Figure 3.26: Transverse to longitudinal expansion ratio of Jobe (F1) blocks.

The expansion plots shown above provide a good indication of the reactivity of the aggregates used on the exposure site. For brevity, only selected expansion data is shown for the larger exposure site elements. Since they were fabricated four to six months after the exposure blocks, their expansions at the time of this writing are considerable less in some cases.

In Figure 3.27, the expansions are presented for two on-grade and two reinforced bridge deck specimens. The expansions are an average of the four sides of each specimen. S1 and D1 contain the Wright (F7) aggregate, while S3 and D3 contain the El Indio (C2) aggregate. This figure shows that the vertical expansions were consistently greater than those measured in the horizontal direction. This is to be expected for the bridge decks as there is considerably less confinement in this direction; however, the reasons are less clear for the unreinforced slabs. It is

possible that the subgrade provided some resistance to horizontal expansion. These observations also agree with Smaoui et al. (2004c), who noted that ASR expansion is influenced by the orientation of concrete placement; that is, the direction normal to the casting plane tends to experience greater expansion. This figure also shows that the reinforcement in specimens D1 and D3 reduced expansions by 50% or more compared to specimens S1 and S3, and that a strain gradient has developed as a result of the increasing confinement provided by reinforcement from top to bottom of the specimens. Figure 3.28 presents the expansion data for two of the reinforced column specimens; the expansions are of similar magnitude as the reinforced bridge decks.

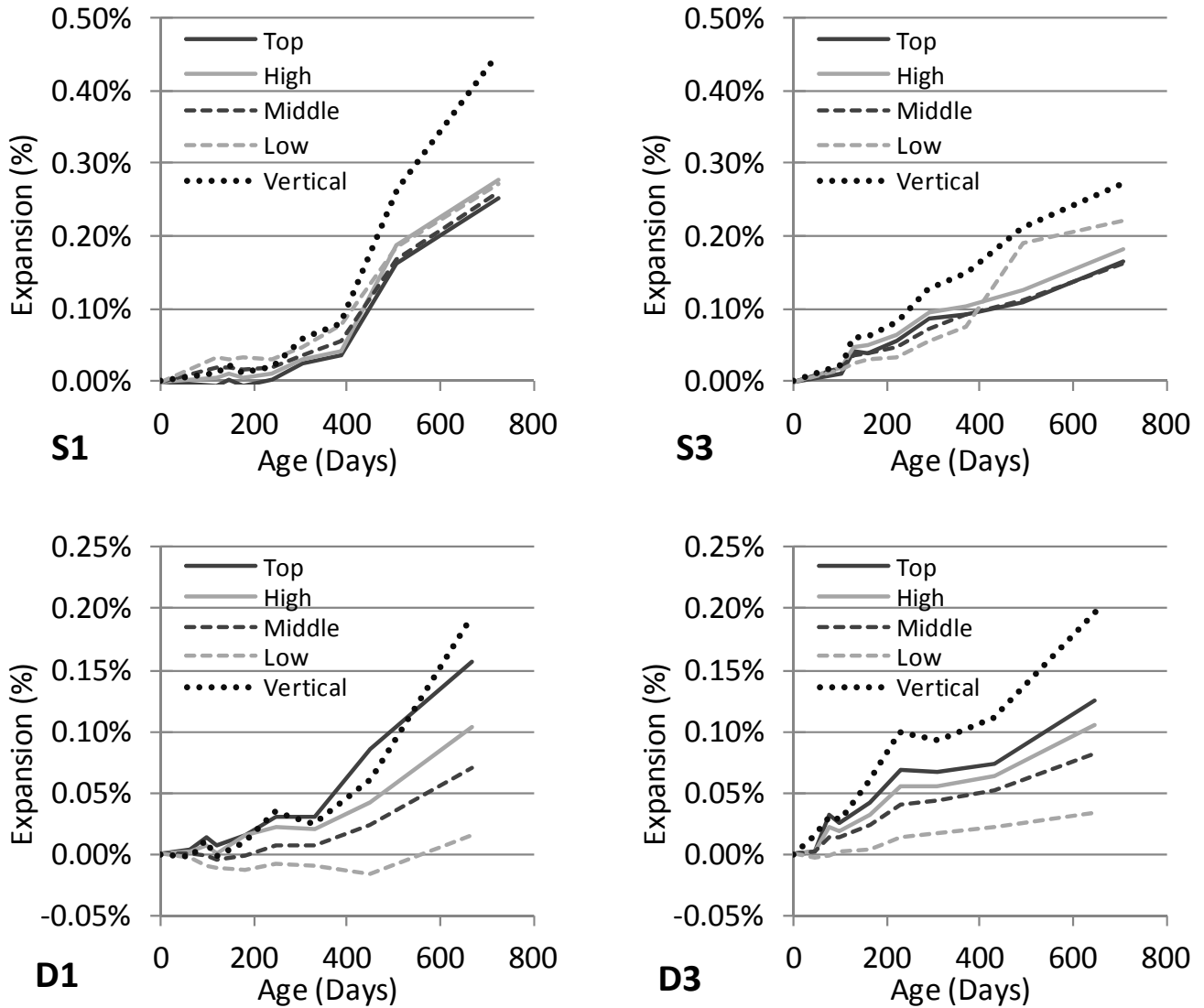


Figure 3.27: Expansion data for selected slab and deck specimens.

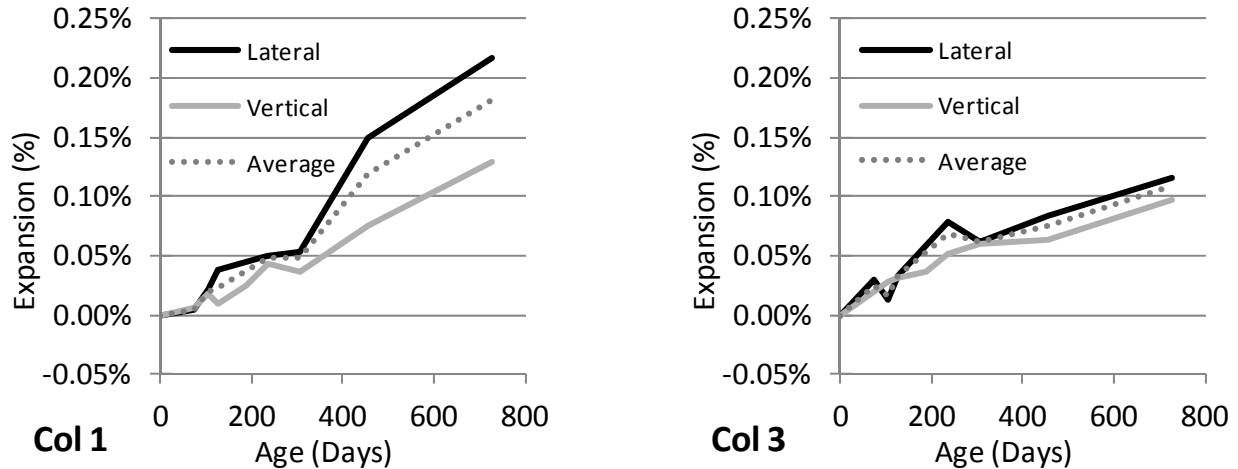


Figure 3.28: Expansion data for selected columns.

3.3.2 In-Situ NDT

Relevant data from the in-situ NDT program are presented in this section. A particular emphasis is given to UPV, which was the most frequently applied technique. In all cases, the goal is to determine whether a change in a particular parameter (such as velocity for UPV) can be correlated to expansion and damage caused by ASR and DEF.

Two vertical lines are also included in most figures, indicating 0.10% and 0.207% expansion. A value of 0.10% is the approximate expansion at which cracking is noticeable from a distance and could potentially prompt an investigation of its cause. Thus, it is important to know how sensitive a particular NDT parameter is to expansions in excess of this value. The second value, 0.207%, is the assumed yield strain of Grade 60 reinforcing steel. If expansion causes yielding of the steel, it is essentially unable to provide additional confinement in response to continuing expansion.

UPV

The UPV results are presented primarily in terms of the percentage change in velocity from the initial measurement, at which time the specimen is assumed to be undamaged. In order to provide a reference for the velocity changes presented below, Figure 3.29 shows the average initial velocity for each of the exposure blocks. While the Wright (F7) and El Indio (C2) blocks are all very consistent, with initial velocities in the range of 4400 to 4500 m/s, there is a marked difference in between the Jobe (F1) blocks that were cured at elevated temperatures and those that were not. The initial velocity of block 3 is 15% lower than that of block 1. According to the classification system devised by Malhotra (1976), the initial UPVs for blocks 3 and 4 correspond to the high end of the “questionable” quality range and the low end of the “good” quality range, respectively.

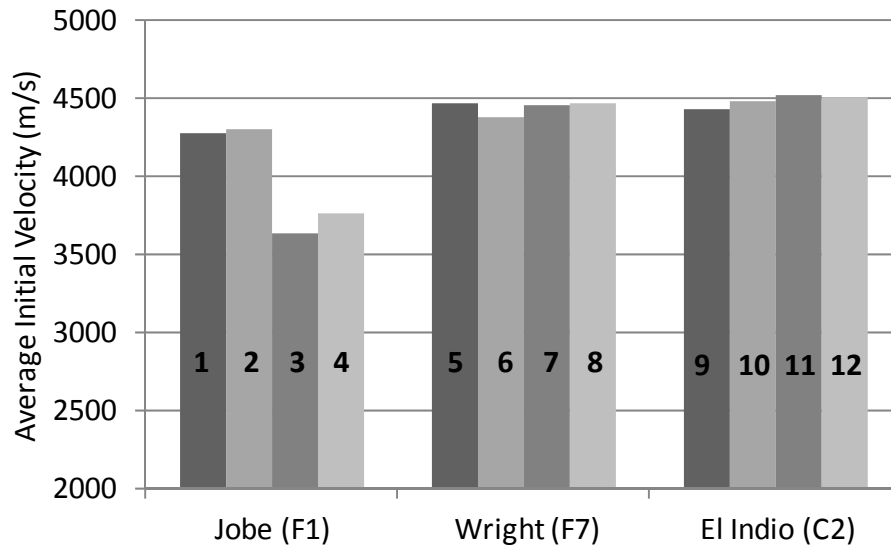


Figure 3.29: Average initial velocity for exposure blocks (1 m/s = 3.28 ft/s).

This suggests that structures cured at temperatures high enough to potentially result in DEF may exhibit significantly lower velocities long before any damage is evident. Similar, but less dramatic differences were observed in tests of the full-scale beam specimens, and are discussed in Chapter 5. Attempts to reproduce this effect with cylinders cured at a peak temperature of 194 °F (90 °C) and tested under laboratory conditions resulted in velocities just 6.6% lower than for cylinders cured at 73 °F (23 °C) (Giannini and Zhu 2012). Blocks 3 and 4 reached slightly lower peak temperatures, but had higher fresh temperatures and took longer to cool down. This may have contributed to the differences in initial velocity compared to the lab specimens.

Figure 3.30 presents the change in UPV plotted against the average expansion of the Jobe (F1) exposure blocks. This figure shows that the ASR blocks (1 and 2) experienced a much more rapid decrease in UPV for a given amount of expansion than the ASR+DEF blocks (3 and 4). This may be partly a result of the fact that blocks 3 and 4 already had much lower velocities. Blocks 3 and 4 also exhibit very little change in velocity between 0.2 and 1.0% expansion; this would be quite problematic if attempting to monitor the progress of ASR and DEF using UPV. For the ASR blocks, a velocity decrease of 7 to 9% was observed at an expansion of 0.1%, and the maximum decrease ranged from 21 to 24% at the end of the monitoring period. These specimens exhibited the greatest decrease in UPV in response to increasing expansion; however, the data for the rest of the exposure site is not as promising.

Because the reinforcement in blocks 2 and 4 resulted in much higher expansions in the transverse direction, the UPV data was further examined to see if it was influenced by the degree of expansion in the direction of the measurement. Figure 3.31 compares the change in UPV in each direction to both the directional expansion (i.e., transverse velocity change vs. transverse expansion) and the average expansion. This figure clearly demonstrates that UPV is influenced by the average, or volumetric, expansion, rather than the expansion in a particular direction.

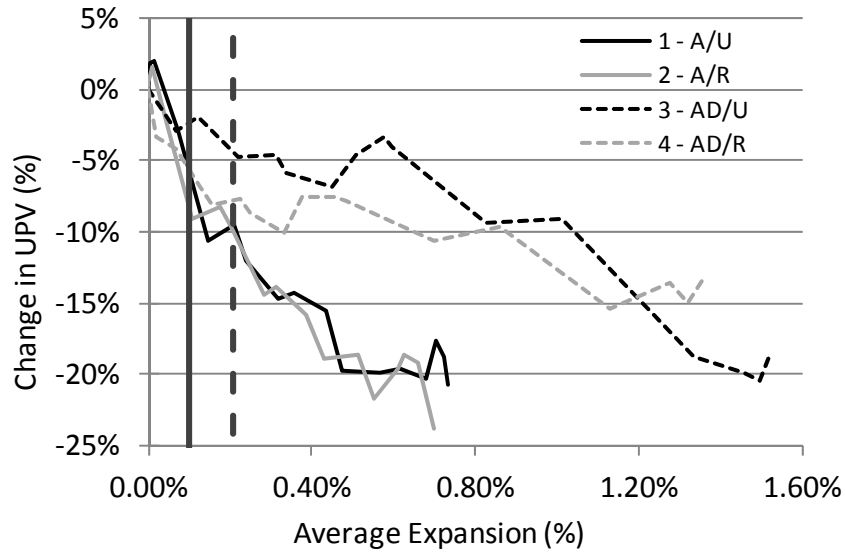


Figure 3.30: Change in UPV vs. average expansion for Jobe (F1) exposure blocks.

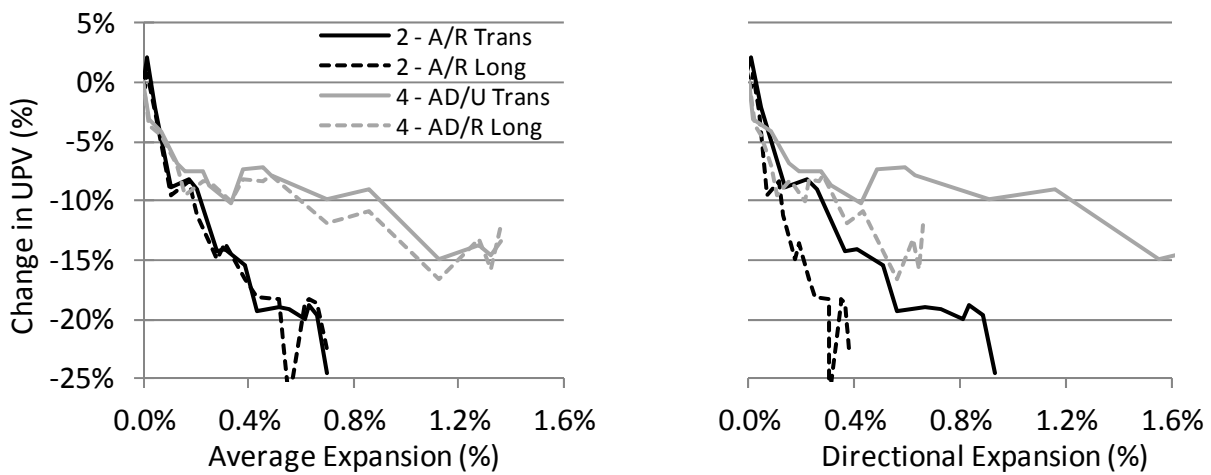


Figure 3.31: Change in transverse and longitudinal UPV vs. average (left) and directional (right) expansion, Blocks 2 and 4.

Figures 3.32 and 3.33 show the UPV data for the Wright (F7) and El Indio (C2) exposure blocks, respectively. Velocities for the Wright (F7) blocks initially increased, then began to decline around 0.05% expansion. At 0.10% expansion, the velocity was less than 1% below the initial measurement. Up to a 10% decrease in velocity was observed between 0.35 and 0.40% expansion; however, at 0.45% expansion, the velocity measured for block 7 had recovered to just 6% below the initial velocity. The El Indio (C2) blocks also showed an initial velocity increase, but by 0.10% expansion the velocities were between 1 and 5% below the initial measurement. A maximum velocity decrease of 7% was observed for blocks 10 and 11, although this occurred at different expansions. As with the Wright (F7) blocks, the velocity decreases were partly reversed at later ages.

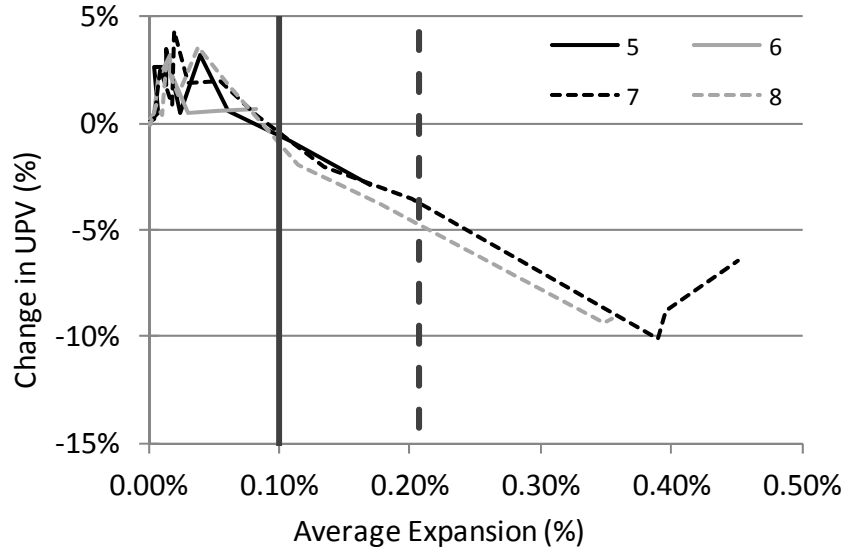


Figure 3.32: Change in UPV vs. average expansion for Wright (F7) exposure blocks.

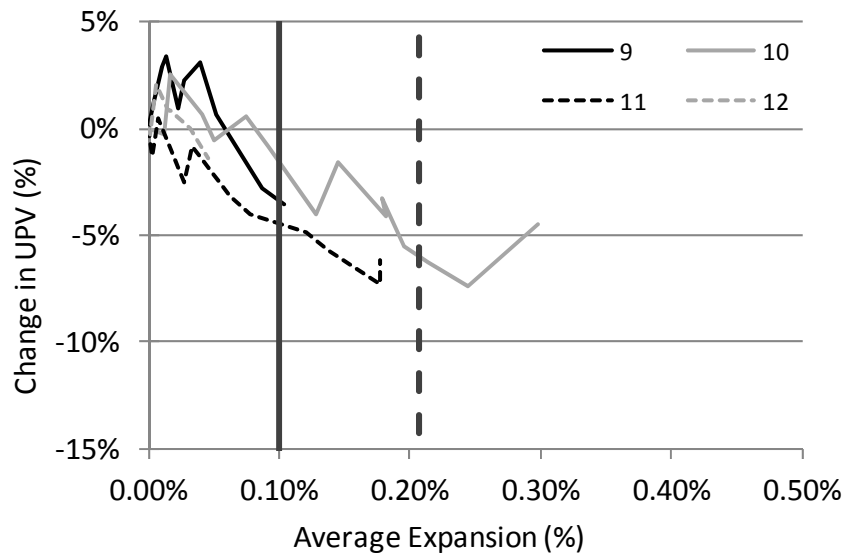


Figure 3.33: Change in UPV vs. average expansions for El Indio (C2) exposure blocks.

Obtaining quality UPV data from the larger exposure site specimens was more problematic. All specimens exhibited initial velocities in the range of 4500 to 4600 m/s—comparable to the exposure blocks containing the same materials. In the columns, the travel path for the ultrasonic pulses was slightly less than the longitudinal axis of the exposure blocks. However, for the on-grade slabs and reinforced bridge decks, the travel path was 71% longer. After they began to expand due to ASR, the received signal was too weak to trigger the timer reliably. Furthermore, measurements in the plane of a pavement slab or bridge deck are unlikely to be taken in the field. Thus, only the data for the columns are presented in Figure 3.34, with the change in UPV plotted against the average expansion of the columns. The data for the Wright (F7) columns (1 and 2) indicate a slightly greater loss of velocity at 0.1% expansion compared to

the exposure blocks; however, this may be in part due to moisture effects. A 2.5% decrease in velocity was measured for the El Indio columns (3 and 4) at 0.1% expansion; this is consistent with the exposure block data.

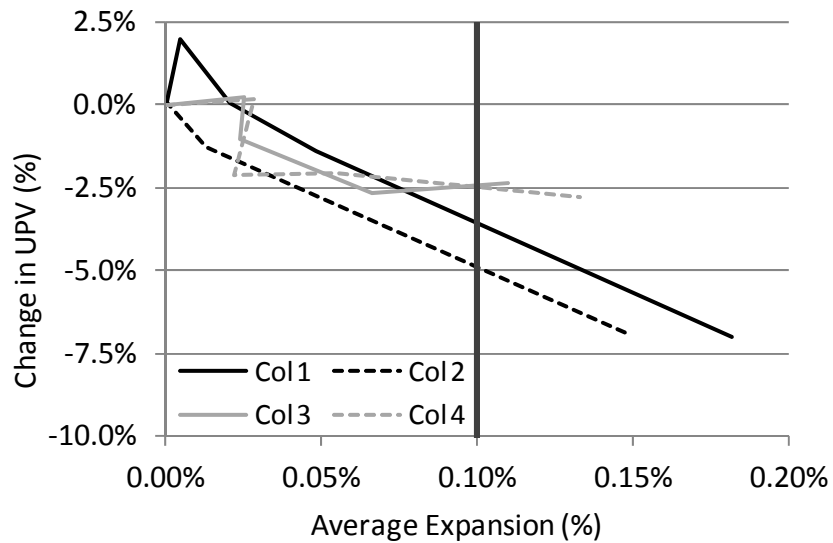


Figure 3.34: Change in UPV vs. average expansion of columns.

The UPV data for the exposure site specimens demonstrates the difficulty of correlating a change in velocity to a certain amount of expansion, even if an undamaged reference is available. The observed changes in velocity are not particularly significant considering that the degree of moisture saturation can affect results by as much as 5% (Naik, Malhotra and Popvics 2004). Furthermore, the degree to which any significant change in UPV may be detected for expansions in excess of 0.10% appears to be dependent on the reactive aggregate. Thus, the use of UPV measurements may be able to help qualitatively assess whether certain regions of the structure are more damaged than others, and perhaps identify areas of interest for more invasive testing (core sampling).

3.3.3 Impact-Echo

The discussion of impact-echo results will be limited to tests performed on the on-grade slab and reinforced deck specimens. Although the geometries of the specimens were better suited to impact-echo than the other specimen types, data collection was halted before significant expansions occurred. This is because the p-wave velocities calculated from impact-echo were being compared to those measured using through-transmission UPV, which could no longer be measured after the onset of expansion and cracking. The p-wave velocity was calculated using frequency domain analysis for each impact location, as described in Chapter 2, and averaged for the nine impacts per specimen.

Table 3.6 shows a comparison of p-wave velocities measured using UPV and calculated from the impact-echo response. Both sets of data are the initial measurements, taken within four weeks of specimen fabrication. As can be seen, the velocities are very similar, although UPV generally gave a higher velocity. This could in part be due to the difficulty of accurately measuring the specimen thickness at the impact-echo test locations. Also, the ultrasonic pulses

for UPV must only traverse the specimen a single time, whereas impact-echo relies on the compression wave echoing back and forth through the depth of the specimen. In the case of the bridge decks, the presence of reinforcement along both axes of UPV measurements may have resulted in slightly higher calculated velocities compared to impact-echo, in with the compression waves path is normal to the plane of the reinforcement.

Table 3.6: P-wave velocities from UPV and Impact-echo tests. (1 m/s = 3.28 ft/s).

Specimen	P-wave velocity (m/s)		Δ (%)
	UPV	IE	
Slab 1	4536	4511	0.6%
Slab 2	4465	4438	0.6%
Slab 3	4565	4438	2.8%
Slab 4	4597	4452	3.2%
Deck 1	4510	4378	2.9%
Deck 2	4512	4429	1.8%
Deck 3	4493	4260	5.2%
Deck 4	4504	4321	4.1%

Figure 3.35 compares the p-wave velocities calculated from UPV and impact-echo measurements during the initiation of expansion from ASR in two specimens. From this figure, it is clear that even at low levels of expansion, the velocities calculated based on the impact-echo frequency response decrease more rapidly than those measured using UPV. For slab 3, the velocity calculated from the impact-echo data is 10% lower at 0.035% expansion, compared to a reduction of just 2% in the velocity measured using UPV. Thus, the two techniques will not necessarily give the same p-wave velocity, particularly if the measurements are taken in different directions as they were in this case. The orientation of the measurements exposes the stress waves to internal defects at different angles.

It is also important to note that the UPV utilizes focused pulses with a central frequency of 54 kHz, while impact-echo excites specimens using a point impact that propagates throughout the concrete. For the data shown in Figure 3.35, the peak impact-echo frequencies were in the range of 7 to 10 kHz, depending on the specimen thickness and expansion. Therefore, UPV and impact-echo can be expected to be influenced by different types of defects.

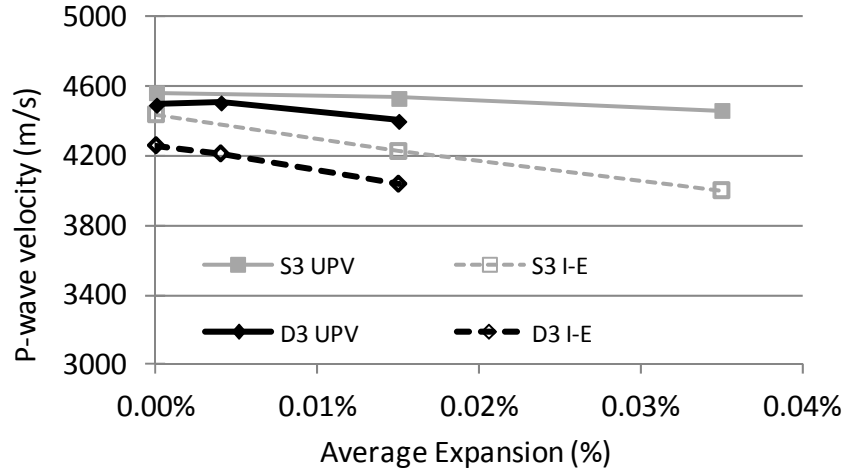


Figure 3.35: P-wave velocities vs. expansion for Slab 3 and Deck 3 (1 m/s = 3.28 ft/s).

SASW and SWT

The two methods of analyzing surface wave test data will be covered in greater detail in Chapter 5, as the significantly more data were collected from the full-scale beams. The analyses of tests on the beams had led the research team to cease surface wave testing before the exposure site specimens, except of the Jobe (F1) exposure blocks, had undergone significant expansion. The greatest challenge to the use of surface wave methods is the near-field effect caused by the presence of distributed cracking on the concrete surface; reflections from these cracks have a disproportionate influence on the received signals if the impacts or sensors are located too close to them. Given the nature of surface cracking caused by ASR and DEF, it becomes impossible to consistently locate the sensors and impacts any appreciable distance from the cracks and use the same locations for repeated measurements in a long-term monitoring program. Since the Jobe (F1) exposure blocks experienced expansion at a similar rate as the full-scale beams, the data for these specimens are presented here, with the caveat that the small size of the specimens meant that only one set of sensor and impact positions could be used.

The SASW method involves calculating the phase velocities of various frequency components of surface waves traveling along the concrete surface. The signals from all ten impacts are average and plotted as a dispersion curve (phase velocity vs. frequency). For purposes of this research, the phase velocity at 16 kHz was extracted, representing the approximate central frequency of the received signals. Similar to UPV and impact-echo, the goal is to correlate a loss of velocity to damage caused by ASR and DEF. Initial velocities ranged from 1730 to 2210 m/s; this is similar to what would be expected based on the p-wave velocities of these specimens. The change in phase velocity at 16 kHz is then plotted against expansion, as shown in Figure 3.36.

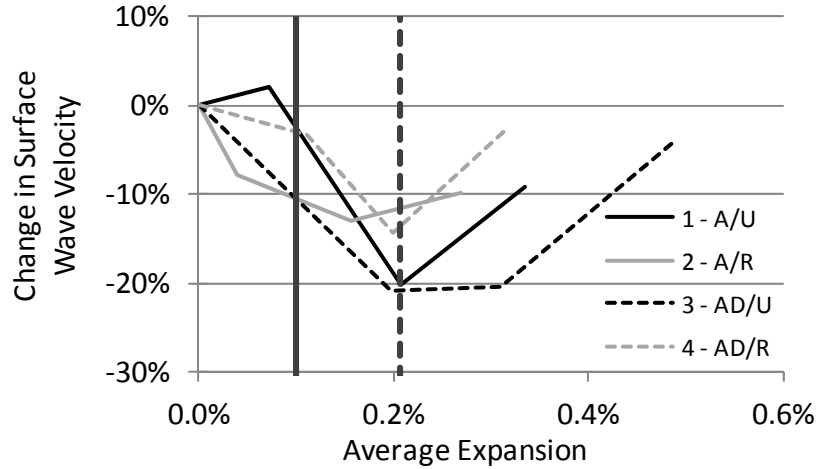


Figure 3.36: Change in 16 kHz phase velocity vs. expansion for Jobe (F1) exposure blocks.

This figure shows the difficulty in applying this technique to the assessment of damage caused by ASR and DEF. There is initially a loss in velocity of 12 to 20%, which reached a maximum in the range of 0.15 to 0.20% expansion; this was approximately twice the decrease in ultrasonic pulse velocity measured over the same range of expansions for these specimens. However, this was followed by an increase in velocity that, in the case of two of the specimens, represents a near-complete recovery of any velocity loss. If monitoring had commenced at 0.1% expansion, as might be the case in a field investigation, the observed trends would be a smaller velocity decrease, followed by an overall increase in velocity. The reasons for this are not entirely clear, but the development of distributed open surface cracks characteristic of ASR may have affected the results. Although this represents a relatively small amount of data (for the full-scale beams, 100 impacts were used for each test grid), the pattern of velocity change is quite consistent for the four specimens, and it is clear that this method is not useful for characterizing the progress of ASR and DEF.

The second method of analyzing the surface wave data, SWT, involves comparing the energy transmission of various frequency components between the two sensors. The transmission coefficient is simply the ratio of the energy received by the two sensors. As with SASW, the signals are averaged for ten impacts, and the energy transmission at 16 kHz is extracted. The transmission coefficients were then normalized to the theoretical transmission coefficient of an undamaged material. Ideally, surface wave energy decays according to the square root of distance from the impact, so the ideal transmission coefficient, calculated as:

$$Tr = \sqrt{\frac{D_1}{D_2}} \quad (\text{Equation 3.4})$$

D_1 and D_2 are the distances from the impact to the first and second sensors, respectively. If the normalized transmission coefficient is less than 1, the additional energy loss is attributed to normal attenuation in undamaged concrete, or some sort of damage to the specimen (ASR and/or DEF, in this case).

Figure 3.37 shows the normalized transmission coefficients plotted against velocity for the Jobe (F1) exposure blocks. The initial values are very close to 1, indicating that the specimens behave very similar to an ideal solid before any expansion has taken place. An examination of later measurements should focus on changes from the initial measurement.

However, no clear trends can be distinguished for later measurements. Normalized transmission coefficients range from 0.46 to 1.38, and fluctuate considerably for blocks 1 and 4. The near-field effect is a likely contributor to the observed fluctuations in the data, as the increased reflection and scattering of the surface waves off the cracks can both amplify or reduce the received energy at the sensors. As with the SASW results, it should be noted that this represents a relatively small amount of data, but for the characterization of damage in these specimens, the SWT technique is of little or no use.

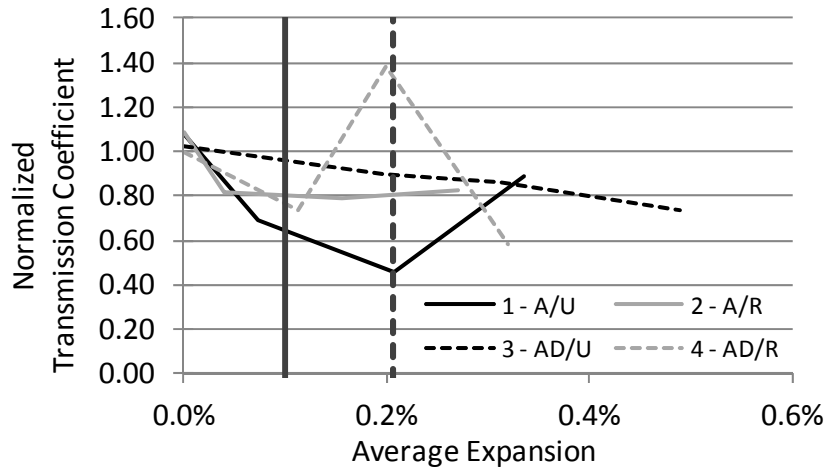


Figure 3.37: Normalized transmission coefficients vs. expansion for Jobe (F1) exposure blocks.

3.4 Results and Discussion: Tests on Cores

This section discusses the results of the comprehensive core sample testing program. Tables 3.7 and 3.8 list all the cores extracted from the Wright (F7) and El Indio (C2) exposure blocks, respectively. These tables also show the age and expansion of the blocks at the time of coring, and the specific tests performed on each core. In addition to the exposure block cores, four cores were extracted from the each of the two El Indio (C2) unreinforced slabs near the end of the project for NDT and mechanical testing only.

Table 3.7: List of cores extracted from Wright (F7) exposure blocks.

Block	Expansion & Age	Core	NDT & Mechanical Testing	Chemical Testing		Residual Expansion	Petrography	Short or extra		
				WSA	PSEA					
6	0.082% 373 days	1				Not enough cores of sufficient length		X		
		2						X		
		3	X							
		4							X	
		5						X		
		6							X	
		7					X			
		8	X	X						
		9								X
		10	X	X						
5	0.172% 524 days	1	X	X						
		2			X					
		3							X	
		4					X			
		5	X							
		6					X			
		7	X	X						
		8						X		
8	0.354% 663 days	1	X							
		2				X				
		3					X			
		4	X	X						
		5	X	X						
		6					X			
		7							X	
		8				X				
7	0.451% 797 days	1			X					
		2	X	X						
		3					X			
		4	X	X						
		5	X							

Table 3.8: List of cores extracted from El Indio (C2) exposure blocks.

Block	Expansion & Age	Core	NDT & Mechanical Testing	Chemical Testing		Residual Expansion	Petrography	Short or extra
				WSA	PSEA			
12	0.075% 229 days	1					X	
		2					X	
		3	X					
		4				X		
		5			X			
		6						X
		7	X	X				
		8						X
		9					X	
		10	X	X				
9	0.119% 343 days	1				X		
		2			X			
		3						X
		4						X
		5	X	X				
		6					X	
		7	X					
		8					X	
		9	X	X				
11	0.177% 419 days	1				X		
		2	X	X				
		3			X			
		4	X					
		5						X
		6	X	X				
		7					X	
		8						X
10	0.295% 790 days	1					X	
		2	X	X				
		3	X	X				
		4			X			
		5	X					

3.4.1 NDT

Relevant data from UPV and resonant frequency testing for the cores are discussed in this section. As with the in-situ tests, attempts were made to correlate the results of these tests to the expansion of the exposure block or on-grade slab from which they were obtained.

UPV

The UPV data for the core samples are presented in Figure 3.38; velocity is plotted against expansion of the source exposure block or on-grade slab at the time of coring. Results for every core tested are included in this plot, to illustrate the velocity distribution of samples taken from each exposure site specimen. Velocity variations of 100 to 200 m/s were typical within each set of cores (about 2-4% of the mean). This figure shows that only small changes in velocity were detected with increasing expansion, although no cores were taken at zero expansion. The Wright (F7) cores showed the greatest decrease in velocity, yet this was just 4.6% for a ten-fold

increase in expansion. This is less than half of the velocity change measured using in-situ monitoring. Figure 3.38 also shows that the cores from the El Indio (C2) slabs show the greatest variation, but the velocities are similar to those measured for cores from the blocks.

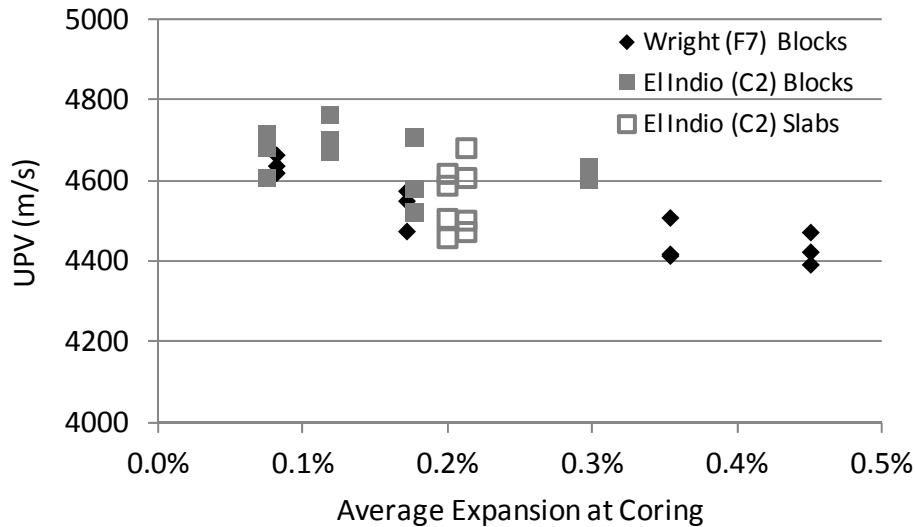


Figure 3.38: UPV vs. expansion for core samples. (1 m/s = 3.28 ft/s).

It is worth noting that the core samples had higher velocities than their source specimens—a difference on the order of 200-400 m/s. However, the core samples were saw-cut and saturated with moisture prior to testing, while the source specimens had experienced drying and macro-cracking in their outer layers, and often had rougher surface textures. The combination of these factors leads to higher apparent velocities for the core specimens.

The velocities of the core specimens were also used to calculate the dynamic modulus of elasticity (E_d). However, the values calculated for E_d from the UPV tests were exceptionally high compared to those calculated using the resonant frequency method (below), and on the order of two to two-and-a-half times those measured in the static elastic modulus test (covered in 3.4.2). Therefore, the use of UPV testing to determine dynamic modulus is not recommended.

3.4.2 Resonant Frequency

The results of the resonant frequency tests of core samples are presented in Figure 3.39. The dynamic elastic modulus was calculated for both the longitudinal (L) and transverse (T) fundamental resonant frequencies of each specimen. Figure 3.39 shows the average dynamic elastic modulus for each set of cores plotted against the average expansion of the source specimen. Three cores were tested from each exposure block, and four each from the two El Indio (C2) on-grade slabs.

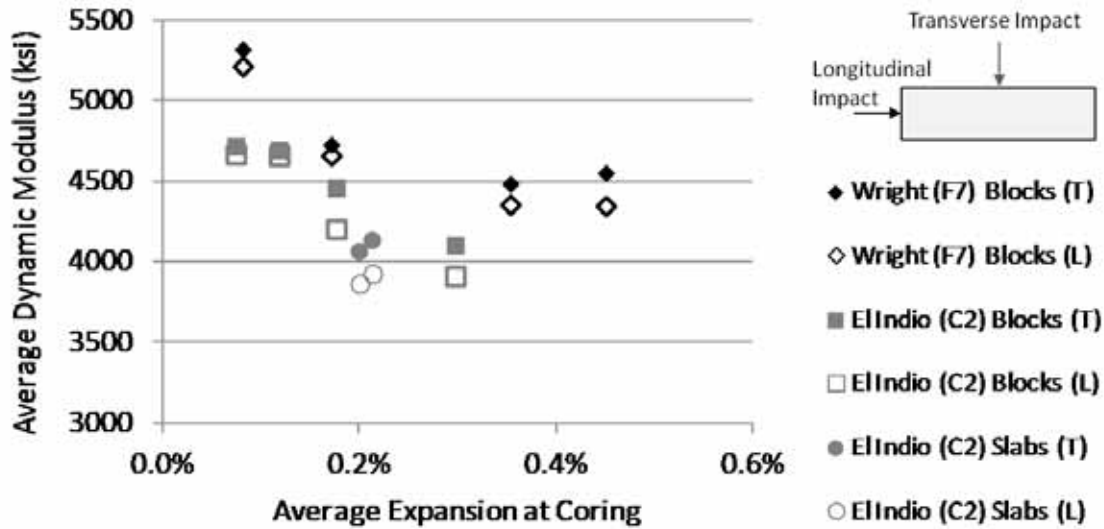


Figure 3.39: Dynamic modulus of elasticity (from resonant frequency tests) vs. expansion for core samples (145 ksi = 1 GPa).

For the Wright (F7) cores, the dynamic moduli decrease 16.7 and 14.4% in the longitudinal and transverse modes, respectively. Similar values were observed for the El Indio (C2) block cores over a smaller range of expansions—16.2 and 13.1% decreases in the longitudinal and transverse modes, respectively. This suggests that the dynamic modulus is more sensitive to ASR damage than the p-wave velocity. However, the cores from the third and fourth Wright (F7) blocks have nearly identical moduli, despite an increase of 0.1% expansion. This is quite similar to the trend observed from the UPV tests on these cores.

The dynamic moduli of the cores from the El Indio (C2) on-grade slabs are approximately 5% lower than would be expected based on the data from the exposure block cores. The concrete in the two specimen types is for all practical purposes, identical, so it is difficult to explain the differences in the dynamic moduli. Even if a calibration curve (E_d vs. expansion) can be established for a given concrete mixture, it may not be possible to accurately assess ASR expansion based on the dynamic moduli of cores from a field structure.

3.4.3 Mechanical Testing

The results of the mechanical testing of cores are discussed in this section. This includes the stiffness damage, static elastic modulus, and compressive strength tests. The tests are evaluated for their usefulness in quantifying the effects of ASR on concrete. Testing involved the same set of cores used for the non-destructive tests.

3.4.4 Stiffness Damage Test

The stiffness damage test results in load-deformation data, from which numerous parameters can be selected for analysis. The parameters recommended by Chrisp et al. (1993) were developed using a test conducted at a lower maximum load, and were not supported by any published correlation to expansion due to ASR. Based on the work of Smaoui et al. (2004a), two parameters were chosen—the area of the first hysteresis loop (1st Cycle Area) and the total accumulated plastic strain over all five load cycles (Total Plastic Strain), which were shown to

have a nearly linear correlation to expansion. The load deformation data are converted to a stress-strain plot, from which the two parameters can be extracted, as shown in Figure 3.40.

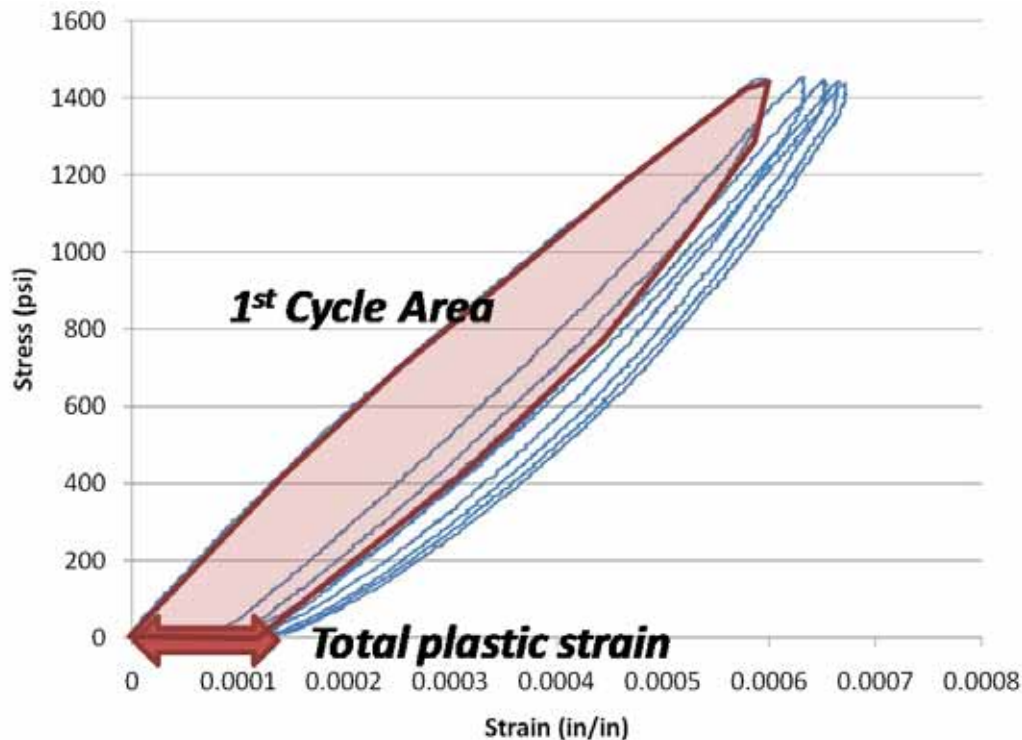


Figure 3.40: Sample SDT data and analysis parameters.

Figures 3.41 and 3.42 present the average 1st Cycle Area and Total Plastic Strain for each set of cores, respectively, with these parameters plotted against the source specimen *average* expansion at the time of coring. These figures also show the linear best-fit of the data; with the exception of the El Indio (C2) blocks, the concept of a linear relationship to expansion is tenuous at best. The Wright (F7) cores at 0.172% expansion are significant outliers in both figures, contributing to the very low R^2 values. An R^2 of 0.83 was calculated for the El Indio (C2) block cores, and this prompted extraction and testing of cores from the on-grade slabs containing the same mixture. Both parameters calculated from the slab cores fall well above the best fit lines established by the block cores. This casts some doubt about the use of this test to quantify ASR expansion with any precision. Attempts to correlate the two parameters to the vertical expansion of the source specimens (parallel to the applied load in the test), did not result in a better fit to a linear relationship.

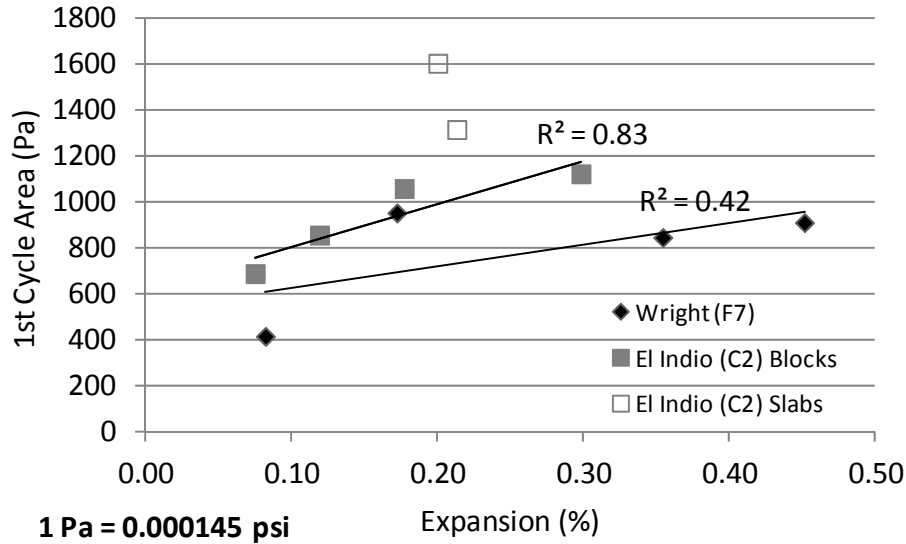


Figure 3.41: Averaged 1st Cycle Area vs. expansion for core samples.

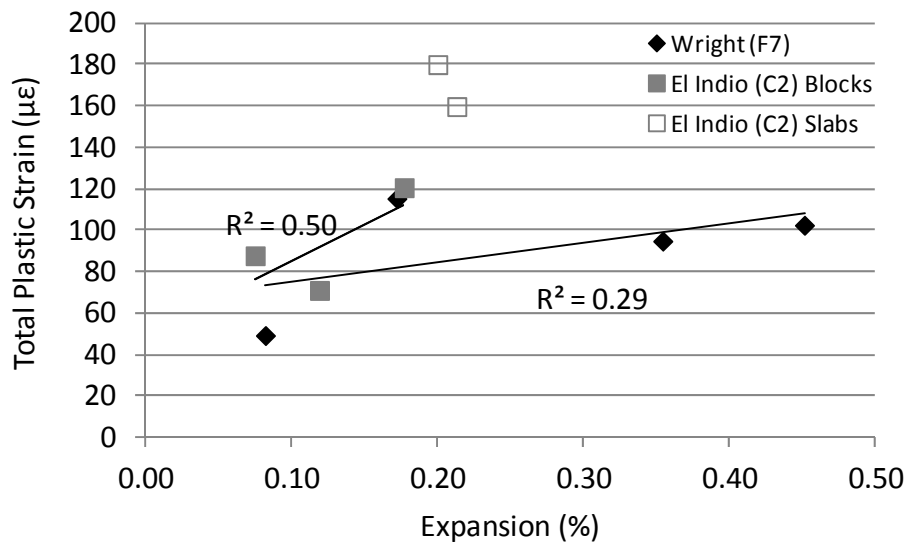


Figure 3.42: Averaged total plastic strain for core samples.

Table 3.9 provides a summary of the SDT results for each individual core for the exposure blocks, as well as information on the statistical variation in the data, and the percentage of compressive strength at 28 days and at the time of testing to which the specimens were loaded. Because of the small sample size (three, or in a few cases, two specimens per set), calculation of standard deviations or coefficients of variation was not possible, however, the range of values of each parameter was divided by the average in each set of cores (shown as “Var %”). This variation would be approximately twice the coefficient of variation, if one could be calculated. The 1st cycle area had, on average, less variation in each set of cores compared to the plastic strain parameter (27.7% vs. 45.1%). However, both exhibit a very high variation, demonstrating the need for multiple cores to obtain even somewhat reliable data. This could be largely

attributable to the fact that ASR damage varies throughout a structure, or even within an exposure block.

Table 3.9: SDT results for exposure block cores.

		Wright (F7) Blocks				El Indio (C2) Blocks			
		Expansion Level (%)				Expansion Level (%)			
		0.082	0.172	0.354	0.451	0.075	0.119	0.177	0.298
1st Cycle Area (Pa)*	Core 1	371	1133	921	964	n/a	984	1322	1074
	Core 2	412	766	855	957	615	989	810	1171
	Core 3	466	959	761	810	763	595	1044	n/a
	Average	416	953	846	910	689	856	1059	1123
	Var %	22.8	38.5	18.9	16.9	21.5	46.0	48.4	8.6
Plastic Strain ($\mu\epsilon$)	Core 1	48	131	108	110	n/a	121	144	109
	Core 2	45	88	98	108	84	27	87	n/a
	Core 3	54	127	79	90	92	65	131	n/a
	Average	49	115	95	102	88	71	121	109
	Var %	19.7	36.7	30.6	20.1	9.7	133.0	47.2	n/a
f' _c (28 day), MPa*		46.4	45.0	45.6	45.5	36.1	33.3	35.6	36.1
Load, % of 28-day f' _c		21.5	22.2	21.9	22.0	27.7	30.0	28.1	27.7
Load, % of f' _c at test		20.6	21.2	25.8	26.6	27.0	30.2	33.6	37.9

* 1 Pa = 0.000145 psi; 1 MPa = 145 psi

It should also be noted that because of the degradation of strength with increasing ASR damage, the specimens were not loaded to a consistent percentage of their current strength. Differences in the strengths of two mixtures also meant that the Wright (F7) specimens were loaded, on average to 22% of their 28-day strength, vs. 28% for the El Indio (C2) cores. As mentioned in Chapter 2, recent work by Sanchez et al. (2012) suggests that the ratio of maximum load to compressive strength has a significant influence on the results; the test must be conducted at 30% or more of the compressive strength in order to effectively quantify ASR damage. This is problematic for field structures, because even if the design strength is known, the strength of the damaged concrete can be difficult to estimate.

Aging of the ASR gel in the specimens in this study is likely to have contributed to some of the difficulty in establishing useful relationships of the stiffness damage parameters to specific levels of expansion. Swamy (1997) suggested that as ASR gel aged and become less fluid, it would contribute to a recovery of the mechanical properties of the affected concrete. Since the exposure site specimens were, in some case, as much as two years old at the time of coring, it is possible that some aging of the gel could have occurred and mitigated the impact of ASR on the stiffness of the concrete.

3.4.5 Elastic Modulus and Compressive Strength

Figures 3.43 and 3.44 present the average elastic modulus and compressive strength results for each set of cores, respectively. These values are plotted against the *average* expansion of the source specimens. The cores from both sets of exposure blocks follow a similar trend with respect to the elastic modulus. Although the undamaged elastic moduli were not measured, losses of 25% and 23% were observed for the Wright (F7) and El Indio (C2) cores, respectively. No decrease in modulus was observed for expansions above 0.30%. The magnitude of compressive strength loss was similar—23% for Wright (F7) and 29% for El Indio (C2). The elastic moduli of the cores from the El Indio (C2) slabs were approximately 600 ksi (4 GPa)

lower than expected based on the exposure block cores; this is consistent with higher-than-expected SDT parameters measured for these cores. The compressive strengths of the slab cores, however, were an excellent fit to the data from the block cores.

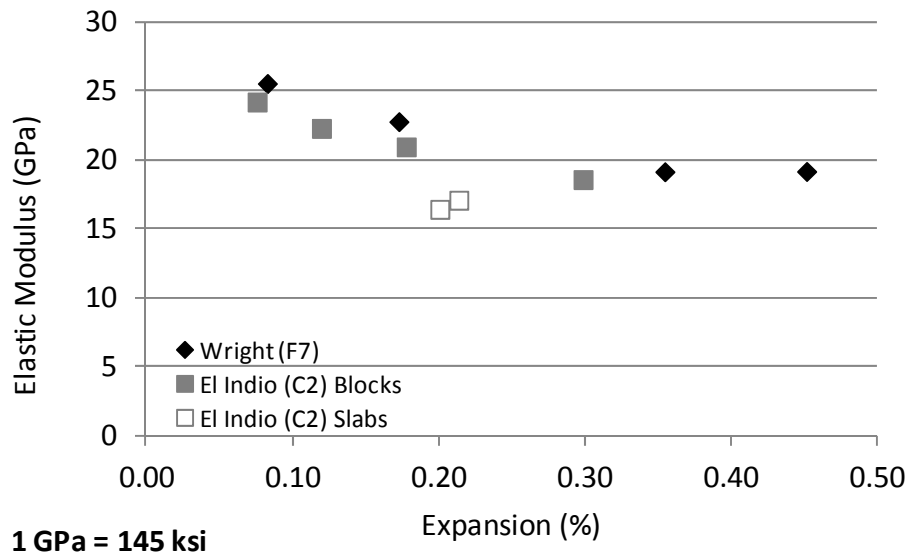


Figure 3.43: Averaged elastic moduli vs. expansion of core samples.

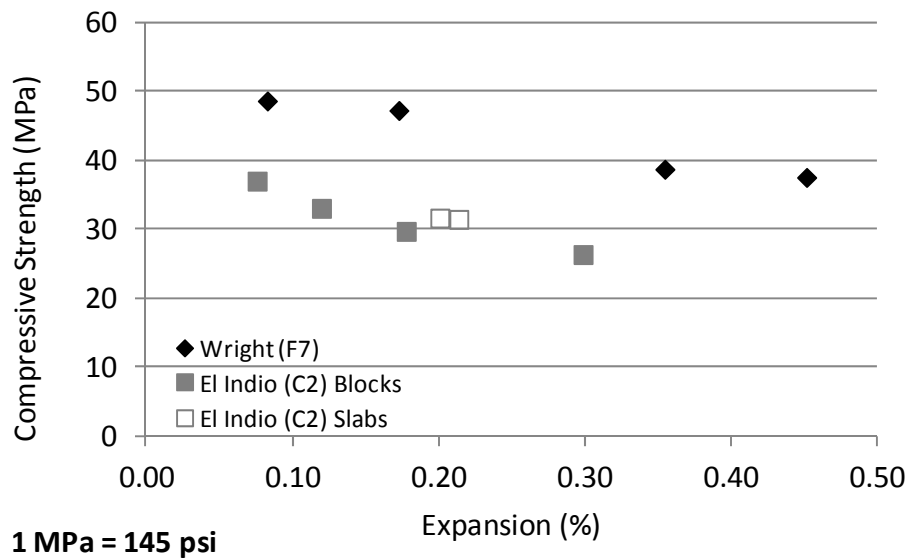


Figure 3.44: Averaged compressive strength vs. expansion of core samples.

Table 3.10 provides a summary of the elastic modulus and compressive strength results for each individual core for the exposure blocks, as well as information on the statistical variation in the data. The “Var %” values were calculated in the same manner as in Table 3.9, and show that these tests had significantly less variation within each set of cores compared to the stiffness damage test. The elastic modulus results had an average variation of 15.2%, while the compressive strength results had an average variation of 9.9%, within each set of cores.

Table 3.10 also compares the measured elastic moduli to that which is commonly assumed based on the compressive strength, using the equation:

$$E = 4700\sqrt{f'_c} \text{ (SI units)}; = 57,000\sqrt{f'_c} \text{ (English units)} \quad \text{Equation 3.5}$$

The measured moduli are as much as 35% below the value predicted by this equation; thus, the elastic modulus should be measured directly from core samples of ASR-damaged concrete, rather than inferred from compressive strength tests.

Table 3.10: Elastic modulus and compressive strength results for exposure block cores.

		Wright (F7) Blocks				El Indio (C2) Blocks			
		Expansion Level (%)				Expansion Level (%)			
		0.082	0.172	0.354	0.451	0.075	0.119	0.177	0.298
E (GPa)*	Core 1	25.3	22.4	18.1	18.0	29.0	20.9	19.2	19.3
	Core 2	25.1	24.4	18.7	19.3	23.8	22.6	24.0	18.3
	Core 3	26.3	21.5	20.8	20.3	19.8	23.4	19.7	18.2
	Average	25.6	22.8	19.2	19.2	24.2	22.3	21.0	18.6
	Var %	5.0	12.9	14.2	12.0	38.1	11.0	22.8	5.6
f' _c (MPa)*	Core 1	48.1	45.9	37.9	35.8	38.6	29.7	31.6	26.2
	Core 2	49.3	48.4	38.8	38.1	37.5	33.6	31.8	27.9
	Core 3	48.4	47.4	39.4	38.7	34.9	36.0	25.8	25.1
	Average	48.6	47.3	38.7	37.6	37.0	33.1	29.7	26.4
	Var %	2.4	5.3	3.8	7.7	10.0	18.9	20.1	10.8
E, % of predicted by f' _c		77.4	70.0	65.0	66.1	83.8	81.9	81.3	76.5

* 1 GPa = 145 ksi; 1 MPa = 145 psi

The elastic modulus and compressive strength data suggest that these tests provide more consistent results, and therefore would be more useful in characterizing ASR damage in a field structure than the stiffness damage test (as conducted in this research). However, the challenge remains to apply the data from these tests to prediction of structural performance.

3.4.6 Chemical Testing

Water-Soluble Alkalis

Tables 3.11 and 3.12 present the water-soluble alkali results for the Wright (F7) and El Indio (C2) blocks, respectively. The data in these tables are the average of the three sub-samples tested for each core. Figure 3.45 also shows the water-soluble alkali contents plotted against expansion for all the exposure blocks. A dashed line represents the 8.85 lb/yd³ (5.25 kg/m³) alkali contribution from the cement and NaOH added to the mixture. It should be noted that the results are not adjusted for the expected alkali contribution by the aggregates.

The water-soluble alkalis do not decrease with expansion, as is generally the case in the literature. The trend for both sets of blocks is an increase in water-soluble alkalis, and in the case of the El Indio (C2) blocks, to eventually stabilize around 7.4 to 7.5 lb/yd³ (4.4 to 4.5 kg/m³). The average alkali content of the final Wright (F7) block was actually in excess of that supplied by the cement and NaOH. Since some fraction of the alkalis are assumed to be bound in either cement hydration products or ASR reaction products, the total alkali load estimated with this test is much higher than expected. One possible explanation is that the aggregates are contributing alkalis to the system, either during the life of the concrete prior to coring, or during the test itself.

As mentioned in Chapter 2, some aggregates (actually, certain minerals in the aggregates) are capable of leaching significant alkalis during an extraction process, such as this test. These aggregates can also contribute alkalis to the pore solution during the life of the concrete. The results of a water-soluble alkali test are influenced by both of these processes.

Table 3.11: Water-soluble alkali results, Wright (F7) cores.

Block	Expansion (%)	Age (Days)	Core	Na ₂ O (%)	K ₂ O (%)	Na ₂ O _e		
						(%)	lb/yd ³	kg/m ³
6	0.082%	373	8	0.110	0.125	0.193	7.54	4.48
			10	0.113	0.130	0.198	7.77	4.61
			<i>Average</i>	<i>0.111</i>	<i>0.128</i>	<i>0.196</i>	<i>7.66</i>	<i>4.54</i>
5	0.172%	524	1	0.112	0.134	0.201	7.85	4.66
			7	0.121	0.146	0.217	8.50	5.04
			<i>Average</i>	<i>0.117</i>	<i>0.140</i>	<i>0.209</i>	<i>8.18</i>	<i>4.85</i>
8	0.354%	663	4	0.107	0.122	0.187	7.32	4.34
			5	0.111	0.124	0.192	7.53	4.47
			<i>Average</i>	<i>0.109</i>	<i>0.123</i>	<i>0.190</i>	<i>7.43</i>	<i>4.40</i>
7	0.451%	797	2	0.141	0.157	0.244	9.55	5.67
			4	0.136	0.154	0.237	9.29	5.51
			<i>Average</i>	<i>0.138</i>	<i>0.155</i>	<i>0.241</i>	<i>9.42</i>	<i>5.59</i>

Table 3.12: Water-soluble alkali results, El Indio (C2) cores.

Block	Expansion (%)	Age (Days)	Core	Na ₂ O (%)	K ₂ O (%)	Na ₂ O _e		
						(%)	lb/yd ³	kg/m ³
12	0.075%	229	7	0.103	0.112	0.177	6.92	4.11
			10	0.087	0.096	0.150	5.89	3.49
			<i>Average</i>	<i>0.095</i>	<i>0.104</i>	<i>0.164</i>	<i>6.41</i>	<i>3.80</i>
9	0.119%	343	5	0.106	0.118	0.184	7.19	4.27
			9	0.108	0.118	0.186	7.27	4.31
			<i>Average</i>	<i>0.107</i>	<i>0.118</i>	<i>0.185</i>	<i>7.23</i>	<i>4.29</i>
11	0.177%	419	2	0.113	0.122	0.193	7.56	4.48
			6	0.111	0.122	0.192	7.50	4.45
			<i>Average</i>	<i>0.112</i>	<i>0.122</i>	<i>0.192</i>	<i>7.53</i>	<i>4.47</i>
10	0.298%	790	2	0.112	0.121	0.192	7.51	4.46
			3	0.107	0.121	0.187	7.31	4.34
			<i>Average</i>	<i>0.110</i>	<i>0.121</i>	<i>0.189</i>	<i>7.41</i>	<i>4.40</i>

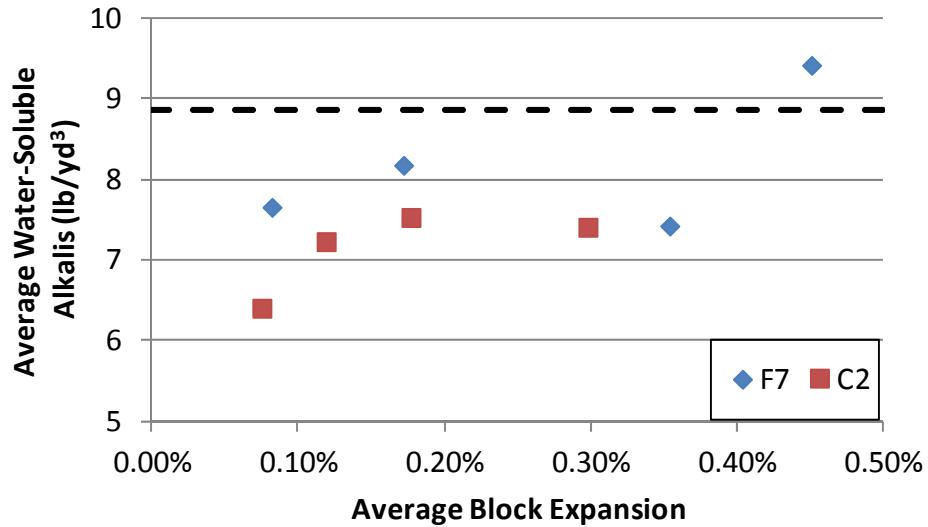


Figure 3.45: Water-soluble alkalis vs. average block expansion.

Table 3.13 shows the water-soluble alkali test results using the cold (room-temperature) water extraction method, compared to the hot-water extraction results from the same core samples. The data are the average of the three sub-samples. It is apparent that in some cases, the hot-water extraction method resulted in a significantly higher quantity of extracted alkalis. This is in contrast with data presented by Bérubé et al. (2002b), which showed almost no influence of the extraction temperature on their results. In this study, there is no good explanation for the extreme variation in the influence of the water temperature.

Table 3.13: Comparison of hot vs. cold water extracted water-soluble alkalis.

Block	Core	% Na ₂ O _e		Difference (%)
		Hot	Cold	
7	2	0.244	0.236	3.4%
9	5	0.184	0.148	19.5%
9	9	0.186	0.142	23.5%
10	2	0.192	0.190	1.0%
12	10	0.150	0.131	12.8%

Since the water-soluble alkali testing was completed near the end of this project, there wasn't sufficient time to cast reference specimens to gauge the expected alkali contributions of the aggregates during the life of the concrete, as suggested by Bérubé et al. (2002a). However, a small study was conducted to determine the potential of the Wright (F7) and Jobe (F1) aggregates to leach alkalis during the extraction process. These aggregates were selected because the Wright (F7) blocks had the highest water-soluble alkali contents and the Jobe (F1) sand was used in the reactive full-scale beams discussed in Chapters 5 through 7. The aggregates were sampled and quartered to produce a 2.2 lb (1.0 kg) sample. Each sample was then prepared generally following the hot-water extraction method, although a total of six sub-samples were

tested. Two sub-samples each were allowed to rest for 6, 24, and 48 h before filtering and chemical analysis.

The results are presented in Table 3.14. In this table, the sodium- and potassium oxide percentages are by mass of the aggregate used in the test, while the mass per volume of concrete has been adjusted for the mass fraction of the aggregates in their respective mixtures (26.7% for Wright (F7) and 30.0% for Jobe (F1)). These results show that the Wright (F7) sand is unlikely to leach significant alkalis during hot-water extraction, while the Jobe (F1) sand can be expected to contribute the equivalent of approximately 0.40 lb/yd³ (0.24 kg/m³) of alkalis during the test. Based on these results, it can also be concluded that in concrete, the Jobe (F1) sand may be capable of contributing significantly more alkalis over a period of years. The relatively high alkali levels measured in the Wright (F7) cores may also be the result of alkali contributions from either the reactive sand, albeit at a slower rate than the Jobe (F1) sand appears capable of, or from the non-reactive coarse aggregate (C6), which was not evaluated due to time constraints.

Table 3.14: Water-soluble alkalis in Wright (F7) and Jobe (F1) sands.

Aggregate	Rest Period	Sample	Na ₂ O (%)	K ₂ O (%)	Na ₂ O _e		
					(%)	lb/yd ³	kg/m ³
Wright (F7)	6 h	A	0.006	0.007	0.010	0.11	0.06
		B	0.006	0.007	0.010	0.11	0.07
		<i>Average</i>	<i>0.006</i>	<i>0.007</i>	<i>0.010</i>	<i>0.11</i>	<i>0.06</i>
	24 h	A	0.006	0.007	0.011	0.11	0.07
		B	0.006	0.007	0.011	0.11	0.07
		<i>Average</i>	<i>0.006</i>	<i>0.007</i>	<i>0.011</i>	<i>0.11</i>	<i>0.07</i>
	48 h	A	0.007	0.007	0.011	0.11	0.07
		B	0.006	0.006	0.011	0.11	0.07
		<i>Average</i>	<i>0.006</i>	<i>0.007</i>	<i>0.011</i>	<i>0.11</i>	<i>0.07</i>
Jobe (F1)	6 h	A	0.023	0.018	0.035	0.41	0.25
		B	0.027	0.023	0.042	0.50	0.30
		<i>Average</i>	<i>0.025</i>	<i>0.021</i>	<i>0.039</i>	<i>0.46</i>	<i>0.27</i>
	24 h	A	0.022	0.016	0.033	0.38	0.23
		B	0.025	0.017	0.036	0.43	0.25
		<i>Average</i>	<i>0.024</i>	<i>0.016</i>	<i>0.035</i>	<i>0.41</i>	<i>0.24</i>
	48 h	A	0.023	0.012	0.031	0.36	0.22
		B	0.024	0.015	0.034	0.39	0.23
		<i>Average</i>	<i>0.023</i>	<i>0.013</i>	<i>0.032</i>	<i>0.38</i>	<i>0.22</i>

3.4.7 Pore Solution Analysis

The results of the pore solution analysis are presented in Table 3.15. This table shows average calculated concentrations of Na⁺, K⁺, and OH⁻ for each sample, in mol/L. Also shown are the expansion of the parent exposure block at the time of coring, summation of the cation concentrations, [Na + K], the calculated pH of the expressed pore solution, and the percentage of pore solution recovered, based on the evaporable water content of the sample material. For each series of exposure blocks, the alkalinity of the pore solution reaches a peak at the second

expansion level, and then declines. However, the cores from the El Indio (C2) specimens exhibit markedly lower concentrations than those from the Wright (F7) specimens (although both have much lower concentrations than would be expected if no ASR had taken place). The final specimen in the El Indio (C2) series has a hydroxyl concentration of only 0.30 mol/L, while the final Wright (F7) specimen contains a hydroxyl concentration of 0.48 mol/L. Both specimens were cored at similar ages (790 and 797 days), but the Wright (F7) block had a much higher average expansion. It is possible that ASR involving the Wright (F7) aggregate consumes fewer alkali hydroxides to cause a given amount of expansion than does ASR involving the El Indio (C2) aggregate.

In comparison to the water-soluble alkali results, the data are somewhat consistent in that the alkali levels are higher in the Wright (F7) cores than the El Indio (C2) cores. However, the eventual decrease in pore solution alkalinity with increasing expansion can be seen in the pore solution data, and was not apparent in the water-soluble alkali data.

The measured alkalis and hydroxyls are not in balance—in every case a higher concentration of alkalis was measured than hydroxyls. This imbalance ranges from 0.021 to 0.176 mol/L, with the latter figure being extremely high. In most cases, however, the imbalance is consistent with those reported in the literature. It is possible that some carbonation had occurred in either the expressed pore solution or in the crushed concrete used in the test, despite the efforts to protect against this. Titration to both phenolphthalein and methyl red or methyl orange end points would have been able to determine total alkalinity, rather than simply that which could be detected based on hydroxyl concentrations. Unfortunately, insufficient pore solution remained to conduct additional tests. Systemic error may also have been present, either with in the flame photometry (standard solution or equipment) or the titrations (HCl concentration).

Table 3.15: Pore solution analysis.

	Wright (F7) Blocks				El Indio (C2) Blocks			
	6	5	8	7	12	9	11	10
Average Block Expansion (%)	0.082	0.172	0.354	0.451	0.075	0.119	0.177	0.298
Expressed Pore Solution (g)	2.38	3.07	2.13	3.14	3.27	3.70	4.01	3.83
Evaporable Water (g)	14.4	14.1	13.4	14.8	17.1	17.2	17.2	17.6
% Pore Solution Extracted	14.2	17.9	13.7	17.5	16.1	17.7	18.9	17.9
[Na] mol/L	0.337	0.386	0.413	0.308	0.236	0.274	0.267	0.251
[K] mol/L	0.250	0.298	0.288	0.196	0.132	0.156	0.147	0.119
Total Alkalis (mol/L)	0.587	0.684	0.701	0.504	0.368	0.430	0.414	0.370
[OH-] (mol/L)	0.545	0.585	0.525	0.483	0.328	0.370	0.335	0.295
pH	13.74	13.77	13.72	13.68	13.52	13.57	13.53	13.47
[Na+K] - [OH] (mol/L)	0.042	0.099	0.176	0.021	0.041	0.060	0.079	0.075

3.4.8 Residual Expansions

The residual axial expansions for each core are summarized in Table 3.16, while Figures 3.46 and 3.47 present the residual expansion and mass gain of the Wright (F7) and El Indio (C2) cores, respectively. Table 3.16 presents the block expansion at the time of coring, the length of expansion monitoring, maximum residual expansion (after 14 days), and the sum of the block

and core expansions. A comparison of the mass gain and expansion data in Figures 3.46 and 3.47 also provides an indication of the presaturation of the cores prior to the start of the test. The cores from Blocks 5 and 12, in particular, experienced rapid mass gain in the first two weeks of the test, indicating that they were not completely saturated by the start of the test. Core 1 from Block 9 also exhibited a lack of complete saturation, albeit to a less extent; however the expansion during this period was very rapid. Consequently, expansion in that time frame should be discounted.

In general, compared to the expansions of the final exposure block in each set, the cores in the residual expansion test under-predicted the potential ultimate expansion of their parent blocks. This is consistent with concerns expressed in the literature about the test; that increased temperatures may result in more rapid expansion, but a lower ultimate expansion. But, since the goal of the test is also to provide an indication that is likely to continue, it could also be considered quite successful. Based on the criteria given in Table 2.1, the tests all indicate a potential for continued expansion. Furthermore, based on the criteria given by Bérubé et al. (2000) and shown in Table 2.2, the expansion potential of all cores would be classified as “very high.”

Table 3.16: Residual expansion summary.

Reactive Aggregate	Block	Block Expansion (%)	Core	Expansion > 14 d		Estimated Max Expansion (%)
				Days	(%)	
Wright (F7)	5	0.172	4	273	0.129	0.301
			6		0.119	0.291
	8	0.354	2	154	0.048	0.402
			6		0.050	0.404
El Indio (C2)	12	0.075	4	455	0.123	0.198
			9		0.140	0.215
	9	0.119	1	455	0.120	0.239
			8		0.110	0.229
	11	0.177	1	280	0.041	0.218
			7		0.051	0.228

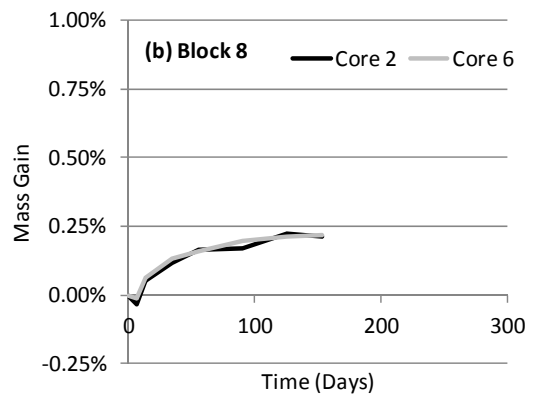
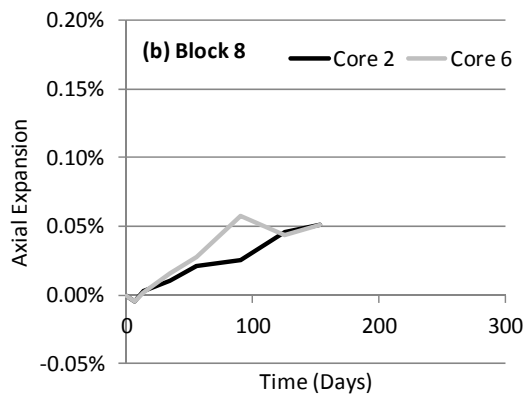
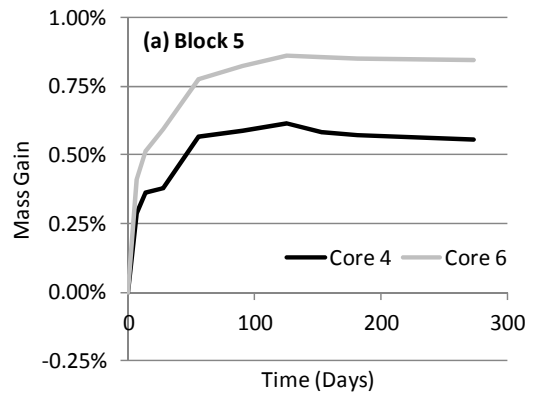
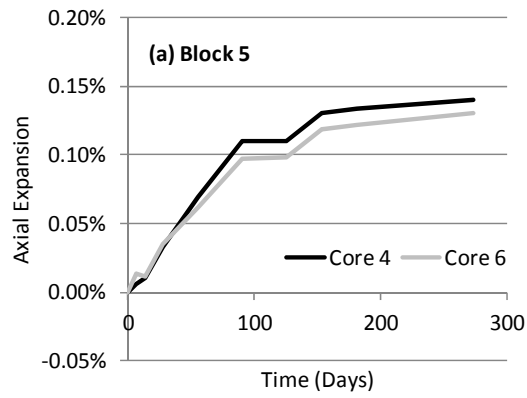


Figure 3.46: Residual expansions and mass gain of Wright (F7) exposure block cores.

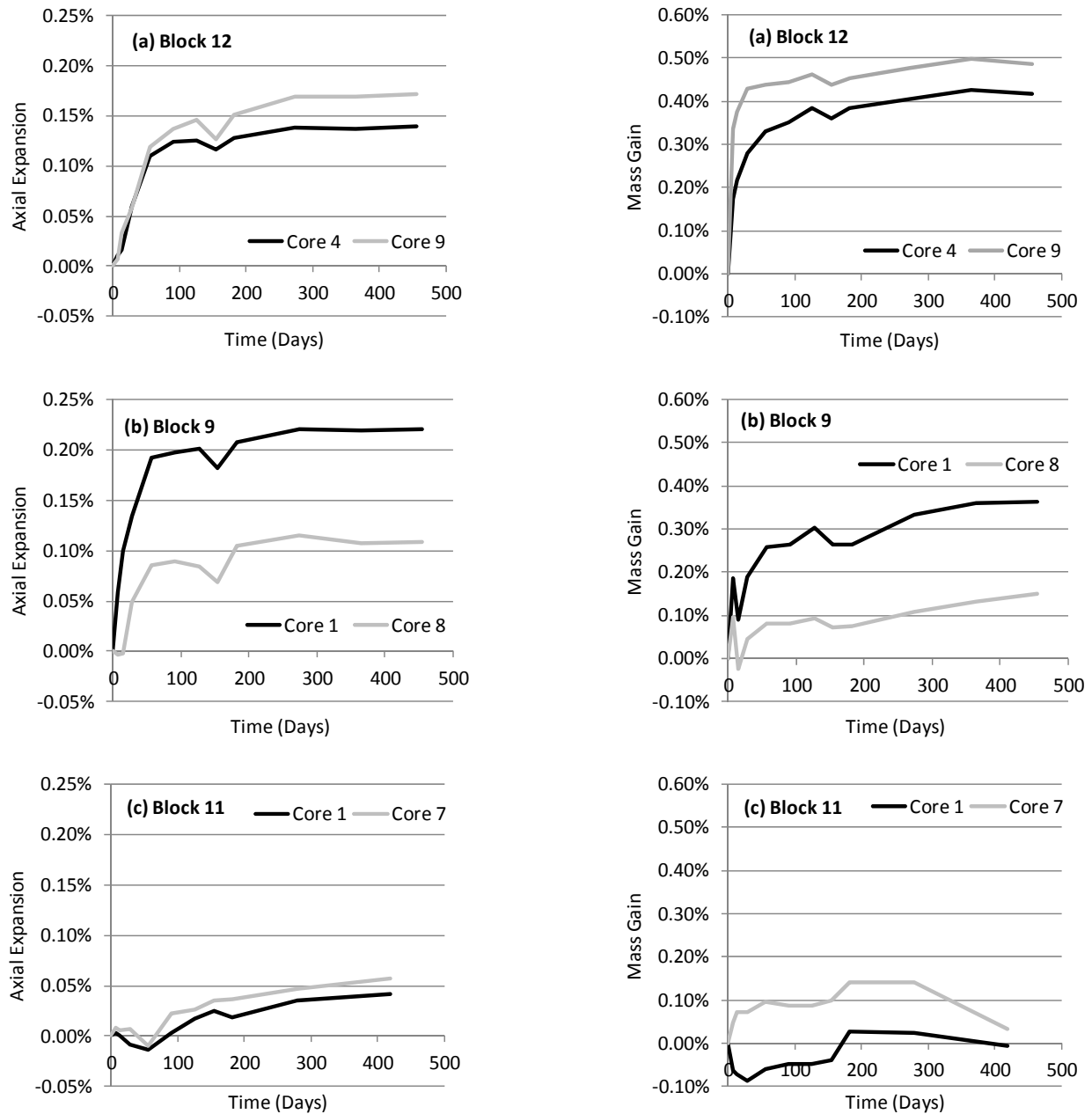


Figure 3.47: Residual expansions and mass gain of El Indio (C2) exposure block cores.

3.4.9 Petrographic Testing

The goal of the petrographic testing in this study was to develop calibration curves of DRI vs. expansion for the Wright (F7) and El Indio (C2) aggregates, which have not been studied in this manner before. At the time of this writing, petrography is still in progress at Université Laval; however completion is expected in time for inclusion in the final report to TxDOT.

3.5 Summary

A comprehensive test program involving outdoor exposure specimens affected by ASR and a combination of ASR and DEF was conducted, which covered in-situ monitoring and extensive testing of core samples from selected specimens.

The results of the in-situ monitoring showed that UPV and impact-echo testing have some usefulness in quantifying early expansions, although the results are somewhat mixed at higher levels of expansion. The impact-echo test was shown to be more sensitive than UPV to ASR damage in the unreinforced on-grade slabs. UPV may also have some potential for identifying concrete that is susceptible to DEF as a result of excessively high curing temperatures.

Resonant frequency testing of core specimens was found to be more effective than UPV in quantifying ASR damage. Stiffness damage testing of cores, as conducted in this research, was largely ineffective, despite promising results reported in earlier studies. However, conducting the test at a particular percentage of the compressive strength may yield more useful results. The ratio of measured to predicted elastic modulus (based on compressive strength) may also be useful in quantifying the severity of ASR damage. Chemical testing of cores confirmed that the contribution of alkalis from aggregates is potentially very significant over the life of the concrete. In some cases, it can skew the results of water-soluble alkali tests. Residual expansion tests were able to predict that expansion would continue in the exposure site specimens, but predicting the rate or ultimate amount of expansion remains a greater challenge.

It may not be possible to determine the exact expansion to-date using any one or a combination of these test methods, but certain tests were clearly found to be more useful than others in providing a reasonable estimate of the severity of damage. With regards to prognosis, the combination of chemical and residual expansion testing can be used to show that there remain sufficient reactive components for continued expansion due to ASR.

Chapter 4. Small-Scale Mechanical Testing

4.1 Overview

Two sets of 4 x 8 in. (100 x 200 mm) cylinders were produced for the purpose of further evaluating the effects of ASR and DEF on the mechanical properties of concrete. This study expands on and complements the mechanical tests conducted on the core samples extracted from the exposure site specimens. Two reactive aggregates, Jobe (F1) sand, and Placitas (C10) gravel were used, bringing the total number of reactive aggregates investigated in the overall project to four. A non-linear resonant frequency test method was also employed for selected test specimens. In this study, the cylinders are intended to represent a laboratory analog for core samples extracted from a field structure.

4.2 Experimental Program

This study comprised 129 reactive and 18 non-reactive specimens that were placed in three types of conditioning regimes to promote the development of ASR, DEF and a combination of both ASR and DEF. The large number of specimens allowed for the testing of sets of three cylinders at increasing expansion levels. Table 4.1 provides an overview of the test program.

Table 4.1: Summary of small-scale mechanical test program.

Reactive Aggregate	Jobe (F1)	Placitas (C10)
Reactive Specimens		
ASR Specimens	21	18
ASR+DEF Specimens	21	18
DEF Specimens	21	18
Tests Performed	SDT, E, f'_c	SDT, E, f'_c , nonlinear RF*
Quality Control Specimens (Reactive Mixture)		
Cured at 73°F (23°C)	3	3
Cured at 194°F (90°C)	3	3
Tests Performed	f'_c at 28 days	
Non-reactive Specimens		
Cured at 73°F (23°C)	9	9
Tests Performed	SDT, E, f'_c at 28 and 364 days	

**Instrumented cylinders only*

4.2.1 Materials and Mixture Proportions

Table 4.2 details the aggregates used in the small-scale mechanical test program. This table includes both the designations used in previous TxDOT research projects (starting with project 0-4085) to provide anonymity to the aggregate provider, as well as the common name used by researchers and geographical origin. This provides some continuity to readers familiar with previous TxDOT research and testing involving these aggregates, although this results in a discontinuous numbering scheme for this project.

Table 4.2: Aggregates used in small-scale test specimens.

Aggregate		Source	Mineralogy and Aggregate Type	Reactivity
ID	Common Name			
F1	Jobe (Newman)	El Paso, TX	Natural sand: quartz, feldspars, siliceous volcanics, chert	Very highly reactive
F6	Evans Road	San Antonio, TX	Manufactured sand: limestone	Non-reactive
C6	Martin Marietta	San Antonio, TX	Crushed limestone	Non-reactive
C10	Placitas	Bernalillo, NM	Mixed gravel: rhyolite and other volcanics	Highly reactive

Jobe (F1) was selected because it was also used in the large scale specimens discussed in Chapters 5 through 7. Placitas (C10) was selected because it was deemed necessary to explore whether different aggregates affect mechanical properties differently at similar levels of expansion. Both aggregates have been used extensively at UT-Austin and elsewhere for ASR research and therefore could be expected to provide sufficient expansion to assess the impacts on mechanical properties even at extreme levels of deterioration.

Common mixture proportions were used for all specimens containing each reactive aggregate under study, generally adhering to the requirements of ASTM C1293 (2008). Type I portland cement with an alkali content of 0.90% Na_2O_e was paired with 50% w/w NaOH solution to ensure that the reactive specimens would undergo significant expansions within the time constraints of the project. Lithium nitrate (LiNO_3) was added to two smaller batches so that non-reactive control specimens could be fabricated using otherwise identical mixtures as the reactive specimens. The full mixture design details can be found in Table 4.3. The mixtures are classified based on the reactive aggregate; the corresponding non-reactive aggregate is also listed in the table.

Table 4.3: Mixture proportions for small-scale test specimens.

Component	Jobe (F1)	Placitas (C10)
Coarse Aggregate (SSD) lb/yd ³ (kg/m ³)	Martin Marietta (C6)	1957 (1161)
	1866 (1107)	
Fine Aggregate (SSD) lb/yd ³ (kg/m ³)	1055 (626)	Evans Road (F6)
		946 (561)
Cement lb/yd ³ (kg/m ³)	Type I, 0.90% Na_2O_e	
	708 (420)	
w/cm	0.42	
Water	297 (176)	
<i>(for reactive specimens)</i>		
NaOH added	3.20 (1.90)	
Total Na_2O_e , lb/yd ³ (kg/m ³)	8.85 (5.25)	
<i>(for non-reactive specimens)</i>		
LiNO_3 , lb/yd ³ (kg/m ³)	13.19 (7.83)	

4.2.2 Specimen Fabrication and Conditioning

In order to minimize experimental variability, all reactive cylinders in each set were made from the same batch of concrete. The plastic molds were sealed after the concrete had set. They were then placed in curing and storage conditions that would promote the development of one of three types of deterioration.

One-third of the specimens (ASR) were moist-cured at 73 °F (23 °C) for 24 h to ensure that only ASR could develop. They were then demolded and moist-cured for an additional 24 h while the reference specimens were instrumented. Finally, they were stored at 100 °F (38 °C) and >95% R.H. to accelerate expansion, as per ASTM C1293 (2008).

Two-thirds of the specimens were cured in an oven at a peak temperature of 194 °F (90 °C) for 12 h, using a programmed temperature profile recommended by Kelham (1996) for promoting development of DEF (Figure 4.1). Figure 4.2 shows the specimens in the oven. The actual specimen temperatures lagged somewhat, particularly with respect to cooling down after 12 hours at 194 °F (90 °C). These specimens were also moist-cured for an additional 24 h at 73 °F (23 °C), and then subdivided for long-term conditioning. Half (ASR+DEF) were stored in the same conditions as the ASR specimens to promote development of both ASR and DEF. The other half (DEF) were stored in saturated limewater at 73 °F (23 °C). The limewater promotes leaching of alkalis from the cylinders and therefore prevents development of ASR; consequently, all expansion in this regime is attributed to DEF.

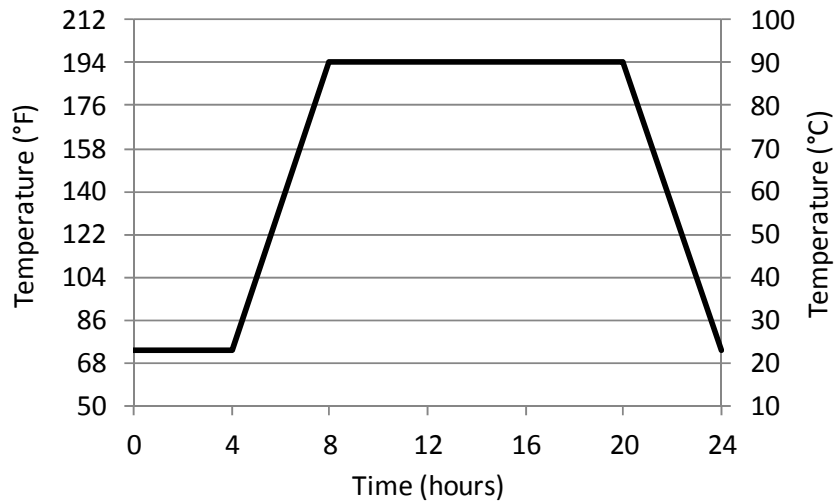


Figure 4.1: Curing temperature profile to promote DEF.



Figure 4.2: Cylinders in ramping oven used for high-temperature curing cycle.

For each of the two curing methods, a set of three cylinders was also set aside in the moist-curing room at 73 °F (23 °C). These were intended to serve as controls to be tested at 28 days of age. At this temperature, ASR would be much slower to develop and no deterioration would be expected at this age.

In each subset (ASR, ASR+DEF and DEF), three cylinders were instrumented for expansion measurements after 24 hours of curing in the conditions described above. A drill press was used to drill out a small opening on each end, and 0.25 in. (6.4 mm) diameter stainless steel gauge studs were inserted and bonded with epoxy, providing a gauge length of 6.81 in. (173 mm). The cylinders were wrapped in plastic to prevent moisture loss while the epoxy hardened.

Nine non-reactive control cylinders were also made from separate batches that contained a lithium nitrate admixture to prevent the development of ASR. They were moist-cured for 24 hours at 73 °F (23 °C) to prevent development of DEF and then placed in storage at 100 °F (38 °C) and >95% R.H. Three were instrumented for expansion measurements, while six were set aside for mechanical testing. These cylinders were intended to provide a representative indication of undamaged mechanical properties at 28 days and one year of age. Without ASR or DEF, some improvement in the mechanical properties can be expected between 28 days and one year of age.

4.2.3 Expansion Monitoring

Expansions of the reference cylinders were measured in accordance with ASTM C490 (2011). Specimens stored at 100 °F (38 °C) and >95% R.H were moved to a 73 °F (23 °C) room at least 12 hours prior to measurements. All specimens were moved along with the reference specimens to ensure they experienced the same temperature and moisture conditions throughout

the monitoring period. Specimens stored in limewater at 73 °F (23 °C) did not require an acclimatization period prior to measurements, but the solution was periodically agitated to ensure saturation.

The change in length of the instrumented reference cylinders was measured in reference to a 6.81 in. (173 mm) Invar bar using a digital comparator with 0.0001 in. (0.0025 mm) precision. Early in the test program, expansions were measured weekly or biweekly in order to capture differences in the expansion rates of the various specimen subsets. This was particularly important for the Jobe (F1) cylinders because of their exceptional rate of expansion. As the rate of reaction slowed, the remaining specimens were monitored at less frequent intervals. The non-reactive control specimens were measured on the same schedule specified by ASTM C1293: at 1, 2, 4, 8, 13, 26, 39, and 52 weeks of age. The average expansions calculated for each set of reference specimens were assumed to be representative of the average expansions of the non-instrumented specimens.

4.2.4 Mechanical Testing

Non-instrumented specimens were selected for mechanical testing at increasing amounts of expansion, as measured for the reference cylinders. For the reactive specimens, an initial set of three specimens was tested at 7 days of age. Then, three specimens were tested at each expansion interval; targeted intervals were as follows:

1. Jobe (F1) – ASR, ASR+DEF and DEF – 0.10% intervals
2. Placitas (C10) – ASR – 0.04% intervals
3. Placitas (C10) – ASR+DEF and DEF – 0.08% intervals

The instrumented reference specimens were also tested, if possible, either after reaching near-ultimate expansion levels, or prior to going out of the range of the comparator. In some cases, removal of the gauge studs damaged the specimen, and testing could not be conducted. The non-reactive specimens were tested at ages of 28 and 364 days.

The mechanical test program was similar to the one used for the exposure block core samples. A brief review of the procedures is provided here, but for a fuller description, the reader should refer to Chapter 3 (Section 3.2.6).

Prior to the mechanical tests, the ends of the specimens were made plane and parallel with a diamond grinder. After grinding and in between each test in the series, the specimens were stored in water to ensure they remained saturated with moisture. In the cast of the instrumented specimens, the gage studs were first carefully removed prior to end-grinding.

The stiffness damage test was first conducted, following the procedure outlined by Smaoui et al. (2004a). This was followed by determination of the elastic (secant) modulus in accordance with ASTM C469 (2010), and the compressive strength in accordance with ASTM C39 (2010). In the elastic modulus tests, the actual applied load ranged from 29 to 46% of the compressive strength (with one outlier at 55%). This series of tests typically involves the application of increasing loads from one test to the next, so each test is not expected to influence the one(s) which follow. However, if the compressive strength is less than 3625 psi (25 MPa), the loads used in the stiffness damage test will exceed those used to determine the elastic modulus.

4.2.5 Resonant Frequency Testing

For the reactive Placitas (C10) specimens, resonant frequency testing was also applied to the instrumented reference specimens. The test was a variation on ASTM C215 (2008), which was used on the exposure block core specimens. Specimens were subjected to approximately seven non-destructive impacts of increasing intensity at each of three locations, approximately one-third of the cylinder circumference apart. Cylinders were tested only in the transverse mode; the test equipment and data acquisition setup are identical to that shown in Figures 3.17 and 3.18.

Both linear and nonlinear analyses of the data were performed using a MATLAB program. The nonlinear analysis employed the resonant frequency shift method, which has previously been applied to small ASR-affected mortar bars, but not to relatively larger concrete specimens. Using FFT, the fundamental resonant frequency of the specimen as a result of each impact was calculated. A downward shift in the resonant frequency was expected with increasing impact force, with a greater shift expected to coincide with increasing damage due to ASR or DEF. This shift was quantified as a non-linear parameter, α , equal to the slope of the fundamental resonant frequency shift ($\Delta f/f_0$), to the change in normalized signal amplitude. The linear analysis involved simply determining the fundamental resonant frequency of the least intense impact, and calculating the dynamic modulus of the specimen in accordance with ASTM C215 (2008).

4.3 Results and Discussion

The results of this study are presented here and the various test methods are evaluated for their usefulness in characterizing each type of deterioration. Particular attention is given to the stiffness damage test, which gave generally poor results with respect to the ASR-damaged exposure block cores, but has shown promise in prior studies. This study also represents the first known application of the SDT to concrete affected by DEF or a combination of ASR and DEF.

4.3.1 Expansions

The expansions with time of the instrumented cylinders are presented in Figures 4.3 and 4.4 for the Jobe (F1) and Placitas (C10) series, respectively. The markers in each series show when a set of cylinders was removed for testing. Unsurprisingly, the ASR+DEF cylinders expanded the fastest. The DEF cylinders initially expanded more slowly than the ASR cylinders, but ultimately expanded more quickly than the ASR cylinders after sufficient alkali leaching had occurred to allow the development of DEF. The non-reactive control cylinders containing lithium showed negligible expansion over a full year of monitoring.

The cylinders were also examined visually for damage. The DEF cylinders began to exhibit open surface cracking at higher levels of expansion. An example of this is shown in Figure 4.5. Closed cracking was more commonly observed on the ASR and ASR+DEF cylinders—this is also typically reported for highly reactive prisms in ASTM C1293 testing.

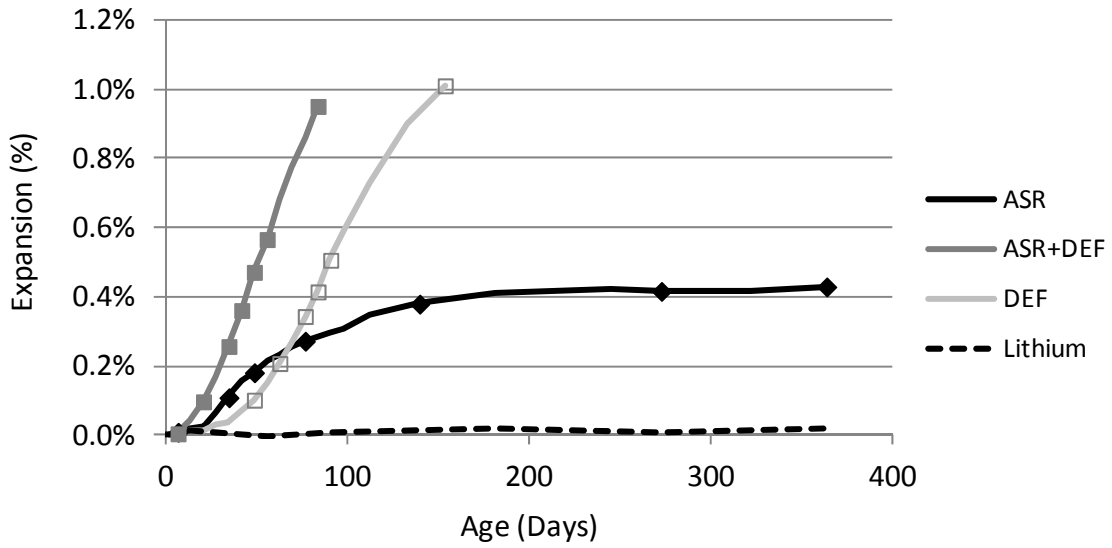


Figure 4.3: Averaged expansions of Jobe (F1) reference cylinders.

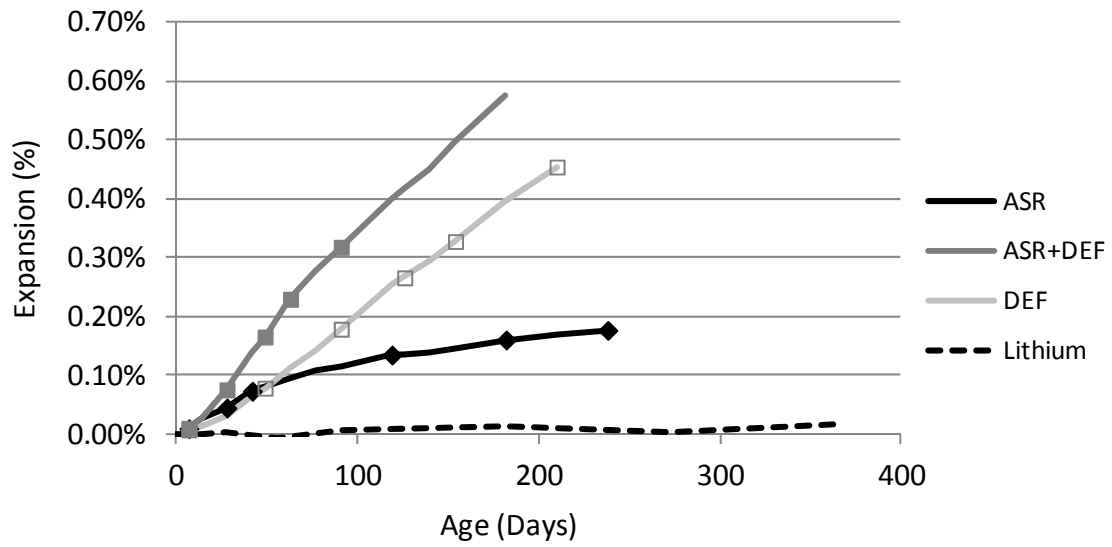


Figure 4.4: Averaged expansions of Placitas (C10) reference cylinders.



Figure 4.5: DEF cylinder with open crack at surface.

4.3.2 Stiffness Damage Test

Typical stress-strain plots are presented in Figure 4.6, taken from six of the Jobe (F1) ASR cylinders. This figure shows the general increase in size of the hysteresis loops and accumulated plastic strain with increasing expansion. The SDT results were analyzed to determine the area of the first hysteresis loop (1st Cycle Area) and the total accumulated plastic strain over all five load cycles (Total Plastic Strain). This follows the same procedure applied to the exposure block core data in Chapter 3. A linear regression analysis was also performed on each parameter.

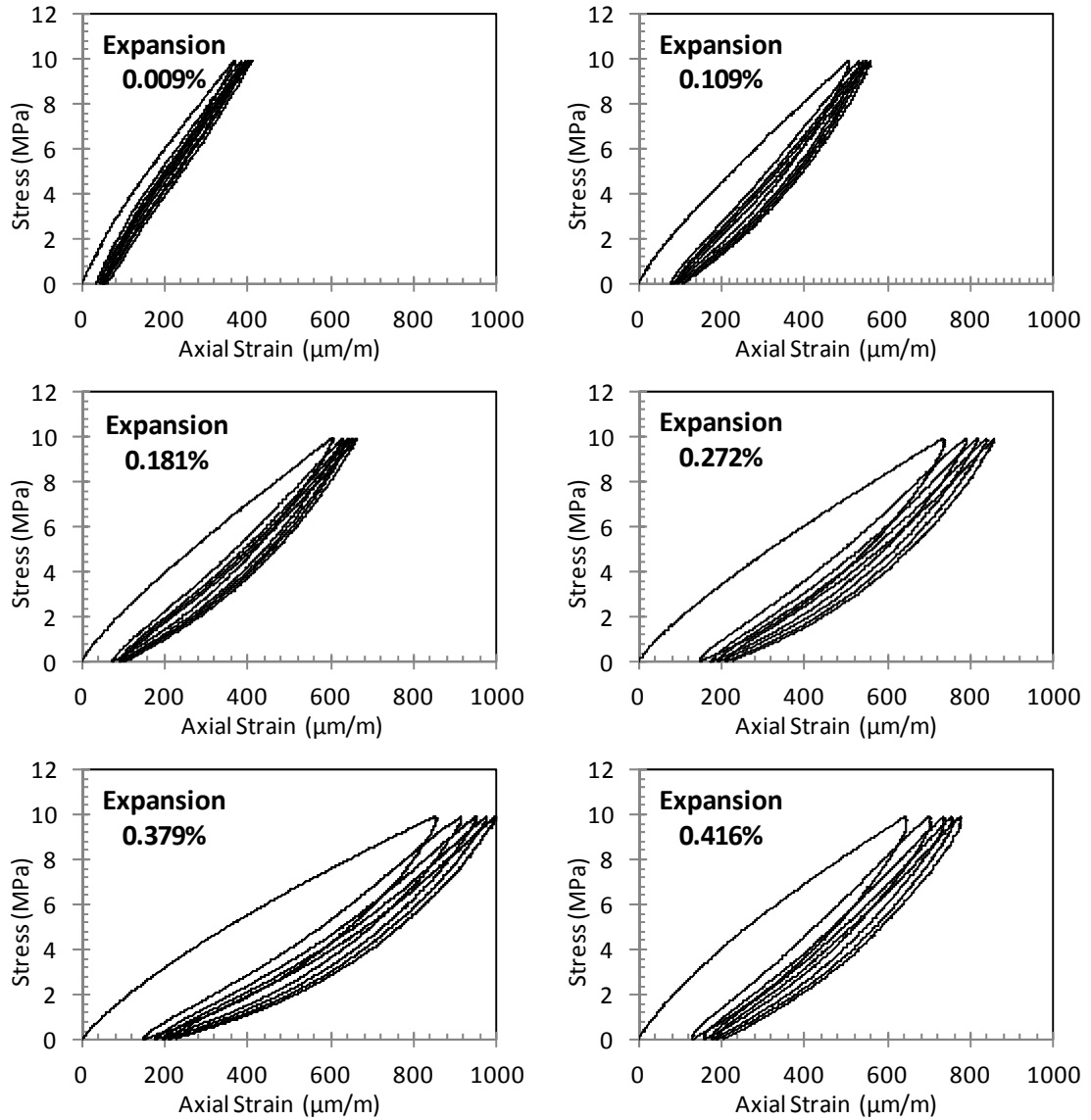


Figure 4.6: Typical SDT stress-strain data for Jobe (F1) ASR cylinders (1 MPa = 145 psi).

Figures 4.7 and 4.8 show the 1st Cycle Area calculated for the Jobe (F1) and Placitas (C10) cylinders, respectively, plotted against the average expansion of the instrumented reference cylinders at the time of testing. Each datum represents the average of three cylinders. These figures also show the linear best-fit line and the R^2 value for each data set. Three common features are evident from these figures:

1. DEF cylinders exhibit a larger 1st Cycle Area for a given expansion.
2. Initial values for 1st Cycle Area are higher for DEF and ASR+DEF cylinders than for the ASR cylinders.
3. The slopes of the ASR and ASR+DEF best-fit lines are nearly identical.

The results for the Jobe (F1) DEF and ASR+DEF cylinders are considerably more encouraging than those for the ASR cylinders, as well as the exposure block cores. The R^2 of 0.97 for the ASR+DEF cylinders indicates a nearly linear relationship between 1st Cycle Area and expansion. The Jobe (F1) ASR cylinders, however, have an R^2 of only 0.58; this is largely a result of the decrease in 1st Cycle Area for the final two sets of cylinders. An examination of Figure 4.3 shows that expansion had slowed considerably by the time these cylinders were tested. The results of the Placitas (C10) show a poorer fit to a linear relationship. The ASR cylinders, in particular, exhibit almost no change in 1st Cycle Area with increasing expansion.

In comparison, Smaoui et al. (2004a) reported (for ASR damage only) an R^2 of 0.92 for cylinders made with Jobe (F1) and 0.99 for cylinders made with Placitas (C10). The difference in the Placitas results is difficult to explain. However, the Jobe (F1) specimens were only tested up to an expansion of 0.38% by Smaoui et al., which suggests that their tests were completed before the expansion rate had slowed. If only the first five sets of Jobe (F1) cylinders are considered from this study (max expansion = 0.38%), the R^2 improves to 0.97.

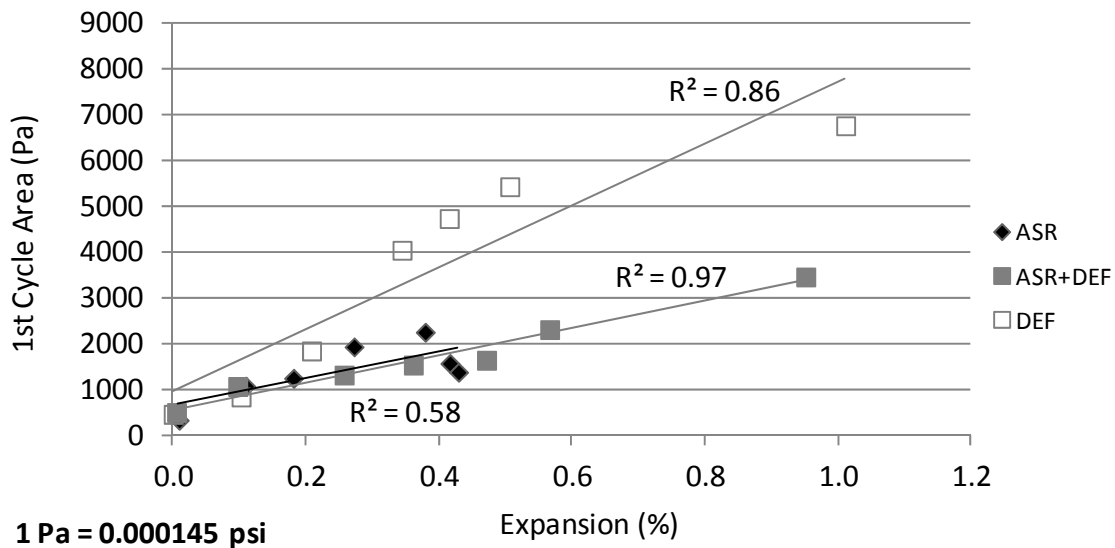


Figure 4.7: Averaged 1st Cycle Area vs. expansion for Jobe (F1) cylinders.

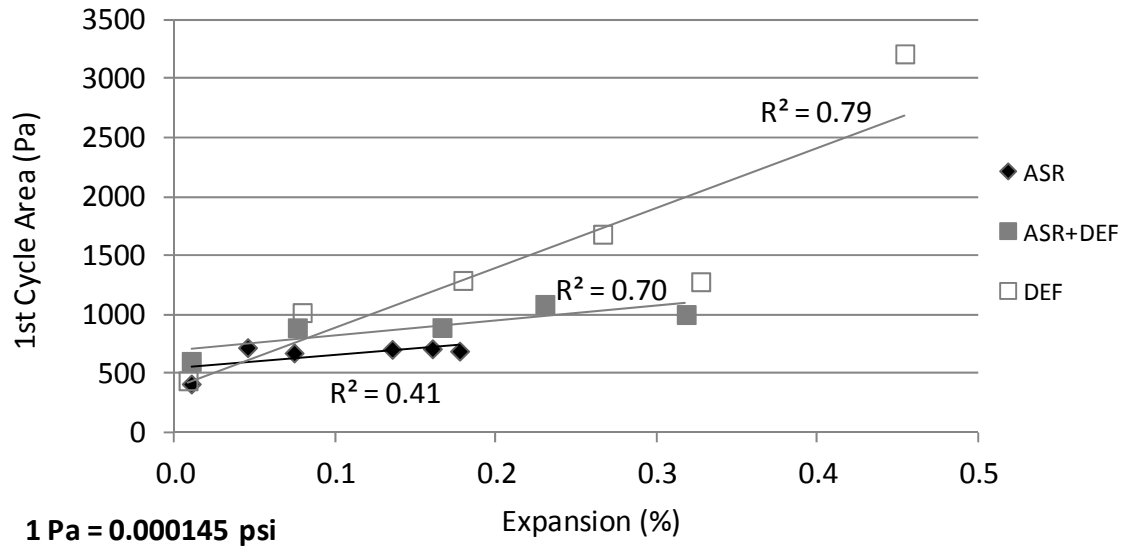


Figure 4.8: Averaged 1st Cycle Area vs. expansion for Placitas (C10) cylinders.

Figures 4.9 and 4.10 provide the Total Plastic Strain calculated for the Jobe (F1) and Placitas (C10) cylinders, respectively, plotted against expansion of the instrumented reference cylinders. The data follow a similar trend as the 1st Cycle Area results, with Jobe (F1) ASR+DEF cylinders exhibiting the best linear relationship to expansion ($R^2 = 0.96$), while the Jobe (F1) ASR cylinders and all Placitas (C10) cylinders cannot be described as correlating linearly to expansion. The DEF cylinders again display a much greater response to a given amount of expansion, while the best-fit lines for the ASR and ASR+DEF cylinders again have similar slopes.

Smaoui et al. (2004a) reported a better correlation for ASR-damaged cylinders with Jobe (F1) sand as the reactive aggregate ($R^2 = 0.94$ vs. 0.50 in this study). Their results involving Placitas (C10) indicated no linear correlation to expansion ($R^2 = 0.27$), consistent with this study. If only the first five sets of Jobe (F1) cylinders are considered from this study (max expansion = 0.38%), the R^2 improves to 0.94, exactly the same as Smaoui et al. reported. It seems quite clear that both SDT parameters examined in this study are influenced not only by the absolute amount of expansion, but also the rate of expansion of laboratory specimens.

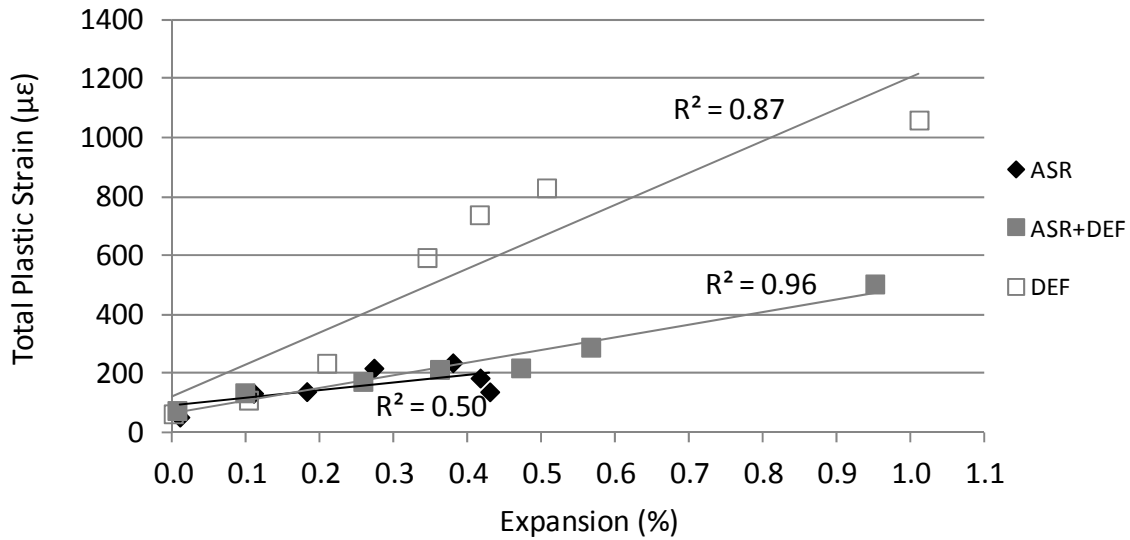


Figure 4.9: Averaged total plastic strain vs. expansion for Jobe (F1) cylinders.

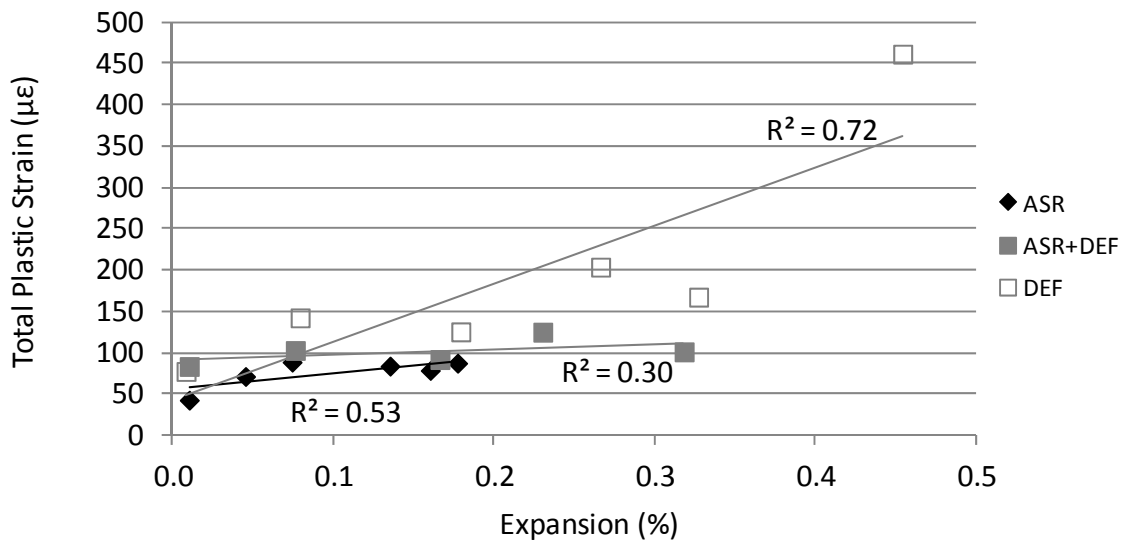


Figure 4.10: Averaged total plastic strain vs. expansion for Placitas (C10) cylinders.

Tables 4.4, 4.5 and 4.6 provide a summary of the SDT results for each cylinder tested from the ASR, ASR+DEF and DEF series, respectively. These tables also provide information on the statistical variation in the data, and the percentage of compressive strength at 28 days and at the time of testing to which the specimens were loaded. Because of the small sample size (three specimens per set), calculation of standard deviations or coefficients of variation was not possible, however, the range of values of each parameter was divided by the average in each set of cores (shown as “Var %”). This variation would be approximately twice the coefficient of variation, if one could be calculated.

The 1st Cycle Area showed significant variation; the average variation ranged from 22.1% (ASR) to 56.4% (DEF). Even greater variation was found in the Total Plastic Strain data,

with the average variation ranging from 32.9% (ASR+DEF) to 64.7% (DEF). Even though the SDT parameters are more sensitive to damage caused by DEF alone, the data are clearly much less consistent when comparing cylinders with similar degrees of damage. The overall variability in the SDT data is similar to that reported in Chapter 3 for the exposure block cores. This shows that the test is feasible only if multiple specimens are used.

Differences in initial strengths and changes in strength with increasing expansion also meant that the specimens were not tested to the same percentage of compressive strengths. The maximum load applied in the test varied from 23.8 to 62.7% of the compressive strength. All of the Placitas (C10) specimens were tested at 39.7% or less of the compressive strength, while half of the Jobe (F1) ASR+DEF and DEF specimens were tested above 40% of their compressive strength. The latter is cause for concern due to the potential to affect the results of the static elastic modulus tests that followed. The poor correlation between the SDT parameters and expansion for the Placitas (C10) ASR cylinders can be explained in part by the fact that the test was conducted at just 23.8 to 27.9% of the compressive strength, well below the 40% level recently recommended by Sanchez et al. (2012a).

Table 4.4: SDT results for ASR cylinders.

		Jobe (F1)							Placitas (C10)					
		Expansion Level (%)							Expansion Level (%)					
		0.009	0.109	0.181	0.272	0.379	0.416	0.429	0.010	0.045	0.074	0.135	0.160	0.177
1st Cycle Area (Pa)*	Cyl 1	362	1251	1457	2140	2408	1662	1368	422	753	674	632	641	698
	Cyl 2	278	1022	1128	1830	2254	1428	1475	481	648	742	831	700	585
	Cyl 3	383	979	1178	1845	2110	1640	1313	339	766	615	661	796	796
	Average	341	1084	1254	1938	2257	1577	1385	414	722	677	708	712	693
	Var %	30.8	25.1	26.2	16.0	13.2	14.8	11.7	34.3	16.3	18.8	28.1	21.8	30.4
Plastic Strain ($\mu\epsilon$)	Cyl 1	62	179	194	236	270	200	137	45	92	77	62	57	109
	Cyl 2	53	111	119	196	226	153	145	61	62	97	125	86	70
	Cyl 3	46	113	108	226	217	206	136	23	61	92	65	93	84
	Average	54	134	140	220	238	186	139	43	71	89	84	79	88
	Var %	29.3	50.5	61.4	18.2	22.4	28.6	7.0	87.7	44.1	21.8	75.0	46.2	44.2
f _c (28 day)		37.8							37.2					
Load, % of 28-day f _c		26.4							26.9					
Load, % of f _c at test		29.5	28.3	30.1	32.7	34.6	34.0	33.4	27.9	27.3	26.4	25.2	24.1	23.8

* 1 Pa = 0.000145 psi; 1 MPa = 145 psi

Table 4.5: SDT results for ASR+DEF cylinders.

		Jobe (F1)							Placitas (C10)				
		Expansion Level (%)							Expansion Level (%)				
		0.005	0.097	0.257	0.361	0.471	0.566	0.951	0.010	0.076	0.166	0.230	0.318
1st Cycle Area (Pa)*	Cyl 1	433	1158	1476	1420	1474	2154	4003	746	1021	982	1231	980
	Cyl 2	605	957	1038	1500	1507	2424	3179	650	950	830	1096	1051
	Cyl 3	489	1111	1459	1709	1961	2365	3205	421	701	866	941	978
	Average	509	1075	1324	1543	1647	2314	3462	606	891	893	1089	1003
	Var %	33.8	18.7	33.1	18.7	29.6	11.7	23.8	53.7	35.9	17.0	26.6	7.3
Plastic Strain (µε)	Cyl 1	71	160	197	192	180	275	590	100	125	86	134	109
	Cyl 2	92	121	131	197	207	315	464	98	119	90	116	80
	Cyl 3	64	127	195	255	274	282	461	52	65	100	125	115
	Average	76	136	174	215	220	291	505	84	103	92	125	101
	Var %	36.7	28.5	38.2	29.3	42.3	13.7	25.4	58.0	57.6	15.8	14.5	34.7
f _c (28 day)		29.8							33.9				
Load, % of 28-day f _c		33.6							29.5				
Load, % of f _c at test		35.8	35.8	38.4	40.5	43.5	46.8	56.3	29.9	32.5	30.9	31.3	35.8

* 1 Pa = 0.000145 psi; 1 MPa = 145 psi

Table 4.6: SDT results for DEF cylinders.

		Jobe (F1)							Placitas (C10)					
		Expansion Level (%)							Expansion Level (%)					
		0.000	0.102	0.208	0.344	0.415	0.506	1.011	0.008	0.079	0.179	0.266	0.327	0.454
1st Cycle Area (Pa)*	Cyl 1	324	494	917	3850	3699	5655	5399	435	1034	1592	1892	1363	3348
	Cyl 2	507	720	2576	3311	6598	5265	9375	177	807	1268	1800	775	3346
	Cyl 3	576	1327	2058	4971	3904	5367	5495	714	1216	1015	1359	1705	2942
	Average	469	847	1850	4044	4734	5429	6756	442	1019	1292	1684	1281	3212
	Var %	53.7	98.3	89.7	41.0	61.2	7.2	58.8	121.5	40.1	44.7	31.7	72.6	12.6
Plastic Strain (µε)	Cyl 1	27	69	91	557	494	878	787	52	140	145	206	214	616
	Cyl 2	88	104	364	479	1122	793	1569	n/a	108	145	253	109	421
	Cyl 3	79	160	253	747	602	821	826	103	179	86	153	179	347
	Average	65	111	236	594	739	830	1060	78	142	125	204	167	462
	Var %	95.6	81.8	115.9	45.0	85.0	10.2	73.7	65.8	50.1	47.3	49.3	62.9	58.2
f _c (28 day)		29.8							33.9					
Load, % of 28-day f _c		33.6							29.5					
Load, % of f _c at test		36.6	35.2	38.1	50.9	53.4	54.5	62.7	30.3	30.4	30.8	34.1	30.4	39.7

* 1 Pa = 0.000145 psi; 1 MPa = 145 psi

It is also important to consider the results for tests of the non-reactive control specimens. At 28 days, the Jobe (F1) controls had an average 1st Cycle Area of 281 Pa and an average Total Plastic Strain of 33 µε. The Placitas (C10) controls had an average 1st Cycle Area and Total Plastic Strain of 301 Pa and 33 µε, respectively. These values are slightly less than the initial measurements for the ASR cylinders, and reflect the fact that the controls were more mature at testing than the reactive specimens (28 vs. 7 d old). After one year, the SDT parameters for the non-reactive controls had decreased marginally. Values for Jobe (F1) were 250 Pa and 27 µε, while values for Placitas (C10) were 241 Pa and 18 µε.

4.3.3 Elastic Modulus and Compressive Strength

Figures 4.11 and 4.12 show the static elastic modulus results for the Jobe (F1) and Placitas (C10) cylinders, respectively, plotted against the average expansion of the instrumented reference cylinders at the time of testing. Each datum represents the average of three cylinders. The elastic moduli of the Jobe (F1) cylinders were greatly affected by each type of deterioration,

with decreases of 55%, 63%, and 75% for the ASR, ASR+DEF and DEF cylinders, respectively. For the Placitas (C10) cylinders, the decrease in modulus was less, but still very significant—24%, 31% and 59% for the ASR, ASR+DEF and DEF cylinders, respectively. Figure 4.11 also shows a recovery in elastic modulus for the Jobe (F1) ASR cylinders as the expansion rate slowed; this is consistent with the decrease in SDT parameters for these specimens discussed above. As with the SDT parameters, the elastic modulus was most affected by expansion due to DEF.

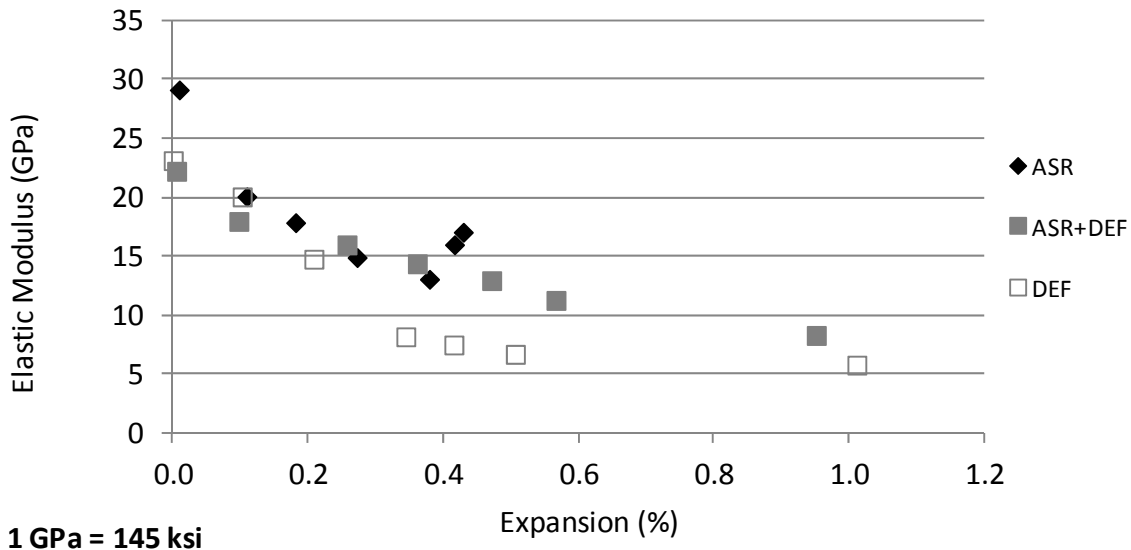


Figure 4.11: Averaged elastic moduli vs. expansion of Jobe (F1) cylinders.

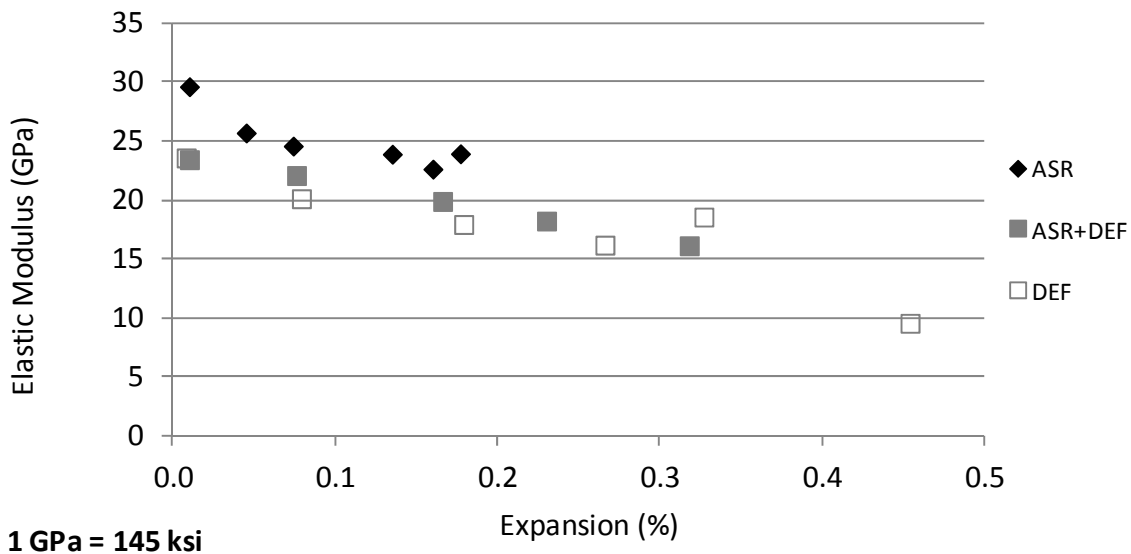


Figure 4.12: Averaged elastic moduli vs. expansion of Placitas (C10) cylinders.

Figures 4.13 and 4.14 show the compressive strength results for the Jobe (F1) and Placitas (C10) cylinders, respectively, plotted against the average expansion of the instrumented reference cylinders at the time of testing. Each datum represents the average of three cylinders.

Compressive strength was less affected than elastic modulus, with the greatest effects resulting from DEF. For the Jobe (F1) cylinders, decreases of 15% (ASR), 36% (ASR+DEF) and 41% (DEF) were measured. For the Placitas (C10) cylinders, an increase of 17% was measured for the ASR cylinders, and decreases of 16% and 24% measured for the ASR+DEF and DEF cylinders, respectively. The Placitas (C10) ASR cylinders expanded much more slowly than all other specimens in this study, and therefore were able to gain strength (possibly due to continued hydration of cement) more quickly than ASR could degrade it. However, the strength at 0.177% expansion (approximately 8 months of age) was almost 18% lower than that of the non-reactive control specimens at one year, so ASR did still have a negative impact on strength.

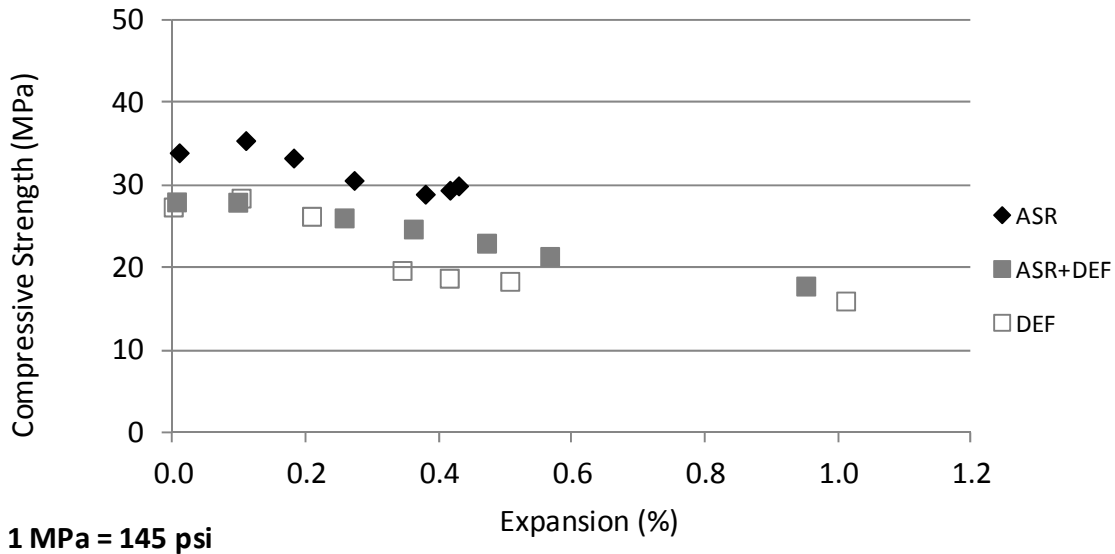


Figure 4.13: Averaged compressive strength vs. expansion of Jobe (F1) cylinders.

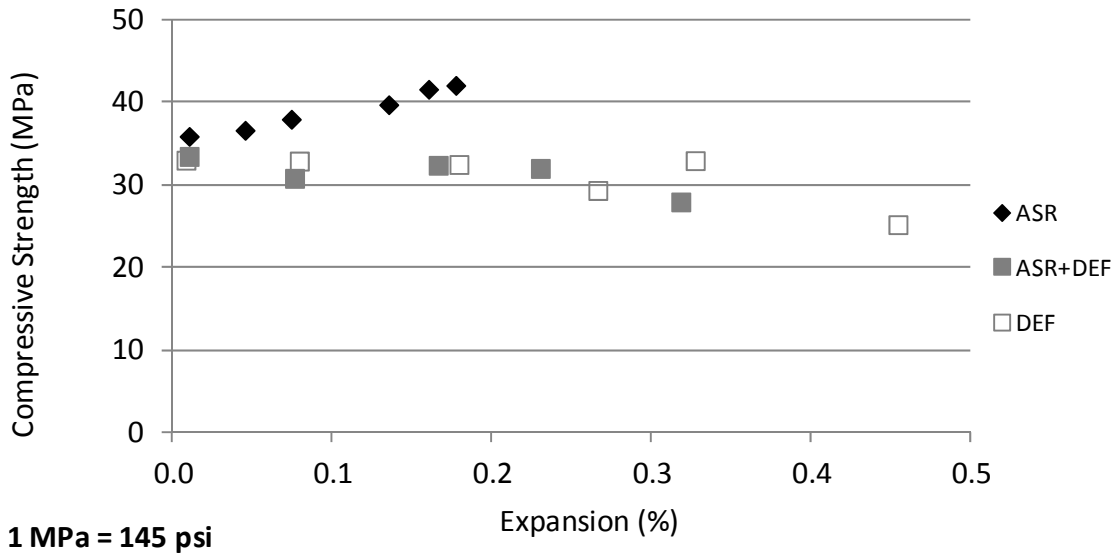


Figure 4.14: Averaged compressive strength vs. expansion of Placitas (C10) cylinders.

Tables 4.7, 4.8 and 4.9 provide a summary of the elastic modulus and compressive strength results for each individual cylinder tested from the ASR, ASR+DEF and DEF series, respectively. These tables also provide information on the statistical variation in the data. The “Var %” values were calculated in the same manner as in Tables 4.4, 4.5 and 4.6, and show that these tests had significantly less variation within each set of cylinders compared to the stiffness damage test.

Variation in the elastic modulus test data ranged from an average of 9.3% for the ASR cylinders to 26.7% for the DEF cylinders. This is less than half of the variation reported for the 1st Cycle Area in the SDT. Variation in the compressive strength results ranged from an average of 4.9% for the ASR cylinders to 13.1% for the DEF cylinders. Although some of cylinders had previously been tested in the SDT to loads greater than 40% of the compressive strength, this does not correlate to a greater variability in the elastic modulus tests which followed. It is impossible to judge whether the actual measured modulus was influenced, however.

Table 4.7: Elastic modulus and compressive strength results for ASR cylinders.

		Jobe (F1)							Placitas (C10)					
		Expansion Level (%)							Expansion Level (%)					
		0.009	0.109	0.181	0.272	0.379	0.416	0.429	0.010	0.045	0.074	0.135	0.160	0.177
E (GPa)*	Cyl 1	27.9	20.0	17.6	13.4	13.0	15.8	n/a	29.5	26.3	24.3	23.5	21.8	22.6
	Cyl 2	29.2	21.2	19.3	15.5	12.4	16.7	16.6	30.3	25.6	23.9	22.7	23.1	25.8
	Cyl 3	30.2	19.0	16.6	15.7	13.8	15.4	17.5	29.0	25.2	25.6	25.6	23.0	23.4
	Average	29.1	20.1	17.9	14.9	13.1	16.0	17.1	29.6	25.7	24.6	23.9	22.6	23.9
	Var %	7.9	11.0	15.2	15.4	11.3	7.8	5.3	4.5	4.3	7.2	12.1	5.7	13.4
f _c (MPa)*	Cyl 1	33.0	35.2	32.2	30.1	28.7	28.9	n/a	35.4	36.0	35.3	39.9	42.2	40.5
	Cyl 2	33.8	34.6	34.8	30.4	29.3	29.6	30.0	36.8	37.2	41.5	39.2	41.0	44.1
	Cyl 3	34.9	36.3	32.8	31.1	28.7	29.6	29.8	35.4	36.7	37.1	40.0	41.5	41.5
	Average	33.9	35.4	33.3	30.6	28.9	29.4	29.9	35.9	36.6	37.9	39.7	41.6	42.0
	Var %	5.4	4.6	7.9	3.3	2.1	2.3	0.7	3.9	3.2	16.4	1.9	2.9	8.6
E, % of predicted by f _c		105.6	71.3	65.4	56.9	51.3	62.3	66.0	104.5	89.7	84.5	80.1	74.1	78.0

* 1 GPa = 145 ksi; 1 MPa = 145 psi

Table 4.8: Elastic modulus and compressive strength results for ASR+DEF cylinders.

		Jobe (F1)							Placitas (C10)				
		Expansion Level (%)							Expansion Level (%)				
		0.005	0.097	0.257	0.361	0.471	0.566	0.951	0.010	0.076	0.166	0.230	0.318
E (GPa)*	Cyl 1	21.8	17.2	15.7	15.9	12.1	11.3	7.4	22.7	23.2	19.8	17.3	17.1
	Cyl 2	22.2	19.2	15.4	13.3	14.3	11.2	8.8	24.2	20.8	19.8	18.4	14.7
	Cyl 3	22.7	17.5	16.9	13.9	12.5	11.2	8.7	23.4	22.3	20.1	19.0	16.6
	Average	22.2	18.0	16.0	14.4	13.0	11.3	8.3	23.4	22.1	19.9	18.2	16.1
	Var %	4.3	10.9	9.7	18.2	16.7	0.8	16.2	6.7	11.0	1.5	9.2	15.1
f _c (MPa)*	Cyl 1	27.6	27.1	26.3	25.7	21.8	22.1	16.9	32.7	24.0	31.3	30.4	29.1
	Cyl 2	27.2	28.6	25.3	24.4	24.6	20.6	18.4	33.4	32.6	32.3	31.2	26.5
	Cyl 3	29.1	28.0	26.5	23.9	22.6	21.4	18.1	34.2	35.8	33.5	34.4	28.1
	Average	28.0	27.9	26.0	24.7	23.0	21.4	17.8	33.4	30.8	32.4	32.0	27.9
	Var %	6.7	5.3	4.7	7.4	12.1	7.0	8.6	4.3	38.2	6.6	12.5	9.4
E, % of predicted by f _c		88.8	71.8	66.2	61.1	57.0	51.6	41.6	85.6	85.3	73.9	68.2	64.5

* 1 GPa = 145 ksi; 1 MPa = 145 psi

Table 4.9: Elastic modulus and compressive strength results for DEF cylinders.

		Jobe (F1)							Placitas (C10)					
		Expansion Level (%)							Expansion Level (%)					
		0.000	0.102	0.208	0.344	0.415	0.506	1.011	0.008	0.079	0.179	0.266	0.327	0.454
E (GPa)*	Cyl 1	22.6	24.4	20.0	8.5	8.4	6.3	6.3	23.1	20.4	16.2	13.4	19.6	8.7
	Cyl 2	24.6	18.8	10.8	9.1	5.7	7.2	4.6	23.8	21.6	17.5	15.5	20.7	9.5
	Cyl 3	22.2	16.9	13.5	6.9	8.5	6.6	6.6	23.8	18.4	20.1	19.7	15.5	10.6
	Average	23.1	20.0	14.8	8.2	7.5	6.7	5.8	23.6	20.1	17.9	16.2	18.6	9.6
	Var %	10.1	37.3	62.5	26.5	37.1	12.4	34.8	3.1	15.9	21.8	38.6	28.0	19.1
f _c (MPa)*	Cyl 1	27.6	33.2	30.7	20.2	20.5	19.1	16.9	32.9	31.9	33.4	28.9	32.7	27.3
	Cyl 2	27.6	26.1	23.1	20.4	16.5	18.2	14.3	33.9	33.7	30.9	30.4	35.6	25.0
	Cyl 3	26.9	25.9	24.8	18.4	19.3	17.7	16.6	32.2	33.1	33.0	28.7	30.4	23.1
	Average	27.3	28.4	26.2	19.7	18.7	18.3	16.0	33.0	32.9	32.5	29.3	32.9	25.2
	Var %	2.5	25.5	29.2	10.5	21.4	7.9	16.4	5.3	5.4	7.6	5.6	15.9	16.7
E, % of predicted by f _c		93.4	79.2	60.3	39.0	36.5	33.1	30.5	86.8	74.2	66.6	63.3	68.3	40.5

* 1 GPa = 145 ksi; 1 MPa = 145 psi

The above tables also compare the measured elastic moduli with that which would be predicted which is commonly assumed based on the compressive strength (see Equation 3.5). The measured moduli are as much as 60 to 70% below values predicted by the compressive strength for ASR+DEF and DEF cylinders. As was also noted in Chapter 3, it is critical that elastic modulus be measured directly rather than inferred based on compressive strength tests.

4.3.4 Resonant Frequency Testing

The linear analysis of the resonant frequency tests on the instrumented Placitas (C10) cylinders is shown in Figure 4.15. In this figure, dynamic elastic modulus is plotted against the measured expansions of the cylinders. Compared with the data presented in Chapter 3 for the exposure block cores, the results are rather inconclusive. The moduli generally increase, then decrease as expansion increases. The results may have been complicated by conducting the initial test at an age of only 3 d; ongoing strength development and hydration most likely contributed to the initial increase in dynamic modulus.

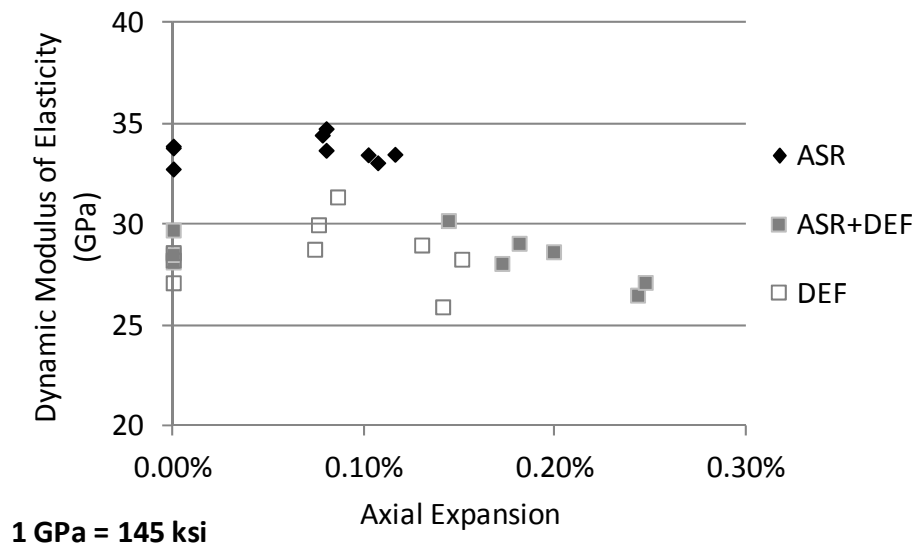


Figure 4.15: Linear resonant frequency results (E_d vs. expansion).

Figure 4.16 presents the results of the nonlinear resonant frequency analyses for the Placitas (C10) reference cylinders. The nonlinear parameter, α , is plotted against the axial expansion of each cylinder. The DEF cylinder data omitted from the plot on the left and all three sets of cylinders shown in the plot on the right—note the massive difference in scale between the two plots.

Testing was halted after three sets of measurements were taken because of concerns that the test may be potentially somewhat destructive to the specimens, due to the impact force required to obtain a shift in the resonant frequency. Additionally, the data obtained was rather inconclusive.

Compared to the dynamic moduli in the linear analysis, the magnitude of changes in the nonlinear parameter is considerably greater. As expansion of the ASR cylinders increased, α first tripled, then decreased. This was similar to results reported for mortar bars made with Jobe (F1) sand (Chen, et al. 2010). A consistent decrease (over 30%) in α was found for the ASR+DEF cylinders. The DEF cylinders generally showed the greatest sensitivity to expansion, increasing almost five-fold for one cylinder, but there was considerable variation in the data for cylinders with similar expansions. Nonlinear acoustic methods have often been described as being most sensitive to the development of microcracking, which would correspond to the onset of damage from ASR and DEF. In this case, the results are conflicting, depending on the damage mechanism. It is also possible that the rapid expansion of the ASR+DEF specimens prevented measurement of a rise in the nonlinear parameter that would have been evident expansions below 0.10%. Given that this analytical technique was developed to identify the onset of ASR in mortar bars, this technique may simply be unsuitable for characterizing the damage caused by ASR and/or DEF to concrete in field structures.

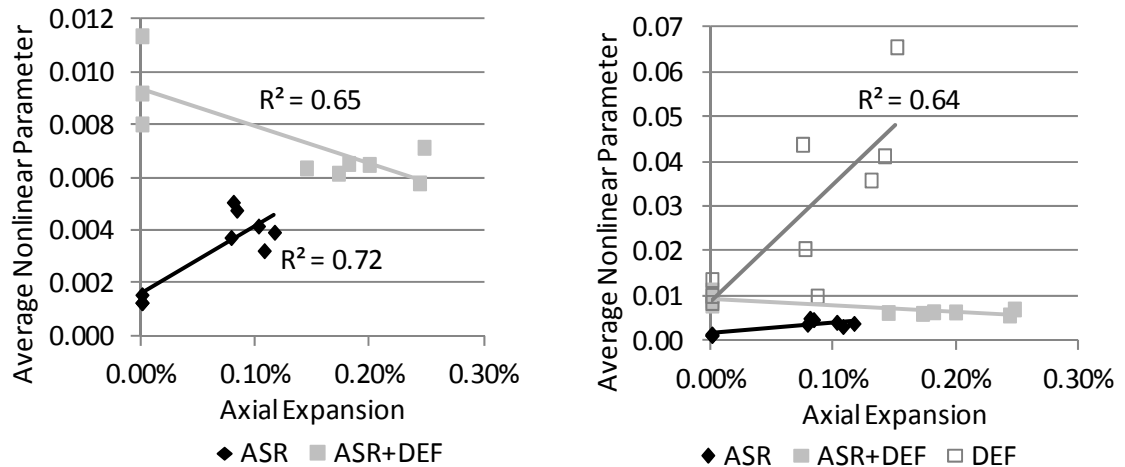


Figure 4.16: Nonlinear resonant frequency results for Placitas (C10) cylinders.

4.4 Summary

Concrete cylinders expanding due to ASR, DEF, and a combination of ASR and DEF were used to evaluate the applicability of a suite of tests for characterizing the damage incurred by these mechanisms. These included the stiffness damage test, elastic modulus, compressive strength, and resonant frequency.

Stiffness damage testing, as performed in this study, has significant challenges. The use of a fixed maximum load is difficult to justify for concretes of differing compressive strengths, while setting the maximum load to a specific percentage of compressive strength requires a method for normalizing the results of the test. The recovery of mechanical properties of the ASR-affected cylinders contributed to a poor correlation of SDT parameters to expansion. SDT does appear to hold considerably more promise for characterizing DEF damage, although this is extremely rare as a sole damage mechanism in field structures. SDT results are also extremely variable among specimens that have been similarly fabricated, conditioned, and damaged, especially in comparison to standardized tests such as static elastic modulus and compressive strength.

The static elastic modulus, as expected, was greatly affected by expansion, but cannot be predicted based on the compressive strength. These two tests, however, provide the least variable and most potentially useful information to an engineer attempting to determine the adequacy of a damaged field structure of the tests examined in this chapter. Although compressive strength is the least sensitive to ASR and DEF, the test is necessary, both for a structural analysis and for confirming that an elastic modulus test was conducted at a proper load. The tensile and flexural strength of concrete, although not examined in this research, are more greatly affected by ASR and DEF than the compressive strength, and therefore may be of greater use in assessing the damage to concrete, particularly if it is not reinforced.

In contrast, the analyses of resonant frequency test results were inconclusive at best. The dynamic modulus, as determined by the linear analysis, was less sensitive to expansion than expected, and the nonlinear analysis of resonant frequency shifts with repeated impacts did not provide useful information.

Chapter 5. Full-Scale Beams: Fabrication and Monitoring

5.1 Overview

Three full-scale reinforced concrete beam specimens were fabricated at the Ferguson Structural Engineering Laboratory at University of Texas at Austin for the purpose of assessing the use of NDT methods on ASR- and DEF-affected field structures and to determine the effects of these distress mechanisms on flexural behavior. Two beams, referred to as the reactive specimens, were designed to experience severe deterioration from ASR or a combination of ASR and DEF. A third, nonreactive control specimen was also fabricated, and designed not to experience any deterioration. All three specimens were stored under similar conditions of load and moisture to simulate worst-case field exposure conditions. A comprehensive expansion and NDT monitoring program was conducted over a 20-24 month period as the specimens were allowed to deteriorate. Several smaller specimens were also fabricated and tested under laboratory conditions. This chapter details the design, fabrication, conditioning, and in-situ monitoring of the specimens, and serves as an update to the work of Kreitman (2011).

5.2 Specimen Design, Fabrication, and Conditioning

Previous work at the University of Texas at Austin by Deschenes (2009) provided a baseline for the three beam specimens in this study. Although the reinforcement details were altered to ensure flexural, rather than shear failure, the fabrication process, mixture design and conditioning of the specimens were very similar. Figure 5.1 provides an overall introduction to the fabrication and conditioning of the beams, showing the timing of various key events. The beams were fabricated over a four month period in early 2010, followed by the movement to outdoor exposure and the application of load and moisture conditioning. These events are described in greater detail below.

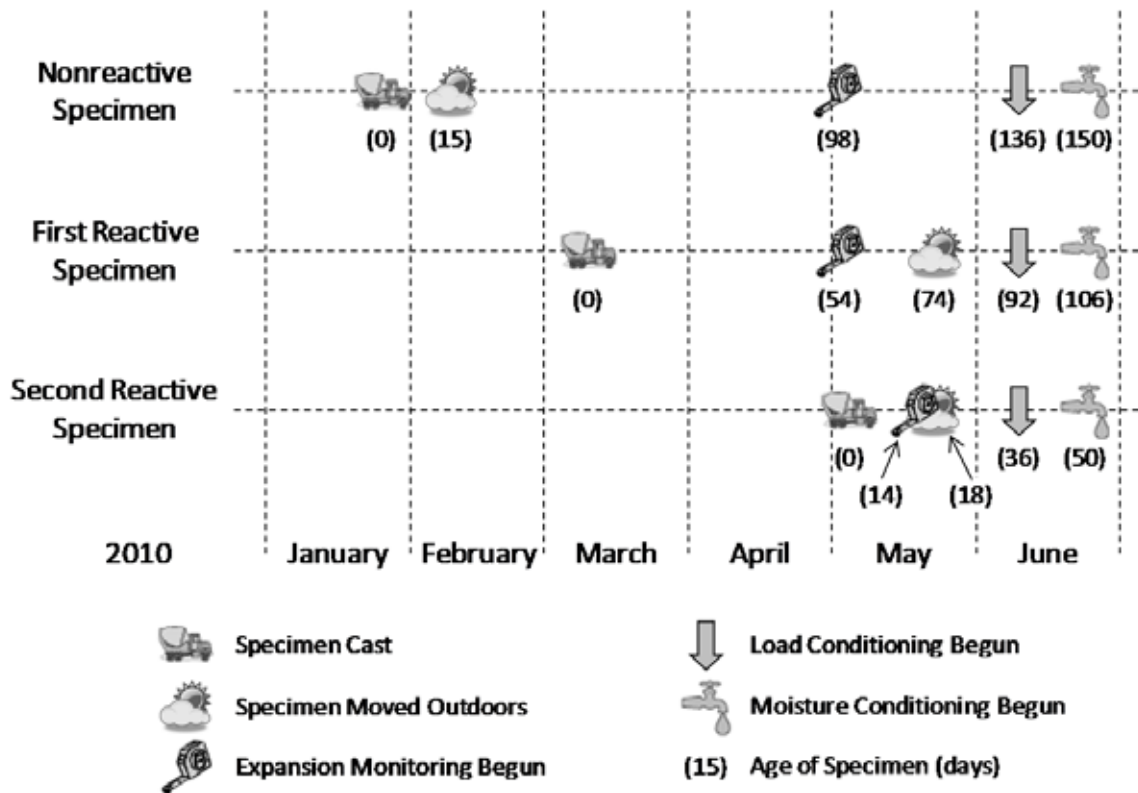


Figure 5.1: Timeline of beam fabrication and conditioning, from Kreitman 2011.

5.2.1 Design

The design of the beam specimens was tailored to ensure that the reactive specimens experienced significant distress from ASR and DEF during the time constraints of the project, while maintaining as much similarity in scale to in-service structures.

5.2.2 Specimen Geometry and Reinforcement

A cross section of 21 x 42 in. (533 x 1067 mm) and length of 27 ft 8 in. (8433 mm) was used for the beams specimens. The depth is comparable to bent caps used in bridge structures in Texas (Deschenes 2009), while the width was chosen to limit the weight of the specimens so that they could be moved in and out of the laboratory with existing equipment. The length was controlled by the spacing of the high-strength rods and reaction beams in the laboratory's Large-Scale Beam Testing Facility. Along with the shear-critical beams tested by Deschenes, these are some of the largest ASR- and DEF-affected beams fabricated for laboratory testing, and are of comparable scale to the commercially-produced specimens tested by Larson (2010), which were intended to be placed in service before cracking was discovered. The cross section and elevation views of the specimens with reinforcing details are shown Figures 5.2 and 5.3, respectively.

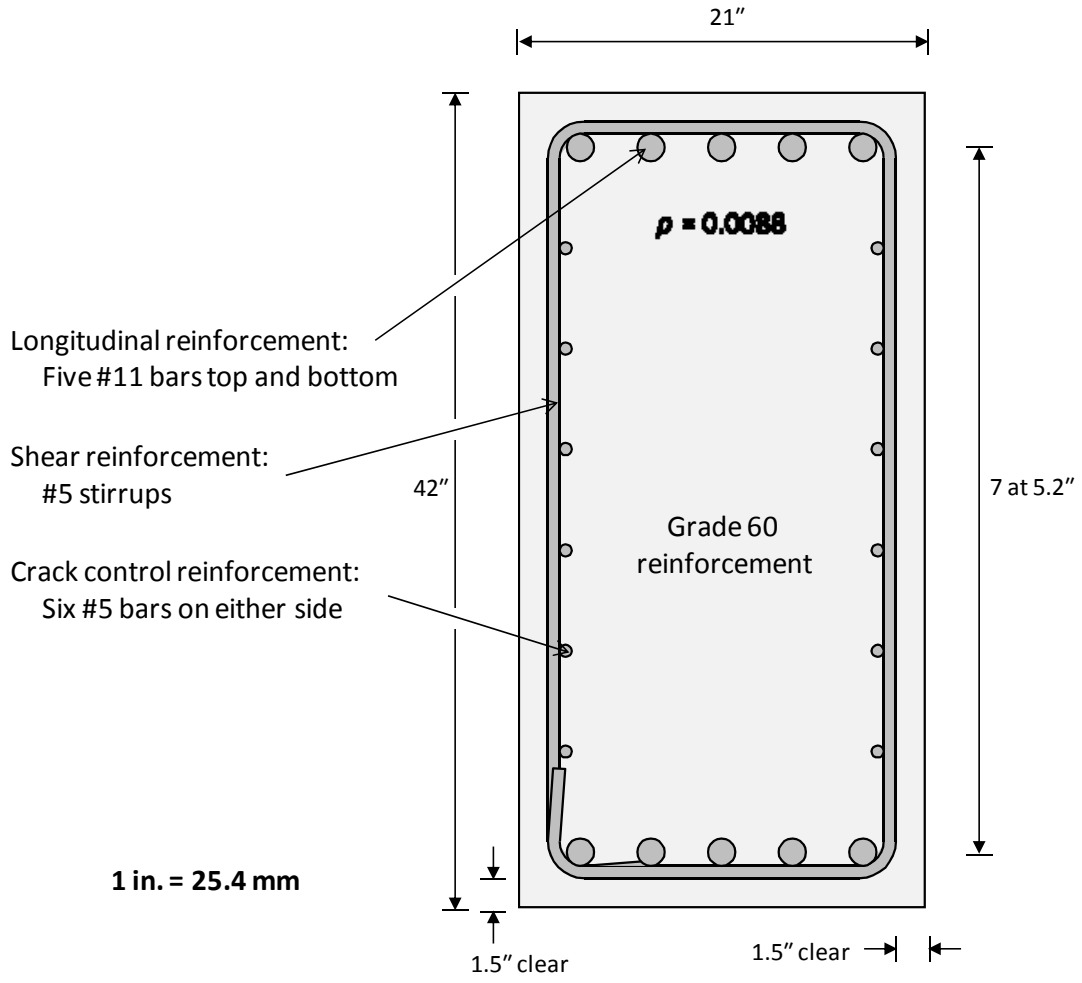


Figure 5.2: Cross-sectional view of beam specimen, from Kreitman 2011.

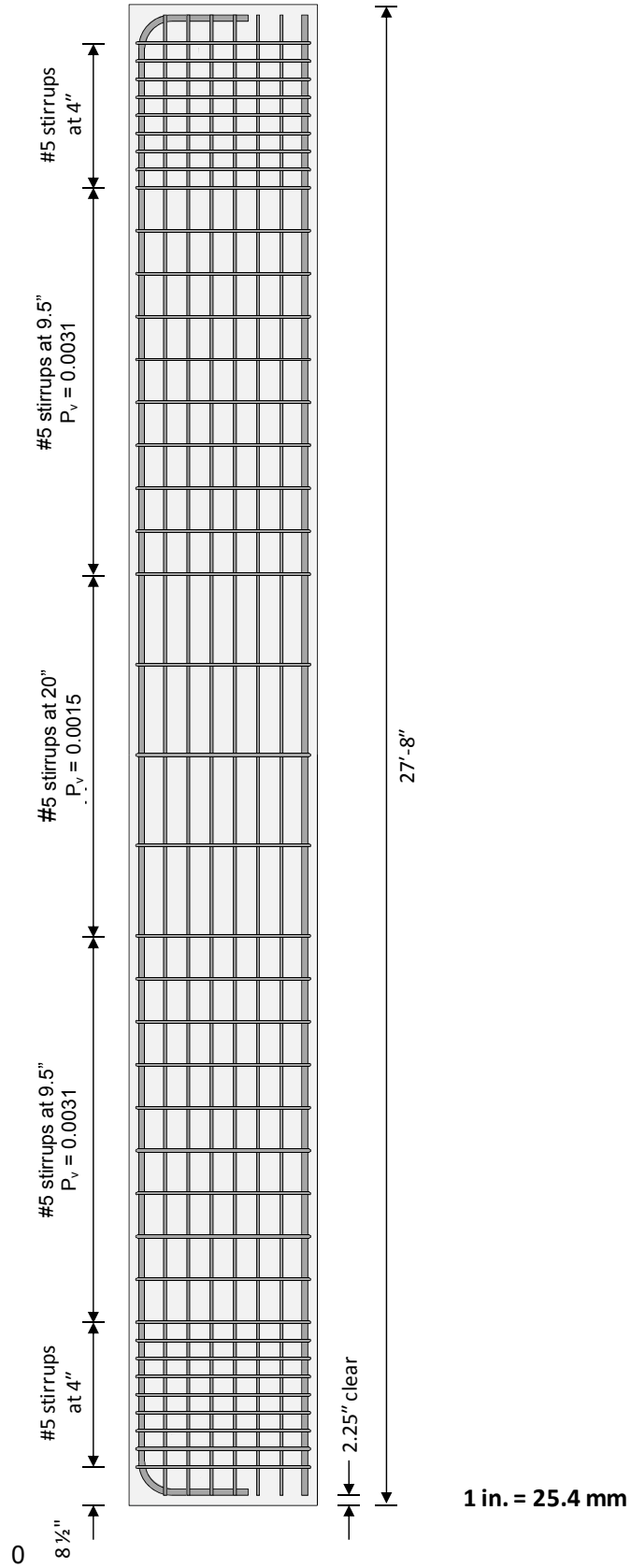


Figure 5.3: Elevation view of beam specimen, from Kreitman 2011.

The beams were doubly reinforced with five #11 bars each for tension and compression reinforcement. Since the specimens were fabricated upside down to accommodate placement of the reaction beams and loading rams in the test facility, the tension reinforcement is actually located along the top of the beams. Twelve #5 longitudinal bars were provided for crack-control reinforcement. Shear reinforcement consisted of #5 stirrups, the spacing of which was varied along the length of the beam to ensure flexural failure in the middle third of the span. A spacing of 20-in. (508 mm) was used in this middle test region, which constituted a zero-shear, constant moment zone spanning between the two applied loads during conditioning and flexural testing. A constant shear region located between the applied loads and the reaction points at each end of the span contained stirrups at a spacing of 9.5 in. (241 mm). These spacings met requirements for minimum transverse reinforcement ratios for the expected loads in these regions, and were consistent with those used in the Deschenes' work (2009). In the ends of the beams outside the loaded span, stirrups were spaced at 4 in. (102 mm) to prevent any local failure.

5.2.3 Materials and Mixture Proportions

Design of the concrete mixtures was also based on the specimens tested by Deschenes (2009). Design strength of 5000 psi (35MPa) was selected for the specimens, which is typical of bent caps in Texas. This required a design w/cm of 0.50, although in practice it ranged from 0.48 to 0.52. The details of the mixtures for each specimen and their 28-day compressive strengths are given in Table 5.1.

In order to produce significant ASR- and DEF-related distress in the two reactive specimens within the project timeframe, a highly reactive aggregate was required. For this, Jobe (F1) sand from El Paso, Texas was selected. The testing described in Chapters 3 and 4 should leave no doubt as to the potential for very large expansions with this aggregate. The alkali-silica reactivity of these specimens was enhanced by added sodium hydroxide (in aqueous solution) to the mixture to raise the equivalent alkalis to approximately 1.25% by mass of cement.

A crushed limestone coarse aggregate with a maximum size aggregate (MSA) of 0.75 in. (19 mm) from Georgetown, Texas (Georgetown Limestone) was used in both the reactive and nonreactive specimens; this aggregate has no history of causing deleterious expansion. Natural sand from Del Valle, Texas (Colorado Riversand) was used as the fine aggregate in the nonreactive specimen, and was not expected to cause expansion during the project timeframe. A low-alkali Type III portland cement was also used for the nonreactive specimen to minimize the risk of expansion.

DEF also requires high temperatures that could only be achieved in the laboratory by the use of Type III portland cement, hot mixing water, and heat applied during curing (discussed in 5.2.2). A fresh concrete temperature target of 90-100 °F (32-38 °C) was used for the reactive beam specimens, and achieved through the use of 130 °F (54 °C) water for a large portion of the mixing water.

Table 5.1: As-batched mixture proportions and 28-day strengths.

Component	Nonreactive Beam	First Reactive Beam	Second Reactive Beam
Coarse Aggregate (SSD) lb/yd ³ (kg/m ³)	Georgetown Limestone		
	1550 (920)	1556 (923)	1565 (929)
Fine Aggregate (SSD) lb/yd ³ (kg/m ³)	Colorado Riversand	Jobe (F1)	
	1232 (731)	1198 (711)	1207 (716)
Cement lb/yd ³ (kg/m ³)	Type III, 0.49% Na ₂ O _e	Type III, 0.80% Na ₂ O _e	Type III, 0.79% Na ₂ O _e
	708 (420)	719 (426)	723 (429)
NaOH added	0	4.33 (2.57)	436 (2.58)
Total Na ₂ O _e , lb/yd ³ (kg/m ³)	3.47 (2.06)	9.10 (5.40)	9.09 (5.39)
w/cm	0.52	0.48	0.49
Water	367 (218)	347 (206)	340
f'c (28 d), psi (MPa)	6180 (42.6)	5200 (35.8)	4700 (32.4)

5.2.4 Instrumentation

Instrumentation of the beams consisted of a robust system of stainless steel targets for expansion measurements and thermocouples to monitor temperature evolution during the early curing period. Figure 5.4 shows the layout of the instrumentation in the two test regions in each specimen. The constant moment middle region and one of the constant shear end regions were instrumented. Targets were located on all four sides of the beam and allowed measurement of transverse (vertical) and longitudinal expansions.

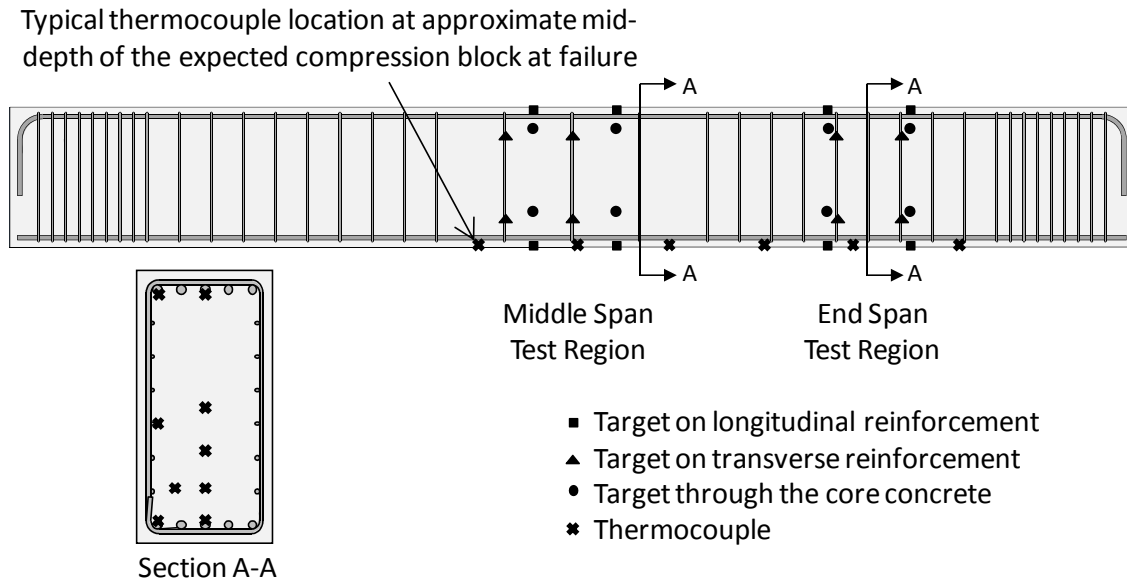


Figure 5.4: Instrumentation layout for beam specimens, from Kreitman 2011.

This author and others (Bentivegna 2009, Deschenes 2009) have noted high failure rates with electrical resistance strain gauges used for monitoring reinforcement strains in ASR-affected concrete. This is likely due in part to the very alkaline environment; damaging during concrete placement is also to be expected. Therefore, expansions were monitored mechanically

using an extensometer to measure the change in distance between the steel targets. This system was shown to be essentially fail-proof by Deschenes and the resulting expansions matched those captured by the surviving electrical strain gauges in his specimens.

The targets consisted of a length of 0.5 in. (12.7 mm) stainless steel rod with a machined divot on the exposed face or faces to receive one tip of the extensometer. Short rods were tack-welded to selected longitudinal bars and stirrups (Figure 5.5a), while long rods (Figure 5.5b) passed completely through the 21 in. (533 mm) width of the specimens and were used to measure expansion of the concrete core. The rods were centered inside a length of 1.5 in. (38 mm) diameter PVC pipe, and expandable foam was placed in the gap (Figures 5.5c and 5.5d). This isolated the rods from the cover concrete and allowed those attached to the reinforcement to move freely as the reinforcement was strained. Figure 5.5e shows a completed and installed set of targets in the outer test region of a specimen.

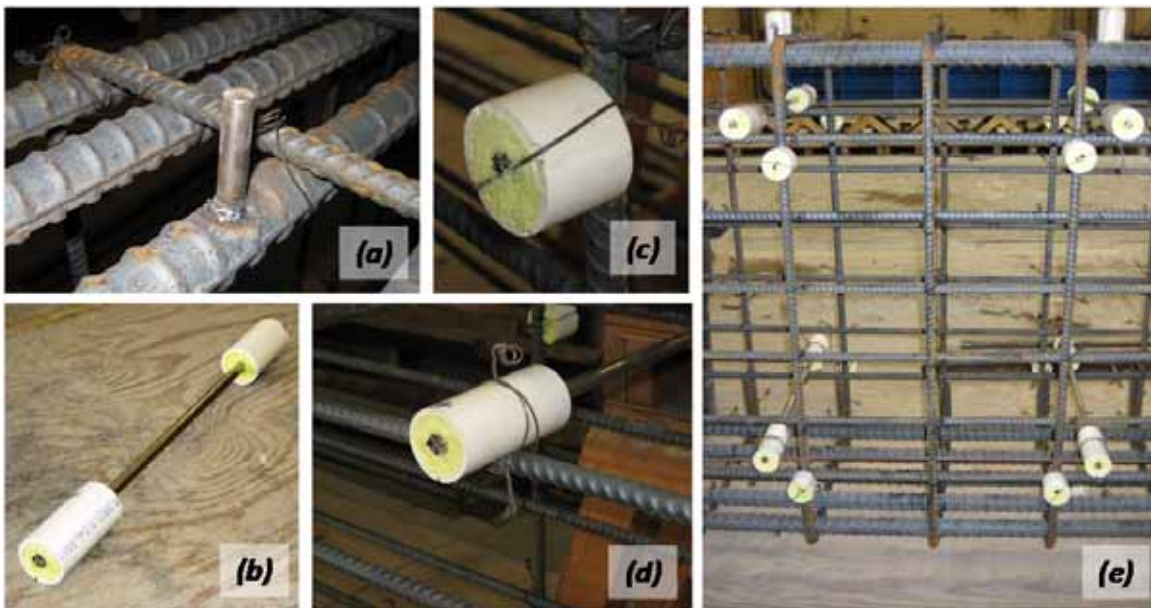


Figure 5.5: Targets for mechanical expansion measurements, from Kreitman 2011.

Type T thermocouples were installed in several location in each test region (Figure 5.4) to monitor the temperature evolution during curing and measure the distribution of peak temperatures in the beam cross-section. This temperature history is extremely important in determining the potential for the development of DEF in each of the reactive specimens, as well as ensuring that the nonreactive specimen is not susceptible. The thermocouples were connected to a Campbell Scientific CR10X data logger

5.2.5 Fabrication

An overview of the fabrication process is shown in Figure 5.6. The reinforcement cage was first constructed, using Grade 60 (420 MPa) bars and stirrups (Figure 5.6a). Tensile tests of coupons from the manufacturer were performed to confirm the yield strength. Average tensile strengths of 70.6 ksi (487 MPa) and 61.9 ksi (427 MPa) were measured for the #11 and #5 bars, respectively. Next, the expansion targets and thermocouples were installed. Steel forms were then constructed, and the completed cage moved into place (Figure 5.6b). Steel rebar chairs were

used to properly center the cage inside the forms. Concrete was then mixed, placed and consolidated. Last, the reactive specimens were heat-cured. Concrete mixing and placement, and the high temperature curing process are discussed in greater detail below.



(a) Construct reinforcement cage



(b) Erect formwork, place cage inside



(c) Mix concrete



(d) Place concrete



(e) Heat cure (reactive specimens only)

Figure 5.6: Full-scale beam fabrication process, from Kreitman 2011.

5.2.6 Concrete Mixing and Placement

The concrete for all three specimens was mixed on-site using a ready mix concrete truck. This was necessary due to the unusual mixture design and high fresh concrete temperature for the reactive mixtures. The truck arrived at the laboratory with the coarse aggregate (and, in the case of the nonreactive mixture, the fine aggregate). Jobe (F1) sand was the first item batched on-site (reactive specimens only), followed by water, cement and sodium hydroxide (diluted in approximately 30 gal (114 L) of water for safety reasons) (Figure 5.6c). A water-reducing and retarding admixture (Sika Plastiment) meeting the requirements of ASTM C494 (2011) Types B and D was also added to improve the workability of the concrete for the second reactive specimen. The mixing drum was turned slowly throughout the batching process; once batching was complete, the drum was turned at high speed for at least 200 revolutions to thoroughly mix the materials.

A small sample of concrete was first collected to conduct slump, unit weight and air content tests. The concrete was then discharged into a 1 yd³ (0.76 m³) hopper, transported with an overhead crane, placed in the forms, and consolidated using sideform and handheld stinger vibrators (Figure 5.6d). The top surface was struck off until level with the top of the forms, and finished with a trowel. After initial set, wet burlap was placed over the top of the specimen to ensure a moist-curing environment; the burlap was rewetted each day for seven days.

A collection of smaller concrete specimens was also fabricated for quality control and laboratory testing. This included 4 x 8 in. (100 x 200 mm) cylinders for compressive strength tests and eight 3 x 3 x 11.25 in. (75 x 75 x 286 mm) prisms for expansion and resonant frequency testing. The small specimens were cured at a temperature profile matched to that recorded by a thermocouple located in the bottom of each beam specimen (approximately in the center of the expected compression block at failure). A commercial Sure Cure system consisting of insulated metal molds with embedded heating elements was used to match-cure the cylinders, shown in Figure 5.7. The prisms were placed in an oven and the temperature adjusted manually each hour for the 18-24 h.



Figure 5.7: Sure Cure cylinder molds, from Kreitman 2011.

5.2.7 High-Temperature Curing

The heat generated by Type III cement in combination with the high fresh concrete temperature is not sufficient to bring temperatures over the 158 °F (70 °C) threshold required to force the dissolution of ettringite during the early curing period. Therefore, to create the potential for DEF in the reactive specimens, external heat was applied during the first 12 to 16 h after concrete placement. After initial set, the specimen was wrapped in a fireproof tarp, shown in Figure 5.6e, and two portable heaters provided the heat source. Air temperatures in the enclosure ranged from 150 to 196 °F (66 to 91 °C) during the heating period.

Figure 5.8 shows the temperature evolution with time in each specimen, as recorded by the thermocouple used for match-curing of the small cylinder specimens. Other thermocouples located at the same depth along the length of the beams recorded similar temperature profiles.

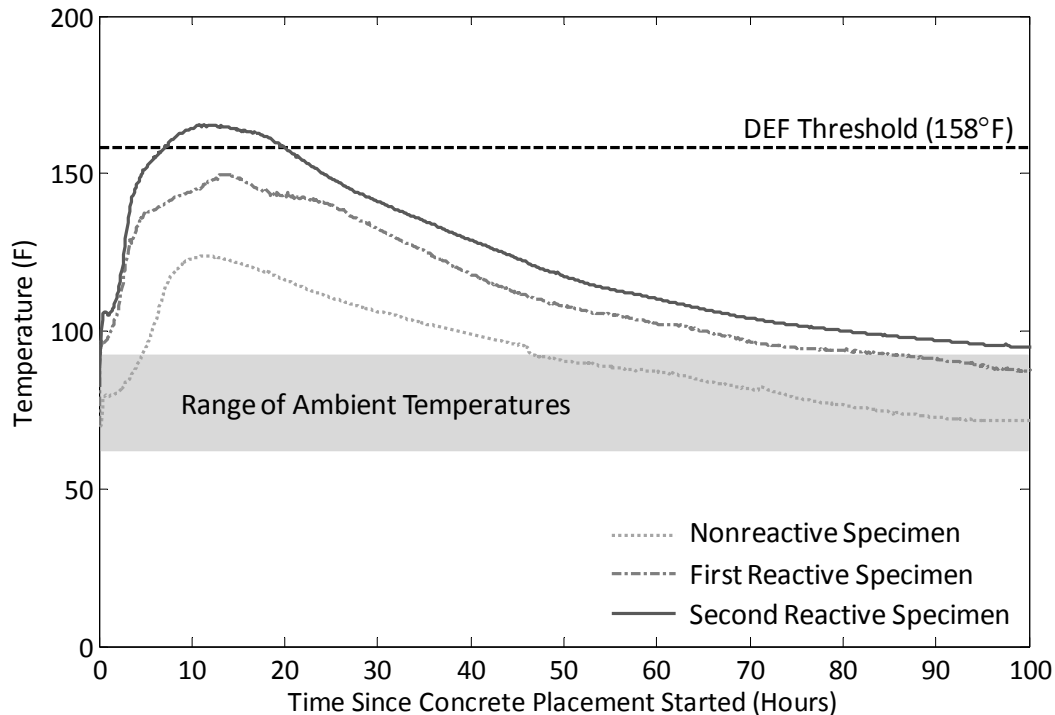


Figure 5.8: Temperature evolution with time for beam specimens ($1\text{ }^{\circ}\text{C} = 1.8\text{ }^{\circ}\text{F}$), from Kreitman 2011.

Figure 5.9 shows the distribution of maximum temperatures through the cross section of the nonreactive and second reactive specimens, based on the measurements obtained at the thermocouples noted in the figure. The pattern of temperature distribution is similar, but the scale is significantly different, with maximum temperatures of approximately 174 °F (79 °C) and 137 °F (60 °C) for the second reactive and nonreactive specimens, respectively. The data for the first reactive specimen were not properly recorded, but a similar temperature distribution can be assumed.

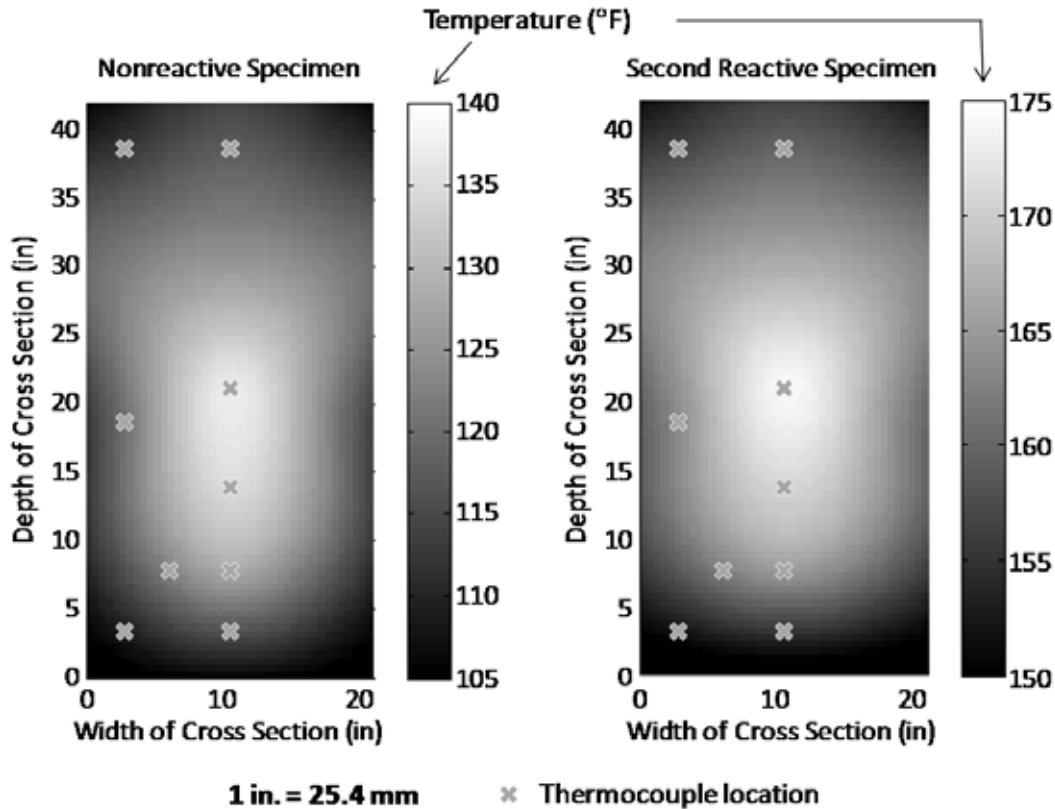


Figure 5.9: Distribution of maximum temperatures through specimen cross section ($1\text{ }^{\circ}\text{C} = 1.8\text{ }^{\circ}\text{F}$), from Kreitman 2011.

It is also important to note that the maximum temperatures at the core of the second reactive specimen were approximately $15\text{ }^{\circ}\text{F}$ ($5.6\text{ to }8.3\text{ }^{\circ}\text{C}$) greater than at the location of the thermocouple referenced in Figure 5.8. Thus, the first reactive specimen likely reached a maximum core temperature of $160\text{ to }165\text{ }^{\circ}\text{F}$ ($74\text{ }^{\circ}\text{C}$), which meant that a portion of the specimen exceeded the DEF threshold. The second reactive specimen exceeded the DEF temperature threshold in the majority of its cross section for 12 h or more.

5.2.8 Conditioning Regime

There were three components to the conditioning of the beam specimens: outdoor exposure, moisture and the application of a typical service load. Outdoor exposure and the supply of moisture through nightly watering cycles served to accelerate the deterioration of the specimens, while the application of load allowed the deterioration to develop under conditions more typical of an in-service structure.

The specimens were moved outside after an initial curing and storage period in the laboratory, ranging from 15 to 74 d. Both reactive specimens were placed outdoors on the same day to ensure that they experienced a similar conditioning process, despite the eight-week gap between fabricating each specimen. The specimens were supported on concrete pedestals at each end, as shown in Figure 5.10. Austin, Texas has a very warm climate with mild winters and temperatures that commonly exceed $100\text{ }^{\circ}\text{F}$ ($38\text{ }^{\circ}\text{C}$). This environment is ideal for producing rapid and severe expansion due to ASR.

A watering system was also installed in order to provide a constant supply of moisture to both enhance expansion from ASR and help trigger DEF by promoting the leaching of alkalis from the concrete. This consisted of soaker hoses placed on top of the beams and a tarp to retain the water, maintaining a moist environment. These can be seen in Figure 5.10. A timer was used to trigger 12-minute watering cycles (12 min on and 12 min off) for 12 h each night. The tarp was only removed for conducting in-situ monitoring. Moisture conditioning of all three specimens commenced at the same time.



Figure 5.10: Beam specimens in outdoor exposure and under load, from Kreitman 2011.

Load conditioning of the specimens simulated the dead load stresses that the specimen would experience if it were in service. This consisted of external loads applied at third points between two support reactions, resulting in a constant moment in the middle third of the span and a constant shear in the outer thirds of the span. Figure 5.11 shows the locations of the loads and support reactions, and the shear and moment diagrams.

Figure 5.12 shows the loading setup. A steel reaction beam under each beam applied the loads through flexible bearing pads (to accommodate rotation). The load was transferred to the reaction points by high-strength Dywidag rods that were anchored to steel tube sections below the reaction beam and above the specimen. Springs were placed between the top of the specimen and the upper steel tubes. During the application of load, 30-ton (267 kN) hydraulic rams compressed the spring assembly, and the load determined by the pressure on the rams. Once the hydraulic pressure reached the necessary amount, nuts were tightened against the steel tubes, fixing the applied load, and the rams were removed.

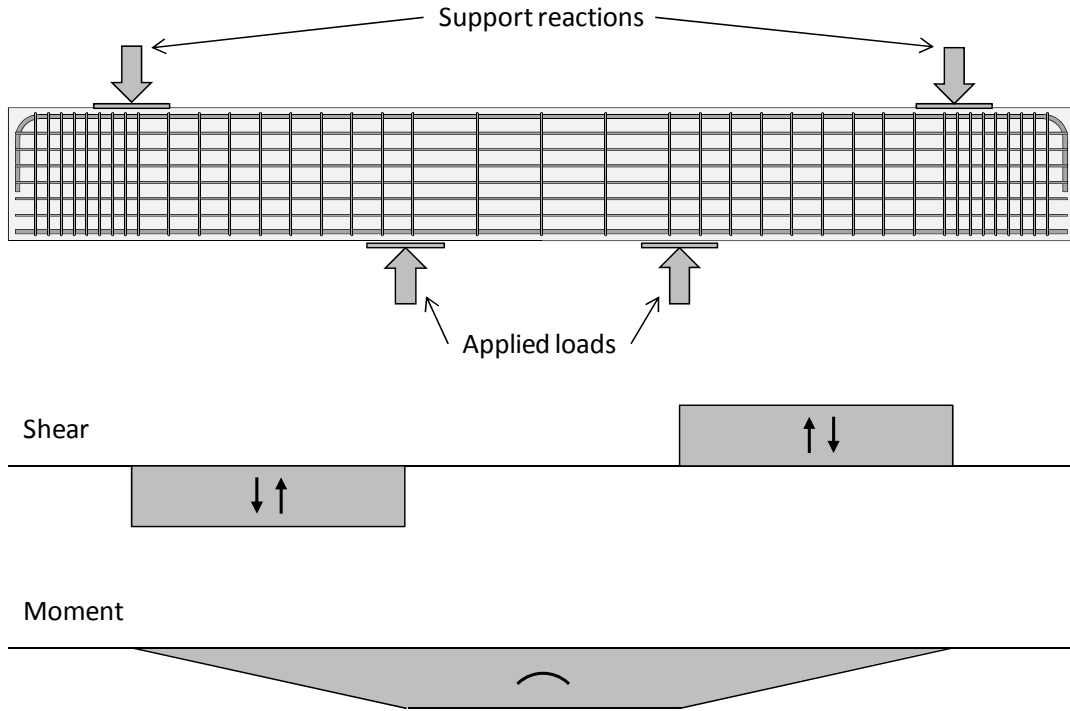


Figure 5.11: Loads and reactions (top) and shear and moment diagrams (bottom), from Kreitman 2011.

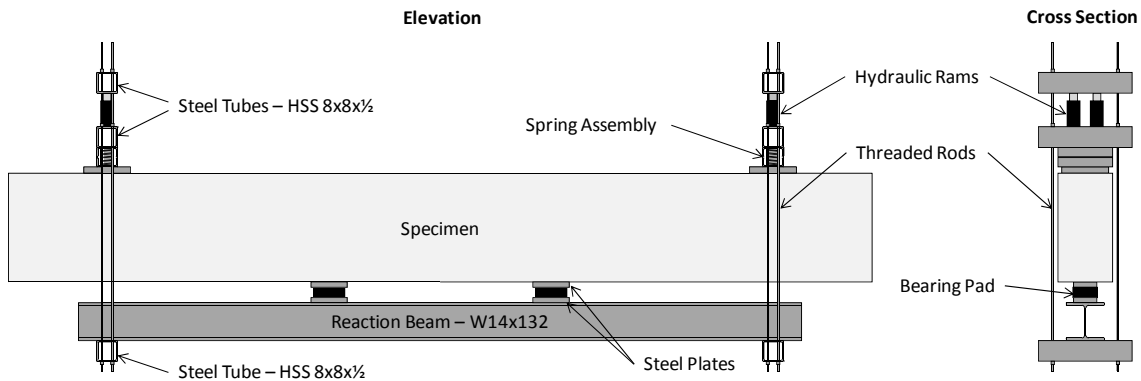


Figure 5.12: Load conditioning setup, from Kreitman 2011.

TxDOT bridge design specifications limit the unfactored dead load stress in tension reinforcement to 22 ksi (152 MPa) to minimize flexural cracking. To induce this stress in the flexural steel, loads of 80 kip (356 kN) each were applied. This resulted in some flexural cracking in the nonreactive specimen; no flexural cracks were observed in the reactive specimens. Since small expansions had already been recorded in the reactive specimens at the time of loading (0.05 to 0.06% transverse, 0.01 to 0.02% longitudinal), some post-tensioning may have occurred, increasing the cracking moment.

5.3 Experimental Procedures

This section will detail the procedures used for testing of the match-cured prisms (5.3.1) and in-situ monitoring of the full-scale beam specimens (5.3.2 and 5.3.3). Expansion measurements and resonant frequency testing were conducted on the match-cured prisms. The in-situ monitoring program for the beam consisted of expansion measurements and a variety of NDT methods. Visual observations and photographic records were also made periodically during the monitoring period.

5.3.1 Match-Cured Prisms

A total of eight match-cured prisms were fabricated along with each beam specimen. Four were instrumented with gauge studs at each end to facilitate expansion measurements in accordance with ASTM C1293 (2008). Four had flat ends to facilitate resonant frequency tests per ASTM C215 (2008).

All prisms were demolded after 24 h and initial expansion measurements were taken for the instrumented specimens after they had cooled to 73 °F (23 °C) in the moist curing room. All were then placed in storage conditions meeting ASTM C1293, in a sealed plastic bucket over water at 100 °F (38 °C). A wicking fabric around the edge of the bucket helped ensure a moist environment of >95% RH. Expansions were measured periodically (at 1, 2, 4, 8, 13, 26, 39, and 52 weeks of age). Figure 5.13 shows four prisms in a storage bucket and the wicking fabric, and a prism being measured for length change.

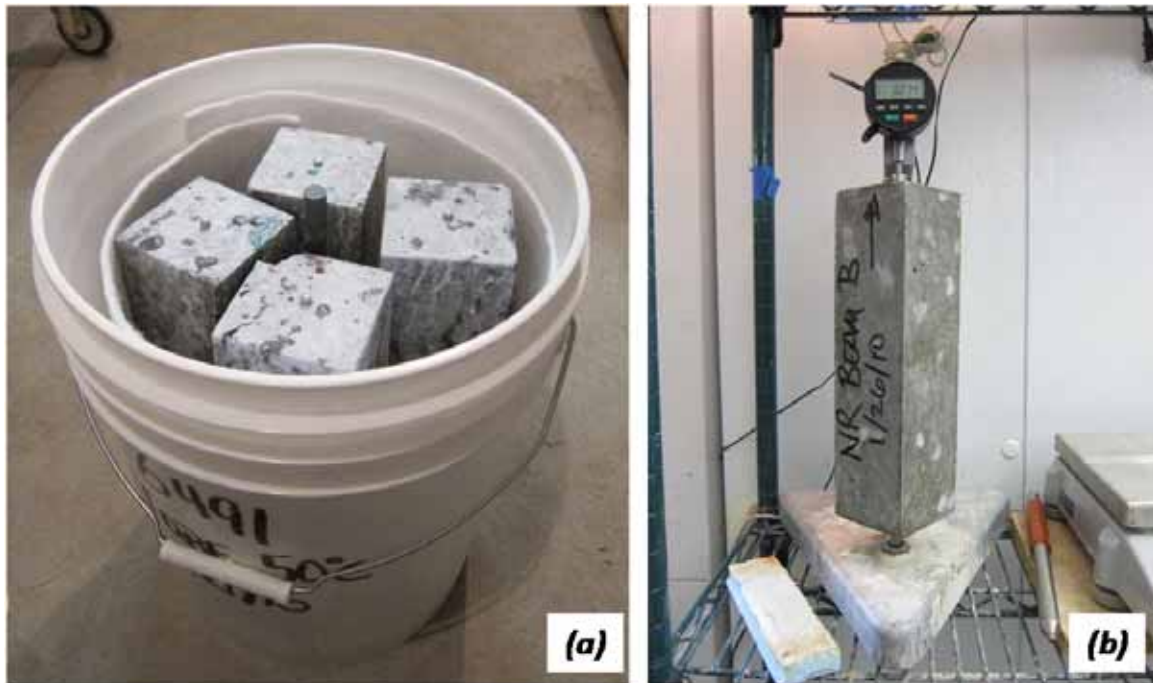


Figure 5.13: Match-cured prisms in storage bucket (a), and being measured for length change (b), from Kreitman 2011.

The ASTM C215 (2008) resonant frequency test was performed on the remaining four prisms to measure the change in dynamic elastic modulus caused by ASR and DEF. The test was performed on the same day as the expansion measurements. Expansions were thus assumed to be

the same as the average of the corresponding instrumented prisms, as all specimens were maintained in the same storage conditions. Both the longitudinal and transverse modes of vibration were tested, following the same procedure described in Chapter 3 (Section 3.2.5.2).

5.3.2 Expansion Monitoring

Expansion measurements of the full-scale beam specimens were conducted to quantify the degree of deterioration from ASR and DEF. The measurements tracked the expansion of both the concrete core and the reinforcement strain in selected locations, using the system of steel targets described in Section 5.2.1.3 and an extensometer with a 24-in. (610-mm) gauge length. The extensometer was connected to a National Instruments data acquisition system and the data recorded in a LabVIEW program. Figure 5.14 shows the measurement apparatus and the extensometer in use.

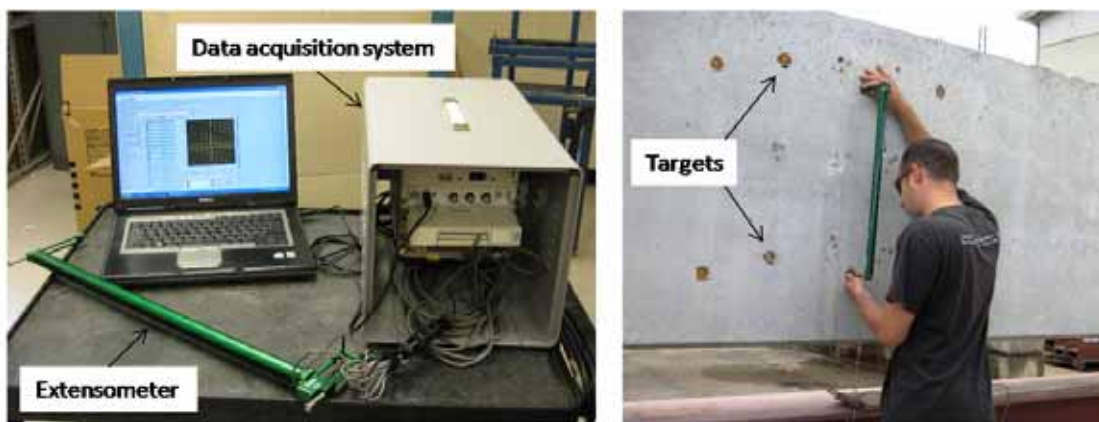


Figure 5.14: Expansion measurement system, from Kreitman 2011.

The locations of the expansion measurements and terminology regarding the measurements which will be used in discussing the in-situ monitoring results are shown in Figure 5.15. Both vertical and longitudinal core concrete expansions were measured on each side of the beams. Reinforcement strain measurements were taken vertically on the sides using targets welded to the stirrups and longitudinally on the top and bottom faces using targets welded to the primary tension and compression reinforcement, respectively. Transverse measurements were not taken on the top and bottom faces because the gauge length was greater than the 21-in. (533-mm) thickness of the beams. Although efforts were made to minimize climatic effects by taking measurements at moderate temperatures and without excessive sun exposure, the necessity of obtaining frequent measurements often required measurements in cooler or warmer than ideal temperatures. Measurements were therefore normalized to a temperature of 70 °F (21 °C) using a thermal coefficient of expansion of $5.5 \times 10^{-6} \frac{1}{^{\circ}\text{F}}$ ($9.9 \times 10^{-6} \frac{1}{^{\circ}\text{C}}$).

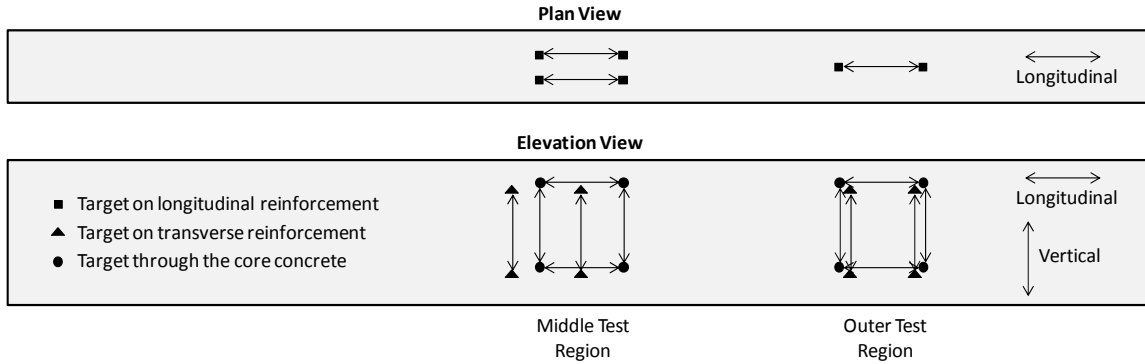


Figure 5.15: Expansion measurements and target locations, from Kreitman 2011.

5.3.3 In-Situ NDT

The in-situ NDT test program included four techniques that were also applied to the exposure blocks discussed in Chapter 3, including ultrasonic pulse velocity (UPV), impact-echo (IE), spectral analysis of surface waves (SASW) and surface wave transmission (SWT). For these techniques, only details specific to the beam specimens will be provided. Two additional methods were employed to a more limited extent: a nonlinear acoustic method developed at Université Sherbrooke, and an adaptation of the resonant frequency test, which will be referred to as full-scale dynamic testing.

5.3.4 UPV and Impact-Echo

UPV and IE measurements were taken at identical locations, shown in Figure 5.16. The through-transmission method, following ASTM C597 (2009), was used to measure travel times and calculate velocities both horizontally and vertically through the specimen cross section. Equipment and procedures are described in greater detail in Chapter 3 (Section 3.2.3.1). IE was performed using the equipment and procedures described in Chapter 3 (Section 3.2.3.2). The bottom face was not tested using IE because of limited space between the specimen and reaction beam.

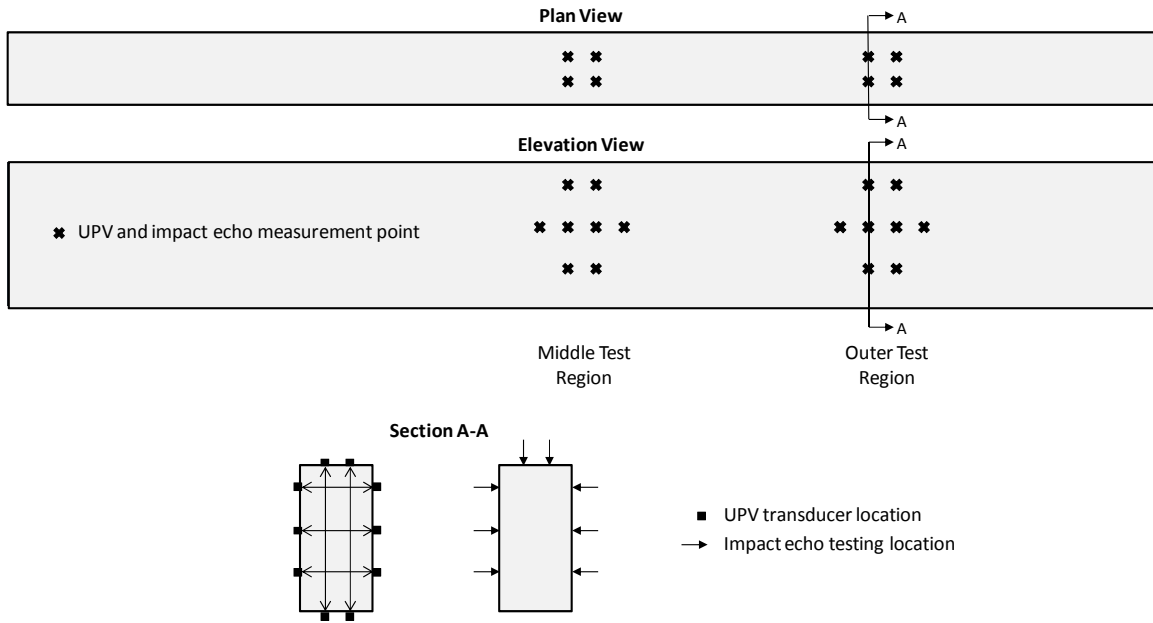


Figure 5.16: Locations of UPV and impact-echo measurements, from Kreitman 2011.

5.3.5 SASW and SWT

Surface wave measurements were conducted using non-contact sensors and procedures described in Chapter 3 (Section 3.2.3.3). The dimensions of the test grid are shown in Figure 5.17; four test grids were used per beam, each overlaid the UPV and IE test grids on the sides of the specimen. Five impacts were recorded at each location; 400 impacts were recorded each time a specimen was tested.

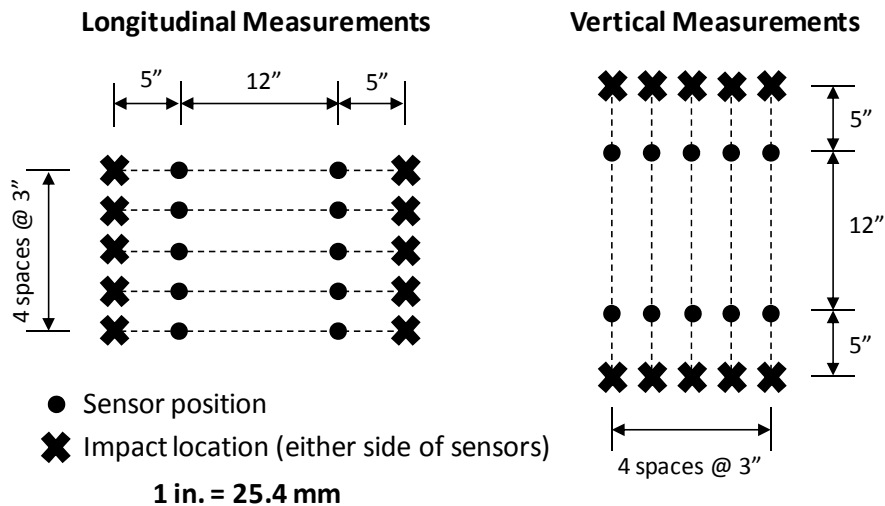


Figure 5.17: Schematic of surface wave test grid, from Kreitman 2011.

5.3.6 Nonlinear Acoustics

A nonlinear acoustic method recently developed at Université Sherbrooke (Kodjo, et al. 2009) was applied to the beam specimens. This method measures the nonlinear effects of a large (but non-destructive) impact on the travel time and amplitude of high-frequency compression waves. The impact causes microcracks in ASR-damaged concrete to open slightly, causing a delay in the arrival of the waves and reducing their amplitude. The tests were performed both by researchers from Université Sherbrooke and later by UT-Austin researchers trained on the technique by the Sherbrooke researchers. The technique is described in greater detail in the thesis of Kreitman (2011), who lead the UT-Austin testing effort.

Figure 5.18 shows the equipment and test configuration used by the UT-Austin team. Ultrasonic pulses were generated at 500 pulses per second using an Olympus square-wave pulser-receiver and transducers with a 250 kHz central frequency. Data were collected through with an 8-bit digital oscilloscope at a sampling rate of 31.25 MHz, and analyzed using a MATLAB program. A small sledgehammer provided the impact necessary to disturb the compression waves.

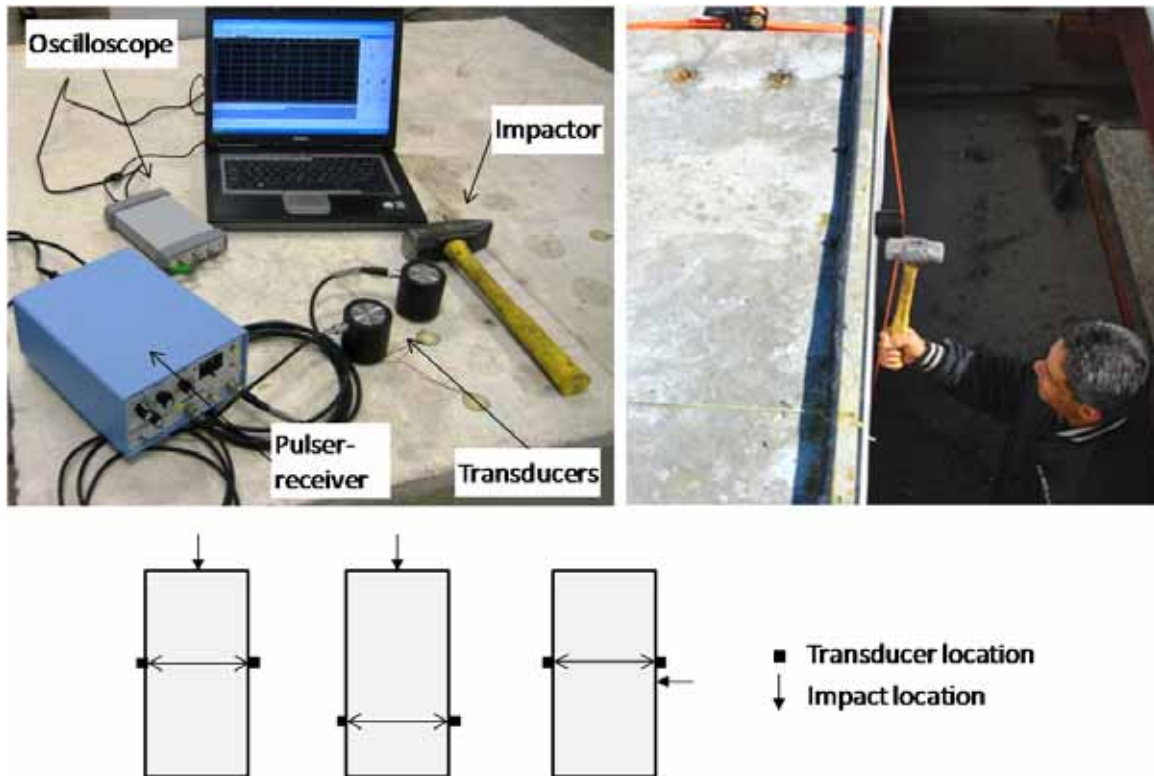


Figure 5.18: Nonlinear acoustic test setup for beam specimens, from Kreitman 2011.

5.3.7 Full-Scale Dynamic Test

The full-scale dynamic test is an adaptation of the ASTM C215 resonant frequency test. The goal of the test was to determine the dynamic stiffness of the entire beam. In contrast to the other NDT methods described in this section, which are more influenced by the local condition of the concrete, this test is global in nature. Because the entire specimen is tested, it should be

able to detect a change in stiffness resulting from ASR and DEF; since the reactive specimens are reinforced, the effects of confinement (self-post-tensioning) may be evident.

However, the test is also greatly influenced by boundary conditions (location of supports and restraints) and external loads, which can induce different modes of vibration than those which would be expected from a structure that is able to vibrate free of external constraints.

The beam specimens were tested both under the conditioning load and after the load was removed. In the latter state, the beams were simply supported on the pedestals at each end, with no other constraints, greatly simplifying interpretation of results. The same equipment was used as for the other resonant frequency tests described in this report, with one exception. The small steel ball impactor was replaced with a sledgehammer (Figure 5.19); a 4-in. (102 mm) diameter, 70-durometer Neoprene disc was affixed to the head of the sledgehammer to increase the contact time and lower the central frequency of the impact. The accelerometer data were sampled for 1.0 s and 10 kHz, providing a 1 Hz resolution for determination of the peak frequency.

Longitudinal vibrations were measured by impacting the beam at one end (Figure 5.19, left image) with the accelerometer located at the opposite end. Transverse vibrations were measured in two configurations: the first, with an impact on the top of the specimen at mid-span and the accelerometer located at one end on the top face; the second, with an impact on one side at mid-span (Figure 5.19, right image) and the accelerometer located on the same side at the end of the specimen. Three impacts were recorded for each configuration. A few tests were also performed in the transverse mode with the accelerometer located at one-fourth of the distance between the supports, but no useful data were obtained.



Figure 5.19: Impacts for dynamic testing of beam specimen.

5.4 Results and Discussion

This section presents the results of the match-cured prism tests and in-situ monitoring program for the full-scale beam specimens. The various test methods are evaluated for their ability to characterize the damage caused by ASR and DEF, as quantified by the measured expansions. With the exception of the full-scale dynamic test, these results either update or

repeat those reported in Kreitman's thesis (2011). For brevity, the reader will be referred to that document with regards to certain tests and analyses.

5.4.1 Match-Cured Specimens

Figure 5.20 shows the axial expansions of the instrumented match-cured concrete prisms stored over water at 100 °F (38 °C). The shaded areas represent the range of measurements in each group of four prisms, with the average denoted by a solid line. The prisms made with the nonreactive beam did not expand over the one-year monitoring period. The reactive prisms expanded considerably; average expansions at one year were 0.60% and 0.85% for prisms matched to the first and second reactive specimens, respectively. Both sets of reactive prisms exhibited similar behavior for the first three months; however, from that point they expanded at different rates. The prisms matched to the second reactive specimen expanded much more quickly, particularly from three to nine months of age. Since the specimens were almost identical except for their curing temperatures, the expansions suggest that the deterioration in the prisms matched to the second reactive specimen is a combination of ASR and DEF, while those matched to the first reactive specimen experienced deterioration from ASR alone.

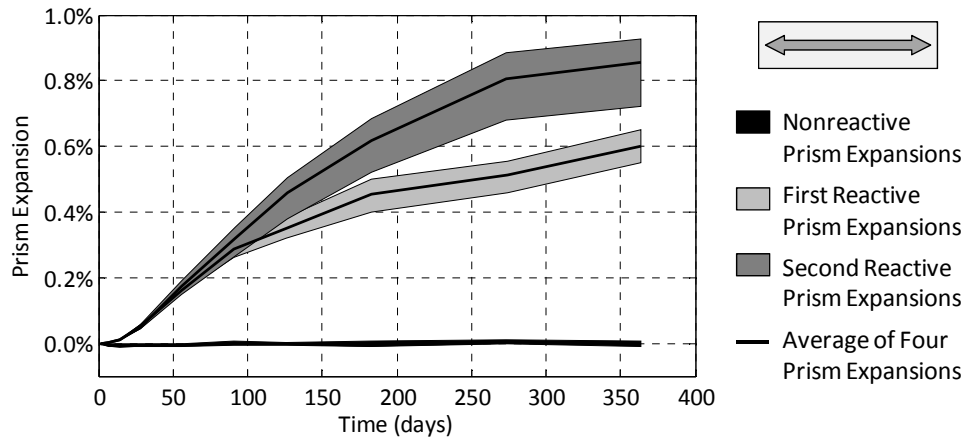


Figure 5.20: Expansions of match-cured prism specimens in ASTM C1293 conditions, from Kreitman 2011.

Results of the resonant frequency tests on the non-instrumented prisms, which were also stored over water at 100 °F (38 °C), are shown in Figure 5.21. The average dynamic elastic moduli of each set of four reactive prisms, calculated according to ASTM C215 (2008), are plotted against the average expansions of the instrumented prisms at the time of each test. Data from both tests of both the transverse and longitudinal modes are shown.

The nonreactive specimens were not tested for the first three months, but maintained average dynamic moduli ranging from 5250 to 5390 ksi (36.2 to 37.2 GPa) throughout the remaining monitoring period. The reactive specimens all exhibited a sharp decrease in dynamic modulus below 0.20% expansion; above 0.20%, there was very little change. A maximum decrease in dynamic modulus of 18% was measured in the transverse mode for the second reactive prisms. Overall, the two sets of reactive prisms showed similar moduli for a given amount of expansion. Although the values for the second reactive were slightly lower, the difference is not enough to distinguish between the two types of deterioration that the expansion measurements suggest have occurred.

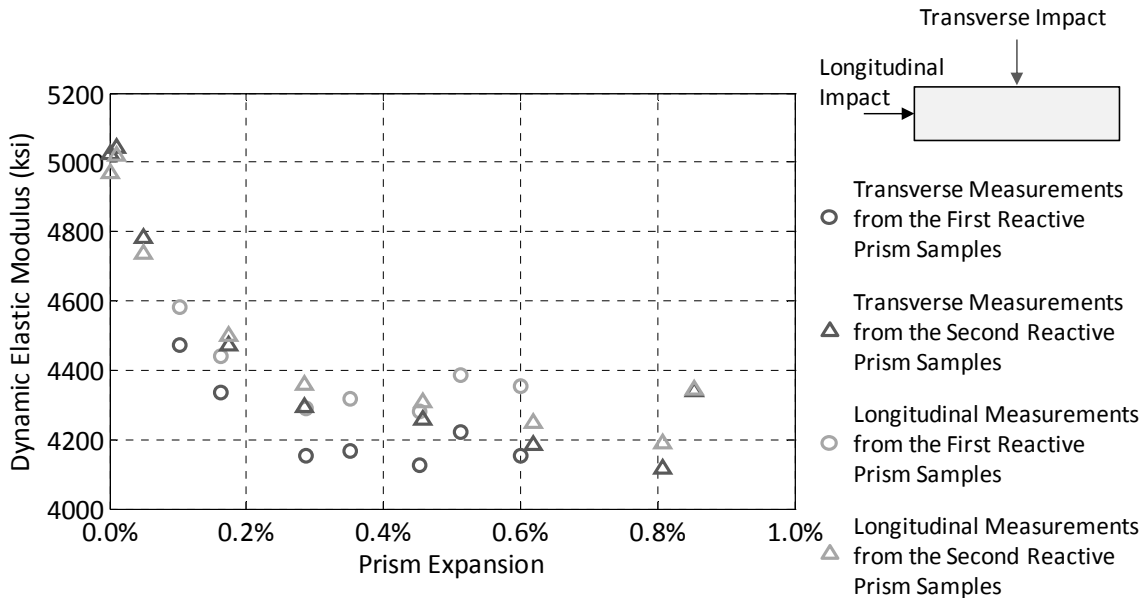


Figure 5.21: Average dynamic moduli of match-cured prisms vs. expansion, from Kreitman 2011.

The prisms matched to the second reactive specimen began to show a recovery in dynamic modulus between 0.80 and 0.85% expansion. These measurements were taken three months apart, and expansion had slowed significantly by this time. This concurrent recovery of stiffness is consistent with the pattern of results reported for ASR-affected cylinders made with Jobe (F1) sand in Chapter 4.

These results suggest that the resonant frequency test is most effective for quantifying the progress of ASR and DEF at lower levels of expansion. However, if a corresponding undamaged region of the structure can be found, the test may have some value in characterizing the extent of damage. Above 0.20% expansion, the moduli of the reactive prisms were 20% or more below the average values for the nonreactive prisms.

Finally, it should be noted that this test is only nondestructive to the prism; if a field structure were under investigation, this test would be performed on multiple core samples extracted from the structure. Not only does this require repairing holes left by the cores, but the removal of the core sample from the in-situ stress state reduces their representivity compared to the parent structure.

5.4.2 Visual Observations

Although not the focus of this research, informal visual observations of the deterioration of the reactive specimens were made throughout the monitoring period. Cracking of the reactive specimens was first noticed after just three weeks of outdoor exposure. Extensive cracking eventually developed on all faces of the reactive specimens, typically aligned with the primary reinforcement—a common feature of ASR in reinforced structures.

Figure 5.22 shows the condition of the second reactive specimen at an age of one year. The aligned cracking pattern is clearly evident in Figure 5.22a, which focuses on the middle (constant moment) test region; cracks have been highlighted for clarity, as the maximum crack widths were only 0.025 in. (0.64 mm). Heavy staining is also evident in this photograph, as is the

presence of white reaction product. The end face of the specimen, shown in Figure 5.22b, exhibited much wider cracks—up to 0.25 in. (6.4 mm). Cracks were not artificially highlighted in this photograph. This cracking can be explained by the facts that the ends of the specimens were not exposed to the moisture conditioning and also lacked shear reinforcement. Stirrups were terminated 8.5 in. (216 mm) short of the end face to accommodate the 90-degree hooks in the tension reinforcement. A large horizontal crack on the end face corresponds to the location of the end of the tension steel hook.

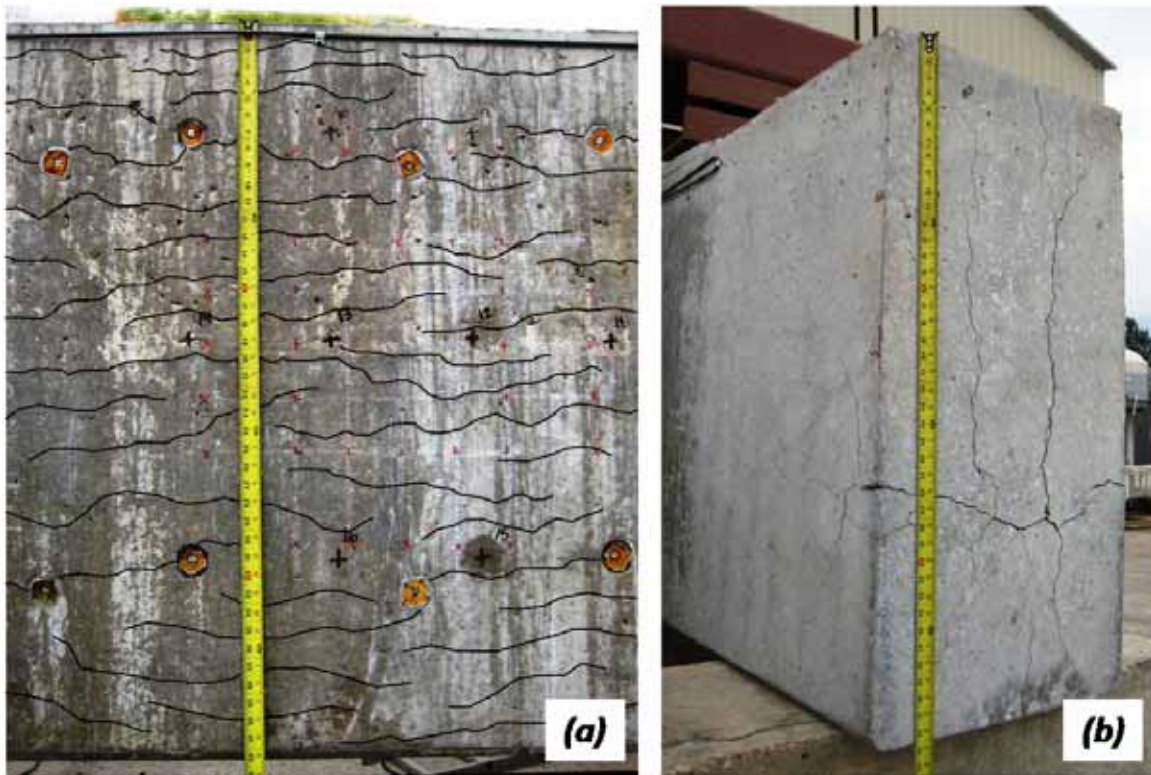


Figure 5.22: Cracking of second reactive specimen at one year of age, from Kreitman 2011.

5.4.3 Expansions

Figure 5.23 presents the expansions of all three specimens with time for each of the two test regions. In each plot, both the vertical and longitudinal expansions are shown. The shaded regions represent the range of measured expansions in each direction, with a solid line representing the average expansion. A dark, dashed line represents the yield strain of the shear reinforcement, as determined by tension tests performed on coupon samples of #5 bars shipped with the stirrups. The times at which moisture and load conditioning began are also noted in each plot. Reactive specimens were stored indoors until initial expansion measurements. No prior expansion is expected to have occurred.

Figure 5.23 shows that the nonreactive specimen did not experience significant expansion—less than 0.02% on average. The greatest expansion was measured in the vertical direction in the middle test region—an average of 0.048% over the monitoring period. However, this specimen also had the longest pre-moisture conditioning period, and clearly responded to the

start of the wetting cycles. The measured “expansion” was more likely a recovery from initial drying shrinkage than an indication of ASR.

Both reactive specimens expanded significantly, primarily in the vertical direction, and more so in the middle test region. Given the relative reinforcement ratios ($\rho_v = 0.15$ and 0.31% in the middle and outer test regions, respectively, and $\rho = 2.2\%$ in the longitudinal direction), this was expected. While the stirrups were strained well beyond their yield point, the majority of the primary reinforcement was not yielded. In the middle region of the second reactive specimen, a few longitudinal expansions were in excess of the yield strain, although on average the longitudinal expansion of this specimen was greater in the outer test region (0.188% vs. 0.156%).

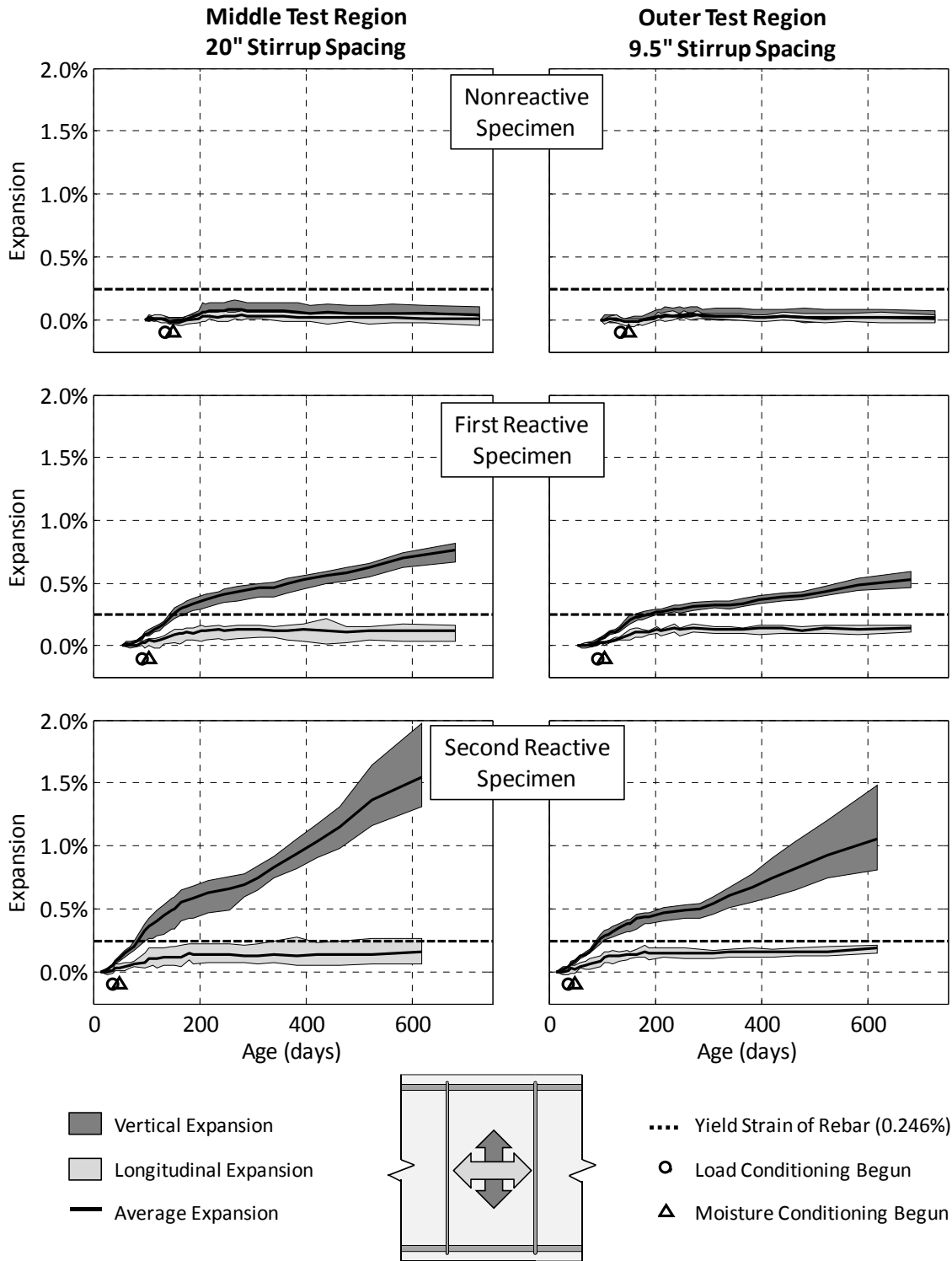


Figure 5.23: Expansions for beam specimens.

The second reactive specimen also expanded approximately twice as much as the first reactive specimen. The disparity in expansions was even greater than was measured for the match-cured prisms. This, combined with the curing temperature history of the specimens,

suggests that the second reactive specimen most likely was affected by a combination of ASR and DEF, while the first reactive specimen was only affected by ASR. A petrographic investigation of core samples can help to confirm whether this is the case, and is discussed in Chapter 6.

5.4.4 In-Situ NDT

The results of the in-situ NDT monitoring program are presented here, as well as an assessment of the ability of each test method to characterize deterioration due to ASR and DEF. Following the work of Kreitman (2011), deterioration is quantified by expansion in the vertical direction for each test region. This was deemed to be the most representative indication of the extent of ASR and DEF in the concrete. The test results of the reactive specimens are also compared to those of the nonreactive specimens. A field structure under investigation is likely to contain regions exhibiting various degrees of distress, and an undamaged portion of the structure may be available for testing, which can provide a baseline for comparison with tests of the damaged regions.

UPV

Results of the UPV testing are presented in Figure 5.24, with compression wave velocity plotted against vertical expansion. Each datum represents the average velocity measured in the horizontal or vertical direction through the cross section in either the middle or outer test region.

Velocities measured for the nonreactive specimen are not shown, but fluctuated between 4225 and 4370 m/s during the monitoring period (approximately $\pm 2\%$ from the mean). The fluctuations were minor and would be expected as a result of environmental fluctuations in good quality concrete. These velocities are very similar to the initial (undamaged) velocities of the reactive specimens.

Velocities of the reactive specimens both initially decreased rapidly with the onset of expansion; the horizontal velocities decreased 4 to 8% between the initial and second measurements. Vertical expansions at the second measurement ranged from 0.036% to 0.058%. Velocities then decreased at a slower rate, with the maximum decrease in horizontal velocity relative the initial measurements reaching 14% for the first reactive specimen (near reinforcement yield) and 18% for the second reactive specimen. At 0.1% expansion, velocity decreases were 9% for the first reactive specimen and 7% for the second reactive specimen. For expansions in excess of the reinforcement yield strain, the velocities of the first reactive specimen were essentially constant; the second reactive specimen exhibited a continued loss of velocity but at an extremely slow rate.

The results are consistent with reports in the literature, but at odds with the results of UPV tests on the Jobe (F1) exposure blocks discussed in Chapter 3. The exposure blocks affected by ASR and DEF exhibited less decrease in velocity compared to those affected only by ASR. In contrast, the second reactive beam specimen, which is thought to have been affected by ASR and DEF, exhibited a greater velocity decrease than the first reactive beam specimen, which is likely only affected by ASR.

The velocity distribution was also directly related to the distribution of curing temperatures in the specimens; the lowest velocities were measured through the middle of the specimens, which had experienced the highest curing temperatures. This disparity in velocities grew as the specimens expanded. For the second reactive specimen, velocities through the top of

the specimen were initially 48 m/s greater than through the middle; this increased to 407 m/s by the conclusion of the monitoring period.

The vertical velocities were typically lower than the horizontal velocities, although this is potentially in part a systemic error. Velocities were calculated based on a nominal dimension of 42 in. (1067 mm) because it was not possible to measure the actual length between each set of transducer locations. The actual depth of the beams may have been slightly larger, and Kreitman (2011) notes that a 0.25 in. (6.4 mm) difference in height would result in apparent velocity change of 25 m/s.

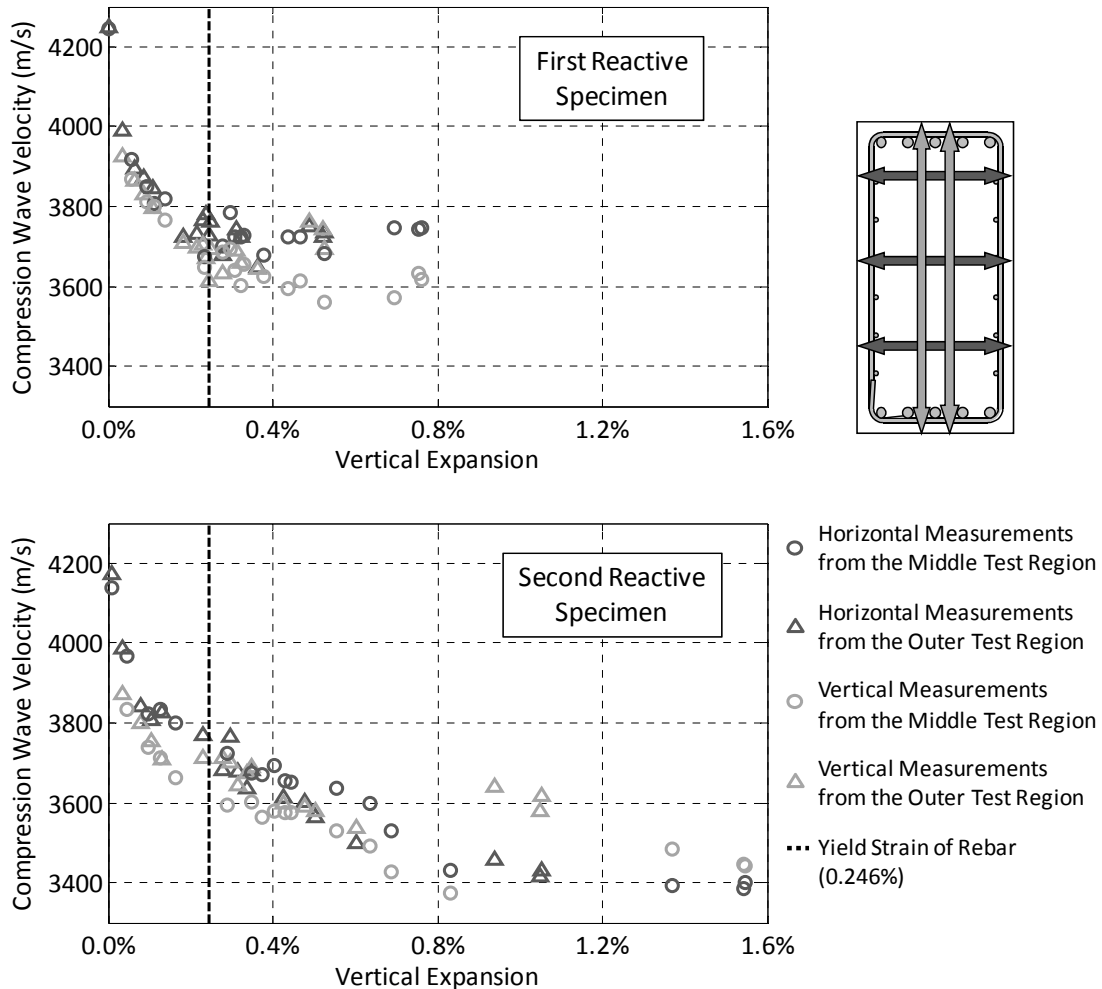


Figure 5.24: UPV vs. vertical expansion of beam specimens.

The results of the UPV testing highlight its utility for evaluating structures affected by ASR and DEF, as well as the difficulties in applying this technique for that purpose. Unless a structure is monitored from the time of construction, it will be very difficult to quantify deterioration through long-term monitoring with UPV. Once expansions are severe enough to prompt an investigation (around 0.10%), a significant portion of the loss of velocity will have already occurred. Future changes will often be within the range of normal fluctuations from

environmental effects. However, if an undamaged portion of the structure (or a similar but undamaged structure) can be tested for comparison, then UPV may contribute to a more holistic evaluation of the structure, in combination with other test methods.

Several other points should be noted with regards to the UPV results and the evaluation of structures. First, this technique can only show that the concrete is damaged. It cannot identify the cause of deterioration. Second, the rate of expansion of the specimens in this study was much faster than would be experienced in the field. Several years or more of monitoring would be required if the goal was to determine the rate of deterioration using this technique. Third, UPV appears to correlate best to the average expansion, rather than the expansion in a particular direction, which may be of more interest for reinforced structures experiencing anisotropic expansion. While this was difficult to show using these results, the results of the reinforced exposure blocks discussed in Chapter 3 support this conclusion. A satellite study associated with this project using also showed similar results when comparing UPV and expansion in all three axes for 48 in. (1219 mm) long specimens with identical cross sections and reinforcing details as the specimens described in this chapter (Webb 2011).

5.4.5 Impact-Echo

Two types of impact-echo analyses were performed: time domain analysis of the attenuation of reflected waves and frequency domain analysis. Time domain analysis did not yield useful data, as even small variations in the length of signal was analyzed completely overwhelmed actual variations in the signal caused by damage to the concrete. A more complete discussion of the technique can be found in Kreitman's thesis (2011). Results of the frequency domain analysis will be discussed in this section.

In order to analyze the impact-echo signal in the frequency domain, the frequency spectrum was calculated and plotted from the time domain signal. Figure 5.25 shows typical frequency spectra for each of the three beam specimens. From the frequency spectrum, the peak, or strongest frequency, can be identified. This corresponds to the echoing of the compression waves through the concrete, and if the thickness is known, the compression wave velocity can be calculated. Concrete affected by ASR and DEF has a lower compression wave velocity, as shown by the UPV results; this will correspond to a decrease in the peak impact-echo frequency, which can clearly be seen in Figure 5.25.

The frequency spectrum can also be examined for the presence of small, high frequency peaks that may be generated by internal cracks, as the shorter distance to the cracks result in more frequent echoes if the crack is large enough (Henriksen 1995). In Figure 5.25, these are not particularly evident, although the peak frequencies are of reduced amplitude after 8-12 months of conditioning. This is true for both the nonreactive specimen, which developed several flexural cracks after the application of load, and the two reactive specimens.

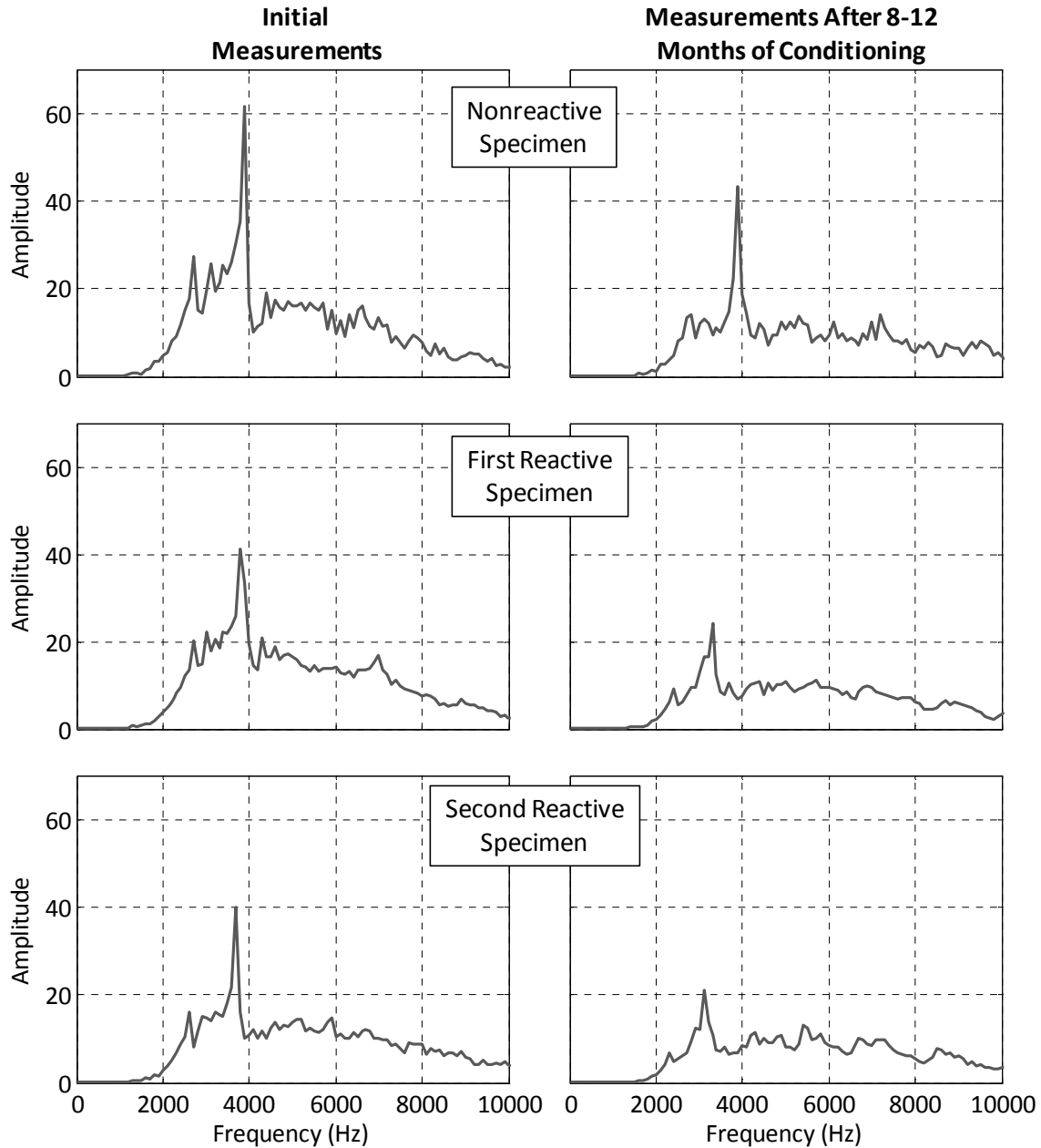


Figure 5.25: Typical impact-echo frequency spectra for beam specimens, from Kreitman 2011.

The shift in the peak frequency with increasing deterioration appeared to be the most useful parameter from the test. Data obtained from the middle row of each test region was the most useful, and the compression wave velocity was calculated using the peak frequency and a nominal specimen thickness of 21 in. (533 mm). Data were averaged for the eight points in each test region (four on each side of the specimen). Figure 5.26 shows the average compression wave velocities of the reactive specimens plotted against vertical expansion.

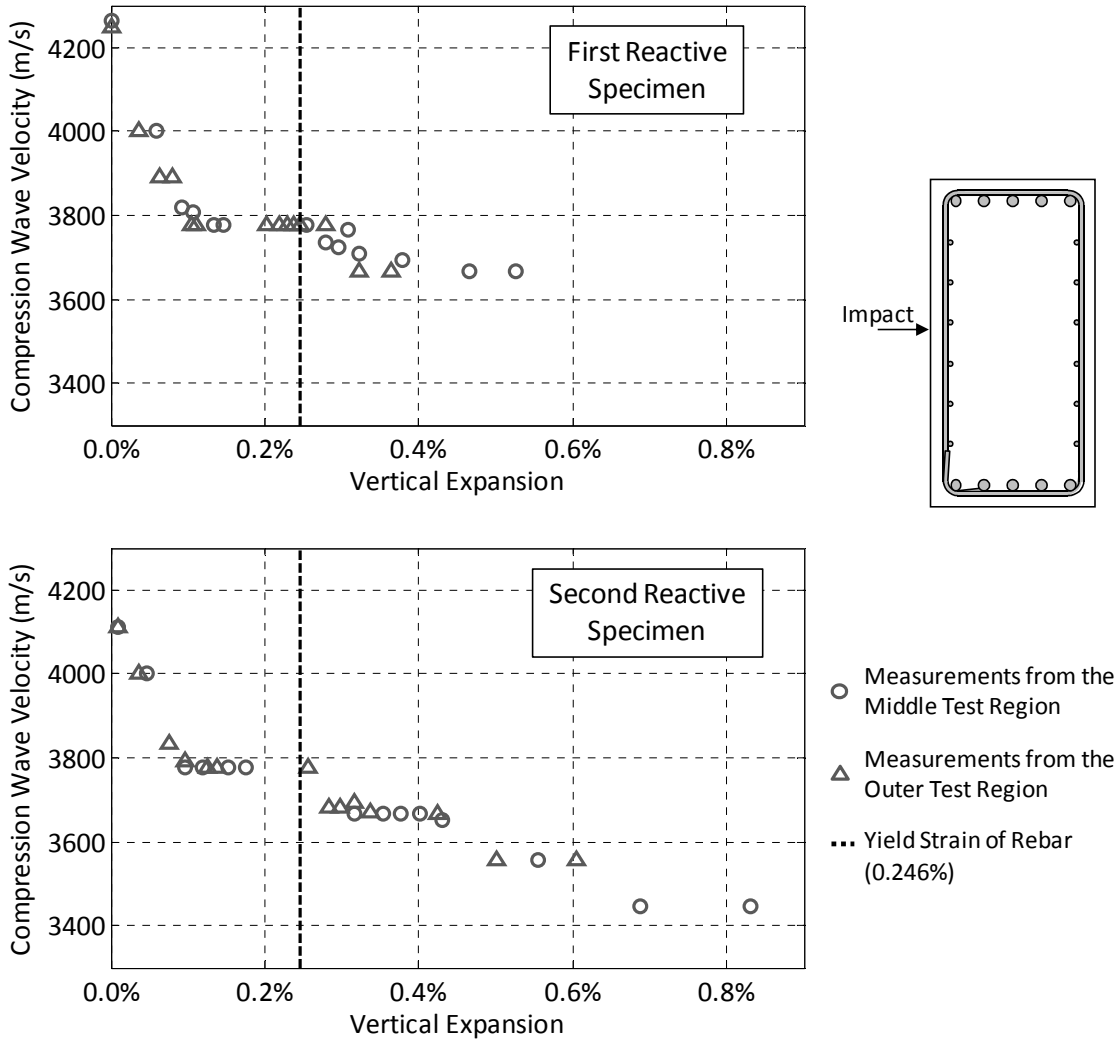


Figure 5.26: Compression wave velocities vs. vertical expansion of beam specimens, ($1 \text{ m/s} = 3.28 \text{ ft/s}$), from Kreitman 2011.

The results are almost identical to the trends reported for UPV. The monitoring period of impact-echo was shorter than for UPV, so the highest expansions are not included. It should also be noted that the frequency resolution was 100 Hz, which contributed to the stair-step nature of the plots. The velocities calculated for the nonreactive specimen ranged from 4220 to 4390 m/s over the monitoring period, which compares well with the range calculated from the UPV tests. Figure 5.27 shows the UPV and impact-echo test results for the second reactive specimen side-by-side. Here, it can be clearly seen that the two tests provide nearly identical results for a given level of expansion.

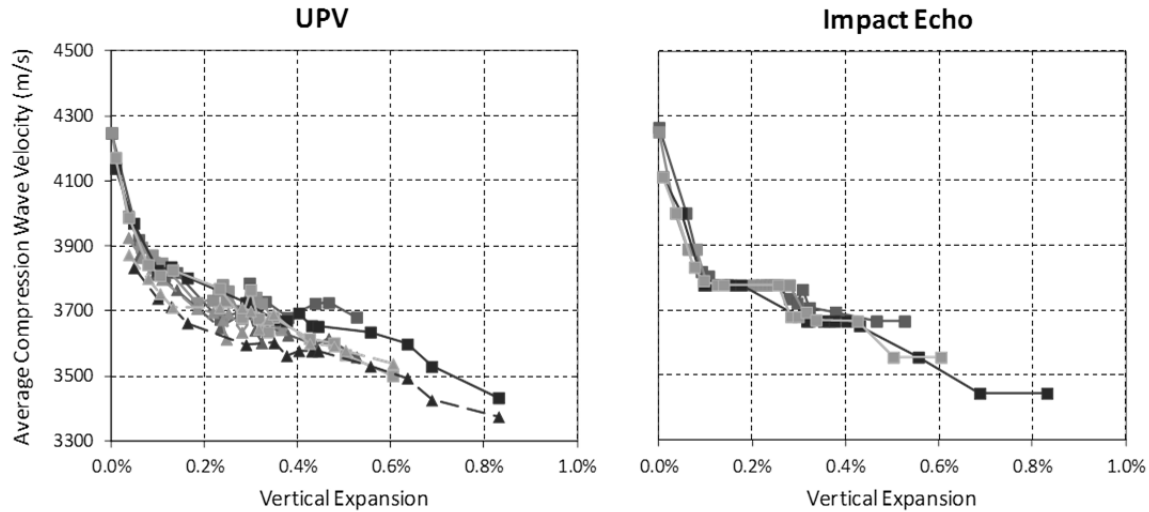


Figure 5.27: Compression wave velocities from UPV and IE testing of second reactive specimen ($1 \text{ m/s} = 3.28 \text{ ft/s}$).

Although both UPV and impact-echo both provide similar compression wave velocities, UPV remains the simpler test to perform. However, for some field structures, through-transmission UPV cannot be performed. This could be because one side of the structure is not accessible, or because the attenuation of the UPV signal is too great (as happened with the slab and deck specimens discussed in Chapter 3). If this is the case, impact-echo would be an acceptable means of determining the compression wave velocity. With regards to evaluating structures specifically affected by ASR and DEF, the same recommendations and caveats stated for UPV apply to impact-echo.

5.4.6 SASW and SWT

Surface wave test data were analyzed using two techniques: SASW and SWT. The analyses were previously reported by Kreitman (2011); they are discussed here for completeness.

The SASW method extracted the surface wave phase velocity at a frequency of 16 kHz, which was the approximate central frequency of the received signals. In each test region, the data from all 100 tests in the vertical or longitudinal direction were averaged.

Figure 5.28 shows the SASW results for the two reactive specimens, with the average surface wave velocity plotted against vertical expansion for each test region. A sharp drop in velocity is observed for both specimens, up to approximately 0.10% expansion. For higher expansions, there is no discernible trend in the data. At all levels of expansion, the surface wave velocity is higher in the longitudinal direction than in the vertical direction. Although this is the opposite of what was seen in the UPV data, it is not surprising. Surface cracking was generally aligned with the longitudinal reinforcement, which means that surface waves traveling in the vertical direction had to cross many more cracks than those traveling longitudinally. This would be expected to reduce the velocity of waves in the vertical direction, but not those moving in the longitudinal direction.

The sensitivity of surface wave velocity to cracking is also illustrated in Figure 5.29, which plots the surface wave velocity against time. A dashed line indicates the start of load conditioning, which was noted to have caused flexural cracks. Several of these cracks penetrated

the middle test region, crossing the longitudinal lines of the testing grids. In this figure, a 5% decrease in longitudinal surface wave velocity can be seen after the application of external load. A subsequent recovery of the velocity loss was also observed, although the reasons for this are not clear.

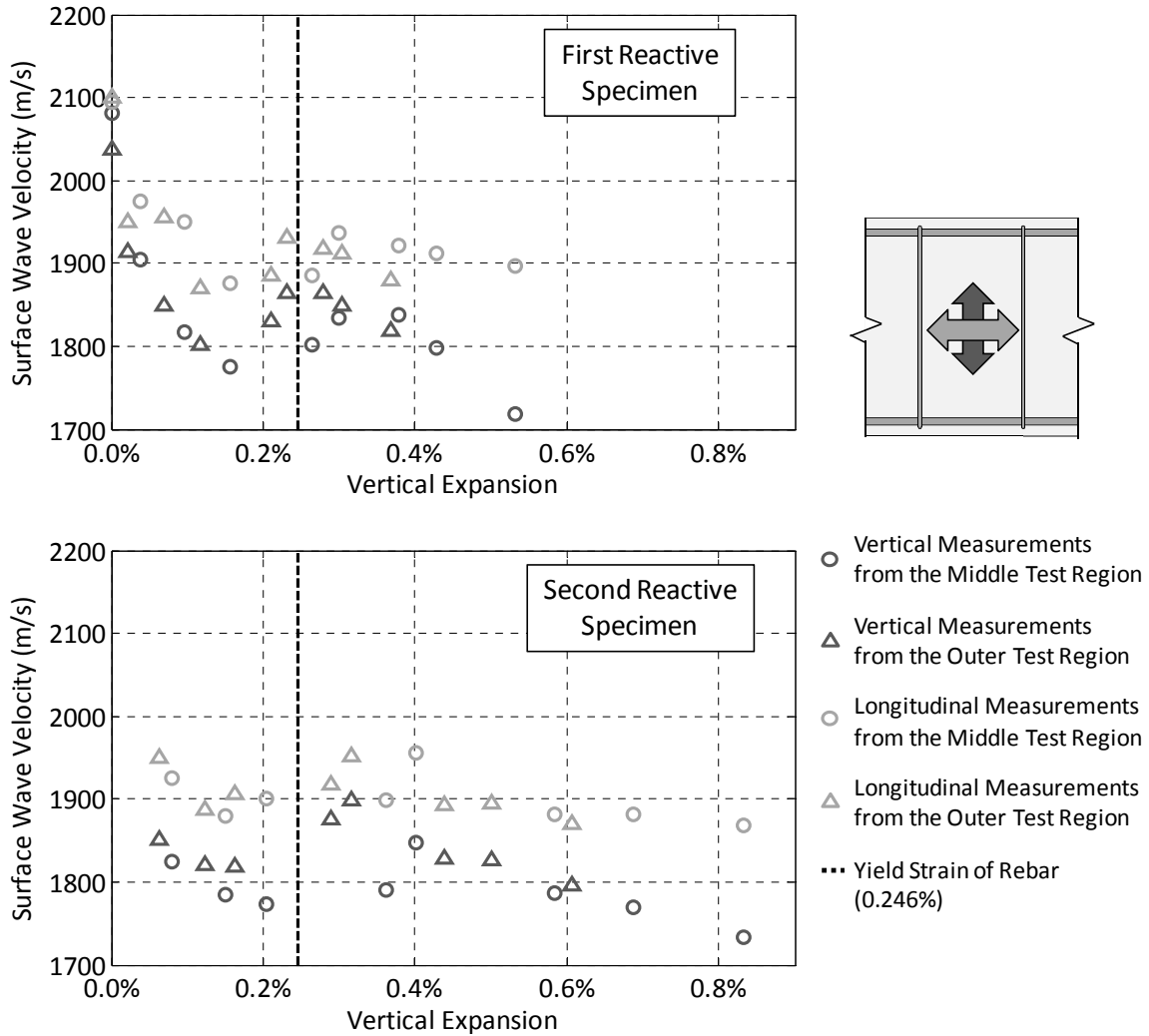


Figure 5.28: Surface wave velocity vs. vertical expansion of beam specimens, (1 m/s = 3.28 ft/s), from Kreitman 2011.

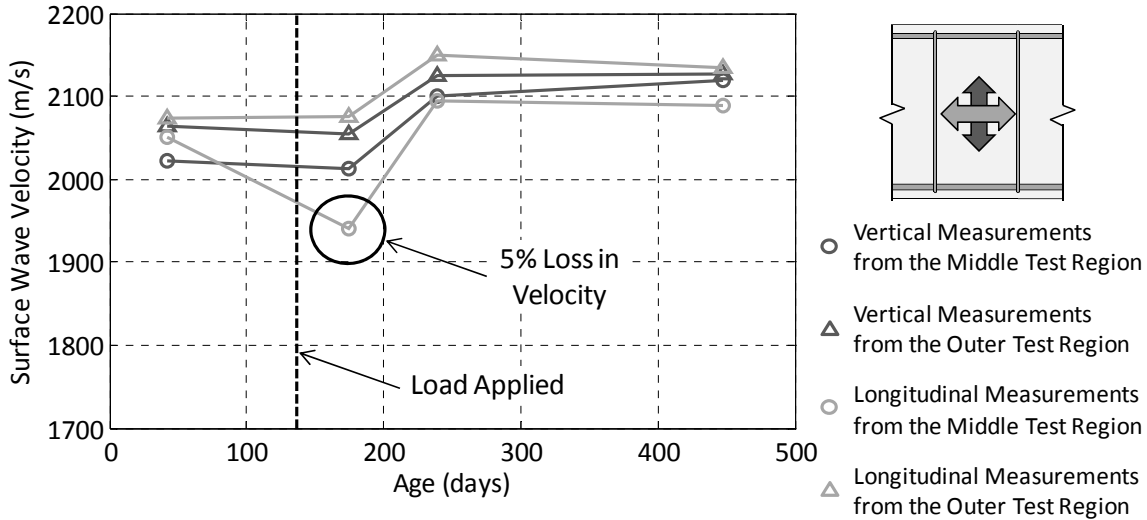


Figure 5.29: Surface wave velocity vs. time for nonreactive specimen ($1 \text{ m/s} = 3.28 \text{ ft/s}$), from Kreitman 2011.

The SWT method compares the energy transmission between the two sensors. A transmission coefficient is calculated, and is simply the ratio of the energy received by the two sensors at a specific frequency. For the beam specimens, the transmission coefficients were calculated at 16 kHz, and averaged for all vertical or longitudinal sensor locations in each test region.

Figure 5.30 presents the SWT results for the two reactive specimens. The average transmission coefficients in each direction for the two test regions are plotted against vertical expansion. Unlike the SWT analysis presented in Chapter 3, the transmission coefficients were not normalized, although the theoretical coefficient for an undamaged material is shown as a dashed horizontal line. No trends can be discerned from this figure, except that the longitudinal coefficients are higher than the vertical coefficients—most likely for the same reason as the surface wave velocities. The data are widely scattered, much as was noted for the Jobe (F1) exposure blocks in Chapter 3.

Figure 5.31 shows the transmission coefficient plotted against time for the nonreactive specimen. The impact of the flexural cracks caused by the application of external load is significant. A 20% decrease in the transmission coefficient occurred after the load was applied, clearly indicating the formation of a crack. The decrease in the transmission coefficient was not sustained and eventually fully recovered with time.

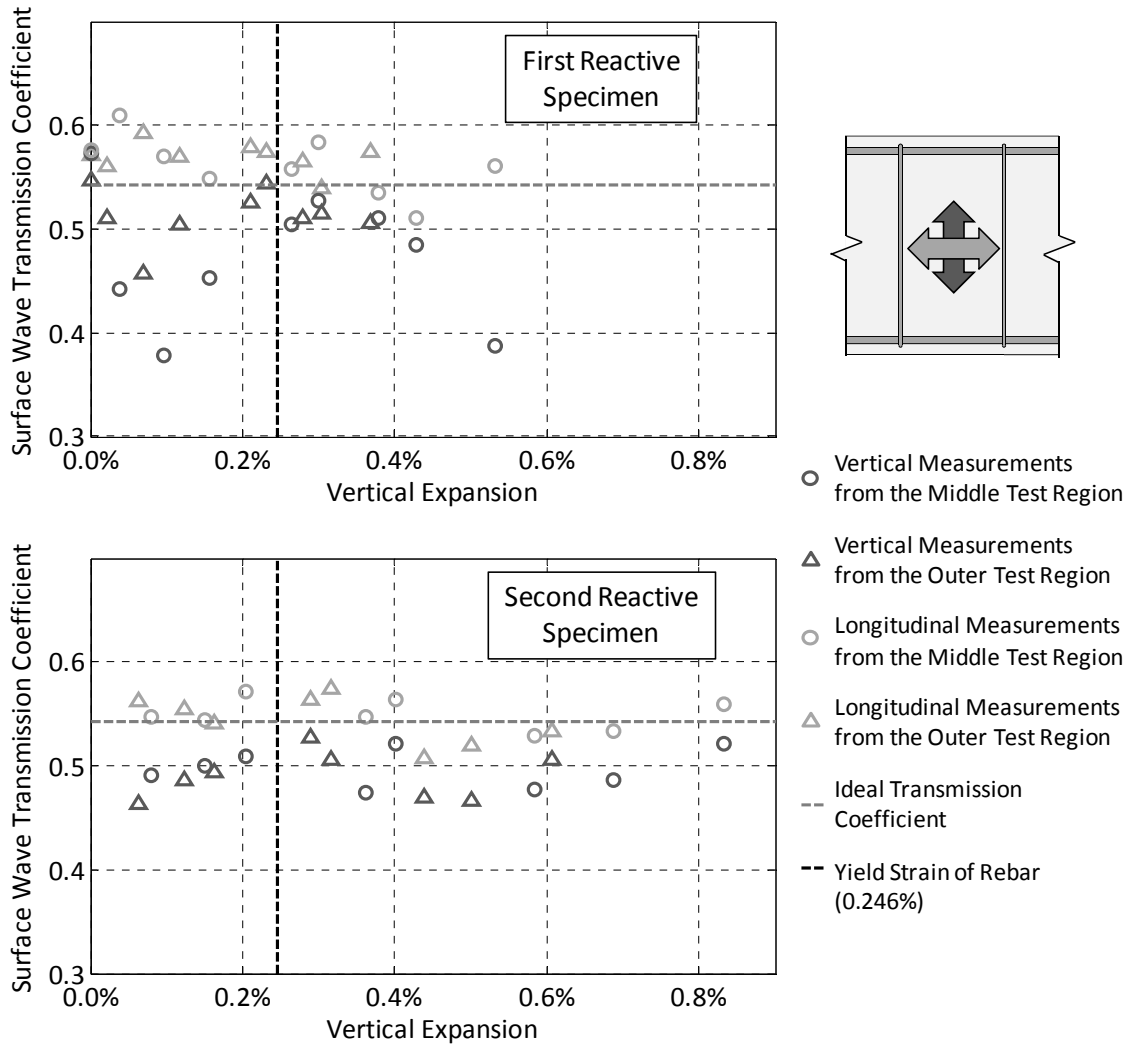


Figure 5.30: Surface wave transmission coefficients vs. vertical expansion of beam specimens, from Kreitman 2011.

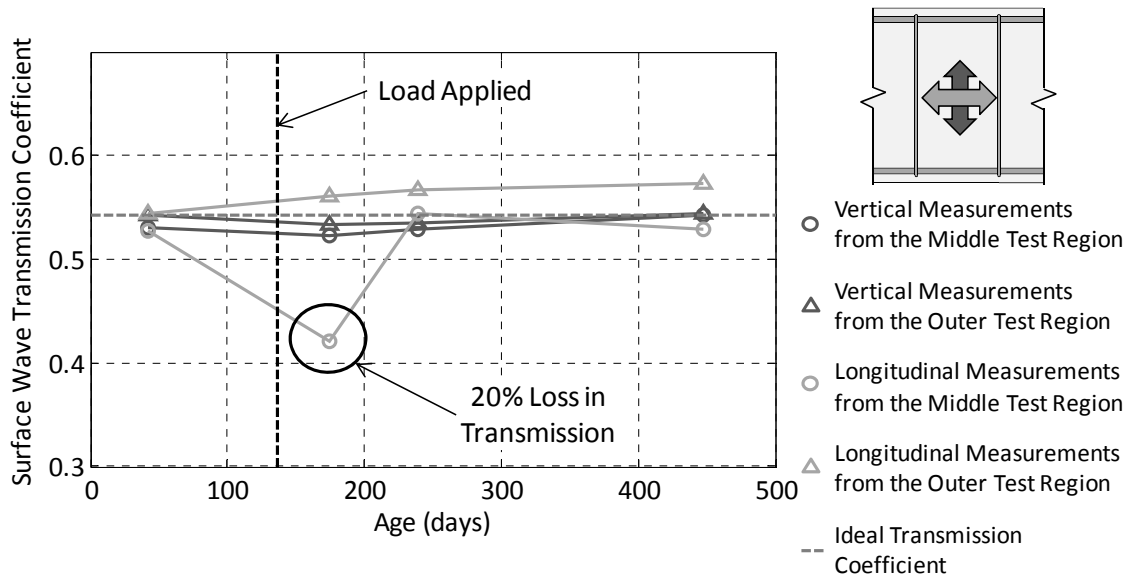


Figure 5.31: Surface wave transmission vs. time for nonreactive specimen, from Kreitman 2011.

The SASW and SWT results show that these methods are not suited to quantifying distress due to ASR and DEF. As noted in Chapter 3, the near-field effect may be responsible for the poor performance of these methods, particularly analysis using SWT. This effect can amplify or cancel out surface waves through interactions with waves reflected off cracks. The distribution of cracking characteristic of ASR and DEF makes it difficult to locate sensors and impacts a sufficient distance from cracks to avoid near-field effects.

5.4.7 Nonlinear Acoustics

The results of nonlinear acoustic testing of the full-scale beam specimens and the time shift method of analysis are detailed in (Kreitman 2011). Testing was hampered by the fact the data acquisition equipment was not capable of capturing the necessary signal data. Only a few tests were performed, and none during the early stages of expansion, when this test is expected to be most sensitive.

The benefit of this type of testing, if it can be developed for field use, is that they are much more sensitive to deterioration than linear methods, such as UPV. This translates to a reduced reliance on undamaged baseline values, which can be very valuable in field investigations where no undamaged areas are available for testing.

5.4.8 Full-Scale Dynamic Test

Full-scale dynamic test results were analyzed in the frequency domain. The peak frequency was identified for each impact to the nearest 1 Hz, and the results averaged for all three impacts. Next, the dynamic elastic modulus of the specimen was calculated using the formulae in ASTM C215 (2008) for the longitudinal and transverse modes of vibration. Since the specimens were supported at each end, rather than as specified by ASTM C215, it is possible that this analytical procedure was not entirely correct. Even if the dynamic moduli are incorrect, the frequency peaks are worth examining.

Table 5.2 presents the results of tests performed on all three specimens after the removal of the conditioning load prior to final structural testing. While tests were also conducted while the structure was under load, this represents the simplest analytical scenario possible. Longitudinal mode and transverse mode (side impact only) results are shown. Transverse mode tests with impacts on the top face of the beam gave inconsistent results that were difficult to interpret and are not shown. Figure 5.32 shows a representative set of frequency spectra generated by the longitudinal mode (end impact) tests on all three specimens. Although there was some variation in amplitude from one impact to the next, the peak frequencies identified in the analyses were consistent.

Table 5.2: Full-scale dynamic test results after unloading of beams.

Specimen	Longitudinal Mode Peak Frequency (End Impact)	E_d ksi (MPa)	Transverse Mode Peak Frequency (Side Impact)	E_d ksi (MPa)
Nonreactive	210 Hz	4380 (30.2)	25	3770 (26.0)
First Reactive	224 Hz	4980 (34.3)	26	4080 (28.1)
Second Reactive	213 Hz	4520 (31.1)	25	3770 (26.0)

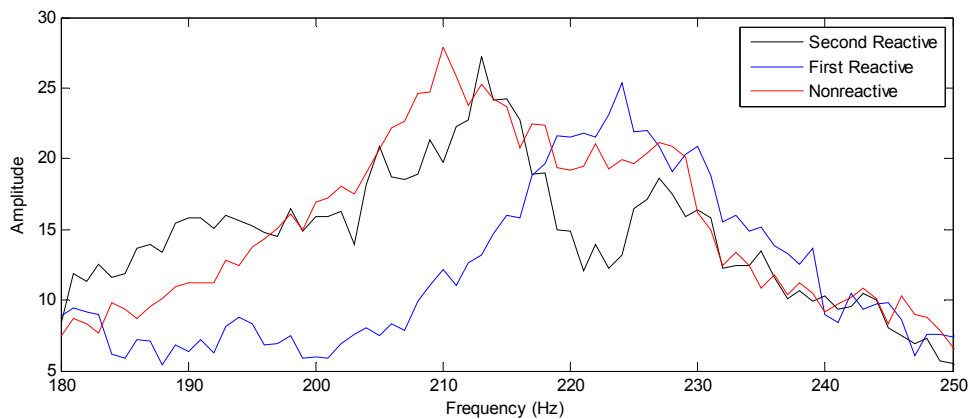


Figure 5.32: Representative frequency spectra for longitudinal mode dynamic tests.

The longitudinal mode results suggest that the two reactive specimens may have experienced some self-post-tensioning as a result of their expansions from ASR and DEF. They both have higher peak frequencies than the nonreactive specimen, indicating a higher stiffness. The dynamic modulus of the first reactive specimen was calculated to be over 13.7% *greater* than that of the nonreactive specimen. In comparison, the dynamic moduli of the match-cured prisms from the first reactive specimen were as much as 21% *below* the mean for the nonreactive prisms.

The results of the transverse mode tests were less conclusive. The peak frequencies of all three specimens were within 1 Hz of each other. Once again, the first reactive specimen exhibited the greatest stiffness. However, it is clear that a higher frequency resolution is needed.

The general consensus in the literature is that ASR and DEF induce self-post-tensioning of reinforced structures. It seems likely that this test has the potential to detect the stiffening of

the structure that would result. Flexural load testing, discussed in Chapter 7, will test the validity of the full-scale dynamic test results. However, this test is a long way from being field-ready. Real structures are more complicated and will be subject to more complex boundary conditions that impose constraints on their resonant behavior. Computer models would be needed to determine the expected modes of vibration and analyze the test results on actual field structures.

5.5 Summary

Three full-scale reinforced concrete beam specimens were fabricated and subjected to a conditioning regime that produced rapid expansion due to ASR and possibly, DEF, in two specimens. The specimens were monitored for up to two years to measure expansions, and evaluate the applicability of several NDT methods for characterizing the damage to ASR and DEF affected structures.

The expansions of the reactive specimens and their companion match-cured prisms suggest that the first reactive specimen may have only been affected by ASR. This is supported by the temperature history of the specimen, which barely exceeded the threshold for DEF and in only a small fraction of the cross-section. The second reactive specimen, however, was most likely affected by a combination of ASR and DEF, based on its higher curing temperature profile and expansions that were double that of the first reactive specimen.

UPV and impact-echo were similarly effective at assessing deterioration due to ASR and DEF, and much more so at low levels of expansion. As expansions exceeded 0.20%, these methods gave very little indication of the progress of deterioration, even as reached very high levels (1.0% or more). Therefore, the utility of these methods in the long term monitoring of severely damaged structures is quite limited. They may be more useful in providing a qualitative assessment of the condition of the structure and mapping relative differences in the severity of damage. The latter may help identify locations suitable for core sampling, which will remain essential to the evaluation process, as present NDT methods are unable to diagnose the cause of distress. Both of these methods are most effective if a baseline for undamaged concrete can be established.

SASW and SWT proved to have little value in evaluating the effects of ASR and DEF. While the surface wave velocity, calculated with SASW, showed similar trends to the compression wave velocity, the test and data analysis are very time consuming, and the results were much more scattered. The SWT method is particularly unsuitable, as the cracking characteristic of ASR and DEF interferes with the behavior of the surface waves in an unpredictable manner.

Finally, the two methods under development may have some future potential for improving the assessment of affected structures. The time shift nonlinear acoustic method is potentially at least an order of magnitude more sensitive to damage than linear acoustic methods such as UPV. The full-scale dynamic test shows promise in that it may be able to detect the effects of self-post-tensioning in reinforced structures undergoing expansion. The consequent stiffening of the structure leads to better structural performance than would be predicted by the degraded mechanical properties of core samples. Both methods require significant developmental resources to test their full potential, but the expected benefits are worth pursuing.

Chapter 6. Full-Scale Beams: Core Sample Testing

6.1 Core Sampling Protocol and Test Matrix

Core samples were extracted from the full-scale beam specimens both before and after the flexural load tests (discussed in Chapter 7). A similar test program to that used for the exposure block cores was conducted. The test program was used to diagnose the presence of and potential for ASR and DEF in the beams, assess the impact of these deterioration mechanisms on the properties of the concrete, and calculate the estimated flexural load-carrying capacity and deflections under load. Table 6.1 summarizes the core sample test program.

Table 6.1: Core sample testing program.

Core Dia. in. (mm)	NDT	Mechanical Testing	WSA	Residual Expansion			Petrography
				Test A	Test B	Test C	
2 (51)		0	0	2	2	2	0
4 (102)		6	2	0	0	0	1

**Numbers are cores tested from each beam specimen*

NDT = UPV and Resonant Frequency

Mechanical Testing = SDT, elastic modulus (E) and compressive strength (f'_c)

WSA = Water-soluble alkalis

Cores extracted prior to the load tests were 2 in. (51 mm) in diameter, and removed from the 4 in. (102 mm) stirrup spacing region near the ends of the beams (Figure 6.1a and 6.1b). They were extracted several weeks before the load tests were conducted. This location was selected to avoid any impact on the load tests. These were used for residual expansion testing, following the three parallel tests recommended by Folliard et al. (2007) and shown in Table 2.3. One core from each end of a specimen was placed in each of the three residual expansion tests; procedures are described in greater detail in 6.2.1. Following extraction of the cores, the holes were filled with a commercial concrete repair mixture (Figure 6.1c).



Figure 6.1: Extraction of 2 in. (51 mm) diameter cores from second reactive specimen and repaired core holes.

Following the flexural load tests, three 4 in. (102 mm) diameter cores were extracted from each test region of each specimen, with the locations carefully selected to avoid areas damaged by the load test. The same sequence of tests as shown in Figure 3.6 was conducted on these six cores, although only two of the six were tested for water-soluble alkalis. A seventh core was extracted from the middle test region of each beam for petrographic examination. Figure 6.2 shows the core locations for the first reactive specimen; more than seven core holes can be seen as not all cores were extracted intact. In the course of an actual investigation, these core samples would not be taken after a load test, although this was necessary in this study to avoid weakening the beams in their expected failure regions.



Figure 6.2: 4 in. (100 mm) diameter core locations for first reactive beam.

6.2 Experimental Procedures: Cores

As noted in Table 6.1, the 2 in. (51 mm) and 4 in. (102 mm) diameter cores were used for separate tests, with the former being placed in a set of residual expansion tests and the latter used for a series of tests similar to that applied to the exposure block cores in Chapter 3.

6.2.1 Residual Expansion Tests

Three parallel residual expansion tests were conducted on the 2 in. (51 mm) diameter cores, with two cores from each beam specimen used for each test. They are, with one modification, the same tests detailed in Table 2.3. Specimen preparation and instrumentation procedures were identical to those detailed in Chapter 3 (Section 3.2.8) for the exposure block cores. Great care was taken in specimen preparation as obtaining cores which could be trimmed to 8 in. (204 mm) in length was a difficult task that requires core samples with an L/D ratio in excess of 4. The storage and measurement procedures are detailed below.

The first test, referred to as Test A, involves storing the specimens in a 1N NaOH solution at 100 °F (38 °C). This test is designed to determine the maximum potential for expansion due to ASR, while the storage solution inhibits the development or progress of DEF. The storage temperature is less than the 176 °F (80 °C) recommended by Folliard et al. (2007). The lower temperature may provide a more realistic prediction of expansion potential, although storage at 176 °F (80 °C) would be guaranteed to prevent the formation of ettringite. In the end, the lack of a storage chamber capable of 176 °F (80 °C) in the building where the length-change comparator was located governed the decision to store at 100 °F (38 °C). The cores were first stored in room-temperature water for 24 h and heated to 100 °F (38 °C). After 24 h, an initial measurement was taken and the cores transferred to the 1N NaOH solution that had also been heated to 100 °F (38 °C). The cores were also weighed at the time of each length change measurement. Cores were measured frequently—initially at three and seven days, then weekly, and eventually biweekly. They were only removed from the 100 °F (38 °C) chamber for a few minutes for measurements to prevent shrinkage due to the cooler environment in the room where the comparator and scale were located.

The second test, referred to as Test B, involves storing the specimens in a saturated limewater bath at 73 °F (23 °C). This test is designed to determine the maximum potential for expansion due to DEF, while the storage solution inhibits the development or progress of ASR

(due to leaching of alkalis into the water). Cores were measured for length and mass change weekly initially and later, biweekly.

The third test, referred to as Test C, involves storage over water in a sealed container at 100 °F (38 °C), an environment which has a relative humidity in excess of 95%. This storage condition is identical to that specified by ASTM C1293 (2008) and was also used for residual expansion testing of the exposure block cores. This test is designed to allow expansion due to both ASR and DEF. The storage conditions do not suppress the development of either expansion mechanism. Cores were measured for length and mass change at the same frequency as Test B, and placed in a 73 °F (23 °C) to cool for 12 to 20 h prior to each measurement. After the measurements, they were returned immediately to the 100 °F (38 °C) chamber.

6.2.2 NDT

NDT of the 4 in. (102 mm) diameter cores consisted of performing UPV and resonant frequency tests. These tests were the first in series of increasingly destructive tests performed on six of the seven cores extracted from each specimen after load testing. The procedures for specimen preparation and testing are identical to those described in Chapter 3 for the exposure block cores. The reader may refer to Sections 3.2.4, 3.2.5.1, and 3.2.5.2 for more details.

6.2.3 Mechanical Testing

Following the UPV and resonant frequency tests, a series of mechanical tests were conducted on the cores. Stiffness damage was performed first, using the procedure described by Smaoui et al. (2004a), followed by static elastic modulus (ASTM C469-10 2010), and finally compressive strength (ASTM C42-11 2011). The procedures for each test are identical to those described in Chapter 3 for the exposure block cores, and the reader may refer to Section 3.2.6 for more details.

6.2.4 Chemical Testing

Chemical testing of the core samples consisted of measuring the water-soluble alkalis. One of the three cores from each test region was randomly selected for testing, for a total of two cores per specimen. The hot-water extraction method described by Bérubé et al. (2002b) was used. Test procedures were identical to those described in Chapter 3 for the exposure block cores, and the reader may refer to Section 3.2.7.1 for more details. Additionally, the potential alkali contribution during the test from the Jobe (F1) sand present in the concrete was investigated, and the results were presented in Chapter 3 (Table 3.14).

6.2.5 Petrographic Analysis

A petrographic investigation was conducted following the flexural load test for the purpose of qualitatively and quantitatively evaluating the condition of the concrete and assisting in the diagnosis of the damage mechanism(s) present. One core from each beam specimen was sent to DRP Consulting, where they were prepared and examined by David Rothstein, a concrete petrographer familiar with cases of ASR and DEF.

Procedures for the preparation and examination of the cores are fully described in Dr. Rothstein's report (2012b), although a brief summary of the methods used is provide here. In the context of the petrographic investigation, the longitudinal orientation refers to the long axis of the core, which originally extended inward from the side face of the beam specimen.

The core samples were prepared and examined according to ASTM C856 (2011). The cores were sliced twice lengthwise to obtain a slab from the central portion of the core, which was prepared for examination as a polished section. One of the remaining longitudinal sections was set aside for phenolphthalein staining to detect carbonation. A petrographic thin section (~20 µm thickness) was prepared using the other remaining longitudinal section from the nonreactive beam core only.

The polished sections were examined visually and with a stereomicroscope with magnification capability ranging from 3-180X. The microscopic examination included both a qualitative description of the condition of the concrete and features relevant to ASR and DEF, and determination of the Damage Rating Index (DRI). The DRI was performed as described by Grattan-Bellew (1995) and, with several modifications. Since the test was developed for reactive coarse aggregates, the fine aggregate was also examined for signs of damage. Additionally, three types of ettringite deposits were included in the rating system, to better address the possibility of DEF. The full rating system is detailed in Table 6.2. Further details on the DRI method can also be found in Chapter 2 (Section 2.4.4.2).

Table 6.2: DRI weighting factors, from Rothstein 2012b.

Factor	Weight
Coarse Aggregate with Fracture	X 0.25
Coarse Aggregate with Fracture & Gel	X 2.0
Coarse Aggregate Debonding	X 3.0
Coarse Aggregate Reaction Rim	X 0.50
Fine Aggregate Reaction Rim	X 0.25
Fine Aggregate with Fracture & Gel	X 1.0
Cracks in Paste	X 2.0
Cracks with Gel in Paste	X 4.0
Gel in Voids	X 0.50
Ettringite in Voids	X 0.25
Ettringite in Fractures	X 2.25
Ettringite at Interfacial Transition Zone	X 0.50

Some scanning electron microscopy (SEM) was also performed on the polished section from the second reactive specimen to further examine deposits of ettringite. This employed a backscatter electron microscope and magnification up to 2175X. The thin section was examined under a petrographic microscope using plane- and cross-polarized light, at magnifications up to 1000X.

6.3 Results and Discussion

This section discusses the results of the core sample testing program. Residual expansion results for the 2 in. (51 mm) diameter cores are presented in Section 6.3.1. NDT, mechanical and chemical test results of the 4 in. (102 mm) diameter cores are presented in Sections 6.3.2, 6.3.3, and 6.3.4, respectively. Finally the results of the petrographic investigation with 4 in. (102 mm) diameter cores are discussed in Section 6.3.5.

6.3.1 Residual Expansion Testing

Residual expansion tests are normally used to help make a prognosis for the future potential for continuing expansion and distress due to ASR and DEF. However, in this case, the combination of tests performed has a diagnostic function as well, and will contribute to the determination of the type of deterioration occurring in each reactive specimen. The monitoring periods ranged from 126 to 132 d.

The results of the three tests are summarized in Figure 6.3, which plots axial expansion and mass gain of the cores with time. Cores from the nonreactive beam exhibited little or no expansion in all three tests. Cores from the first reactive beam expanded an average 0.04% in each of Tests A and B, and 0.06% in Test C. No rapid expansion was observed in association with the rapid mass gain in the first two weeks of Tests A and B. Cores from the second reactive beam expanded an average of 0.19% in Test A, 0.96% in Test B and 0.63% in Test C.

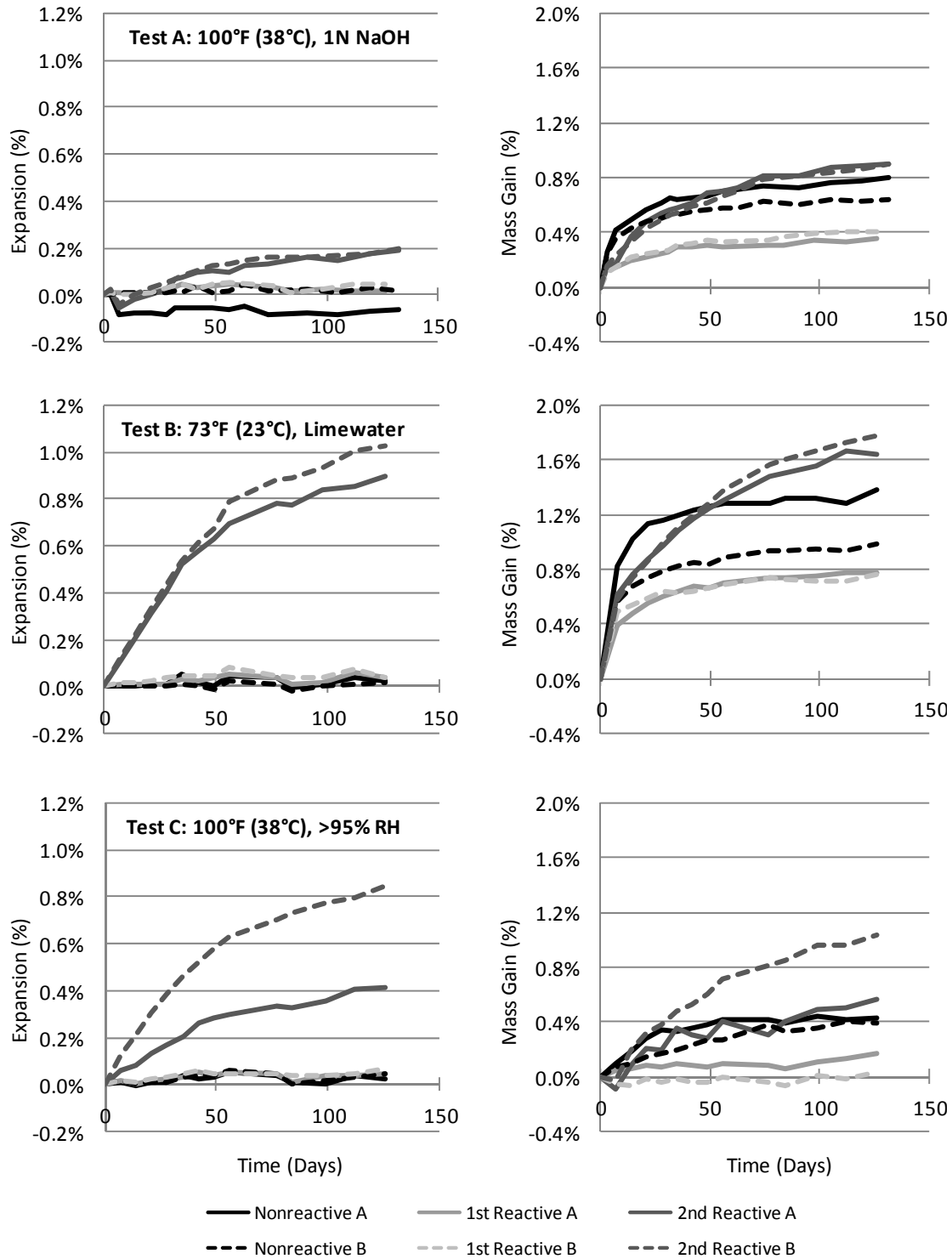


Figure 6.3: Residual expansion tests of beam cores.

Although the cores have not been monitored for as long as recommended by Folliard et al. (2007), it is still possible to draw some conclusions based on the trends observed to date. The nonreactive specimen appears to be unaffected by either ASR or DEF and has no potential to be affected at a future date. The first reactive specimen has been affected by ASR and possibly to a

slight degree, DEF. The results of Tests A and C both suggest the potential for some future expansion due to ASR. Results of Test B do not strongly indicate the potential for DEF. There is a high probability that the second reactive specimen has been and will continue to be affected by both ASR and DEF. These samples expanded significantly in all three tests.

6.3.2 NDT

A summary of the results of UPV and resonant frequency tests on the 4 in. (102 mm) cores is presented in Table 6.3. The average values of the three cores from each test region are shown.

Table 6.3: UPV and Resonant Frequency results for beam cores.

Beam Specimen	Test Region	UPV (m/s)	E _d , Longitudinal		E _d , Transverse	
			(ksi)	(GPa)	(ksi)	(GPa)
Nonreactive	Outer	4509	4578	31.6	4723	32.6
	Middle	4415	4483	30.9	4588	31.7
First Reactive	Outer	3894	3165	21.8	3205	22.1
	Middle	3924	3166	21.8	3257	22.5
Second Reactive	Outer	3602	2614	18.0	2640	18.2
	Middle	3730	2805	19.4	2835	19.6

Compression wave velocities of the second reactive specimen, measured in the UPV test, are an average of 18% lower than that of the nonreactive; velocities for the first reactive specimen are 12% lower on average. They are also on the order of 200 to 300 m/s higher than the in-situ measurements presented in Chapter 5; the same observation was made regarding the exposure block cores in Chapter 3.

The resonant frequency test, which measured the dynamic elastic modulus, was even more sensitive to damage in the reactive specimens. Compared to the nonreactive specimen, the average elastic moduli of the first and second reactive specimens were 30% and 40% lower, respectively.

These results clearly indicate that two reactive specimens are damaged compared to the nonreactive specimen, and that the second reactive specimen is damaged to a greater degree. Without the baseline provided by the cores from the nonreactive specimen, it would not be as simple to quantify extent of the distress. However, the tests would allow the qualitative assessment that the compression wave velocities and dynamic moduli are quite low for concrete with a design strength of 5000 psi (34.5 MPa). If the velocities of the core samples are adjusted downward by 300 m/s to account for the disparity between core sample and in-situ results, the concrete in the reactive specimens would be categorized as “questionable” according to a rating scale (Malhotra 1976) commonly referenced in the interpretation of UPV test results.

6.3.3 Mechanical Testing

Results of the stiffness damage tests conducted on the 4 in. (102 mm) diameter core samples are summarized in Table 6.4. The data were analyzed to determine the 1st Cycle Area and the Total Plastic Strain; this is the same procedure as used in Chapters 3 and 4. Because of the small sample size (three specimens per set), calculation of standard deviations or coefficients

of variation was not possible. However, the range of values of each parameter was divided by the average in each set of cores (shown as “Var %”). This variation would be approximately twice the coefficient of variation, if one could be calculated. The table also shows the percentage of compressive strength at 28 days and at the time of testing to which the specimens were loaded.

Table 6.4: SDT Data for beam cores.

		Beam and Core Location					
		Nonreactive		First Reactive		Second Reactive	
		Middle	Outer	Middle	Outer	Middle	Outer
1st Cycle Area (Pa)*	Core 1	421	426	775	1743	2211	3784
	Core 2	440	416	2211	1359	1315	2203
	Core 3	328	313	2306	2137	2382	2266
	Average	396	385	1764	1746	1969	2751
	Var %	28.3	29.4	86.8	44.6	54.2	57.5
Plastic Strain (µε)	Core 1	29	59	56	207	282	478
	Core 2	75	65	258	172	155	265
	Core 3	36	15	281	245	292	304
	Average	47	46	198	208	243	349
	Var %	98.6	107.9	113.6	35.0	56.3	61.0
f _c (28 day)		42.6		35.8		32.4	
Load, % of 28-day f _c		23.5		27.9		30.9	
Load, % of f _c at test		23.7	22.3	42.5	40.4	48.5	50.6

* 1 Pa = 0.000145 psi; 1 MPa = 145 psi

There was a very high variation in the data within each set of core sample for both parameters investigated. However, the average results from the two test regions in the nonreactive and first reactive specimen were very similar. The outer test region of the second reactive specimen gave higher values for both parameters compared to the middle test region, largely due to the results of Core 1 from the outer region, which also was a significant outlier in the NDT results.

The results do indicate that the two reactive specimens were significantly damaged compared to the nonreactive beam, and the second reactive specimen was more damaged than the first. The SDT parameters of the reactive specimen cores were four to six times higher than the nonreactive specimen cores.

Figures 6.4 and 6.5 place the SDT results in the context of the cylinder tests discussed in Chapter 4. Figure 6.4 plots the average 1st Cycle Area results for the cores from each beam specimen against the average expansion of the specimen in that test region (to account for the fact that the cylinders were unconfined specimens), with the average expansion being calculated as the cube root of the volumetric expansion, as shown in Equation 6.1:

$$EXP_{avg} = \sqrt[3]{(EXP_{vertical})^2 \cdot EXP_{longitudinal}} \quad \text{Equation 6.1}$$

This equation assumes that the transverse expansion normal to the wide face of the beam (which was not measured directly) is the same as the measured vertical expansions. The results are

overlaid with the results of the ASR and ASR+DEF cylinders. Figure 6.5 does the same for the Total Plastic Strain results.

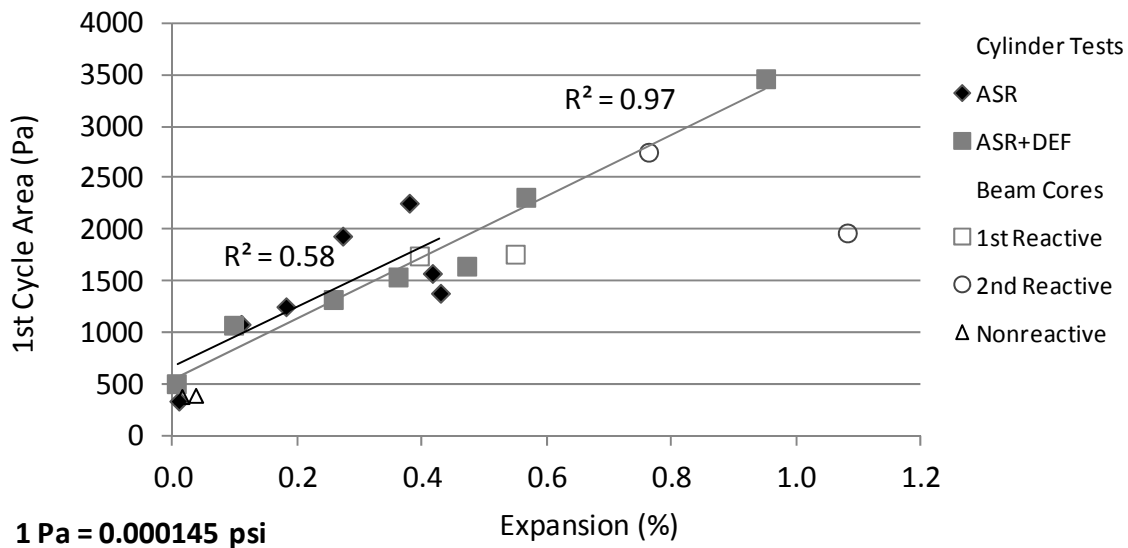


Figure 6.4: SDT—1st Cycle Area of beam cores compared to cylinder tests.

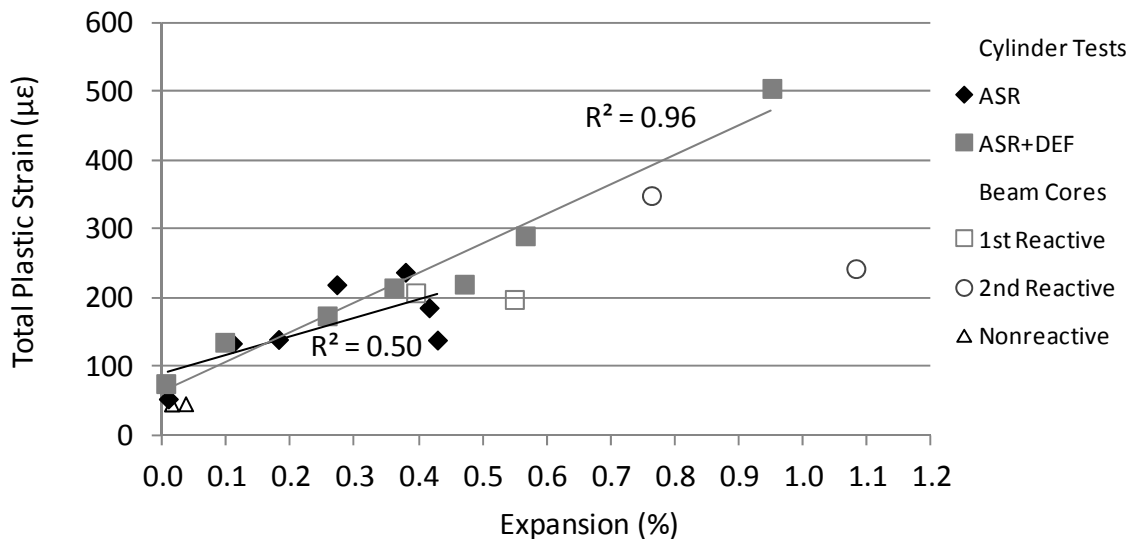


Figure 6.5: SDT—Total Plastic Strain of beam cores compared to cylinder tests.

Figure 6.4 shows that the 1st Cycle Area results of the beam cores compare well to the cylinder results, with the exception of the cores from the middle region of the second reactive specimen. The cores from the first reactive specimen are a close match to the linear best-fit line of the ASR cylinders (recall that this specimen is believed to be only affected by ASR). However, the best-fit line is actually a poor fit to the ASR cylinder data ($R^2 = 0.58$). If, as was suggested in Chapter 4, only the cylinders with expansions of 0.38% or less are considered, the

best fit line has a much improved correlation to expansion, but the slope also increases. This would place the core sample data well below the adjusted best fit line. The same statements can be made regarding the Total Plastic Strain results in Figure 6.5.

It is clear that SDT can provide an indication that a structure is, in fact, damaged by ASR and/or DEF. However, in interpreting the results, it may be difficult to correlate the values of SDT parameters to specific levels of deterioration. While the data presented here appear at first glance to be a good fit to the cylinder test results, the reality is that the results from the first reactive specimen may simply be a fortuitous fit to a poorly conceived best-fit line, and the results from the second reactive specimen are too widely scattered to determine the expansion to-date.

Table 6.5 summarizes the elastic modulus and compressive strength data for the core samples. As with the SDT data, a “Var %” value is calculated in lieu of a standard deviation or coefficient of variation due to the small sample size. The table also shows the static elastic modulus that which is commonly assumed based on the compressive strength (Equation 3.5). Elastic modulus tests were conducted at loads ranging from 31 to 50% of the compressive strength, with one exception—Core 1 from the outer region of the second reactive beam ($0.60f'_c$). That particular core had an unexpectedly low compressive strength which was not known until after then elastic modulus test had been completed.

Table 6.5: Elastic modulus and compressive strength data for beam cores.

		Beam and Core Location					
		Nonreactive		First Reactive		Second Reactive	
		Mid	End	Middle	Outer	Middle	Outer
E (GPa)*	Core 1	27.3	26.8	11.7	13.6	11.3	6.3
	Core 2	27.3	27.4	11.2	15.8	10.2	10.8
	Core 3	27.2	27.3	12.1	10.9	10.2	10.9
	<i>Average</i>	<i>27.2</i>	<i>27.1</i>	<i>11.7</i>	<i>13.4</i>	<i>10.6</i>	<i>9.3</i>
	<i>Var %</i>	<i>0.4</i>	<i>2.4</i>	<i>7.8</i>	<i>36.2</i>	<i>11.1</i>	<i>50.0</i>
f'_c (MPa)*	Core 1	44.6	44.9	25.8	26.7	21.9	16.5
	Core 2	43.1	45.4	24.7	29.3	20.1	22.4
	Core 3	38.9	44.3	20.0	18.4	19.9	20.4
	<i>Average</i>	<i>42.2</i>	<i>44.8</i>	<i>23.5</i>	<i>24.8</i>	<i>20.6</i>	<i>19.8</i>
	<i>Var %</i>	<i>13.6</i>	<i>2.5</i>	<i>25.0</i>	<i>44.0</i>	<i>9.9</i>	<i>29.8</i>
E, % of predicted by f'_c		88.7	85.7	51.1	57.0	49.1	44.0

* 1 GPa = 145 ksi; 1 MPa = 145 psi

The results are more consistent within each set of three cores; variations in the elastic modulus and compressive strength are similar, but higher than reported for the same tests in Chapters 3 and 4. Since these cores were extracted after flexural load testing, it is not unreasonable to expect more variation in the results.

The elastic moduli and compressive strength of the cores from the first reactive specimen were an average of 54% and 44% lower, respectively, than those of the nonreactive specimen. Moduli and compressive strengths of cores from the second reactive specimen were an average of 63% and 54% lower, respectively.

The results clearly indicate that the concrete in both reactive specimens was significantly affected by ASR and DEF, and the second reactive specimen was more affected than the first. Also, the elastic moduli estimated based on compressive strength are significantly greater than the actual elastic moduli of the cores. In some instances, the actual elastic modulus was less than half of the predicted value.

Figures 6.6 and 6.7 place the elastic modulus and compressive strength results, respectively, in the context of the cylinder tests discussed in Chapter 4. In each figure, the average modulus or strength result for cores from each test region are plotted against the average expansion of the specimen in that test region. This accounts for the fact that the cylinders were unconfined specimens; average expansion was calculated as shown in Equation 6.1. The results are overlaid with the results of the ASR and ASR+DEF cylinders. Both the elastic moduli and compressive strengths of the core samples are an excellent fit to the cylinder data. The strength of the second reactive specimen cores from the middle region are 38% below the 28-day compressive strength of cylinders, while the ASR+DEF cores exhibited a 36% decrease in compressive strength at a similar level of expansion.

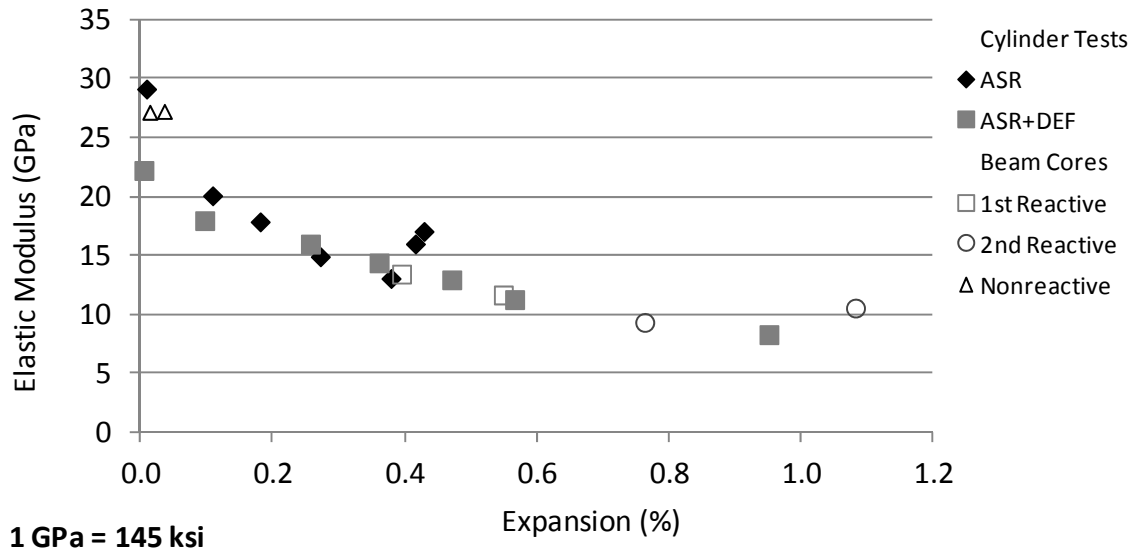


Figure 6.6: Elastic moduli of beam cores compared to cylinder tests.

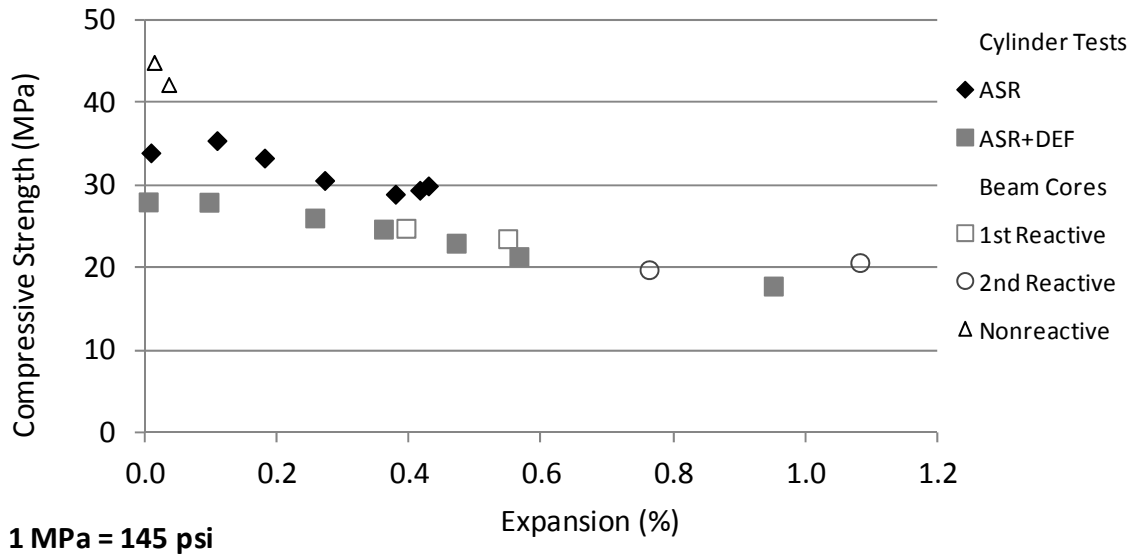


Figure 6.7: Compressive strength of beam cores compared to cylinder tests.

These results confirm the conclusions drawn from the tests on exposure block core samples (Chapter 3) and laboratory-conditioned cylinders (Chapter 4). These elastic modulus and compressive strength tests provide more consistent results than the SDT, as performed in this study. Elastic modulus is far more sensitive to the effects of ASR and DEF, and may be the best way to characterize the extent of deterioration. Further refinement to the SDT, as recommended by Sanchez et al. (2012a), may improve the utility of that test. However, all of these tests involve core samples which are removed from the confining effects of reinforcement in the parent structure. The actual capacity of the structure to bear load may not be affected in the same manner as the core samples.

6.3.4 Chemical Testing

Table 6.6 summarizes the water-soluble alkali results for the core samples. The data represent an average of three sub-samples prepared from each core sample. Data are not corrected for any expected contributions by the aggregates.

Table 6.6: Water-soluble alkali results for beam cores.

Beam	Location	Avg. Transverse Expansion (%)	Na ₂ O (%)	K ₂ O (%)	Na ₂ O _e		
					(%)	lb/yd ³	kg/m ³
nR3	Outer	0.02	0.019	0.124	0.100	3.93	2.33
	Middle	0.05	0.020	0.134	0.108	4.21	2.50
R5	Outer	0.53	0.151	0.151	0.251	9.81	5.82
	Middle	0.76	0.155	0.155	0.257	10.06	5.97
R6	Outer	1.05	0.165	0.167	0.274	10.74	6.37
	Middle	1.55	0.180	0.184	0.301	11.80	7.00

Alkali levels in the nonreactive specimen are higher than the 3.47 lb/yd^3 (2.06 kg/m^3) that was calculated based on the alkali content of the cement used in the mixture. The source of the additional alkalis is not clear, although it is possible that the alkali content of the cement was higher than expected, although samples were tested by TxDOT using X-ray fluorescence (XRF). It is also possible that the aggregates could have contributed alkalis over the two year period between fabrication and testing. Finally, there may have been some systemic error, either with the flame photometer used to analyze the samples or in specimen preparation.

Both reactive specimens also have alkali levels in excess of the 9.10 lb/yd^3 (2.06 kg/m^3) initially supplied by the cement and NaOH admixture. Cement samples for these specimens were also tested by TxDOT in XRF, and the NaOH used was a laboratory grade solution that was purchased specifically for the fabrication of these specimens. This leaves the possibility of systemic error in the equipment or specimen preparation, or alkali contributions from the aggregates. If the measured values are accurate, then the use of moisture conditioning to promote the leaching of alkalis (to help promote development of DEF) from the concrete has been ineffective.

In Chapter 3, tests on the potential alkali contribution of Jobe (F1) sand in the hot-water extraction method indicated that this aggregate could increase measured water-soluble alkalis by 0.41 lb/yd^3 (0.24 kg/m^3) through the release of alkalis during the extraction process. In light of this data, it is not unlikely that over the 20 to 22 months between fabrication and testing of these specimens, that the Jobe (F1) sand was responsible for the higher than expected water-soluble alkali results. Berubé et al. (2002a) note that in some structures, aggregates have been reported to contribute similar or great amounts of alkalis over a number of years in service.

The water-soluble alkali levels in both reactive specimens are certainly sufficient to sustain continued ASR, as they are higher than the initial alkali loading of the concrete. The only limitation in this respect would be the continued availability of reactive silica and moisture. Most indications from other test methods are that the second reactive specimen has been affected by DEF. However, it has been suggested that DEF is triggered in part by a reduction in pore solution pH because of leaching of alkalis, or consumption of alkalis by ASR (Famy, et al. 2001). An investigation using cores from structures in Texas affected by ASR and DEF showed that those affected solely by DEF had lower water-soluble alkali levels than those that were affected by ASR or were undamaged (Folliard, et al. 2006). While the pore solution pH and composition was not tested, the water-soluble alkali results suggest a highly alkaline pore solution. Thus, the second reactive specimen may present the coexistence of DEF and a highly alkaline pore solution.

6.3.5 Petrographic Analysis

The results of the petrographic examination are provided in the petrographer's report (Rothstein 2012b); a summary of the report is provided here. This includes carbonation testing, the qualitative assessment of the polished section, and the DRI analysis.

Phenolphthalein staining showed that the carbonation depth of all three cores samples was 0.04 in. (1 mm) or less. Therefore, carbonation is not believed to have had a major impact on the concrete. This is unsurprising given the highly alkaline environment of the reactive specimens and the fact that all three specimens were constantly exposed to water, which would limit carbon dioxide ingress.

The qualitative assessment of the polished sections noted that the fine aggregate in the reactive specimens was siliceous and contained granitic particles, volcanic particles, quartz, and

feldspars. The volcanic particles contained reaction rims, “extensive” internal microcracking and deposits of ASR gel. This is illustrated in Figure 6.8. Both core samples from the reactive specimens exhibited “extensive hairline and microcracking” throughout; cracks were noted to “radiate from reactive aggregate particles” and were typically filled with either ASR gel or ettringite. The fine aggregate in the nonreactive specimen was noted to be a mix of siliceous and carbonate particles, with “rare” chert particle. Chert can be susceptible to ASR, but the polished section showed no signs of ASR were observed in the qualitative examination.

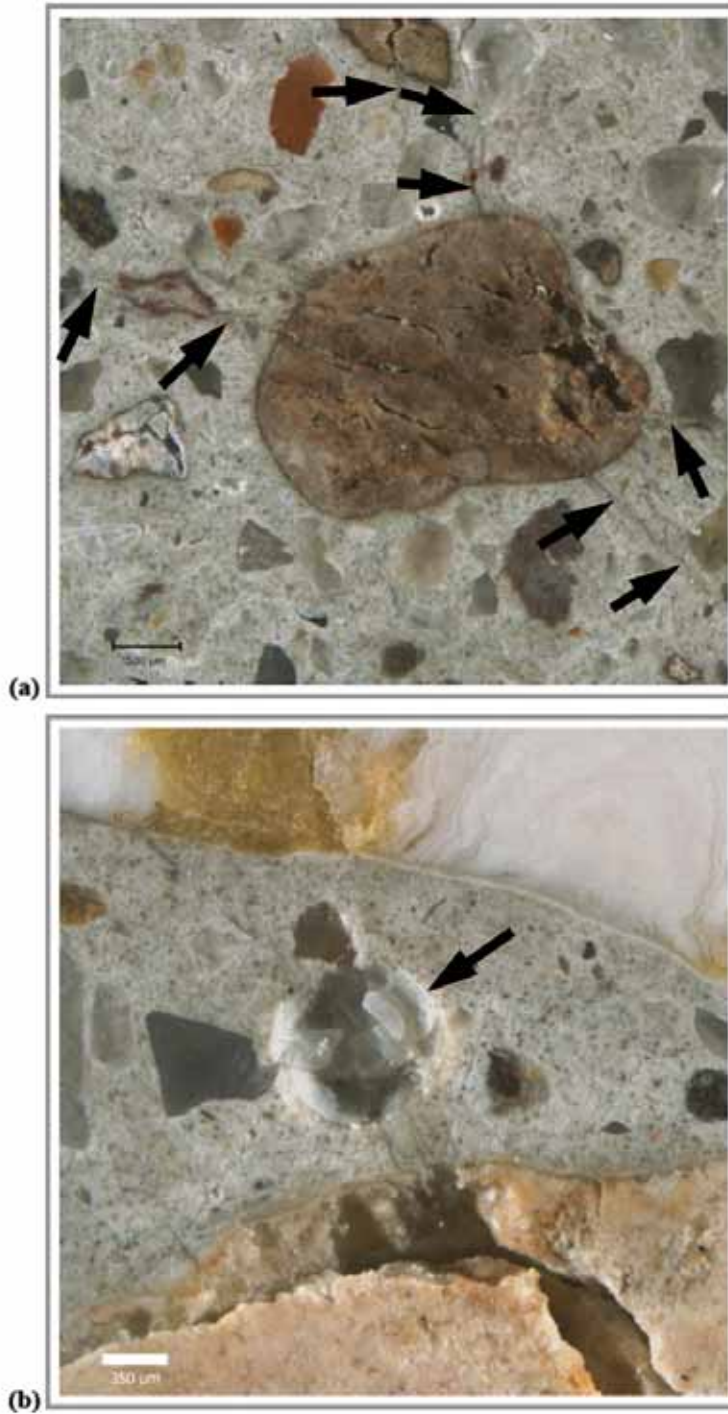


Figure 6.8: Photomicrograph of polished section showing (a) microcracks in fine aggregate particles and (b) ASR gel in a void, from Rothstein 2012b.

DRI scores were normalized for each core specimen, and are summarized in Table 6.7. The two cores from the reactive specimens had similarly high DRI scores (525 and 516), while the core from the nonreactive specimen had a DRI of only 39.

Table 6.7: Normalized DRI analysis, from Rothstein 2012b.

Factor	NR3	R5	R6
Coarse Aggregate with Fracture	0	3	5
Coarse Aggregate with Fracture & Gel	0	0	3
Coarse Aggregate Debonding	0	5	19
Coarse Aggregate Reaction Rim	0	0	1
Fine Aggregate Reaction Rim	2	49	21
Fine Aggregate with Fracture & Gel	0	25	100
Cracks in Paste	32	53	61
Cracks with Gel in Paste	0	304	215
Gel in Voids	0	6	12
Ettringite in Voids	5	57	39
Ettringite in Fractures	0	16	12
Ettringite at Interfacial Transition Zone	0	7	28
Total	39	525	516

NR3 = Nonreactive R5 = First Reactive R6 = Second Reactive

Most of the DRI score for the nonreactive core was due to cracks in the paste (32); the remainder of the score was attributed to reaction rims on fine aggregate particles (2) and ettringite in voids (5). Ettringite is commonly found in voids in concrete, and is not necessarily a sign of distress. This core was also extracted after a flexural capacity load test, so some cracking should be expected. No ASR gel was observed.

Although the reactive specimens had similar DRI scores, there are some important differences. Figures 6.9 and 6.10 provide a graphical representation of the composition of the DRI scores for all factors, and factors only related to DEF, respectively.

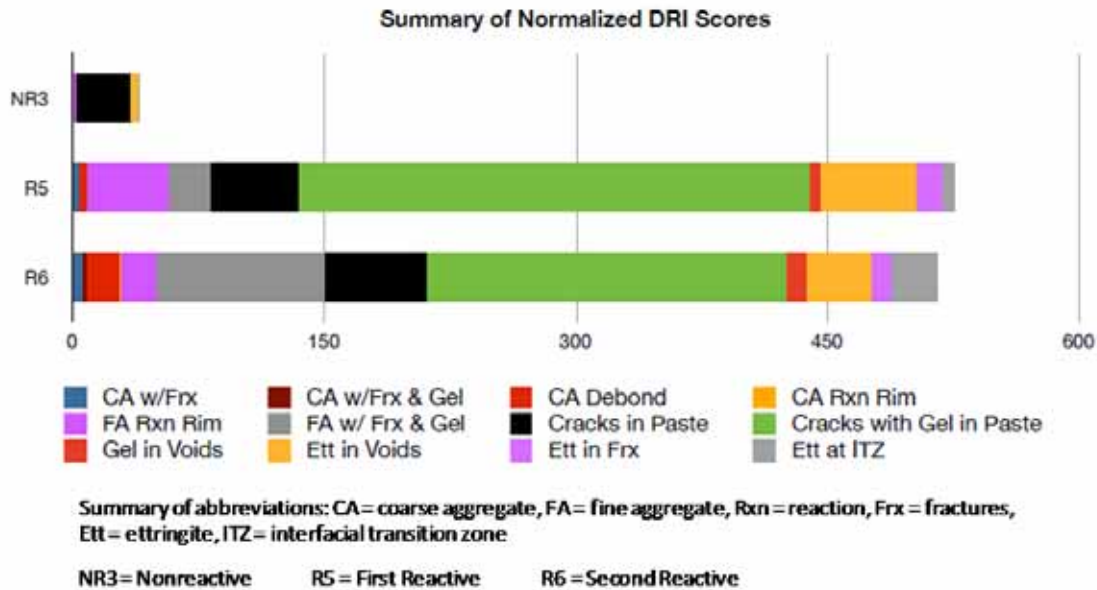


Figure 6.9: Normalized DRI scores, including all features related to ASR and DEF, adapted from Rothstein 2012b.

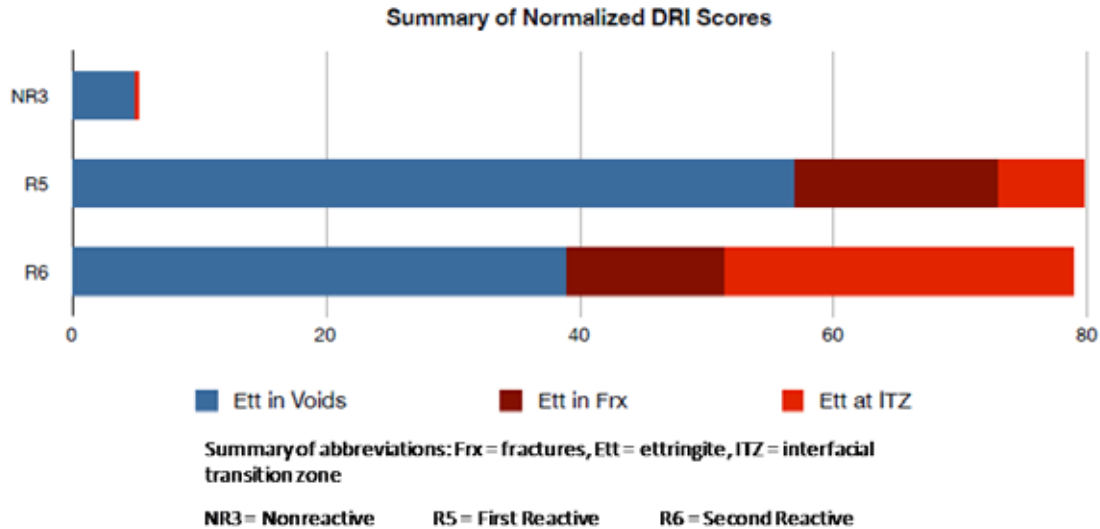


Figure 6.10: Normalized DRI scores, counting only DEF-related features, adapted from Rothstein 2012b.

The DRI method has not been widely adopted or standardized for ASR, let alone DEF, so interpreting results can be difficult. However, some general conclusions can be made based on above data. Both reactive specimens are clearly affected by ASR, as indicated by the many instances of ASR gel. The first reactive specimen had more instances of ASR gel in cracks in the paste, while the second reactive specimen had a greater contribution to the DRI from ASR gel in or around fractured fine aggregate particles.

With regards to DEF, there are a greater number of instances of ettringite in the interfacial transition zone (ITZ) and coarse aggregate debonding in the second reactive specimen compared to the first reactive specimen. The ITZ is a region of higher w/cm around aggregate particles in ordinary portland cement concrete and ettringite deposits in the ITZ are typically observed in DEF-affected concrete (Thomas, et al. 2008). Since the coarse aggregate did not participate in ASR, debonding may have been caused by the surrounding paste expanding, another characteristic of DEF. The presence of ettringite in voids and fractures, however, is not necessarily linked to DEF, although it is often observed in DEF-affected concrete. Figure 6.11 shows both reflected light and SEM images of the polished section from the second reactive specimen indicating ettringite deposits in the ITZ around aggregate particles.

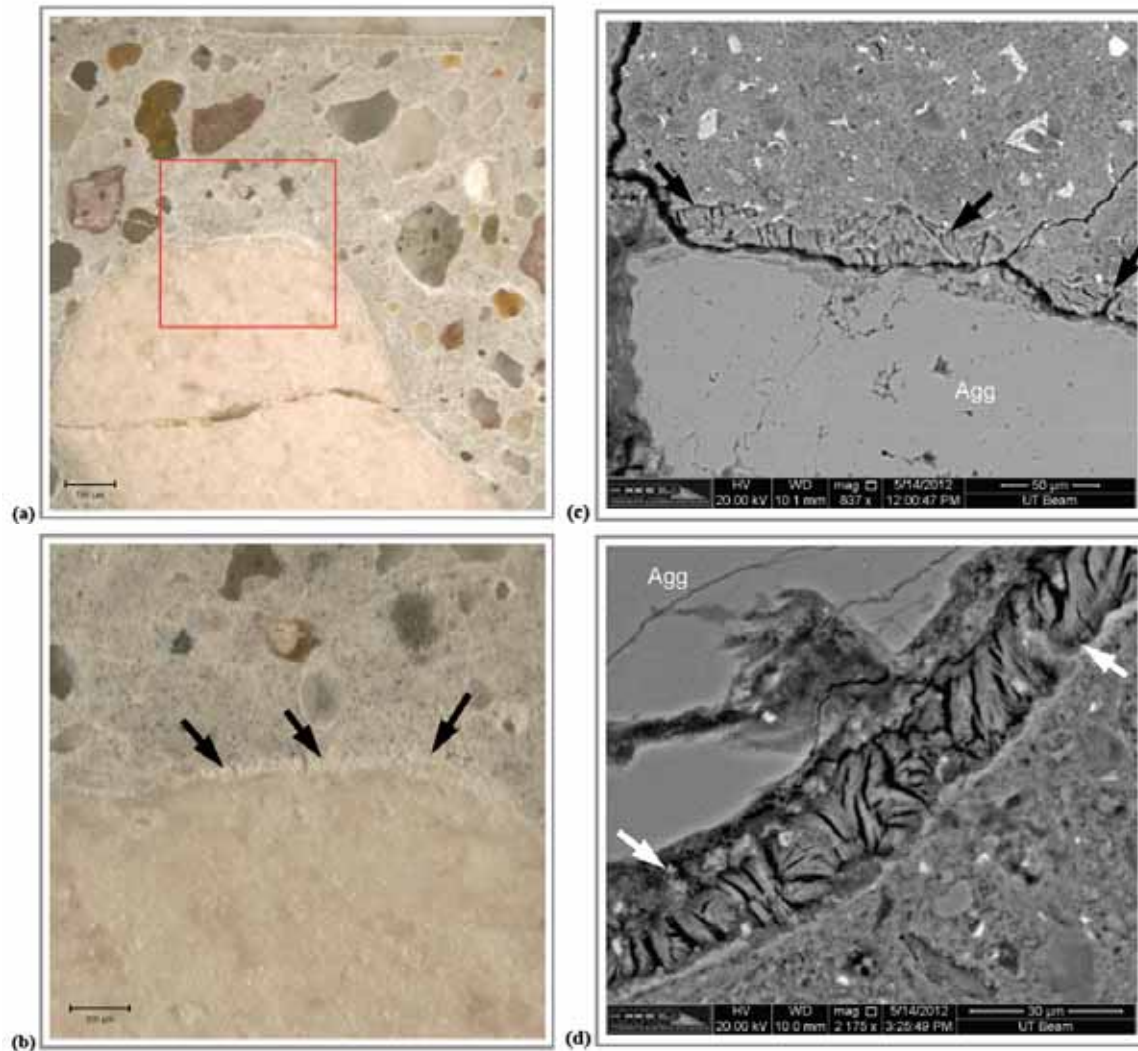


Figure 6.11: Reflected light (a and b) and backscatter SEM (c and d) images of ettringite deposits (indicated by arrows) in the ITZ around aggregate particles, from Rothstein 2012b.

6.4 Summary

An extensive testing program was conducted on core samples extracted from all three beam specimens, both before and after the flexural capacity load tests. The following summarizes the findings of this testing:

- Both the nondestructive and mechanical test methods indicated a significant degradation of the concrete in the reactive specimens. The concrete in the second reactive specimen was more deteriorated than that of the first reactive specimen, which is consistent with the expansion results presented in Chapter 5.
- A petrographic examination confirmed that the nonreactive specimen was unaffected by ASR or DEF, and the reactive specimens were severely affected by ASR, and possibly DEF.

- Residual expansion tests indicated little probability of future expansion for the nonreactive specimen and a high probability of continued rapid expansion for the second reactive specimen. These tests also suggest that the second reactive specimen had the potential for expansion, or had been expanding from both ASR and DEF.
- Chemical testing showed that the water-soluble alkali levels in the reactive specimens were much greater than the amount of alkalis initially supplied by the cement and NaOH admixture, indicating that there are sufficient alkalis to allow continued ASR, and a strong possibility exists that aggregates have released alkalis to the pore solution over the life of the concrete.

These observations, when combined with the curing temperatures experienced by the specimens during curing and their expansion histories, support the conclusion that the first reactive specimen has only been affected by ASR and the second reactive specimen has been affected by a combination of ASR and DEF. If DEF has occurred in the first reactive specimen, it has not been a significant factor in the observed deterioration. Finally, the coexistence of a very large amount of water-soluble alkalis and DEF in the second reactive specimen may be of interest for future studies of the mechanism of DEF.

Chapter 7. Full-Scale Beams: Flexural Behavior

7.1 Overview

This chapter describes the flexural load tests conducted on the three full-scale beam specimens. The tests were intended to determine the effects of ASR and DEF on the flexural capacity and serviceability of reinforced concrete beams. As noted in Chapters 5 and 6, very large expansions were measured for the two reactive specimens over 20 to 22 months of outdoor exposure and moisture/load conditioning, and the mechanical properties of the core samples extracted from these specimens were greatly degraded at the time of testing. The nonreactive specimen was 24 months of age at the time of testing. It served as a control, allowing the results of the reactive specimens to be compared not only to predicted behavior but also to the actual behavior of an undamaged beam.

7.2 Experimental Procedures

The specimens were tested in four-point flexure, with loads applied at third-points along a 21 ft 4 in. (6.60 m) span. During the test, both loads and deflection data were recorded. This section details the procedures followed in preparing the specimens for testing and during test; a description of the test setup is also provided.

7.2.1 Preparation for Testing

Preparation of the specimen began with the removal of the watering system, tarp, and the external conditioning load several days prior to the test. A final set of expansion measurements were taken both before and after the removal of load. Although this data was presented in Chapter 5, a simplified representation of expansions in the middle test region of each beam after the removal of external load is shown in Figure 7.1. Longitudinal expansions are for the primary reinforcement only, while the vertical expansions are the average of the concrete and steel measurements.



Figure 7.1: Expansions of specimens after removal of conditioning load.

A visual assessment of the specimens was also made in preparation for testing. Both reactive beams also had developed a visible camber, or upward deflection, as a result of expanding under load, and the longitudinal expansions reflect this, with greater expansions, or strains, measured in the top longitudinal bars than the bottom. However, it should be noted that while camber is typically observed in prestressed concrete beams, in this case, due to the orientation of the specimen and applied loads, the deflection would actually be viewed as a sag in the beam if they had been loaded from above.

Some crazing was observed on the surface of the nonreactive specimen; this was noted shortly after fabrication and is not believed to be associated with any expansive behavior. Small flexural cracks, which had developed upon application of the conditioning load, were also evident. Cracking in the reactive specimens was extensive and predominantly aligned with the longitudinal reinforcement, as described in Chapter 5 (Section 5.4.2). No flexural or shear cracks were evident prior to the load tests. Cracks in the middle test regions of the specimens were up to 0.04 in. (1.0 mm) in width.

The final stage of preparation involved moving the specimens inside the laboratory and placing them in the test setup. This was done one or two days prior to testing. Once in place, the cracks in each test region (bounded roughly by the expansion targets on each face) were mapped with black permanent marker to identify them in photographs taken during the tests.

7.2.2 Test Setup

A schematic of the test setup is presented in Figure 7.2, while Figure 7.3 shows the first reactive specimen in the test setup, along with the shear and moment diagrams for reference. The tests were conducted in the Large Scale Beam Testing Facility at the Ferguson Structural Engineering Laboratory in Austin, Texas.

The specimen was initially set on two concrete pedestal supports while other components of the test setup were moved into place. A strong floor, composed of a 92,000 lb (41,820 kg)

steel platen, resisted the applied loads and anchored the support reactions. Two 2,000,000 lb (909,100 kg) capacity hydraulic rams, the source of the applied loads, were placed atop (12 in. (315 mm) thick steel spacers. A steel plate girder, or transfer beam, was located above each specimen at each end of the loaded span to resist the applied load. Loads were transferred from the transfer beam to the strong floor by four 3 in. (76 mm) diameter high strength steel threaded rods; nuts on the rods anchored the transfer beam. A roller and bearing plate assembly at the load and reaction points allowed free rotation. Each assembly consisted of two 2 in. (51 mm) thick plates with a 2 in. (51 mm) diameter steel rod between them. At the reaction points, the rods were welded to one of the bearing plates to resist horizontal movement. Figure 7.4 shows a close-up image of one of the roller and bearing assemblies.

Load and deflection data were collected during the test using a data acquisition system and displayed in LabVIEW program. Load cells were positioned between the nuts and transfer beam to measure the reaction force in each rod. Three linear potentiometers (L-pots) positioned on the bottom (compression) face of the specimen recorded deflections. They were located at mid-span and the support reactions. The latter were needed to account for the lengthening of the threaded rods under load.

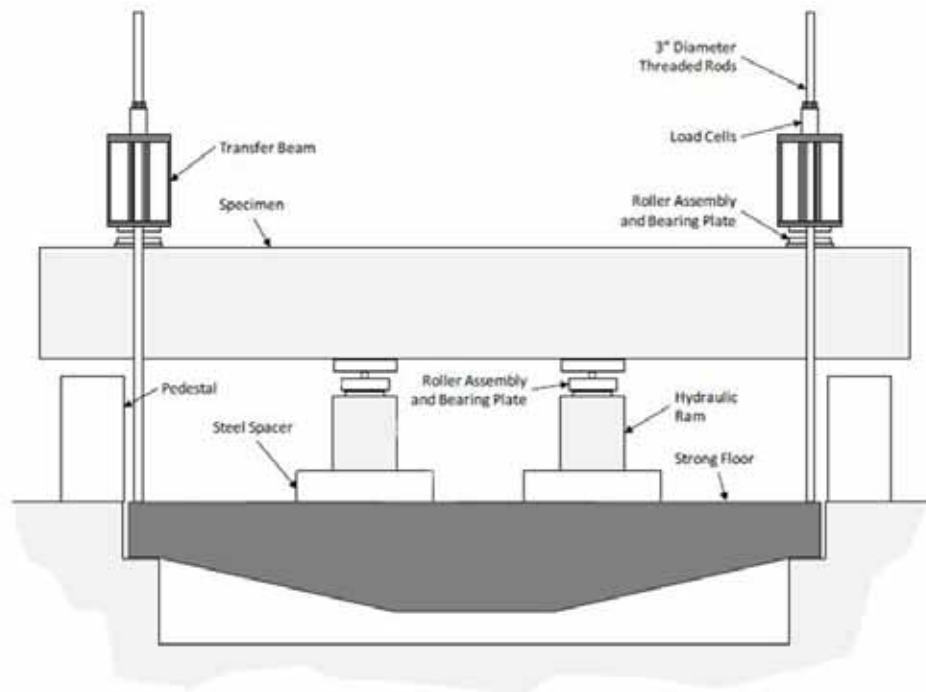


Figure 7.2: Schematic of test setup for four point flexural loading, from Hanson 2012.

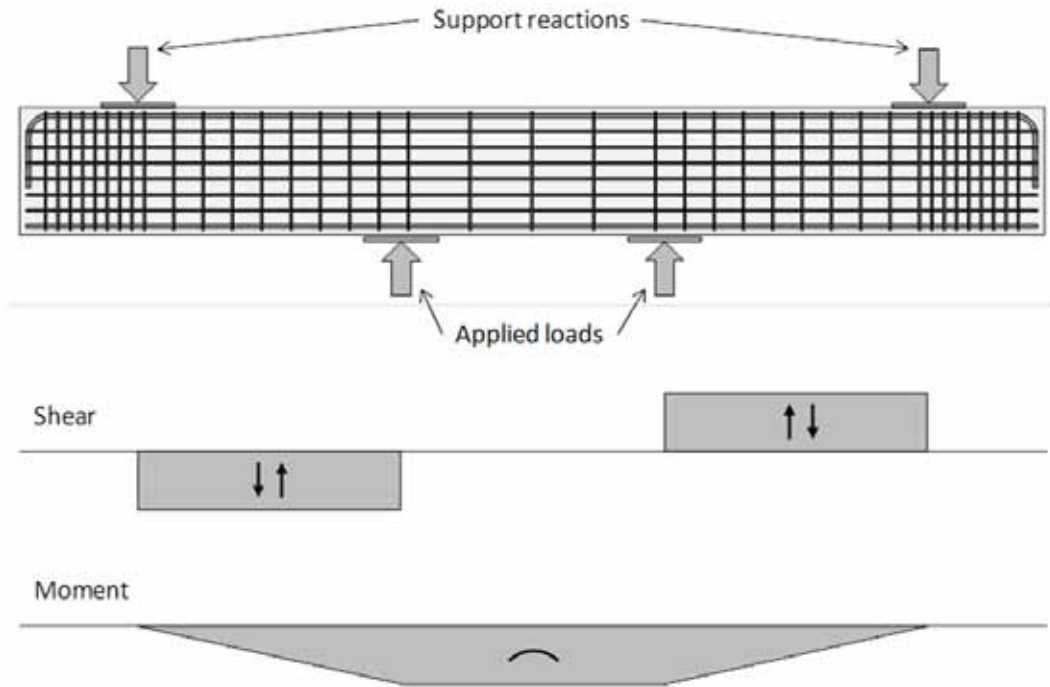


Figure 7.3: First reactive specimen in test setup (top), free body, shear and moment diagrams (bottom), adapted from Kreitman 2011.



Figure 7.4: Roller-bearing assembly at applied load.

7.2.3 Flexural Test Procedure

The three full-scale beam specimens were each tested in four-point flexure. Hydraulic pumps controlled the load applied by the rams. The specimen was first raised up until the roller-bearing assemblies at the reaction points were in contact with the transfer beams. At this point, the nuts on the threaded rods were tightened so that load could be applied by the rams, and the load and deflections were set to zero.

Loads and deflections were monitored continuously throughout the test. Load was applied to the specimens in increments of approximately 60 kips (267 kN). At each loading increment, a set of expansion measurements were taken and new cracks which formed in each test region were marked with red permanent marker. Several significant cracks in each test region were monitored for changes in width. Photographs at each load increment documented the propagation of cracks in each test region. Near the expected failure load, a video camera recorded the application of load to the specimen.

Researchers from G2MT, LLC, a materials characterization company, installed penetrating electromagnetic strain sensors to monitor changes in the strain of one longitudinal (tension) bar and one stirrup in the middle test region of the second reactive specimen. These are shown in Figure 7.5. Electromagnetic sensors, discussed in Chapter 2, have the potential to measure the strain in steel reinforcement without the need to install strain gauges on the bars. These prototype sensors involved proprietary technology and signal processing; their presence was intended as proof-of-concept testing to show that they could detect changes in the steel which correlated to the application of loads. They were monitored continuously until just below the failure load to protect the sensors from damage.

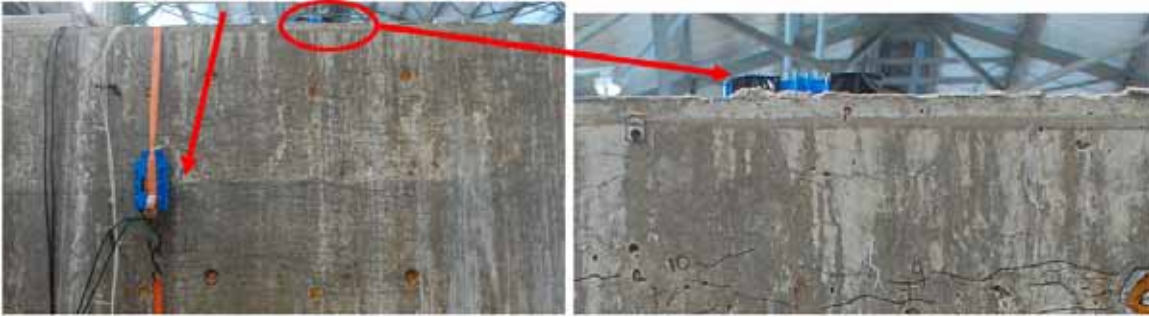


Figure 7.5: Electromagnetic sensors, second reactive specimen.

7.3 Flexural Capacity and Serviceability Predictions

Obtaining an accurate prediction of flexural capacity and deflections can be a challenging exercise when dealing with undamaged structures; the effects of ASR and DEF serve to further complicate matters. Two analyses of flexural moment capacity (M_n) and deflections at M_n are presented here, both following sectional analysis procedures given by the ACI 318-11 building code. The first uses the compressive strengths of match-cured cylinders at 28 days, and an elastic modulus assumed based on the compressive strength; this is standard procedure for design calculations according to the ACI building code (ACI Committee 318 2011). The second follows the same procedures outlined in the ACI building code, but uses the measured elastic moduli and compressive strengths of cores extracted from the constant-moment middle region of each specimen.

Figure 7.6 presents the ACI building code approach to analyzing the flexural moment capacity of a beam, where M_{max} is the nominal moment capacity. This was followed in both analyses presented in this section. Additionally, f_y and f'_y , the yield strength of the tension and compression reinforcement, are taken to be 70.6 ksi (487 MPa), based on tests of coupon samples of #11 bars provided by the manufacturer.

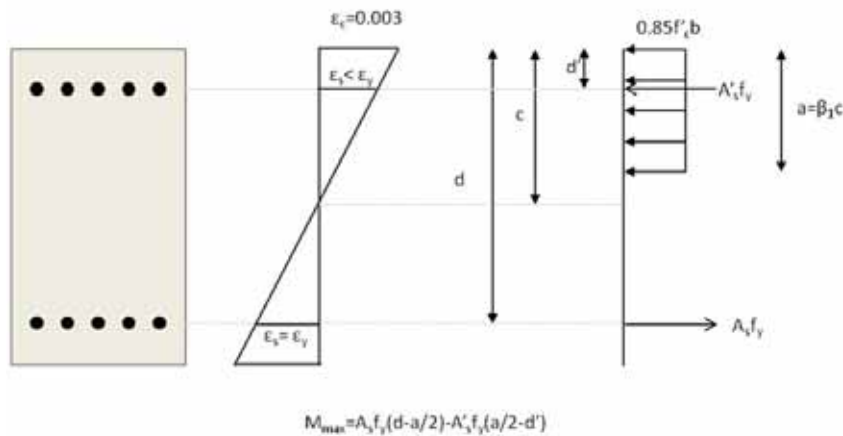


Figure 7.6: Overall approach for predicting nominal moment capacity, from Hanson 2012.

Both analyses assumed that the steel and concrete were initially at zero strain before the application of external load. A tensile failure of the steel was assumed to occur prior to crushing failure of the concrete at a compressive strain of 0.003. The applied load at M_n was calculated

using the equation $M_n = \frac{PL}{3}$, where P is one-half the total applied load and L the clear span from the support reaction to the applied load. Deflections were calculated using the equation $\Delta = \frac{PL^3}{28EI}$, where E is the elastic modulus of the concrete and I is the moment of inertia based on the cracked, transformed section. Neither analysis accounts for the creep deflections which have accompanied the development of ASR and DEF under sustained load conditioning.

7.3.1 Analysis Based on 28-Day Properties

Table 7.1 presents the predicted nominal moment capacity (M_n), total applied load at M_n and mid-span deflection at M_n , based on the 28-day compressive strength of match-cured cylinders. There are small differences between the three specimens, both with respect to moment capacity and mid-span deflections. Because the flexural capacity of a tension-controlled section is primarily governed by the strength of the reinforcement, this is to be expected. The predicted changes in deflections are also minor. As the elastic modulus of concrete decreases, the modular ratio ($E_{steel}/E_{concrete}$) increases, which increases the calculated cracked, transformed moment of inertia. The net effect is that the lower compressive strengths of the two reactive specimens have little impact on the predicted moment capacities or deflections in this analysis.

Table 7.1: Predicted moment capacities and deflections based on 28 day strength.

Specimen	28 Day Cylinder Compressive Strength psi (MPa)	Elastic Modulus (assumed) ksi (GPa)	M_n kip-ft (kN-m)	Total Applied Load at M_n kips (kN)	Mid-span Deflection in. (mm)
Nonreactive	6180 (42.6)	4480 (30.9)	1704 (2310)	481 (2139)	0.515 (13.1)
First Reactive	5200 (35.8)	4110 (28.3)	1696 (2299)	479 (2128)	0.518 (13.1)
Second Reactive	4700 (32.4)	3910 (26.9)	1692 (2294)	477 (2124)	0.520 (13.2)

7.3.2 Analysis Based on Core Properties

Table 7.2 presents the predicted nominal moment capacity (M_n), total applied load at M_n and mid-span deflection at M_n based on the measured elastic moduli and compressive strengths of cores from each specimen. Only the cores extracted from the middle region of each specimen were used for this analysis. The compressive strengths of the cores were not adjusted to account for any potential damage during extraction, although this is sometimes done in practice.

ASTM C42 (2011) states that “historically, it has been assumed that core strengths are generally 85% of the corresponding standard-cured cylinder strengths, but this is not applicable to all situations,” and that “there is no universal relationship between the compressive strength of a core and the corresponding compressive strength of standard-cured molded cylinders.” It should be noted that in this study, the cylinders were not standard-cured—they were match-cured to the temperature profile of a thermocouple embedded in each specimen. Additionally, this analysis concerns in-place strength at a time well after construction. Based on the variability of the core compressive strengths, it would seem to be unconservative to assume that the in-place

strengths are greater than the measured strengths of the cores. Furthermore, variations in the damage caused by ASR and DEF in the reactive specimens may have resulted in compressive strengths in the compression block of the specimens that are lower than the reported core strengths. Thus, the more conservative approach of using the actual measured core compressive strengths is warranted.

As with the previous analysis, there are only slight differences in the predicted moment capacities and mid-span deflections of the three specimens. Although the strength of the concrete is severely degraded due to the effects of ASR and DEF, the strength of the steel remains the primary influence on the predicted moment capacity. And, despite an even greater loss of elastic modulus in the reactive specimens, the predicted deflections are only slightly greater than those calculated based on the 28-day cylinder properties. The modular ratio of the reactive specimens is greatly increased, which translates to a cracked, transformed moment of inertia more than twice that of the nonreactive specimen, minimizing the impact on predicted deflections.

Table 7.2: Predicted moment capacities and deflections based on core properties.

Specimen	Compressive Strength, Cores psi (MPa)	Elastic Modulus, Cores ksi (GPa)	M_n kip-ft (kN-m)	Total Applied Load at M_n kips (kN)	Mid-span Deflection in. (mm)
Nonreactive	6500 (42.2)	3940 (27.2)	1706 (2313)	481 (2141)	0.515 (13.1)
First Reactive	3410 (23.5)	1690 (11.7)	1682 (2280)	474 (2111)	0.533 (13.5)
Second Reactive	2990 (20.6)	1530 (10.6)	1678 (2275)	474 (2106)	0.540 (13.7)

7.3.3 Alternate Approaches

Both of the above analyses neglect several important features of ASR- and DEF-affected reinforced concrete structures. The first is that the expansion of the concrete has placed the steel in tension. This places the concrete within the reinforcement cage in compression. This is not unlike prestressed concrete. However, the effect is unintended by the designer and still is accompanied by the undesired surface macro-cracking. Figure 7.7 shows a conceptual diagram of the effects of confinement on the reactive specimens in this study.

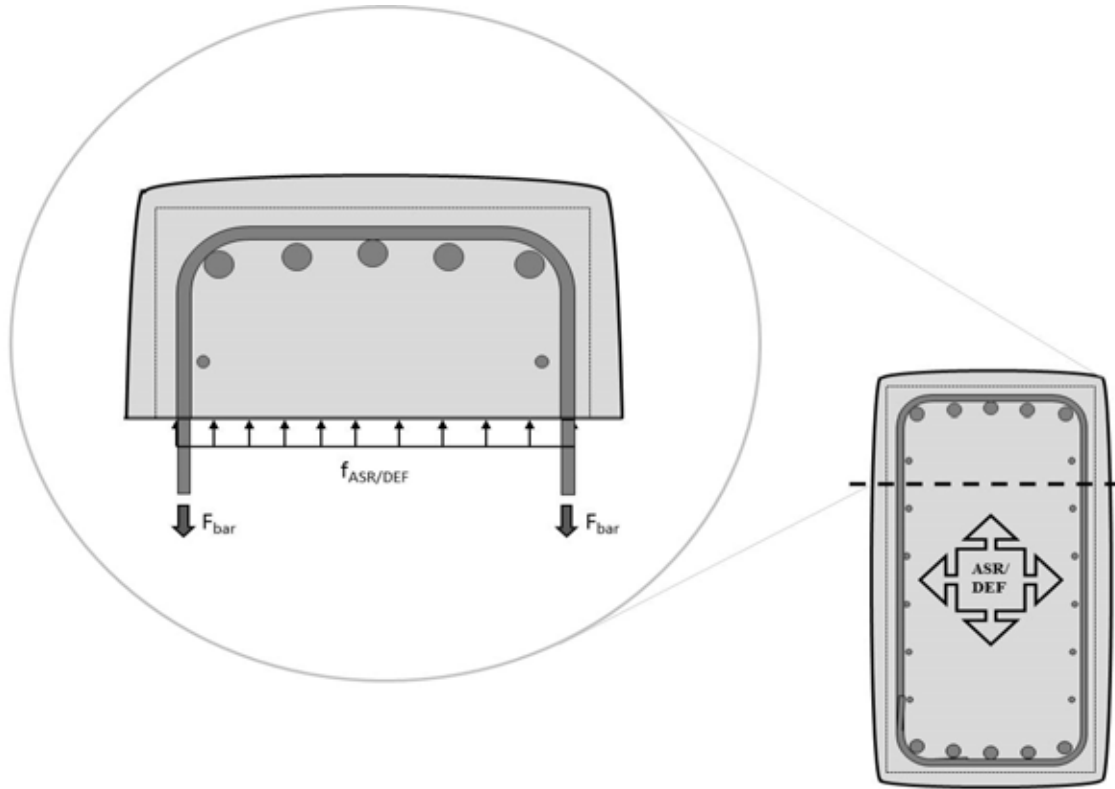


Figure 7.7: Confinement in reinforced concrete affected by ASR and DEF, from Webb 2011.

This poses some significant challenges in the analysis of the specimens in this study. The strains in the reinforcement are known, but whether than can fully be considered as a compressive strain on the concrete is less certain. If the concrete is in compression, then the remaining capacity for strain prior to crushing failure is reduced, if the failure strain of 0.003 remains a valid assumption. Likewise, the tension steel has a reduced capacity for additional strain before yield, unless some strain relaxation has occurred with time.

Another complicating factor is that the elastic modulus of concrete is not linear-elastic, that is, the tangent modulus decreases with increasing load, although in undamaged concrete this nonlinearity is quite limited so long as the load is less than approximately 50% of the compressive strength. For concrete affected by ASR and DEF, the tangent modulus decreases much more rapidly with increasing load; this was demonstrated with the stiffness damage test. In addition to a more rapid decrease in the elastic modulus with increasing load, there is also the potential for accumulated plastic strain, either under cyclic loads or sustained loading.

This uncertainty among all these variables makes it extremely difficult to conduct an analysis that accounts for the above effects with any degree of certainty. However, it has been proposed that an analysis can be conducted assuming that the structures is post-tensioned. The ISE recommended applying 50% of the concrete expansion as a prestressing force in the steel (ISE 1992). The best approach for field structures, when feasible, is to conduct a full-scale load test at service load levels. In the laboratory, a test can be run until failure to fully study the effects of ASR and DEF, as was done in this research.

7.4 Test Results

Failure in flexure is typically ductile and gradual, rather than sudden and easily defined. Therefore, the tests were run as long as deflections could be recorded and sufficient hydraulic oil was available to power the rams. The one exception was the nonreactive specimen, which suffered fracture of two primary tension reinforcing bars near mid-span; the fractures were adjacent to the welds which attached the targets to the bars.

This section presents the results of the flexural load tests on the three full-scale beam specimens. The measured loads and deflections are presented, followed by measured changes in strains using the extensometer-target system, and visual observations of crack propagation with during the tests.

7.4.1 Loads and Deflections

The measured loads and deflections on all three system specimens are presented in Figure 7.8. The loads include the self-weight of the specimens and the weight of the transfer girders—a total of 40 kips (178 kN). The “notches” in the load-deflection plots indicate a slight relaxation of the load that occurred at each increment while loaded was paused to allow expansion measurements and crack mapping. Comparisons of the predicted and measured deflections each specimen can be found in Tables 7.3 and 7.4, respectively. The measured deflections in these tables are the deflections recorded at the predicted nominal moment capacity of the specimen, not at the maximum tested moment.

Three things are clear based on the data presented in Figure 7.8 and Tables 7.3 and 7.4:

1. All specimens outperformed their predicted moment capacity, including the nonreactive specimen (bar fracture occurred after exceeding the predicted load).
2. The reactive specimens both sustained greater loads than the nonreactive specimen.
3. The reactive specimens exhibited stiffer responses to the applied loads than the nonreactive specimen, and experienced smaller-than-predicted deflections.

The bending moments at maximum tested loads ranged from 112 to 131% of the predicted moment capacity of the specimens, with the first reactive specimen performing the best. Had the test of the second reactive specimen been continued, Figure 7.8 suggests that the maximum load would have been similar to that of the first reactive specimen. Based on Figure 7.8, it also appears that the tension reinforcement in the nonreactive specimen had yielded just prior to fracture. The trend of the load-deflection curve for this specimen suggests that it would have behaved similarly to the second reactive specimen after yield. Measured mid-span deflections at the predicted moment capacity ranged from 141% of the predicted deflection for the nonreactive specimen, to just 76% of the predicted deflection for the first reactive specimen.

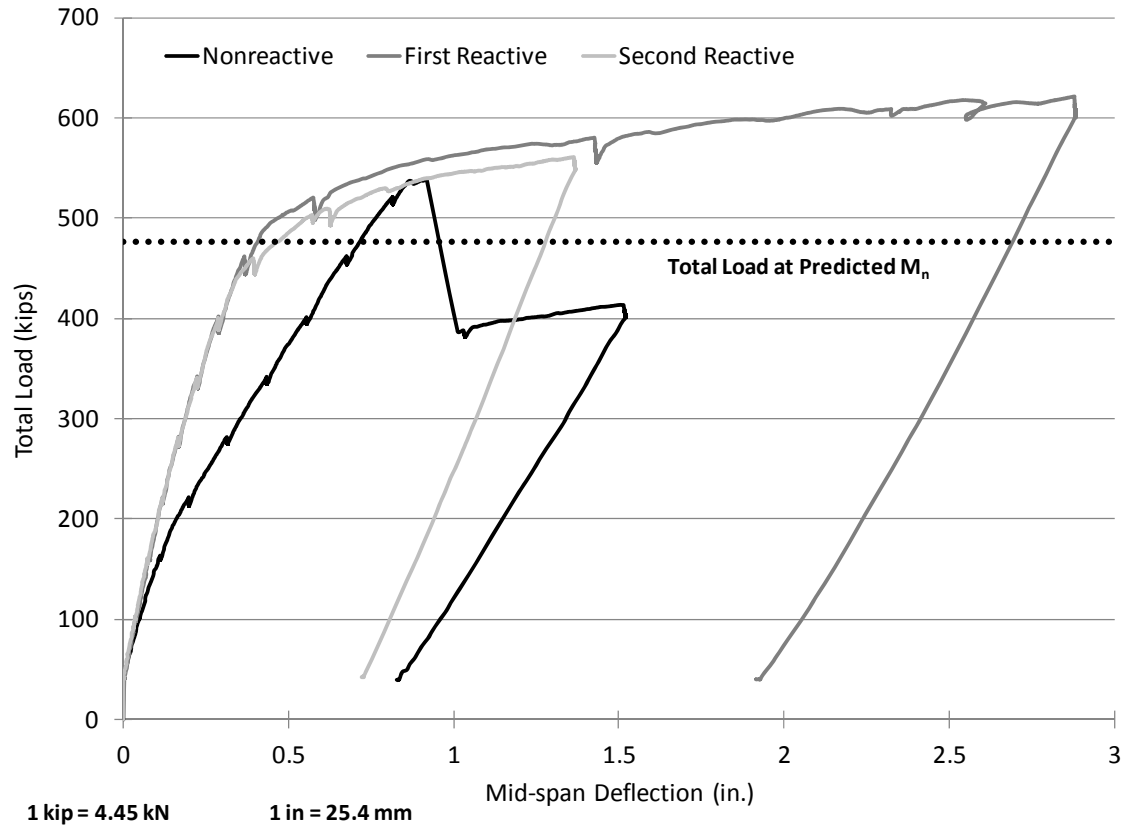


Figure 7.8: Load vs. deflection for all specimens.

Table 7.3: Predicted and measured moment capacities.

Specimen	M_n k-ft (kN-m)	M_{test} k-ft (kN-m)	M_{test}/M_n
Nonreactive	1706 (2313)	1916 (2598)	1.12
First Reactive	1682 (2280)	2211 (2998)	1.31
Second Reactive	1678 (2275)	1995 (2705)	1.19

Table 7.4: Predicted and measured deflections at mid-span.

Specimen	$\Delta_{predicted}$ in. (mm)	Δ_{test} in. (mm)	$\Delta_{test}/\Delta_{predicted}$
Nonreactive	0.515 (13.1)	0.724 (18.4)	1.41
First Reactive	0.533 (13.5)	0.403 (10.2)	0.76
Second Reactive	0.540 (13.7)	0.451 (11.5)	0.84

7.4.2 Expansion Measurements

Expansion measurements taken at each load increment showed that essentially no changes occurred for measurements in the vertical direction, but as expected, significant changes for measurements in the longitudinal direction. Changes in the longitudinal reinforcement strains are summarized in Table 7.5, which compares the strains at zero load to those at a load of 520 kips (2320 kN), which corresponds to the last measurements prior to fracture of the reinforcement in the nonreactive specimen. At this load, it is clear that the tension reinforcement is near yield in the nonreactive specimen, but is well past the expected yield point in both reactive specimens. In fact, the tension steel in the first and second reactive specimens reached its expected yield strain around 400 kips (1780 kN) and 143 kips (640 kN), respectively.

Table 7.5: Reinforcement strains in middle test region before and after loading.

Specimen	Location	Strains in Longitudinal Reinforcement	
		Before Loading	@ 520 kip (2320 kN)*
Nonreactive	Top	-0.01%	0.22%
	Bottom	0.02%	-0.04%
First Reactive	Top	0.15%	0.40%
	Bottom	0.13%	0.00%
Second Reactive	Top	0.23%	0.40%
	Bottom	0.16%	-0.03%

*Load on Second Reactive was 519 kip (2310 kN)

7.4.3 Visual Observations

Visual observations consisted of crack mapping and measuring selected crack widths at each load increment, as well as photographic documentation of the condition of the specimens at each load increment. A combination of crack mapping and photographs were used to illustrate the propagation of cracks with increasing load. This is shown in Figure 7.9 for the middle test regions of the nonreactive and first reactive specimens. Only four of the load increments are shown in this figure; new cracks are in red. M_n refers to the predicted moment capacity of each specimen, based on the core properties. Note that flexural crack development is much more rapid in the nonreactive specimen, while no flexural cracks had crossed mid-depth of the first reactive specimen at $0.77M_n$. Flexural cracks did not appear in the second reactive specimen until the load reached $0.63M_n$. From this point, crack propagation was similar to the first reactive specimen.

Testing of the first reactive specimen did reach the point of crushing failure in the compression zone, as evidenced by the spalling shown in Figure 7.10. This figure also shows that a plastic hinge has formed at mid-span.

Crack width measurements were conducted on pre-existing cracks in the specimens; that is, those which were present before the load tests. For the two reactive specimens, there were only longitudinal cracks from ASR and DEF; the openings of these cracks generally did not change in width throughout the load tests. The nonreactive specimen initially contained several hairline flexural cracks; these opened up with the application of increasing loads during the test. Crack widths in the nonreactive specimen increased to as much as 0.03 in. (0.75 mm) just before reinforcement fracture.

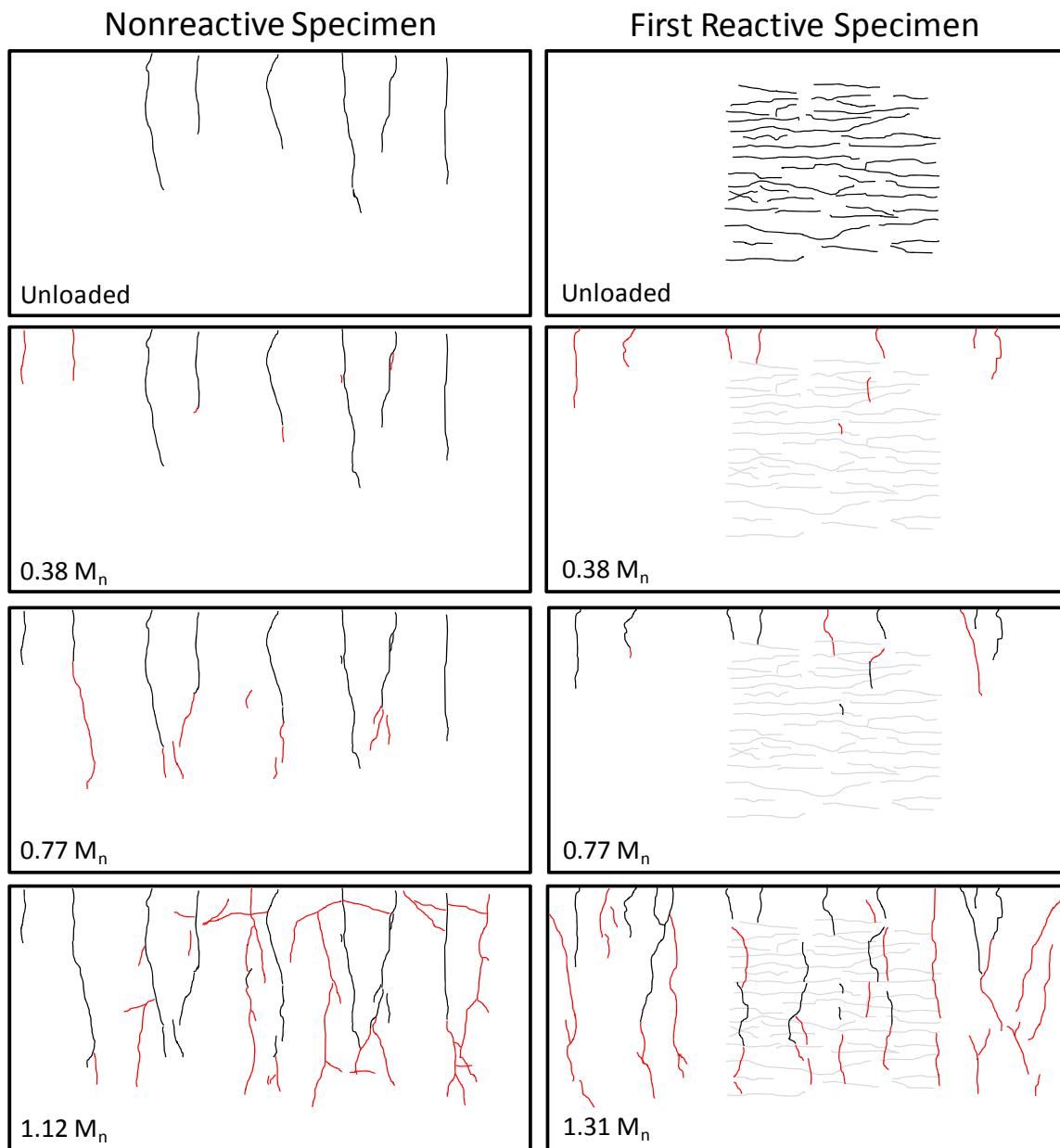


Figure 7.9: Crack propagation in middle region of test specimens.

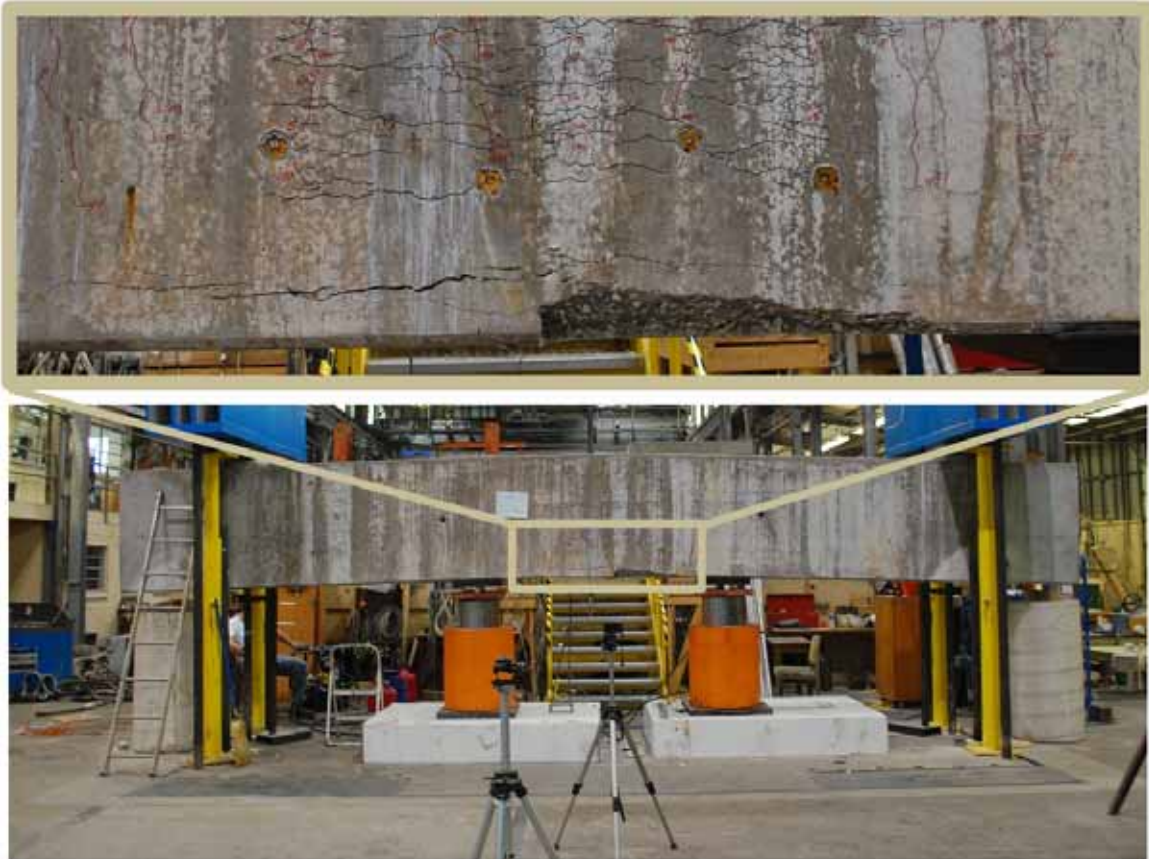


Figure 7.10: Crushing failure, first reactive specimen.

7.5 Discussion of Results

The flexural moment capacities and serviceability of the reactive specimens were not negatively impacted, as compared to their predicted moment capacities, both based on their 28-day (undamaged) concrete properties and the properties of core samples extracted prior to testing. Compared to the nonreactive specimen, the reactive specimens were able to carry a greater load and experienced less deflection at their predicted nominal moment capacity.

However, a closer examination of the load-deflection plots in Figure 7.8 and the reinforcement strains in Table 7.5 will show that yielding of the tension reinforcement appears to have occurred at a higher load for the nonreactive specimen compared to the reactive specimens. In fact, the load at yield was approximately 40 to 60 kips (178 to 267 kN) higher in the nonreactive specimen. It should also be noted the deflections were a result of the applied load only and do not include creep deflections which developed as a result of expansions during the conditioning of the specimens.

In order to more fully assess the results of the tests, the flexural capacity and serviceability data must also be compared to the degree of distress from ASR and DEF, as quantified by expansions prior to tests and the mechanical properties of core specimens. This is presented below, along with a discussion of the electromagnetic strain measurements and the implications of these tests for evaluating structures affected by ASR and DEF.

7.5.1 Comparison to Core Properties and Expansions

Table 7.6 compares the deflections at maximum predicted load, to the mechanical properties of cores and average longitudinal expansions in the middle test region of each specimen. The maximum predicted loads at which deflections are shown were based on the core properties shown in the table. Expansions were prior to loading, and therefore only a result of ASR and DEF; longitudinal expansions are shown as this was responsible for the majority of the confining force on the concrete. This table shows that there is no clear correlation between expansions, core mechanical properties, and deflections. However, the increased stiffness caused by the self-post-tensioning effect in the reactive specimens likely contributed to their smaller deflections during the test.

Table 7.6: Comparison of deflections to expansions and mechanical properties of core samples.

Specimen	Compressive Strength, Cores psi (MPa)	Elastic Modulus, Cores ksi (GPa)	Average Longitudinal Expansion, Middle Region (%)	Mid-span Deflection, Δ_{test} in. (mm)
Nonreactive	6500 (42.2)	3940 (27.2)	0.01%	0.724 (18.4)
First Reactive	3410 (23.5)	1690 (11.7)	0.14%	0.403 (10.2)
Second Reactive	2990 (20.6)	1530 (10.6)	0.20%	0.451 (11.5)

Another way to examine the results is to calculate a flexural stiffness coefficient for each specimen. This is normally a product of the concrete modulus of elasticity and the cracked, transformed moment of inertia of the section, and can be determined from a moment-curvature diagram, where $\frac{M}{\Phi} = EI$. However, the calculation of curvature, Φ , is complicated by the fact that deflections were only measured in three locations. Thus, the flexural stiffness will be calculated as the slope of the P- Δ plot, from zero applied load to 60% of the load at the predicted M_n . Zero applied load corresponds to approximately 40 kips (178 kN), due to the self-weight of the specimens and the weight of the transfer girders. Figure 7.11 presents the flexural stiffness of each specimen, compared to the measured elastic moduli and compressive strengths of cores from the middle test region of each specimen. The first reactive specimen had the highest flexural stiffness, 1419 kips/in. (248 kN/mm), followed by the second reactive specimen at 1395 kips/in. (244 kN/mm). The flexural stiffness of the nonreactive specimen was just over half that of the reactive specimens, 738 kips/in. (129 kN/mm). This confirms that the expansions caused by ASR and DEF have resulted in a stiffening effect on the reactive specimens. In contrast, the mechanical properties of the core samples do not correlate to the measured performance of the specimens.

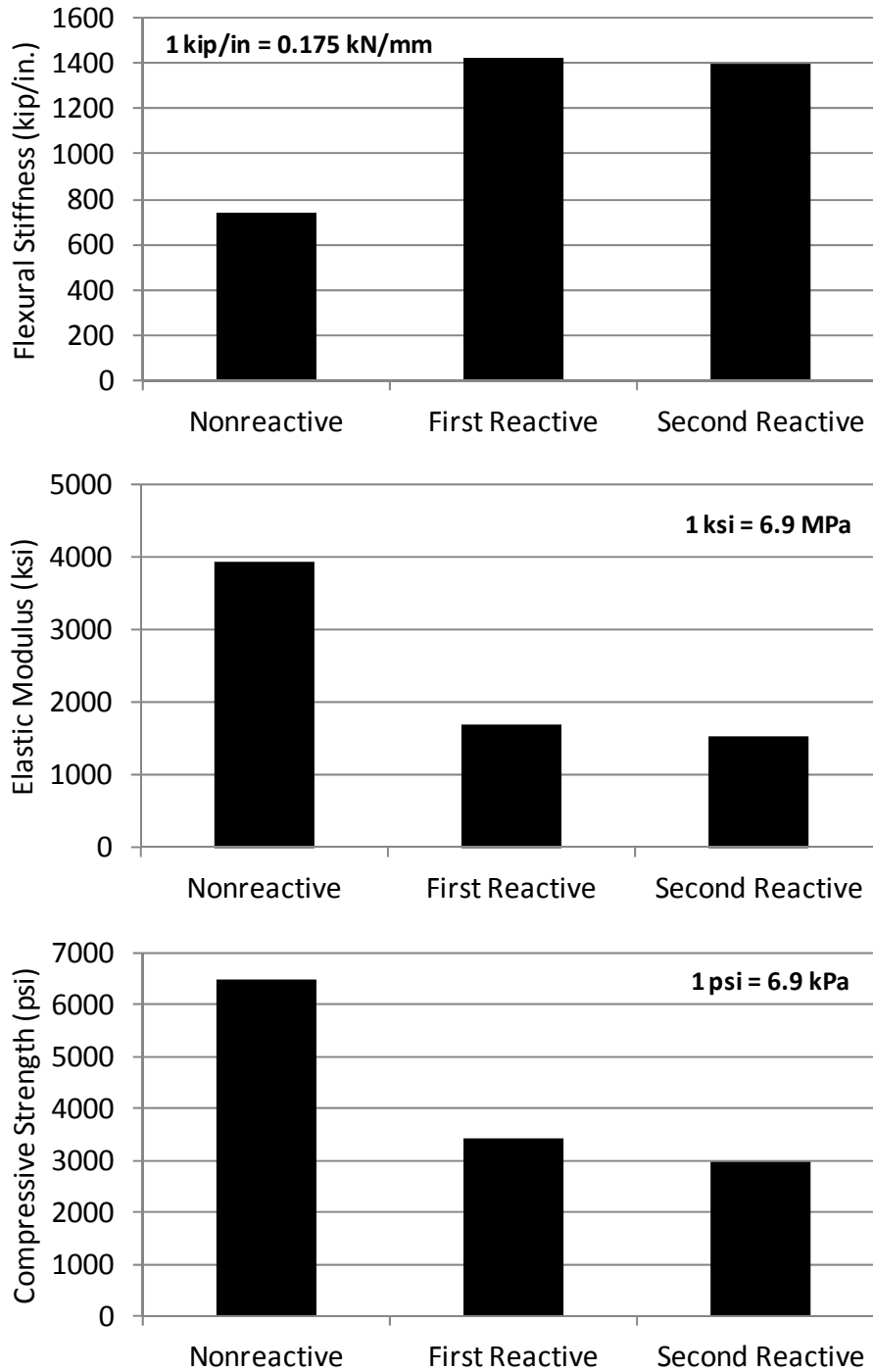


Figure 7.11: Comparison of specimen flexural stiffness, core elastic modulus and core compressive strength.

7.5.2 Comparison to In-Situ NDT

The results of the load tests were generally at odds with the data generated by the in-situ NDT monitoring program. UPV and impact-echo were the two tests that had results consistent

with the expansions measurements on the specimens; both tests indicated that the reactive specimens had been damaged by ASR and DEF. The one test which did produce results somewhat consistent with the load tests was the full-scale dynamic test. This was the only test which indicated a lack of damage to the reactive specimens, or even a potentially enhanced performance compared to the nonreactive specimen.

Table 7.7 compares the flexural stiffness of each specimen to the dynamic moduli calculated from the full-scale dynamic tests in both the longitudinal and transverse modes of vibration. Although a linear correlation cannot be made between the flexural stiffness and dynamic modulus, the data do suggest that full-scale dynamic tests may be able to provide an indication of how a reinforced concrete beam will respond to a flexural load. It appears that this method can detect, to some extent, the effect of self-post-tensioning that occurs in reinforced concrete affected by ASR and DEF. Although these preliminary results are promising, the test is in need of further refinement. As noted in Chapter 5, real structures will be under load and have more complicated boundary conditions than the beams tested in this study. Their modal behavior will be more complex, and results of any similar test in the field will need to be combined with computer models and modal analysis.

Table 7.7: Comparison of full-scale dynamic test results and flexural stiffness.

Specimen	E_d , ksi (MPa)		Flexural Stiffness kip/in. (kN/mm)
	Longitudinal Mode	Transverse Mode	
Nonreactive	4380 (30.2)	3770 (26.0)	738 (129)
First Reactive	4980 (34.3)	4080 (28.1)	1419 (248)
Second Reactive	4520 (31.1)	3770 (26.0)	1395 (244)

Specific results from the penetrating electromagnetic sensors have not been released for discussion due to the proprietary nature of the technology. However, discussions with G2MT, LLC have revealed that the sensors did detect changes in the received signals that corresponded to an increase in the applied loads. Further calibration of the sensors using various sizes of reinforcement and concrete cover depth will likely be required to improve this technology. Should this prove successful, it will be an exceptionally valuable tool for assessing the condition of not only structures affected by ASR and DEF, but any structure where the condition of the reinforcement is in question.

7.5.3 Implications for Evaluating Structures

These results of these tests call in to question the value of mechanical testing of core samples for predicting the flexural load-carrying capacity of reinforced concrete beams affected by ASR and DEF. While the elastic moduli and compressive strengths correspond to the level of distress indicated by the measured expansions, they did not have any correlation to the flexural moment capacity. Since flexural behavior is governed primarily by the reinforcement in a tension-controlled section, the moment capacity is therefore dependent on the condition of the steel, and the confinement that it imposes on the concrete.

A more sophisticated method of predicting load-carrying capacity may be able to account for the combination of confinement effects, reduced concrete mechanical properties, and potential relaxation of strains in the reinforcement, if all these variables could be measured. The

relaxation of strains in the reinforcement is a strong possibility, given that the loads at which expansion measurements indicated yielding of the tension reinforcement did not correspond to the transition to post-yield behavior in the load-deflection plots for the reactive specimens (Figure 7.5). However, a more complicated analytical procedure may not be necessary unless a linear-elastic analysis as performed in this study were to call into question the safety of the structure. In this study, the calculated moment capacity and deflections were relatively unaffected by the decrease in concrete strength and stiffness. There would be no justification for a more complex analysis to determine whether the moment capacity had increased as a result of ASR or DEF.

The cores were also of little value in predicting deflections under short-term loads. It should be noted that the specimens in this study contained equal amounts of compression and tension reinforcement, which certainly limited the development of creep deflections that developed during the conditioning period leading up to the tests. However, since the measured deflections were only slightly smaller than predicted, the current analytical model based on the core mechanical properties could be seen as successful, providing a slightly conservative predication for short-term deflections.

Mechanical tests on cores may still be of value for other failure modes, such as shear, in which strength of the concrete is a more significant factor. Thus, it would not be prudent to eliminate these tests from a testing and evaluation protocol for structures affected by ASR and DEF. However, it is important to keep in mind that these tests only measure the mechanical properties of concrete after it has been removed from the structure, and should not be taken on their own as an indication of the ability of the structure to carry load.

Most NDT methods gave results that conflicted with the observed behavior of the specimens under flexural loading. As with the testing of cores, UPV and impact-echo tests indicated that the reactive specimens had deteriorated. Only the full-scale dynamic test seemed to provide data showing that the reactive specimens would perform at least as well as, if not better than, the nonreactive specimen.

These results should not be taken to show that ASR and DEF are beneficial to a structure, or even benign. Three aspects of safety and serviceability could not be examined in this study, primarily due to the accelerated nature of the conditioning program.

The first is the threat of spalled concrete falling from elevated structures. Over time, the portions of the unconfined cover region can fall off; this is especially true for end regions that are most exposed to wetting and drying cycles, yet lack any confinement from the reinforcement. These do pose a danger to persons or objects located below.

The second factor is the possibility of synergistic deterioration when other damage mechanisms develop, such as corrosion or freezing and thawing. Cracking from ASR and DEF can accelerate the development of these mechanisms, and consequently reducing the service life of the structure. Corrosion is typically inhibited by the highly alkaline environment of ASR-affected concrete, but if open cracks extend to the reinforcement, the steel is no longer protected. Corrosion can cause loss of section in the reinforcement, and consequently will reduce the load-carrying capacity of the structure.

The final aspect is the possibility of fractured shear reinforcement. Although reported cases are so far limited to Japan, the potential impact on the adequacy of the structure makes it imperative that a technique be developed to detect fractured reinforcement or warn of an impending fracture. The penetrating electromagnetic sensors under development by G2MT, LLC may present a solution.

7.6 Summary

Flexural load tests were conducted on all three full-scale reinforced beam specimens. From these tests, the following conclusions can be drawn:

- All specimens exceeded their predicted nominal moment capacities
- The reactive specimens had greater flexural moment capacities than the nonreactive specimen
- The reactive specimens experienced less deflection than the reactive specimens at their predicted nominal moment capacities
- The mechanical properties of core samples did not correlate to the observed moment capacity or deflections under short-term load
- A self-post-tensioning effect was responsible for the increased stiffness, and consequent smaller deflections of the reactive specimens
- This self-post-tensioning effect was evident in the full-scale dynamic test, the only NDT method which gave results consistent with the load tests.

These results suggest that ASR and DEF are not, by themselves, a threat to the flexural load-carrying capacity of well-reinforced concrete beams. Further work may improve the ability of engineers to accurately predict the behavior of affected structures based on the mechanical properties of core samples, although a reasonable estimate of expansion (and therefore, steel strain) will be required. While beams are typically designed to fail in flexure, other failure modes still need to be considered, as the loss of concrete properties may result in a shift to an unexpected mode of failure. Finally, the prospect of other material deterioration mechanisms must be taken into consideration, as these may still cause a reduction in the expected service life of the structure, even if the structural integrity is not in jeopardy at the time of an investigation.

Chapter 8. Conclusions

8.1 Overview

As part of TxDOT project 0-6491, “Nondestructive Evaluation of In-Service Concrete Structures Affected by ASR and/or DEF,” researchers at The University of Texas at Austin conducted a wide range of tests on plain and reinforced concrete at multiple scales. Included in the study were small cylinders and prisms, larger plain and reinforced concrete specimens in outdoor exposure, full-scale reinforced concrete beams, and core samples from the outdoor exposure specimens and full-scale reinforced concrete beams. The full-scale beams were some of the largest specimens affected by ASR and DEF ever fabricated and tested in the laboratory with cradle-to-grave monitoring and testing. Nondestructive test methods were applied at all scales, and the full-scale beams were also tested in four-point flexure to determine the effects of large expansions from ASR and DEF on flexural strength and serviceability.

The conclusions from these tests, described in the previous chapters, are summarized in Section 8.2. It should be noted that these conclusions are based on tests of well-reinforced beams with equal compression and tension reinforcement, and should not be the basis for determining the adequacy of structural members that are either poorly confined or unreinforced, or their performance in other modes of failure.

A major goal of this research was to offer suggested improvements to the latest published guidance for the evaluation of structures affected by ASR and DEF. This could include the removal of ineffective tests, addition of new test methods, or simply additional guidance regarding the use of currently recommended tests. Specific recommendations, based on the results of this research, are provided in Section 8.3. A more holistic synthesis of the lessons learned from this research is discussed in Section 8.4

Finally, several aspects of this research were found deserving of future study for their potential to improve the evaluation of structures affected by ASR and DEF. These will be described in Section 8.5.

8.2 Conclusions

The following represent the most significant conclusions from this research:

1. **The two reactive full-scale beams exceeded their predicted flexural moment capacities and that of the nonreactive specimen.** This is consistent with prior research showing that ASR and DEF are unlikely to result in a loss of the flexural moment capacity of well-reinforced concrete structural elements. A self-post-tensioning effect that has been frequently mentioned in prior research is most likely responsible. Prior studies with laboratory-fabricated specimens involved much smaller specimens, and it is important to confirm that the same behavior occurs on a scale representative of in-service structural elements.
2. **The two reactive full-scale beams experienced less deflection than the nonreactive specimen at their predicted nominal moment capacities.** The two reactive specimens exhibited a much greater flexural stiffness than the nonreactive specimen, despite a severe reduction in the elastic modulus of the concrete in the reactive specimens. A self-post-tensioning effect that has been frequently mentioned in prior research is most likely responsible.

3. **Core sample mechanical properties showed no correlation to either the strength or stiffness of the reactive full-scale beams in flexural load tests.** However, flexural behavior is primarily governed by the condition of the reinforcement. In these tests, the reinforcement, though strained by the expansion of the concrete, remained intact, and the loss of concrete strength and stiffness had little impact on the predicted moment capacities and deflections of the two reactive specimens.
4. **The full-scale dynamic test was the only NDT method that showed any correlation to structural behavior in the four-point flexure testing of the full-scale beams.** Results from this test indicated that the stiffness of the reactive specimens in the longitudinal mode was the same or higher than that of the nonreactive specimen. This is most significant in that this test did not indicate a loss of performance in the reactive specimens. Flexural mode results were more difficult to interpret, but this may improve this in the future if the data can be coupled with computer modeling of modal behavior. Field application of this method will be subject to more complex boundary conditions and will also need to be coupled with computer models.
5. **In-situ UPV and impact-echo tests and laboratory resonant frequency testing of cores were good indicators of low levels of expansion from ASR and DEF.** However, a more detailed investigation of a structure is unlikely unless expansions exceed 0.10%. For expansions above this level, the effectiveness of these NDT methods is greatly reduced, and if applied according to the existing FHWA evaluation protocol, they will be unable to detect significant changes in the structure. Also, they will be most effective if an undamaged portion of the structure can be tested to establish a baseline, or if testing begins before the onset of distress.
6. **Surface wave NDT methods were poor indicators of ASR and DEF damage.** SASW gave results somewhat similar to UPV and impact-echo, but the data were more scattered, while testing and data processing were considerably more time consuming. Results of the SWT tests showed no consistent trends compared to expansion. Both test methods are likely hampered by the near-field effect caused by the dense crack network caused by ASR and DEF.
7. **The stiffness damage test (SDT), as performed in this research, had widely varied success in correlating to expansion caused by ASR and DEF.** The 1st Cycle Area was a better parameter than the Total Plastic Strain, and the test may be able to distinguish between damage from DEF alone vs. ASR or a combination of ASR and DEF. In many cases, the correlation between the 1st Cycle Area and expansion from ASR (the more common condition in field structures) was tenuous at best. The results were also showed much greater variation than standardized elastic modulus tests on the same specimens. Both the concrete strength and the rate of expansion appear to influence SDT results, not just the absolute amount of expansion.
8. **NDT methods cannot diagnose ASR or DEF as a cause of distress.** They can be used to help assess the extent of distress, but a firm diagnosis requires

petrographic examination of cores. Additionally, diagnosis of DEF is improved when coupled with a curing temperature history of the concrete and information regarding the cement chemistry.

9. **Chemical testing and residual expansion testing are useful tools for the prognosis of future expansion.** Both water-soluble alkali and pore solution analysis can be coupled with residual expansion testing of cores to determine whether future expansion is likely. When DEF is suspected, a set of three different residual expansion tests can be used to separately assess the risk (although not necessarily the absolute magnitude) of future expansion from ASR and DEF.
10. **The aggregates in this study, particularly Jobe (F1) may be contributing alkalis both over the life of the concrete and during the water-soluble alkali test.** The latter effect would tend to skew the results of the test, overestimating the alkalis currently available in the pore solution, but can also indicate whether the aggregates are likely to continue to contribute alkalis to the system in the future.

8.3 Recommendations for Evaluation of Structures

Based on this research, the following improvements are offered regarding the FHWA evaluation protocol (Fournier, et al. 2010):

1. **Guidance regarding the structural impact of ASR (and DEF) should be expanded.** Prior guidance documents (ISE 1992, CONTECVET 2000) incorporated more extensive information that would assist structural engineers in evaluating ASR- and DEF-affected structures. Most importantly, the *self-post-tensioning* effect should be discussed with regards to well-reinforced structures, as this appears to be the reason that structural behavior generally not degraded. Although the reactive specimens in this research outperformed the nonreactive specimen, analytical procedures recommended in future guidance should not be aimed at calculating any improvement in performance as a result of ASR or DEF.
2. **Instructions for the stiffness damage test should be modified based on this research and recent work by Sanchez et al., (2012a).** Further refinement and proof of the robustness of the proposed technique will be necessary before an updated procedure can be incorporated; however, the conclusion that loads of 30 to 40% of the compressive strength are required appears to be well-founded. As of this writing, the best guidance would be to include a reference to the recent work and recommend that only the 1st Cycle Area, and not the Total Plastic Strain be used to quantify damage. Additionally, it can be noted that concrete affected solely by DEF tends to produce the highest SDT values, while concrete affected by ASR or ASR and DEF give similar values.
3. **Remove the recommendation for the elastic rebound test.** In a structures affected by ASR and DEF, confinement provided by the reinforcement is critical to maintaining the load-carrying capacity of the structure and preventing excessive deflections. No tests which involve severing reinforcement should be conducted. Additionally, if the test is conducted in a “low-risk” region of the

structure, the strain state of the reinforcement at that location may not necessarily be representative of that in more critical regions of the structure.

4. **Incorporate improved guidance for the interpretation of NDT results and the proper application of these methods.** The current guidance recommends UPV and impact-echo, but not until a Level 3 (detailed investigation) is conducted. UPV in particular is a simple test that can rapidly assess large areas of the structure. Impact-echo requires more operator skill, but can too be applied rapidly and data analysis has been automated with commercial equipment. These tests may be more valuable if applied in regular inspections or lower level investigations, before distress is so great as to limit their effectiveness. Guidance regarding the importance of testing an undamaged portion of the structure to provide a baseline measurement should be included. Finally, a reference to ACI 228.2R (1998), which details NDT methods and interpretation of results, should be included.
5. **Incorporate the three parallel residual expansion tests recommended by Folliard et al. (2007) for cases in which DEF is also suspected as a damage mechanism.** This is a powerful tool which is recommended in TxDOT guidance, but not the FHWA protocol, which deals exclusively with ASR.

8.4 Synthesis

The research covered in this report encompassed a wide variety of test methods and specimen types, although the ultimate goal was to improve the evaluation of real-world concrete structures affected by ASR and DEF. Effective evaluation and management of affected structures involves not only determining which structures require mitigation measures, but also avoiding costly repairs or replacements that are either unhelpful or unnecessary. Table 8.1 provides a summary of the various tests, noting which specimen types they were applied to, and comments regarding the utility of each test for the evaluation of an in-service structure.

Table 8.1: Summary of tests performed.

Test	Small Scale			Exposure Site Specimens	Full-Scale Beams	Comments
	Prisms	Cylinders	Cores			
Expansion Measurements	X	X		X	X	Best indication of progress of reaction. Useful results require several years of monitoring.
Residual Expansion			X			Good prognostic tool in combination with chemical tests. Can help with diagnosis of ASR vs. DEF.
UPV	X	X	X	X	X	Potentially useful in field. Not recommended in lab.
Impact-Echo				X	X	Alternative to UPV in field.
SASW/SWT				X	X	<i>Not recommended.</i>
Nonlinear Acoustics					X	
Resonant Frequency	X	X	X			Recommended over UPV in lab.
Dynamic Testing					X	Simple test with analytical challenges. Some correlation to structural performance.
Stiffness Damage Test		X	X			High variability, needs refinement.
Elastic Modulus		X	X			Good indicators of damage to concrete. No correlation to reinforced concrete performance. Modulus must be measured, not assumed based on strength.
Compressive Strength		X	X			
Water-soluble Alkalis			X			Combine with residual expansion for prognosis of future expansion. Aggregate contributions may skew WSA results.
Pore Solution Analysis			X			
Petrography			X			Critical tool for diagnosing cause of damage. Quantitative (DRI) remains a work in progress.
Full-scale Load Test					X	Best method to assess structural safety, deflection under load.

With regards to nondestructive testing, UPV and impact-echo tests conducted in-situ have proven to be most effective at characterizing small expansions, as they are linked to the drop in stiffness that accompanies the initiation of cracking. However, they are unlikely to be deployed until after ASR or DEF have advanced beyond the stage at which these techniques are sensitive to changes in the concrete. Dynamic testing—if it can be coupled effectively with computer modeling of field structures—holds some promise

A great deal of information can be gained from core samples. However, this information must be considered in the context of conditions specific to a structure under investigation. This includes the environmental exposure conditions (temperature and moisture), loads, and confinement provided by reinforcement and external restraints.

For an unreinforced structure, such as a highway or airfield pavement, the amount of and rate of expansion are very important pieces of information needed to determine when expansion joints can be expected to close. In-situ expansion monitoring coupled with chemical analysis and residual expansion tests can be very useful in this regard. Flexural strength is very important for unreinforced pavements, and this can be evaluated with appropriate tests of extracted specimens. The SDT and DRI techniques remain works in progress, but may someday become refined enough to characterize expansion/distress-to-date more effectively than visual inspection and crack mapping.

In a well-reinforced structure, such as the full-scale beams discussed in Chapters 5 through 7, most tests of core samples would likely prove to be misleading with respect to the load-bearing capacity of the structure. This is primarily a result of confinement, or self-post-tensioning effects that counter the loss of strength and stiffness. However, it would still be important to diagnose the cause of the observed distress by testing core samples, and determine whether other deterioration mechanisms such as corrosion or freezing and thawing are at work. A linear-elastic sectional analysis based on the compressive strength and elastic modulus of core samples should provide a conservative estimate of flexural moment capacity and deflections, if the reinforcement is otherwise undamaged. Elastic modulus should be measured directly, and not calculated based on compressive strength. Should such an analysis suggest the structure may be inadequate or borderline, a load test (to design or service loads, not failure) is the best method of verifying the adequacy of such a structure to carry loads and resist excessive deflections. While a costly and disruptive test, it is a better use of time and money than conducting a wide range of tests that do not have any correlation to structural performance.

8.5 Recommendations for Future Work

The following aspects of this research were found to be deserving of future study:

- 1. Development of a structural evaluation procedure that incorporates the self-post-tensioning effect.** This would be similar to the analysis of prestressed concrete elements, but additional work will be required to verify what fraction of the tensile strain in the steel can be applied as a confining, or post-tensioning force. Creep of the concrete and/or relaxation of steel strain may prevent the use of the full tensile strain.
- 2. Contribution of alkalis by aggregates.** Some aggregates appear capable of contributing large amounts of alkalis in concrete over a period of many years, and even in the short time-frame of the water-soluble alkali test. This not only affects the results of the water-soluble test, but also can have implications for the prevention of ASR. A mixture thought to contain a sufficiently low alkali loading could eventually contain enough available alkalis to trigger expansive ASR. Very little work has been published in this area, and much of it confined to a small group of researchers in Canada, but it is a significant issue deserving of greater attention.
- 3. Further development of the full-scale dynamic test.** Although the challenges of applying this method in the field are great, it is the only NDT method to have shown a correlation to structural performance and the self-post-tensioning effect in the full-scale reinforced beams. For this reason, future work should involve dynamic testing of reactive and nonreactive large-scale prismatic reinforced specimens, coupled with computer modeling and static load testing. If this can be proven effective, then testing can progress to more complex geometries and boundary conditions representative of field structures.
- 4. Refinement of the stiffness damage test (SDT).** As noted above, recommended changes to the stiffness damage test by Sanchez et al. (2012a) appear to have a sound basis. Specimens tested to 30% or more of their compressive strength (ideally 40%) provided more useful data than those tested at lower loads. An

expanded test matrix involving more aggregate types and coupling field and laboratory specimens is needed to prove the robustness of the new test procedure. Some method of normalizing the results of tests performed at different loads (for different strength concretes) will also need to be developed.

5. **Further development of penetrating electromagnetic sensors for the measurement of steel strain.** While this technique is in its infancy (or perhaps a pre-natal state), the potential benefits of non-contact strain measurements of the reinforcement through 2 in. (50 mm) or more of concrete cover are enormous. This could provide a definitive measurement of expansion to-date for structures affected by ASR and DEF, and have significant implications for the evaluation of reinforced concrete structures affected by a wide range of other types of distress. It could also potentially detect reinforcement fracture or provide warning of incipient fracture. Significant challenges remain in calibrating sensors for the metallurgy of reinforcing steel, as well as various bar sizes and cover depths.

References

- ACI Committee 228. *ACI 228.1R-03: In-Place Methods to Estimate Concrete Strength*. Farmington Hills, Michigan: American Concrete Institute, 2003.
- ACI Committee 228. *ACI 228.2R-98: Nondestructive Test Methods for Evaluation of Concrete in Structures*. Farmington Hills, MI: American Concrete Institute, 1998.
- ACI Committee 318. "ACI 318-11: Building Code Requirements for Structural Concrete." Farmington Hills, Michigan, USA: American Concrete Institute, 2011.
- Ahlstrom, G. M., J. Mullarky, and F. Faridazar. "The United States Federal Highway Administrations Effort to Eliminate Alkali-Silica Reaction in Concrete Transportation Structures." Edited by M. A. T. M. Broekmans and B. J. Wigum. *Proceedings of the 13th International Conference on Alkali-Aggregate Reactions in Concrete*. Trondheim, Norway, 2008. 10.
- Ahmed, T., E. Burley, S. Rigden, and A.I. Abu-Tair. "The Effect of Alkali Reactivity on the Mechanical Properties of Concrete." *Construction and Building Materials* 17 (2003): 123-144.
- ASTM C39-10. "Standard Test Method for Compressive Strength of Cylindrical Concrete Specimens." West Conshohocken, Pennsylvania: ASTM International, 2010.
- ASTM C42-11. "Standard Test Method for Obtaining and Testing Drilled Cores and Sawed Beams of Concrete." West Conshohocken, Pennsylvania: ASTM International, 2011.
- ASTM C78-10. "Standard Test Method for Flexural Strength of Concrete (Using Simple Beam with Third-Point Loading)." West Conshohocken, Pennsylvania, USA: ASTM International, 2010.
- ASTM C114-11b. "Standard Test Methods for Chemical Analysis of Hydraulic Cement." West Conshohocken, Pennsylvania: ASTM International, 2011.
- ASTM C192-07. "Standard Practice for Making and Curing Concrete Test Specimens in the Laboratory." West Conshohocken, PA: ASTM International, 2007.
- ASTM C597-02. "Standard Test Method for Pulse Velocity through Concrete." West Conshohocken, Pennsylvania: ASTM International, 2002.
- ASTM C215-08. "Standard Test Method for Fundamental Transverse, Longitudinal, and Torsional Resonant Frequencies of Concrete Specimens." West Conshohocken, Pennsylvania: ASTM International, 2008.
- ASTM C469-10. "Standard Test Method for Static Modulus of Elasticity and Poisson's Ratio of Concrete in Compression." West Conshohocken, Pennsylvania: ASTM International, 2010.
- ASTM C490-11. "Standard Practice for Use of Apparatus for the Determination of Length Change of Hardened Cement Paste, Mortar, and Concrete." West Conshohocken, PA, USA: ASTM International, 2011.

- ASTM C494-11. "Standard Specification for Chemical Admixtures for Concrete." West Conshohocken, Pennsylvania, USA: ASTM International, 2011.
- ASTM C496-11. "Standard Test Method for Splitting Tensile Strength of Concrete Cylindrical Specimens." West Conshohocken, Pennsylvania, USA: ASTM International, 2011.
- ASTM C597-09. "Standard Test Method for Pulse Velocity through Concrete." West Conshohocken, Pennsylvania: ASTM International, 2009.
- ASTM C666-03. "Standard Test Method for Resistance of Concrete to Rapid Freezing and Thawing." West Conshohocken, Pennsylvania, USA: ASTM International, 2008.
- ASTM C702-11. "Standard Practice for Reducing Samples of Aggregate to Testing Size." West Conshohocken, PA: ASTM International, 2011.
- ASTM C856-11. "Standard Practice for Petrographic Examination of Hardened Concrete." West Conshohocken, Pennsylvania, USA: ASTM International, 2011.
- ASTM C1260-07. "Standard Test Method for Potential Alkali Reactivity of Aggregates (Mortar Bar Method)." West Conshohocken, PA, United States: ASTM International, 2007.
- ASTM C1293-08b. "Standard Test Method for Determination of Length Change of Concrete Due to Alkali-Silica Reaction." West Conshohocken, PA, United States: ASTM International, 2008.
- Bach, F., T. Thorsen, and M. Nielsen. "Load carrying capacity of structural members subjected to alkali-silica reactions." *The 9th International Conference on Alkali-Aggregate Reaction in Concrete*. London, 1992. 231-239.
- Baber, T. T., J. C. Lydzinski, and R. S. Turnage. "FEM Analysis and Field Vibration Testing of a Multispan Curved Girder Bridge." *Structures 2009: Don't Mess with Structural Engineers*. Austin, Texas, USA: ASCE, 2009. 174-182.
- Barneyback, R. S. "Alkali-Silica Reactions in Portland Cement Concrete." Ph. D. Thesis, School of Civil Engineering, Purdue University, West Lafayette, Indiana, 1981.
- Barneyback, R. S., and S. Diamond. "Expression and Analysis of Pore Fluids From Hardened Cement Pastes and Mortars." *Cement and Concrete Research* 11 (1981): 279-285.
- Bentivegna, A. B. "Development and monitoring of an outdoor exposure site to mitigate alkali-silica reaction in hardened concrete." MS Thesis, University of Texas at Austin, Austin, Texas, 2009.
- Bérubé, M.-A., and C. Tremblay. "Chemistry of pore solution expressed under high pressure: influence of various parameters and comparison with the hot-water extraction method." Edited by M. Tang and M. Deng. *Proceedings of the 12th International Conference on Alkali-Aggregate Reaction in Concrete*. Beijing, 2004. 833-842.
- Bérubé, M.-A., B. Durand, B. Bissonette, B. Fournier, and N. Smaoui. "Evaluation of the expansion attained to date by concrete affected by alkali silica reaction. Part III:

- Application to existing structures." *Canadian Journal of Civil Engineering* 32, no. 3 (2005): 463-479.
- Bérubé, M.-A., J. Duschene, J. F. Dorion, and M. Rivest. "Laboratory assessment of alkali contribution by aggregates to concrete and application to concrete structures affected by alkali-silica reactivity." *Cement and Concrete Research* 32 (2002a): 1215-1227.
- Bérubé, M.-A., J. Frenette, A. Pednault, and M. Rivest. "Laboratory Assessment of the Potential Rate of ASR Expansion." Edited by M.-A. Bérubé, B. Fournier and B. Durand. *Proceedings of the 11th International Conference on Alkali-Aggregate Reaction in Concrete*. Québec City, 2000. 821-830.
- Bérubé, M.-A., J. Frenette, M. Rivest, and D. Vezina. "Measurement of the alkali content of concrete using hot-water extraction." *Cement, Concrete and Aggregates* 24, no. 1 (2002b): 28-36.
- Blight, G. E., M. G. Alexander, T. K. Ralph, and B. A. Lewis. "Effect of Alkali-Aggregate Reaction on the Performance of a Reinforced Concrete Structure over a Six-Year Period." *Magazine of Concrete Research* 41, no. 147 (1989): 69-77.
- Blight, G. E., M. G. Alexander, W. K. Schutte, and T. K. Ralph. "The effect of alkali-aggregate reaction on the strength and deformation of a reinforced concrete structure." *Proceedings of the 6th International Conference on Alkali-Aggregate Reaction*. Copenhagen: Technical University of Denmark, 1983. 401-410.
- Boenig, A. "Bridges with Premature Concrete Deterioration: Field Observations and Large Scale Testing." MS Thesis, University of Texas at Austin, Austin, Texas, USA, 2000.
- Bremner, T. W., A. J. Boyd, T. A. Holm, and S. R. Boyd. "Tensile Testing to Evaluate the Effect of Alkali-Aggregate Reaction in Concrete." *Proceedings of Alkali-Aggregate Reactions in Concrete*. Dartmouth, NS, Canada: CANMET/NRC, 1996. 311-325.
- BS 6319. "Method for Measurement of Tensile Strength, Part 7: Testing of Resin Compositions for Use in Concrete." 1985.
- Carino, N. J. "Stress Wave Propagation Methods." In *Handbook on Nondestructive Testing of Concrete, 2nd Edition*, edited by V. M. Malhotra and N. J. Carino, 34. West Conshohocken, Pennsylvania, USA: CRC Press, 2004.
- Chana, P. S., and G. A. Korobokis. *The Structural Performance of Reinforced Concrete Affected by Alkali Silica Reaction: Phase II*. Contractor Report 311, Crowthorne, Berkshire, United Kingdom: Transport and Road Research Laboratory, 1992, 68.
- Chatterji, S. "On the Relevance of Expressed Liquid Analysis to the Chemical Processes Occuring in a Cement Paste." *Cement and Concrete Research* 21 (1991): 269-272.
- Chen, J., A. R. Jayapalan, J.-Y. Kim, K. E. Kurtis, and L. J. Jacobs. "Rapid Evaluation of Alkali-Silica Reactivity of Aggregates Using a Nonlinear Resonance Spectroscopy Technique." *Cement and Concrete Research* 40 (2010): 914-923.

- Chrisp, T. M., P. Waldron, and J. G. M. Wood. "Development of a Non-destructive Test to Quantify Damage in Deteriorated Concrete." *Magazine of Concrete Research* 45, no. 165 (1993): 247-256.
- Constantiner, D., and S. Diamond. "Alkali release from feldspars into pore solutions." *Cement and Concrete Research* 33 (2003): 549-554.
- Constantiner, D., and S. Diamond. "Pore Solution Analysis: Are There Pressure Effects?" In *Mechanisms of Chemical Degradation of Cement-based Systems*, edited by K. L. Scrivener and J. F. Young, 22-29. London: E & FN Spon, 1997.
- CONTECVET. *Manual for Assessing ASR Affected Concrete Structures*. EC Innovation Programme IN 30902I, 2000, 95.
- Crouch, R S, and J G M Wood. "Damage Evolution in AAR Affected Structures." *International Symposium on Fracture Damage of Concrete and Rock*. Vienna, 1988.
- CSA. *Guide to the Evaluation and Management of Concrete Structures Affected by Alkali-Aggregate Reaction*. CSA A864-00, Mississauga, Ontario: Canadian Standards Association, 2000.
- CSA International. *Guide to the Evaluation and Management of Concrete Structures Affected by Alkali-Aggregate Reaction*. Toronto, Canada: CSA International, 2000, 116.
- Cyr, M., P. Rivard, F. Labrecque, and A. Daidié. "High-Pressure Device for Fluid Extraction from Porous Materials: Application to Cement-Based Materials." *Journal of the American Ceramic Society* 91, no. 8 (2008): 2653-2658.
- Danay, A. "Structural Mechanics Methodology in Diagnosing and Assessing Long-Term Effects of Alkali-Aggregate Reactivity in Reinforced Concrete Structures." *ACI Materials Journal* 91, no. 1 (1994): 54-62.
- Davies, C. E., and R. E. Oberholster. "Alkali-silica reaction products and their development." *Cement and Concrete Research* 18 (1988): 621-635.
- De Ceukelaire, L. "Alkali-Silica Reaction in a Lightweight Concrete Bridge." *The 9th International Conference on Alkali-Aggregate Reaction in Concrete*. London, 1992. 231-239.
- Deschenes, D. J. "ASR/DEF-Damaged Ben Caps: Shear Tests and Field Implications." MS Thesis, The University of Texas at Austin, Austin, Texas, 2009.
- Diamond, S. "Alkali reactions in concrete - pore solution effects." *Proc. Sixth International Conference on Alkalis in Concrete: Research and Practice*. Copenhagen, 1983. 155-166.
- Diamond, S. "Alkali-Silica Reactions - Some Paradoxes." Edited by A. Shayan. *Proceedings of the 10th International Conference on Alkali-Aggregate Reaction in Concrete*. Melbourne, 1996. 3-14.
- Drimalas, T. "Laboratory Testing and Investigations of Delayed Ettringite Formation." MS Thesis, The University of Texas at Austin, Austin, Texas, 2004.

- Durand, B., J. Bérard, R. Roux, and J. A. Soles. "Alkali-Silica Reaction: The Relation Between Pore Solution Characteristics and Expansion Test Results." *Cement and Concrete Research* 20 (1990): 419-428.
- Duschene, J., and M.-A. Bérubé. "Evaluation of the Validity of the Pore Solution Expression Method from Hardened Cement Pastes and Mortars." *Cement and Concrete Research* 24, no. 3 (1994): 456-462.
- Duschene, J., and M.-A. Bérubé. "The Effectiveness of Supplementary Cementitious Materials in Suppressing Expansion due to ASR: Another Look at the Reaction Mechanisms Part 2: Pore Solution Chemistry." *Cement and Concrete Research* 24, no. 2 (1994): 221-230.
- Famy, C., K. L. Scrivener, A. Atkinson, and A. R. Brough. "Influence of the storage conditions on the dimensional change of heat-cured mortars." *Cement and Concrete Research* 31 (2001): 795-803.
- Folliard, K. J., et al. *Preventing ASR/DEF In New Concrete: Final Report*. Austin: Center for Transportation Research, 2006.
- Folliard, K. J., M. D. A. Thomas, and B. Fournier. *Protocol for the Diagnosis and Prognosis of Concrete Structures Affected by Alkali-Silica Reaction and/or Delayed Ettringite Formation*. Austin, Texas, USA: Concrete Durability Center, The University of Texas at Austin, 2007, 42.
- Fournier, B. *Personal communications*. April 23, 2009.
- Fournier, B., and M.-A. Bérubé. "Recent applications of a modified gel pat test to determine the potential alkali-silica reactivity of carbonate aggregates." *Cement and Concrete Composites* 15, no. 1-2 (1993): 49-73.
- Fournier, B., M.-A. Bérubé, K. J. Folliard, and M. Thomas. *Report on the Diagnosis, Prognosis, and Mitigation of Alkali-Silica Reaction (ASR) in Transportation Structures*. Report No. FHWA-HIF-09-004, Washington, DC: Federal Highway Administration, U.S. Department of Transportation, 2010, 147.
- Fournier, B., M.-A. Bérubé, K. J. Folliard, and M. Thomas. *Report on the Diagnosis, Prognosis, and Mitigation of Alkali-Silica Reaction (ASR) in Transportation Structures*. Report No. FHWA-HIF-09-004, Washington, DC: Federal Highway Administration, U.S. Department of Transportation, 2010, 147.
- Ghorab, H.Y. "Review of Ettringite-Monophase Relationships in Portland Cement Systems." Edited by B. Erlin. *Ettringite - The Sometimes Host of Destruction, SP 177*. Farmington Hills, Michigan: American Concrete Institute, 1999. 65-80.
- Giannini, E. R. "Field Studies of Mitigation Strategies for Alkali-Silica Reaction in Hardened Concrete." MS Thesis, University of Texas at Austin, Austin, Texas, USA, 2009, 152.
- Giannini, E. R., and J. Zhu. "Effects of Elevated Curing Temperatures on the Mechanical Properties of Concrete Cylinders." *Proceedings of the 14th International Conference on Structural Faults and Repair*. Edinburgh, 2012.

- Gibson, A. "Advances in nondestructive testing of concrete pavements." PhD Dissertation, University of Illinois at Urbana-Champaign, 2004.
- Gibson, A., and J. S. Popovics. "Lamb wave basis for impact-echo method analysis." *Journal of Engineering Mechanics* 131, no. 4 (2005): 438-443.
- Godart, B., P Fasseau, and M. Michel. "Diagnosis and Monitoring of Concrete Bridges Damaged by AAR in Northern France." *Proceedings of the 9th International Conference on Alkali-Aggregate Reaction*. London, 1992. 368-375.
- Goguel, R. "Alkali Release by Volcanic Aggregates in Concrete." *Cement and Concrete Research* 25, no. 4 (1995): 841-852.
- Grattan-Bellew, P. E. "Alkali Contribution from Limestone Aggregate to Pore Solution of Old Concrete." *ACI Materials Journal* 91, no. 2 (1994): 173-177.
- Grattan-Bellew, P. E. "Laboratory Evaluation of Alkali-Silica Reaction in Concrete from Saunders Generating Station." *ACI Materials Journal* 95 (March-April 1995): 126-134.
- Grattan-Bellew, P. E., and L. D. Mitchell. "Quantitative Petrographic Analysis of Concrete - The Damage Rating Index (DRI) Method, A Review." Edited by B. Fournier. *Marc-André Bérubé Symposium on Alkali-Aggregate Reactivity in Concrete*. Montréal, 2006. 321-334.
- Grattan-Bellew, P.E. "Laboratory Evaluation of Alkali-Silica Reaction in Concrete from Saunders Generating Station." *ACI Materials Journal* 95 (March-April 1995): 126-134.
- Hanson, B. P. *Flexural Capacity of Reinforced Concrete Beams Affected by Alkali Silica Reaction and Delayed Ettringite Formation*. MS Departmental Report, Austin, Texas, USA: The University of Texas at Austin, 2012.
- Helene, P. H. "Contribution to the Establishment of Parameters for Portland Cement Concrete Mixture and Quality Control." PhD Thesis, Polytechnic School, Civil Engineering Department, University of Sao Paulo, Sao Paulo, Brazil, 1987, 269.
- Henriksen, C. "Impact-echo Testing." *Concrete International* 17, no. 5 (1995): 55-58.
- Hobbs, D. W. "Expansion due to Alkali-Silica Reaction and the Influence of Puverized Fuel Ash." *Proceedings of the 5th International Conference on Alkali-Aggregate Reaction*. Cape Town, 1981.
- Huang, Q., P. Gardoni, and S. Hurlbaas. "Probabalistic Capacity Models and Fragility Estimates for Reinforced Concrete Columns Incorporating NDT Data." *Journal of Engineering Mechanics* 135, no. 12 (2009): 1384-1392.
- Imai, H., T. Yamasaki, H. Maehara, and T. Miyagawa. "The deterioration by alkali-silica reaction of Hanshin Expressway concrete structures." *Proceedings of the 6th International Conference on Alkali-Aggregate Reaction*. Copenhagen: Technical University of Denmark, 1983. 131-135.
- ISE. *Structural Effects of Alkali-Silica Reaction*. London: Institution of Structural Engineers , 1992, 45.

- Jones, A. E. K., and L. A. Clark. "The Practicalities and Theory of Using Crack Width Summation to Estimate ASR Expansion." *Proceedings of the Institution of Civil Engineers: Structures and Buildings* 104, no. 2 (1994): 183-192.
- Kagimoto, H., M. Sato, and M. Kawamura. "Evaluation of the Degree of Deterioration in AAR Damaged Concretes and Analysis of their Pore Solutions." Edited by M.-A. Bérubé, B. Fournier and B. Durand. *11th International Conference on Alkali-Aggregate Reaction*. Québec City, 2000. 859-868.
- Kee, S. *Personal Communication*. 2010.
- Kee, S., and J. Zhu. "Using air-coupled sensors to determine the depth of a surface-breaking crack in concrete." *Journal of the Acoustical Society of America* 127, no. 3 (2010): 1279-1287.
- Kelham, S. "The Effect of Cement Composition and Fineness on Expansion Associated with Delayed Ettringite Formation." *Cement & Concrete Composites* 18 (1996): 171-179.
- Kesner, K., M. Sansalone, and R. W. Poston. "Detection and quantification of distributed damage in concrete using transient stress waves." *ACI Materials Journal* 101, no. 4 (2004): 318-326.
- Kodjo, A., P. Rivard, F. Cohen-Tenoudji, and J. L. Gallias. "Evaluation of Damages due to Alkali-Silica Reaction with Nonlinear Acoustics Techniques." *XIV International Conference on Nonlinear Elasticity in Materials*. Lisbon: Acoustical Society of America, 2009. 1-10.
- Kreitman, K. "Nondestructive Evaluation of Reinforced Concrete Structures Affected by Alkali-Silica Reaction and Delayed Ettringite Formation." MS Thesis, The University of Texas at Austin, Austin, Texas, 2011.
- Langely, W. S., E. Brown, C. T. Chen, and J. Balinski. "Performance of an Alkali-Aggregate Affected Power Dam Upper Lake Falls Dam, Plant #1, Mersey River, Nova Scotia." Edited by M.-A. Bérubé, B. Fournier and B. Durand. *11th International Conference on Alkali-Aggregate Reaction*. Québec City, 2000. 1343-1352.
- Larson, N. "Structural Performance of ASR/DEF Damaged Prestressed Concrete Trapezoidal Box Beams with Dapped Ends." MS Thesis, The University of Texas at Austin, Austin, Texas, 2010.
- Lasseigne, A. *Personal Communication*. 2012.
- Lauer, K. R. "Magnetic/Electrical Methods." Chap. 10 in *Handbook on Nondestructive Testing of Concrete, 2nd Edition*, edited by V. M. Malhotra and N. J. Carino, 21. West Conshohocken, Pennsylvania, USA: CRC Press, 2004.
- Longuet, P., L. Burglen, and A. Zelwer. "La Phase Liquide du Ciment Hydraté." *Revue des Matériaux de Construction et de Travaux Publics*, no. 676 (1973): 35-41.

- Malhotra, V. M. *Testing Hardened Concrete: Nondestructive Methods*. ACI Monograph No. 9. Detroit, Michigan: American Concrete Institute, 1976.
- Mikata, Y., Y. Shimazu, Y. Hatano, and S. Inoue. "Flexural and Shear Capacity of PRC Beams Damaged by Combined Deterioration Due to ASR and Corrosion." Edited by T. Drimalas, J. H. Ideker and B. Fournier. *Proceedings of the 14th International Conference on Alkali-Aggregate Reaction in Concrete*. Austin, Texas, USA, 2012. 10.
- Martin, R.-P., C. Bazin, and F. Toutlemonde. "Alkali Aggregate Reaction and Delayed Ettringite Formation: Common Features and Differences." Edited by T. Drimalas, J. H. Ideker and B. Fournier. *Proceedings of the 14th International Conference on Alkali-Aggregate Reactions in Concrete*. Austin, Texas, USA, 2012.
- Miyagawa, T., K. Seto, K. Sasaki, Y. Mikata, K. Kuzume, and T. Minami. "Fracture of Reinforcing Steels in Concrete Structures Damaged by Alkali-Silica Reaction - Field Survey, Mechanism and Maintenance." *Journal of Advanced Concrete Technology* 4, no. 3 (2006): 339-355.
- Monette, L. J.-G. "Effects of the Alkali-Silica Reaction on Unloaded, Statically Loaded and Dynamically Loaded Reinforced Concrete Beams." MS Thesis, University of Ottawa, Ottawa, 1997. 185.
- Muller, M., A. Sutin, R. Guyer, M. Talmant, P. Laugier, and P. Johnson. "Nonlinear resonant ultrasound spectroscopy (NRUS) applied to damage assessment in bone." *The Journal of the Acoustical Society of America* 118, no. 6 (2005): 3946-3952.
- Naik, T.R., V.M. Malhotra, and J.S. Popvics. "The Ultrasonic Pulse Velocity Method." Chap. 8 in *Handbook on Nondestructive Testing of Concrete*, edited by V.M. Malhotra and N.J. Carino. West Conshohocken, Pennsylvania: ASTM International, 2004.
- Nakagawa, H., M. Yokota, K. Matsuda, and M Matsushima. "Prediction Method for Properties of Concrete on Ultrasonic Non-Destructive Testing." Edited by M.A.T.M Broekmans and B.J. Wigum. *Proceedings of the 13th International Conference on Alkali-Aggregate Reaction in Concrete*. Trondheim, Norway, 2008.
- Neville, A.M. *Properties of Concrete*. New York: John Wiley and Sons, 1963.
- Nixon, P. J., and R. Bollinghaus. "The Effect of Alkali-Aggregate Reaction on the Tensile and Compressive Strength of Concrete." *Durability of Building Materials* 2 (1985): 243-248.
- Ono, K. "Monitoring of AAR Bridge Pier by Vibration Measurement." *Proceedings of the 9th International Conference on Alkali-Aggregate Reaction in Concrete*. London: Concrete Society, 1992. 758-765.
- Pagnotta, A., D. Trejo, and P. Gardoni. "Effects on Impact-Echo Signals Caused by Adjacent Steel Reinforcing Bars and Voids in Lap-Splice Regions: Experimental Study." Edited by T. Drimalas, J. H. Ideker and B. Fournier. *Proceedings of the 14th International Conference on Alkali-Aggregate Reactions in Concrete*. Austin, Texas, USA, 2012.

- Parmelee, C. W., and A. J. Monack. "The Solubility of Feldspars in Water." *Journal of the American Ceramic Society* 13, no. 6 (1930): 386-392.
- Popovics, S. *Strength and Related Properties of Concrete: A Quantitative Approach*. New York: John Wiley & Sons, 1998.
- Popovics, S. *Strength and Related Properties of Concrete: A Quantitative Approach*. New York: John Wiley & Sons, 1998.
- Ramlochan, T. "The Effects of Pozzolans and Slag on the Expansion of Mortars and Concrete Cured at Elevated Temperature." PhD Thesis, Toronto: University of Toronto, 2003.
- Rivard, P., and F. Saint-Pierre. "Assessing Alkali-Silica Reaction Damage to Concrete with Non-destructive Methods: From the Lab to the Field." *Construction and Building Materials* 23, no. 2 (2009): 902-909.
- Rivard, P., and G. Ballivy. "Assessment of the expansion related to alkali-silica reaction by the Damage Rating Index method." *Construction and Building Materials* 19, no. 2 (March 2005): 83-90.
- Rivard, P., M.-A. Bérubé, J. P. Ollivier, and G. Ballivy. "Decrease of pore solution alkalinity in concrete tested for alkali-silica reaction." *Materials and Structures* 40 (2007): 909-921.
- Rogers, C. A., and R. D. Hooton. "Leaching of Alkalis in Alkali-Aggregate Reaction Testing." Edited by K. Okada, S. Nishibayashi and M. Kawamura. *Proceedings of the 8th International Conference on Alkali-Aggregate Reaction in Concrete*. Kyoto, Japan, 1989. 327-332.
- Rothstein, D. *Personal communications*. May 8, 2012a.
- Rothstein, D. *Petrographic Investigation of Concrete Cores from the University of Texas at Austin Field Exposure Test Site Located in Austin, Texas*. DRP Report No. DRP12.952, Boulder, Colorado, USA: DRP Consulting, Inc., 2012b, 42.
- Sagüés, A. A., E. I. Moreno, and C. Andrade. "Evolution of pH during in-situ leaching in small concrete cavities." *Cement and Concrete Research* 27, no. 11 (1997): 1747-1759.
- Sanchez, L., B. Fournier, and M. Jolin. "Critical Parameters of the Stiffness Damage Test for Assessing Concrete Damage due to Alkali-Silica Reaction." Edited by T. Drimalas, J. H. Ideker and B. Fournier. *Proceedings of the 14th International Conference on Alkali-Aggregate Reactions in Concrete*. Austin, Texas, USA, 2012a. 10.
- Sanchez, L., P. Salva, B. Fournier, M. Jolin, N. Pouliot, and A. Hovington. "Evaluation of Damage in the Concrete Elements of the Viaduct "Robert-Bourassa-Charest" After Nearly 50 Years in Service." Edited by T. Drimalas, J. H. Ideker and B. Fournier. *Proceedings of the 14th International Conference on Alkali-Aggregate Reactions in Concrete*. Austin, Texas, USA, 2012b. 10.
- Sansalone, M. "Impact-echo: The Complete Story." *ACI Structural Journal* 94, no. 6 (1997): 777-786.

- Sansalone, M., and W. B. Streett. *Impact-Echo: Non-Destructive Evaluation of Concrete and Masonry*. Jersey Shore, Pennsylvania, USA: Bullbrier Press, 1997.
- Scrivener, K. L., and M. C. Lewis. "Effect of Heat Curing on Expansion of Mortars and Composition of Calcium Silicate Hydrate Gel." Edited by B. Erlin. *Ettringite - The Sometimes Host of Destruction, ACI SP 177*. Farmington Hills, Michigan: American Concrete Institute, 1999. 93-104.
- Shayan, A., R. E. Wark, and A. Moulds. "Diagnosis of AAR in Canning Dam, Characterization of the Affected Concrete and Rehabilitation of the Structure." Edited by M.-A. Bérubé, B. Fournier and B. Durand. *Proceedings of the 11th International Conference on Alkali-Aggregate Reaction in Concrete*. Québec City, 2000. 1383-1392.
- Shrimer, F H. "Application and Use of Damage Rating Index in Assessment of AAR-Affected Concrete - Selected Case Studies." Edited by M-A Bérubé, B Fournier and B Durand. *Proceedings of the 11th International Conference on Alkali-Aggregate Reaction*. Québec City, 2000. 899-908.
- Silva, N. S., A. J. C. T. Cavalcanti, S. C. Kuperman, P. Helene, and N. P. Hasparyk. "AAR at Paulo Afonso Hydroelectric Complex, Part I: Influence on the Mechanical and Elastic Properties of the Concrete." Edited by M. A. T. M. Broekmans and B. J. Wigum. *Proceedings of the 13th International Conference on Alkali-Aggregate Reactions in Concrete*. Trondheim, Norway, 2008. 9.
- Smaoui, N, B Fournier, M-A Bérubé, B Bissonette, and B Durand. "Evaluation of the Expansion Attained to Date by Concrete Affected by Alkali-Silica Reaction. Part II: Application to Nonreinforced Concrete Specimens Exposed Outside." *Canadian Journal of Civil Engineering* 31, no. 6 (2004b): 997-1011.
- Smaoui, N., M.-A. Bérubé, B. Fournier, and B. Bissonnette. "Influence of specimen geometry, orientation of casting plane, and mode of concrete consolidation on expansion due to ASR." *Cement, Concrete and Aggregates* 26, no. 2 (2004c): 58-70.
- Smaoui, N., M.-A. Bérubé, B. Fournier, B. Bissonnette, and B. Durand. "Evaluation of the expansion attained to date by concrete affected by alkali silica reaction. Part I: Experimental study." *Canadian Journal of Civil Engineering* 31, no. 5 (2004a): 826-845.
- Smaoui, Nizar, Marc-Andre Berube, Benoit Fournier, Benoit Bissonette, and Benoit Durand. "Evaluation of the expansion attained to date by concrete affected by alkali silica reaction. Part I: Experimental study." *Canadian Journal of Civil Engineering* 31, no. 5 (2004a): 826-845.
- Stanton, T. E. "Expansion of Concrete through Reaction between Cement and Aggregate." *Publications of the American Society of Civil Engineers* 66 (1940): 1781-1811.
- Stanton, T. E. "Studies to develop an accelerated test procedure for the detection of adversely reactive cement-aggregate combinations." *Proceedings of the American Concrete Institute* 43 (1943): 875-893.

- Swamy, R. N. "Assessment and Rehabilitation of AAR-affected Structures." *Cement and Concrete Composites* 19, no. 5-6 (1997): 427-440.
- Swamy, R. N., ed. *Alkali-Silica Reaction in Concrete*. Glasgow and London: Blackie and Son Ltd., 1992.
- Swamy, R. N., and M. M. Al-Asali. "Engineering Properties of Concrete Affected by Alkali-Silica Reaction." *ACI Materials Journal* 85 (1988): 367-374.
- Swamy, R. N., and M. M. Al-Asali. "Effect of Alkali-Silica Reaction on the Structural Behavior of Reinforced Concrete Beams." *ACI Structural Journal* 86, no. 4 (1989): 451-459.
- Teodoru, G. V. M. "Nondestructive Testing of Concrete from the Research to the Use in the Practice." In *International Advances in Nondestructive Testing, Volume 17*, by W. McGonngale, 117-138. Langhorne, Pennsylvania: Gordon and Breach Science Publishers, 1994.
- Texas Department of Transportation. "Bridge Design Manual - LRFD." 2009.
- Thomas, M. D. A., K. J. Folliard, B. Fournier, T. Drimalas, and P. Rivard. "Study of Remedial Actions on Highway Structures Affected by ASR." Edited by T. Drimalas, J. H. Ideker and B. Fournier. *Proceedings of the 14th International Conference on Alkali-Aggregate Reactions in Concrete*. Austin, Texas, USA, 2012. 10.
- Thomas, M. D. A., K. J. Folliard, T. Drimalas, and T. Ramlochan. "Diagnosing delayed ettringite formation in concrete structures." *Cement and Concrete Research* 38 (2008): 841-847.
- Tinkey, B. V., T. J. Fowler, and R. E. Klingner. *Nondestructive testing of prestressed bridge girders with distributed damage*. Report No 1857-2, Austin, Texas, USA: Center for Transportation Research, The University of Texas at Austin, 2002.
- Torii, K., D. Wasada, T. Sasatani, and T. Minato. "A Survey on ASR-affected Bridge Piers with Fracture of Steel Bars on Noto Expressway." Edited by M. A. T. M. Broekmans and B. J. Wigum. *Proceedings of the 13th International Conference on Alkali-Aggregate Reaction in Concrete*. Trondheim, Norway, 2008. 10.
- Tremblay, S., B. Fournier, M. Thomas, T. Drimalas, and K. Folliard. "The Lomas Boulevard Road Test Site, Albuquerque (New Mexico) - A Case Study on the Use of Preventative Measures Against ASR in New Concrete." Edited by T. Drimalas, J. H. Ideker and B. Fournier. *Proceedings of the 14th International Conference on Alkali-Aggregate Reactions in Concrete*. Austin, Texas, USA, 2012. 10.
- U. S. Nuclear Regulatory Commission. "Inspection Report 0500044312011007." NRC License Renewal Inspection Report, 2011.
- Villeneuve, V., B. Fournier, and J. Duchesne. "Determination of the Damage in Concrete Affected by ASR - The Damage Rating Index (DRI)." Edited by T. Drimalas, J. H. Ideker and B. Fournier. *Proceedings of the 14th International Conference on Alkali-Aggregate Reaction in Concrete*. Austin, Texas, USA, 2012. 10.

- Webb, Z. D. "Experimental Investigation of ASR/DEF-Induced Rebar Fracture." MS Thesis, The University of Texas at Austin, Austin, Texas, USA, 2011.
- Wehrle, E. R. "The Effects of Coatings and Sealers Used to Mitigate Alkali-Silica Reaction and/or Delayed Ettringite Formation in Hardened Concrete." MS Thesis, The University of Texas at Austin, Austin, Texas, 2010.
- Westwood, S., R. Kania, R. Kare, M. Martens, D. Topp, and M. R. Chebaro. "Non-contacting Bi-axial Strain Measurement Method on Steel Pipeline." *Proceedings of IPC2008, 7th International Pipeline Conference*. Calgary, AB, Canada: ASME, 2008. 5.
- Williams, S. A. "Structures Affected by Premature Concrete Deterioration: Diagnosis and Assessment of Deterioration Mechanisms." M.S. Thesis, The University of Texas at Austin, 2005.
- Zhu, J. "Non-contact NDT of concrete structures using air-coupled sensors." PhD Dissertation, University of Illinois at Urbana-Champaign, 2005.